

Stimuli-responsive Supramolecular Materials for Self-healing, Compartmentalization and Strain-stiffening Applications

JOJO P. JOSEPH

*A thesis submitted for the partial fulfillment of
the degree of Doctor of Philosophy*



Institute of Nano Science and Technology
Knowledge City, Sector-81, Mohali, Punjab, 140306, India

Indian Institute of Science Education and Research Mohali
Knowledge city, Sector 81, SAS Nagar, Manauli PO, Mohali, Punjab, 140306, India.

December 2020

Dedicated to

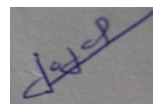
Mother Mary

&

Jesus Christ
my lord and saviour

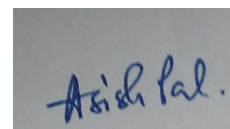
Declaration

The work presented in this thesis has been carried out by me under the guidance of Dr. Asish Pal at Institute of Nano Science and Technology, Mohali. This work has not been submitted in part or in full for a degree, a diploma, or a fellowship to any other university or institute. Whenever contributions of others are involved, every effort is made to indicate this clearly, with due acknowledgement of collaborative research and discussions. This thesis is a bonafide record of original work done by me and all sources listed within have been detailed in the bibliography.



Jojo P. Joseph

In my capacity as the supervisor of the candidate's thesis work, I certify that the above statements by the candidate are true to the best of my knowledge.



Dr. Asish Pal

Acknowledgments

I take this privilege to acknowledge the contributions of many individuals who have been inspirational and supportive throughout my PhD tenure.

At first, I would like to thank my supervisor, Dr. Asish Pal, for his valuable guidance, keen interest, inspiration, unflinching encouragement, patience and moral support throughout my PhD time. He was not only a supervisor but also an encouraging friend. I was always inspired by his scientific thoughts, the way he relates to daily life, systematic working and management. The advice he had given during my struggles gave me the energy to go forward and reach up to this level. He always make sure that I have a very comfortable, competitive and quality environment to conduct my research work. Dear Sir, thanks for uplifting me to a new field of polymer chemistry from a humble background of pharmaceutical chemistry.

I would like to thank the founder-director of INST, Prof. Ashok Kumar Ganguli for giving an opportunity in INST as a PhD student and also for providing all the facilities and encouragement. I will always remember his administrative ways which provided opportunities for me to conduct the research works smoothly. I am thankful for his inspirational words, which he used to deliver during conferences and talks.

I also thank the former director of INST, Prof. H. N. Ghosh for the immense support and advice with a lot of treasured thoughts for my future career.

I am also grateful to the present director Prof. Amitava Patra for his support and encouragement. I always remember his keen interest to provide quality facilities for research by accelerating movement to the new campus despite the Covid pandemic.

I would like to acknowledge my academic committee members Dr. Prakash P. Neelakandan and Dr. Jayamurugan Govindaswamy for their constant advice and support in monitoring my research through the annual review of my progress that helped me a lot in improving the quality of my work.

I am indebted to my internal collaborators Dr. Indranil Sarkar, who gave me an opportunity to become the operator of SAXS and that was my entry to the science of scattering techniques which helped me to enrich my work a lot. I am grateful to Dr. Ehesan Ali for his kind support through theoretical studies which gave me more understanding and revelation into deep chemistry of our systems.

I would like to thank my external SRF committee member, Prof Ravindranath Kartha from NIPER Mohali for his valuable support and advice in work and for the collaboration with organogel work in my first year which was my entry into the science of rheology.

I am thankful to Dr. V. K. Aswal for facilitating me with Small-Angle Neutron Scattering during in BARC Mumbai. I am grateful to Dr. Debes Ray who helped me in analyzing SANS results and gave me a lot of information regarding the theoretical models which gave me more insights about the polymer chain collapse concept.

I am also contented to Dr. Kamlesh Kumar from CSIO, Chandigarh who had rendered an opportunity to work with him in dye related systems and helped me to get more insights in calorimetric techniques.

I would like to greatly appreciate my lab members Dr. Ashmeet Singh, Deepika Gupta, Chirag Miglani, Dr. Nidhi Gupta, Nimisha Mavlinkar and Antarlina Maulik who helped me in conducting my research work and also proof-reading my thesis. I would like to thank Ashmeet Singh for his selfless support even in late night at the lab and also to help me cope with the unfamiliar northern environment. I am thankful to Deepika Gupta for her kind support and comments which also helped to polish and precise the concepts for publishing it to peer researchers. I cannot forget my little brother Chirag Miglani for his considerate help and support without any hesitations which allowed me to conduct my research work smoothly. I also appreciate the efforts and collaborative attitude of Dr. Nidhi Gupta, who allowed me to work with her and helped me to develop my skills in keen-interpretations and new experimentations with analysis especially in Rheology. Her patience and kind attitude have inspired me a lot.

These acknowledgements would not be complete without mentioning my PhD batch mates, seniors, juniors and research lab colleagues: Mr. Anas, Mr. Pushpender, Ms. Ankush, Mrs. Pranjali, Ms. Harsimran, Mr. Pulkit, Dr. Sandeep, Dr. Naimat, Mr Kalpesh, Ms. Renu, Mrs. Rashmi, Dr. Dimple, Dr. Nitya, Mr. Jijo Thomas, Dr. Praveen Kumar, Ms. Neethu K Mani, Ms. Shefali Sartaliya, Ms. Parvathi Marandi, Mr. Arif Dar, Mr. Salim, Mr. Atikur Rahman, Mr. Khalid Naim, Mr. Mujeeb, Mrs. Sanchitha Shah, Ms. Neha, Ms. Ayushi, Ms. Arpana, Dr. Sunil, Mr. Venu, Mr. Vibhav, Mr. Rohit, Ms. Arshdeep and Ms. Chinmayee for their constant support and friendly attitude throughout my days in INST. It's my pleasure to highly appreciate my hardworking interns Mr. Dharmendra Sablaniya and Ms. Nitha George who

had worked with me. I would like to thank my NIPER friends: Mr. Sreejith, Mr. Avinash, Mr. Hari, Mr. Divine for their affection and help to get some chemicals essential for my work. A special thanks to Mrs. Komal Sharma, Mr. Anas Saifi, Mr. Ashish Bhatt with whom I worked in collaboration. My thanks and appreciations also go to my IISER friends Mr. Joydip Dey, Mr. Madhusudhan, Mr. Uttam Mishra, Mr. Mahesh for extending immense help during my course work times and in conducting DSC, TGA experiments at emergency times. I am thankful to all administrative staff of INST especially Mrs. Gurveen Kaur, who makes sure that we get our fellowship in time, Ms. Reena, the receptionist: her smiling face always made my day special. I am also thankful to Dhanjit Ji and Mrs. Suman for timely disbursement of my contingency and travel funds. I am grateful to Mr. Mukesh for his friendly support. My heartfelt acknowledgement to the bus driver Ravinder Ji and the security guards who facilitated constant support for safe commute to the lab and staying there for work in a safe environment.

I cannot forget Malvern GPC engineers and application scientists, Mr. Sombir, Mr. Vikrant, Ms. Zuriath, Mrs. Namratha, Mr. Dipanjan for their constant support in developing my knowledge in Gel Permeation Chromatography. I am also grateful to Mr. Mayank from Anton Paar to help me in developing new experimentations in Rheology.

I am indebted to family, my wife Rosemol Geo and my loving son Joachim for making my PhD life more enjoyable. They spared most of the leisure times which I was supposed to spend with them during my PhD tenure. I also thank my parents for their constant prayer and support. I am thankful to my prayer group members at St. Thomas, Christ the king cathedral as well as Infant Jesus church for the spiritual support and prayers.

No acknowledgments would be complete without thanking INST for providing the top research facility, instruments, space, research funding and state-of-art infrastructure for carrying out my research as well as IISER for providing good academic platform along with my research and for facilitating hostel in initial years of my PhD along with access to other facilities like library, internet *etc.*

TABLE OF CONTENTS

Contents	i
Acronyms	v
Abbreviations	vi
Synopsis	vii

Chapter 1: Introduction

1.1. Stimuli-responsive supramolecular materials to mimic nature	2
1.2. Stimuli-responsive polymeric materials for self-healing applications	3
1.2.1 Self-healing in nature	3
1.2.2 Mimicking self-healing in synthetic systems	4
1.2.3 Design strategies for self-healing polymeric materials	7
1.3. Stimuli-responsive single chain polymeric nanoparticles	13
1.3.1 Mimicking self-folding of protein <i>via</i> chain collapse in polymers	13
1.3.2 Single chain polymeric nanoparticles as catalytic nanocompartments	17
1.4. Mimicking nature's precision with peptide self-assembly	20
1.4.1 Living supramolecular polymerization and control over nanostructures	21
1.4.2 Peptide as building block for nanostructures	26
1.5. Mimicking strain-stiffening in peptide –polymer networks	29
1.5.1 Strain-stiffening in fibrous protein networks	29
1.5.2 Physical origin of strain-stiffening	30
1.5.3 Theoretical models in synthetic systems	31
1.5.4 Measurement of non-linear elasticity	32
1.5.5 Biomimetic strain-stiffening hydrogels	34
1.6 Scope of Research	36
1.7 Objectives of the Present Thesis	37
1.8 References	38

Chapter 2: Photoresponsive Chain Collapse in Flexo-rigid Functional Copolymer to Modulate Self-healing Behavior

2.1. Introduction	48
2.2. Results and Discussions	50
2.2.1 Synthesis and characterization of photo-responsive polymers	50
2.2.2 Monitoring photodimerization	52

2.2.3.	Monitoring chain collapse and nanostructure formation	55
2.2.4.	Monitoring influence of crosslinking over thermal properties	60
2.2.5.	Investigation of self-healing property	63
2.3.	Conclusion	65
2.4.	Experimental Section	66
2.4.1.	Materials	66
2.4.2.	Instrumentation	67
2.4.3.	Methods	68
2.4.3.1.	Synthesis and characterization of the polymers	68
2.4.3.2.	¹ H-NMR characterization of polymers	75
2.4.3.3.	Size Exclusion Chromatography of the polymers	79
2.4.3.4.	Monitoring photodimerization by UV and ¹ H-NMR	85
2.4.3.5.	Monitoring photodimerization by SEC	85
2.4.3.6.	Monitoring chain collapse by DLS	85
2.4.3.7.	Microscopic analysis	85
2.4.3.8.	Thermal studies by Differential Scanning Calorimetry	86
2.4.3.9.	Self-healing studies	86
2.5.	References	87

Chapter 3: Delineating synchronized control of dynamic covalent and non-covalent interactions for polymer chain collapse towards cargo localization and delivery

3.1.	Introduction	92
3.2.	Results and Discussions	94
3.2.1.	Design and characterization of Random co-polymers	94
3.2.2.	Photodimerization mediated chain collapse	95
3.2.3.	Host-Guest complexation mediated chain collapse	99
3.2.4.	Microscopic investigation of Nanoparticles	103
3.2.5.	Modulation of Thermo-responsive behavior	105
3.2.6.	Synergistic and sequential chain collapse	107
3.2.7.	Dye and Drug loading and release	110
3.3.	Conclusion	115
3.4.	Experimental Section	116
3.4.1.	Materials	116
3.4.2.	Instrumentations	117
3.4.3.	Methods	118
3.4.3.1.	Synthesis and characterization of the polymers	118
3.4.3.2.	¹ H-NMR characterization of polymers	121
3.4.3.3.	Mass spectrometry data	124
3.4.3.4.	Characterization of polymers by SEC	125
3.4.3.5.	Monitoring photodimerization by UV and ¹ H-NMR	126
3.4.3.6.	Monitoring host-guest interaction by UV and ITC	126

3.4.3.7.	Monitoring Size compaction by DLS measurements	127
3.4.3.8.	Small angle Neutron scattering (SANS) studies	127
3.4.3.9	Microscopic analysis	129
3.4.3.10	Monitoring LCST by UV-vis transmittance, DLS and SANS	129
3.4.3.11	Sequential folding study	129
3.4.3.12	Molecular Dynamics Simulations	130
3.4.3.13	Determination of percentage loading of the cargo	130
3.4.3.14	<i>In vitro</i> cargo release studies	130
3.5	References	131

Chapter 4: Tandem Interplay of Host-guest Interaction and Photo-responsive Supramolecular Polymerization to 1D and 2D Functional Peptide Materials

4.1.	Introduction	136
4.2.	Results and Discussions	138
4.2.1.	Stepwise self-assembly of peptide	139
4.2.2.	Seeded supramolecular polymerization in 1D and 2D pathways	142
4.2.3	Pathway dictated hydrogel formation	145
4.2.4	Environment friendly exfoliation of MoS ₂ (Molybdenum disulfide)	146
4.3.	Conclusion	147
4.4	Experimental Section	148
4.4.1.	Materials	148
4.4.2.	Instrumentation	148
4.4.3	Methods	149
4.4.3.1	Synthesis of peptide 1	149
4.4.3.2	Preparation of Nanoparticles and Nanofibers	151
4.4.3.3	Preparation of Nanosheets	151
4.4.3.4	Atomic Force Microscopy (AFM)	151
4.4.3.5	Transmission Electron Microscopy (TEM)	151
4.4.3.6	Thioflavin-T binding and Confocal microscopy images	152
4.4.3.7	FT-IR studies	153
4.4.3.8	X-Ray Diffraction studies	153
4.4.3.9	Generation of seeds by mechanical agitation	153
4.4.3.10	Analysis of average length (fibers) and area (sheets)	153
4.4.3.11	Seeded supramolecular Polymerization	154
4.4.3.12	Hydrogel formation and rheological study	155
4.4.3.13	MoS ₂ Exfoliation study	156
4.5.	References	157

Chapter 5: Dynamic Covalent Crosslinks in Peptide-polymer Conjugate towards Strain-Stiffening Behavior

5.1	Introduction	160
5.2	Results and discussion	161
5.2.1.	Design and characterisation of the peptide-polymer conjugate system	161
5.2.2.	Monitoring LCST induced heat-stiffening	166
5.2.3.	Evaluation and quantitation of strain-stiffening <i>via</i> pre-stress protocol	169
5.2.4.	Large amplitude oscillatory strain measurements	172
5.3.	Conclusion	175
5.4.	Experimental Section	176
5.4.1.	Materials	176
5.4.2.	Instrumentation	176
5.4.3.	Methods	177
5.4.3.1.	Synthesis of peptide 1	177
5.4.3.2.	Synthesis of P_{CHO}	177
5.4.3.3	Self-assembly to produce nanofibers	179
5.4.3.4	Preparation of peptide-polymer conjugates (1_{NF}CP_{CHO} and di-1_{NF}CP_{CHO})	179
5.4.3.5	Atomic Force Microscopy (AFM)	179
5.4.3.6	Transmission Electron Microscopy (TEM)	180
5.4.3.7	Determination of persistence length	180
5.4.3.8	Monitoring covalent imine bond and photodimerization	180
5.4.3.9	Monitoring LCST by DLS	181
5.4.3.10	Rheological study	181
5.5.	References	181
	Conclusion, future outlook and perspectives	185
	Publications	189
	Curriculum Vitae	191

ACRONYMS

pH	The negative logarithm of hydronium-ion concentration ($-\log_{10} [\text{H}_3\text{O}^+]$)
UV-vis	UV-Visible Spectroscopy
FTIR	Fourier Transform Infrared
XRD	X-ray Diffraction
TEM	Transmission Electron Microscopy
HRTEM	High Resolution Transmission Electron Microscope
LCST	Lower Critical Solution Temperature
ITC	Isothermal Titration Calorimetry
BA	Butyl acrylate
HEA	Hydroxy ethyl acrylate
TMS	Trimethyl silyl
DNA	Deoxyribonucleic Acid
AFM	Atomic Force Microscopy
CD	Circular Dichroism
NIPAM	N-Isopropyl acrylamide
HEAm	Hydroxy ethyl acrylamide
NMR	Nuclear Magnetic Resonance
SANS	Small Angle Neutron Scattering
β -CD	β -cyclodextrin
γ -CD	γ -cyclodextrin
HPLC	High-Performance Liquid Chromatography
NP	Nanoparticle
NF	Nanofiber
NS	Nanosheet
EtBrib	Ethyl bromo isobutyrate
SEC	Size Exclusion Chromatography
DLS	Dynamic Light Scattering
DSC	Differential Scanning Calorimetry
MoS ₂	Molybdenum disulfide

ABBREVIATIONS

λ	Wavelength
ν	Scaling exponent
α	Alpha
Σ	Sigma
γ	Gamma
Δ	Delta
Π	Pi
\AA	Angstrom
$^{\circ}\text{C}$	Degree Centigrade
Nm	Nanometer
μm	Micrometer
Cm	Centimeter
mL	Millilitre
μL	Microlitre
mM	Millimolar
Θ	Theta
mW	Milliwatt
Jcm^{-2}	Joule/cm ²
τ	Reptation time (Tau)
σ	sigma
ε	Absorption coefficient
ρ	Rho
η	viscosity

Synopsis

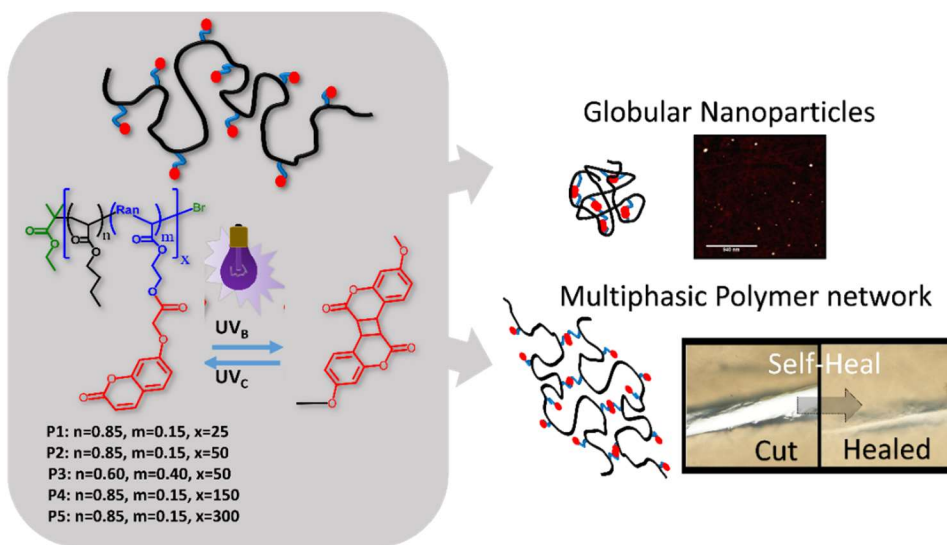
Chapter 1. Introduction

Natural biopolymers *e.g.* proteins, microfilaments in living systems show innate potential to act as smart materials in local microenvironments. This inspires researchers to undertake synthetic design with a biomimetic strategy involving stimuli-responsive properties. Self-healing in natural living systems for damage containment and wound healing is one of the fascinating phenomena. Thus, we discuss on the fundamental understanding of artificial smart self-healing functional materials with respect to their mechanism. Next, we discuss about the various approaches for chain collapse of synthetic single chain polymer *via* stimuli-responsive supramolecular interactions in a bid to mimick folding and compartmentalization of natural biopolymers *e.g.* proteins. A variety of chain collapse strategies ranging from homo-functional, hetero-functional to cross-linker mediated approach are discussed. Further, precision design to give complex architectures *via* out-of-equilibrium self-assembly pathways are discussed with examples exhibiting parameters such as solvents, temperatures, pH to alter the nature of the self-assembly pathways. Living supramolecular polymerization exploiting nucleation-elongation growth to control over morphology and dimension of multi-ordered nanostructures is also discussed here. Finally, strain-stiffening characteristics of biopolymer networks and its implications are discussed. A number of approaches to design artificial networks that show exponential stiffening in response to stress in microenvironment are summarized in a bid to understand the mechanism associated with such exciting natural phenomenon.

Chapter 2. Photoresponsive Chain Collapse in Flexo-rigid Functional Copolymer to Modulate Self-healing Behavior

Synthetic systems mimicking natural self-folding process is attractive to impart multiple structural control over the polymer crosslinking and subsequent alteration of macroscopic self-healing properties. In this chapter, photoresponsive polymers **P1-P5** containing pendant

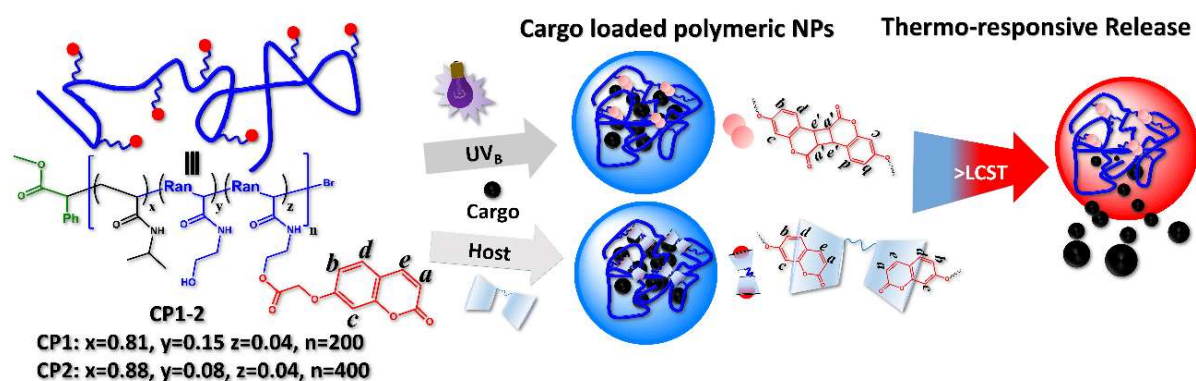
coumarin moieties are synthesized by Atom Transfer Radical Polymerisation (ATRP) which on photoirradiation undergo intra or inter chain collapse to form versatile nanostructures (Scheme 2.1) The morphology as well as size are dependent on concentration, solvent compatibility and chain length of the polymers. Photodimerization of coumarin moieties transforms the extended coiled chain of the polymer to uniform sized nanoparticles in dilute condition. Further, interchain collapse at crowded macromolecular concentration with rigid segments connected by flexible polymer chains is structurally analogous to the elastomers. Thermal studies show that such hardening of rigid segment by photodimerization led to an increase in the glass transition temperature (T_g) that can be reversibly controlled upon decrosslinking. Finally, self-healing properties of the polymer films are explored that show photo-regulated nonautonomic & intrinsic self-healing behavior at ambient condition. This approach shows a fundamental understanding of the photo-modulated self-healing behavior in low T_g polymers with a coexistence of autonomic and non-autonomic self-healing pathways and may have application in smart coating of photovoltaic device.



Scheme 2.1. Schematic diagram and chemical structures of the polymers showing photodimerization of the coumarin moieties to render intra-chain collapse to result in globular nanoparticles and inter-chain collapse to give self-healable multiphasic polymer network.

Chapter 3. Delineating synchronized control of dynamic covalent and non-covalent interactions for polymer chain collapse towards cargo localization and delivery

In this chapter, water soluble and thermo-responsive polyacrylamide polymers **CP1-2** with photodimerizable coumarin moieties grafted in the backbone are employed to design chain collapse mediated polymeric nanoparticles (Scheme 3.1). The chain collapse here is regulated *via* photodimerization under UV_B light ($\lambda_{\text{max}} = 320 \text{ nm}$) and host-guest interaction by addition of



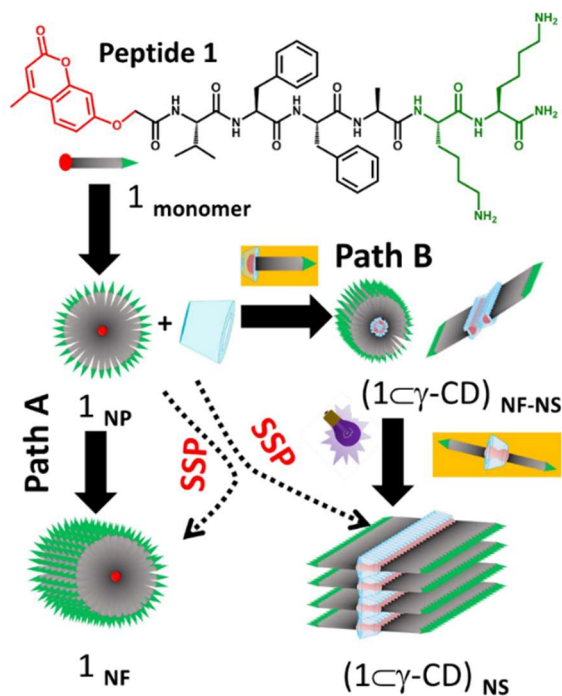
Scheme 3.1. Schematic diagram and chemical structures of the polymers showing photo-responsive dynamic covalent and non-covalent host-guest interaction mediated chain collapse to result in nanoparticles. The cargo loaded nanoparticles owing to thermo-responsive polymeric backbone leads to the augmented release of the cargo above LCST.

bis- β -CD host. Both photoresponsive reversible dynamic covalent chemistry as well as non-covalent host-guest interaction show controlled chain collapse to give **di-CP1-2** and **CP1-2- \subset bis- β -CD** nanoparticles. Further, the polymers unveil interesting thermo-responsive behavior owing to a lower critical solution temperature (LCST) induced hydrophilic to hydrophobic phase transition. Moreover, sequential stepwise folding of the polymers are demonstrated by the addition of the host molecule followed by exposure to UV_B irradiation. Lastly, the polymers in native and folded states are shown to entrap versatile cargos of hydrophilic RhB dye or hydrophobic Ibu drug with good control. The release studies in physiological medium at different temperature showed variable release patterns ranging

from sustained to on-demand burst release from different polymeric states indicated thermo-responsive trigger over the release of cargo.

Chapter 4. Tandem Interplay of Host-guest Interaction and Photo-responsive Supramolecular Polymerization to 1D and 2D Functional Peptide Materials

Designing complex functional supramolecular system to mimic natural biomolecular system demands understanding the fundamentals of nature's engineering with structural control and dynamics due to the pathway dictated out-of-equilibrium self-assembly. In this chapter,



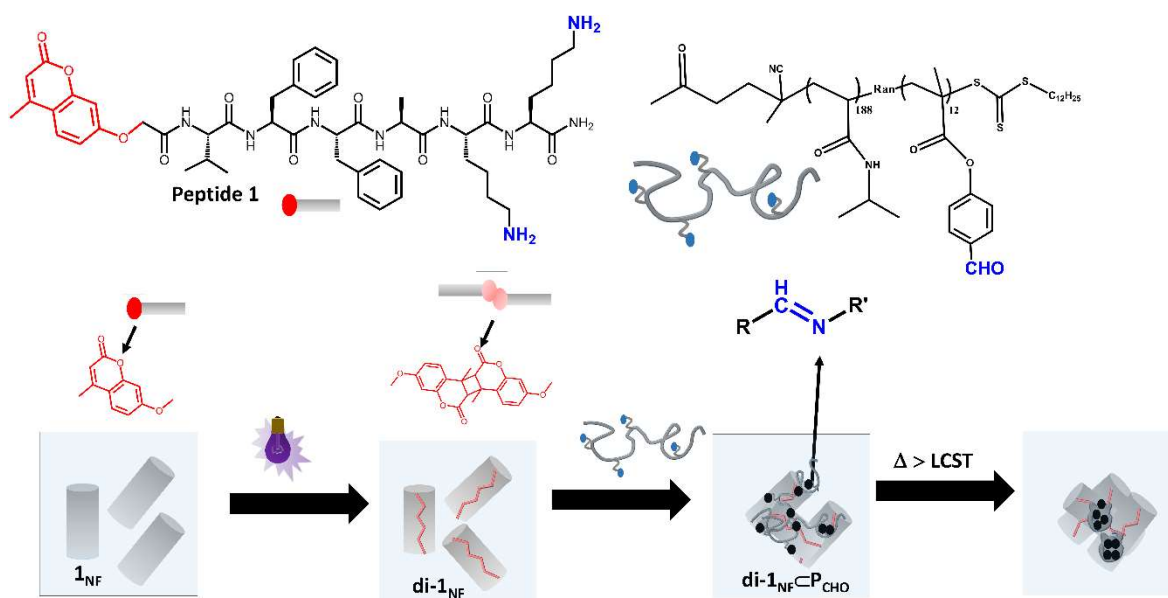
Scheme 4.1. Molecular structure of peptide **1** and its cartoon representation. 1_{monomer} in HFIP-water form metastable nanoparticle, 1_{NP} at low temperature transformation eventually to nanofiber, 1_{NF} on increasing temperature (Path A). Mixing γ -CD to the metastable nanoparticles followed by UV_B irradiation ($\lambda_{\text{max}} = 320$ nm) renders 2D nanosheet ($(\mathbf{1}\text{-}\gamma\text{-CD})_{\text{NS}}$) (Path B).

Peptide **1** with an Aβ42 amyloid nucleating core and photodimerizable 4-methylcoumarin moiety at its *N* terminus is designed which undergoes step-wise self-assembly to form metastable nanoparticles 1_{NP} which eventually transforms to one

dimensional $\mathbf{1}_{\text{NF}}$ nanofibers. Additionally, mixing $\mathbf{1}$ with γ -cyclodextrin (γ -CD) and subsequent UV_B irradiation renders morphological transformation to free standing two dimensional $(\mathbf{di-1}\subset\gamma\text{-CD})_{\text{NS}}$ nanosheets mediated by the host-guest interaction (Scheme 4.1). Further mechanical agitation of the 1D and 2D nanostructures provides seeds with narrow polydispersity indices. Seeded supramolecular polymerization (SSP) on the fiber and sheet seeds demonstrates excellent control over the length and area of fiber and sheet morphology. Such differentiated pathways are utilised to control the mechanical strength of resultant hierarchical hydrogels. Finally, the peptide nanostructures are envisioned as excellent exfoliating agents for inorganic hybrid materials *e.g.* MoS_2 . Thus, a new approach to show unprecedented topological control over dimensions is demonstrated in a synthetic supramolecular material by interplay of orthogonal interactions that leads to self-assembly in multiple pathways.

Chapter 5. Dynamic Covalent Crosslinks in Peptide–polymer Conjugate towards Strain-Stiffening Behavior

Rigidification on inner stress generation plays an important part in many of the biomechanical pathways in living system. One of the finest example of this phenomenon is collagen and fibrin network in rigidification of cell matrix and pulling of actin-myosin filamental network to render stiffening of cytoskeleton. In this chapter, we exhibit dynamic covalent crosslinking of semi-flexible fibers of peptide $\mathbf{1}_{\text{NF}}$ with thermo-responsive NIPAM based polymer \mathbf{P}_{CHO} to result in peptide-polymer conjugate $\mathbf{1}_{\text{NF}}\subset\mathbf{P}_{\text{CHO}}$ network (Scheme 5.1). The network exhibits inner stress generation by onset of a coil-to globule transition upon heating above the lower critical solution temperature of PNIPAM. This renders mechanical heat-stiffening response that extended to higher orders of magnitude in modulus. Furthermore, conjugate of photodimerized covalently fixated peptide fibers ($\mathbf{di-1}_{\text{NF}}$) with the polymeric crosslinker (\mathbf{P}_{CHO}) *i. e.* $\mathbf{di-1}_{\text{NF}}\subset\mathbf{P}_{\text{CHO}}$ network stiffens in response to applied shear stress and large amplitude oscillator strain in rheology with power law exponents that match with the biopolymer networks.



Scheme 5.1. Molecular structure of the peptide **1** and the linear, thermo-responsive poly-(NIPAM-co-formyl phenyl methacrylate) (**PCHO**) linker. Hierarchical self-assembly through intermolecular H-bonding and hydrophobic interactions of peptide result in **1_{NF}** peptide fibers followed by covalent fixation upon irradiation with UV_B light to form **di-1_{NF}** fibers. The crosslinking of **di-1_{NF}** with **PCHO** via amide formation result in **di-1_{NF}-PCHO** network that upon heating above LCST exhibits temperature induced pulling of fibrous network by PNIPAM chains to show stiffening response.

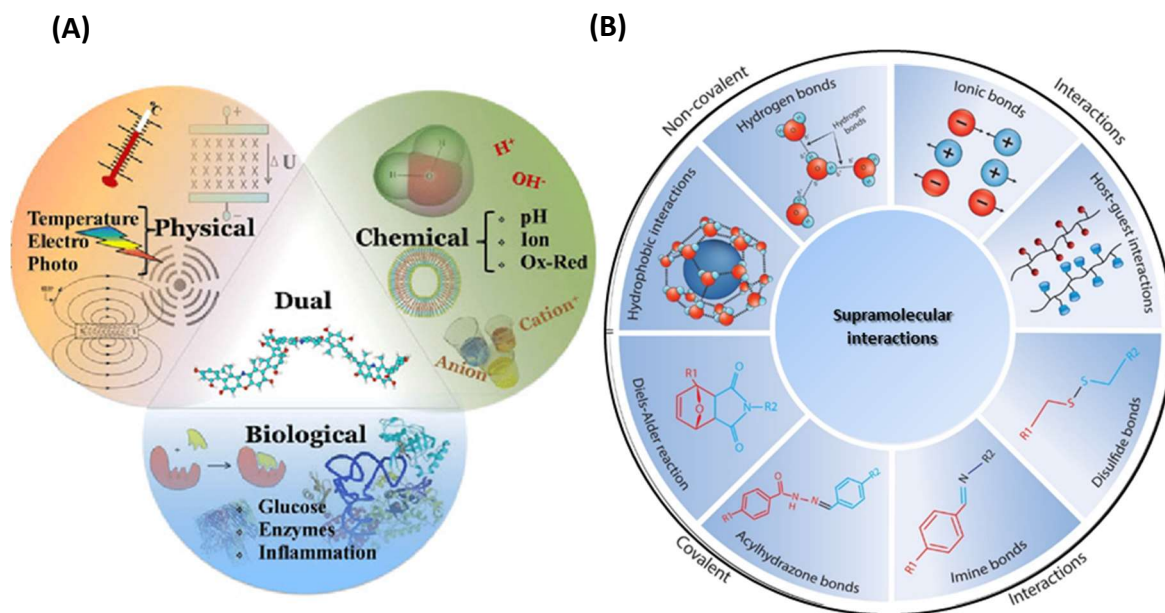
Chapter 1

Introduction

This chapter discusses some fundamentals of stimuli-responsive materials which are formed by supramolecular interactions triggered by physical, chemical or biological stimuli. The smart nature of these materials is utilized for applications in various fields. One such application is self-healing where nature does self-repair of its damage in an autonomous fashion. In pursuit of mimicking such phenomena, thermoplastic elastomer design with soft-hard segments in conjunction with chain collapse in synthetic polymers is discussed. Various chain collapse strategies are listed that show intra-chain collapse to globular nanoparticles and inter-chain collapse to form networks. Further, the single-chain polymeric nanoparticles formed via intrachain collapse and their implications are also discussed in the light of developing dynamic stimuli-responsive nano compartments. Mimicking the precise design of nature to give higher-order nanostructures which nature does throughout of equilibrium self-assembly is also discussed in the light of various synthetic systems including small molecules and peptides. Lastly, strain-stiffening characteristics of natural biopolymers and its significance in life is discussed with ways to mimic the mechanism in a synthetic system.

1.1. Stimuli-responsive supramolecular materials to mimic nature

Stimuli-responsive supramolecular materials respond to small changes in its microenvironment to manifest in large macroscopic property or phase transitions.¹ They are smart or intelligent materials that undergo physical or chemical changes in response to external stimuli mediated by supramolecular interactions.² Further, these are dynamic and adaptive materials that show reversibility on the counter trigger. In nature, biopolymers *e.g.* proteins, nucleic acids *etc.* consist of some stimuli-responsive mechanisms and remains stable over wide arrays of external variations while being subjected to strong morphological changes to endow specific functions at certain critical points.^{3,4} Inspired from these natural synthetic materials, various synthetic polymers, peptides and small molecules have been designed to mimic the stimuli-responsive behaviors. Incorporation of functional groups into these materials that are sensitive to a change in character (*e.g.* conformation, solvent affinity, flowability) along its morphology upon a stimuli *via* supramolecular interaction render dramatic alteration in macroscopic properties. Such strategy are commonly classified



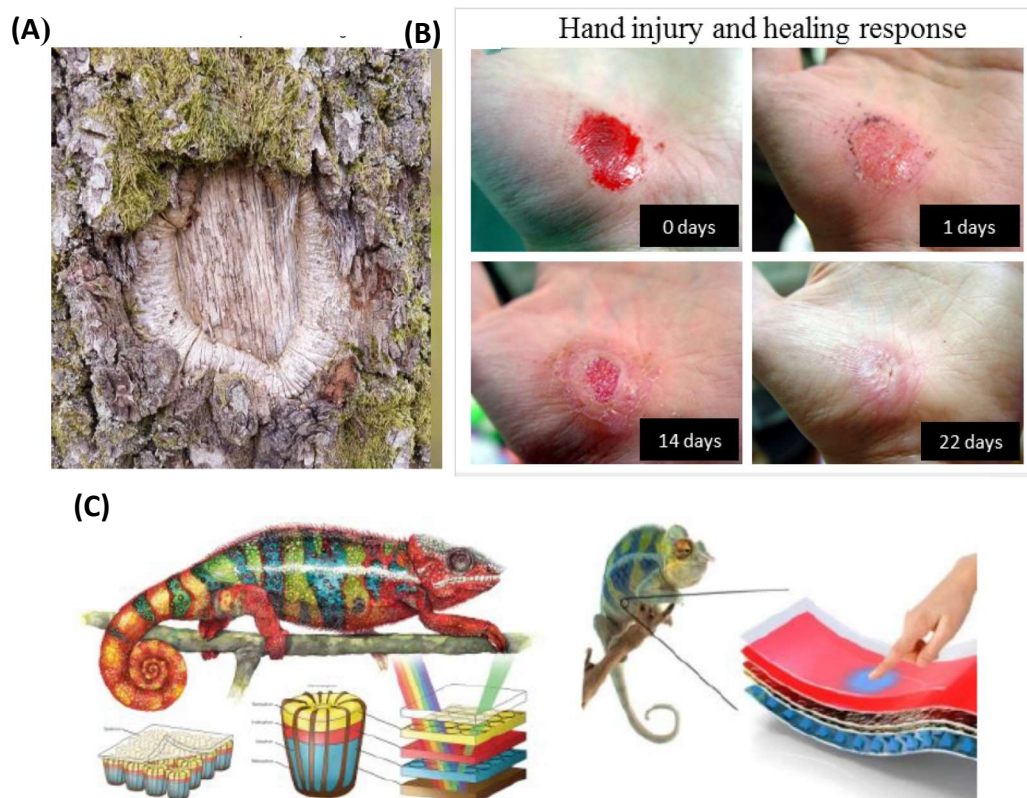
Scheme 1.1. (A) Classification of various stimuli of stimuli-responsive polymers. (Reprinted with permission from reference [5]. Copyright©2012 Springer Nature Switzerland AG. (B) Different supramolecular interactions involved in their design. Reprinted with permission from reference [6]. Copyright©2019 WILEY-VCH Verlag GmbH & Co. KGaA, Weinheim Springer Nature.

under three mechanism *i. e.* physical, chemical, or biological (Scheme. 1.1A).^{7,8} Physical stimuli such as light, heat, sound, mechanical *etc.* are utilised to alter the dynamic nature of the material in its environment *e.g.* the interaction of the material in its solvent system. Chemical stimuli like solvent, ionic strength, pH *etc.* control molecular interactions⁹ while biological stimuli such as enzymatic, receptors components in the system can provide functional or molecular recognition property. Additionally, dual stimuli-responsive approaches can give concurrent response to a plethora of stimuli. The stimuli-responsive mechanisms involve the presence of supramolecular interactions of non-covalent (hydrogen bonding, hydrophobic effects, electrostatic interactions, *etc.*) or dynamic covalent (cycloadditions, isomerization *etc.*) nature (Scheme 1.1B). Further due to the dynamic and reversible nature of supramolecular interactions, these materials have the capability to adjust to the natural milieu and possess a wide range of fascinating nature mimicking applications, such as self-healing, controlled drug delivery, scaffold materials *etc.*

1.2. Stimuli-responsive polymeric materials for self-healing applications

1.2.1. Self-healing in nature: Self-healing is an inherent ability in living system to repair its damage or to protect from damage that gets created through evolution. Plants and animals are equipped with astonishing self-healing and defense mechanisms. One of the processes is damage containment in plants where trees eventually seals its wounded bark with a protective layer of cells to keep it protected from harmful organisms (Scheme 1.2A).¹⁰ The hand injury seen in Scheme 1.2B displays the healing process where the body halts the bleeding and then the tissue regenerate over a time period.¹¹ Another interesting mechanism is reversible muscle control¹² which can be seen in chameleons where they are able to go through muscle movements that incite fluctuations in the distance of the guanine nanocrystal layers in their skin under an external threat that give rise to adaptive camouflage *i. e.* colour change in skin by augmentation of reflectivity of the skin's pigment cells from short to long wavelengths (Scheme 1.2C). The general observation is that self-healing is one of the tools that nature uses to survive its span and it occurs through regeneration, repair, or replacement of damaged tissue. A close look at the ways different organisms heal utilising nature's finest

methods of altering and healing damage and creating bio-inspired self-healing materials is one of the aim that researchers pursue over last decades. Ability to spontaneously heal without external intervention makes the self-healing mechanisms in nature autonomous in character.



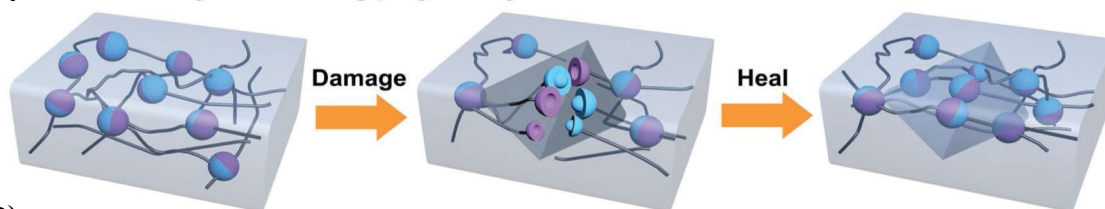
Scheme 1.2. (A) Trees keep harmful organisms away from wounds by creating a protective layer of cells which eventually harden and maintain internal integrity (Source: Wikimedia Commons). (B) Photographs of a hand injury healing over time. The pictures show the immediate need for a healing response to stop blood loss all the way through remodeling and scarring after 22 days. Adapted from reference [13] (C) By controlling muscle movements, chameleons modify the spacing between nanocrystals embedded in their skin, leading to changes in reflectivity and thus in colour. Reprinted with permission from references [12,14]. Copyright ©2015 Macmillan Publishers Limited.

1.2.2. Mimicking self-healing in synthetic systems: Recent years have witnessed an exponential progress in research on self-healing materials, with increasing number of research group being involved and new concepts being explored. The newly developed self-

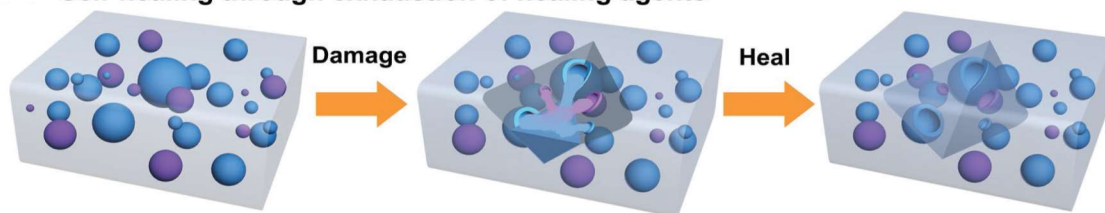
healing systems comprise of interactions at the molecular level with knowledge about the chemistry of the processes involving covalent (irreversible), noncovalent (reversible) bond formation *etc.* Reversible covalent and noncovalent interactions are becoming increasingly significant due to their capability to heal damage recurrently at the same spot. Thus, the current emphasis of self-healing material research dwells on the design of multifunctional materials that have the inherent capability to restore properties such as mechanical strength, fracture, conductivity and toughness that were disrupted due to damages.¹⁵ On the basis of the chemistry of action, self-healing materials are generally classified into autonomic and non-autonomic. In autonomic self-healing systems, an inherent chemical process results in the healing of the damage whereas external stimuli realizes healing in non-autonomic self-healing systems. Heat,¹⁶ chemical environment,¹⁷ light¹⁸ and mechanical forces¹⁹ are some common stimuli used in non-autonomic self-healing. Mostly, the autonomic self-healing system utilizes a microencapsulated healing agent and catalyst that are dispersed within a polymer matrix. The mechanism includes the rupture of the embedded microcapsules mediated by the propagation of the crack to eventually release the healing agent that is subsequently polymerized with or without the aid of catalyst.^{20,21} In some cases, dynamic supramolecular system shows autonomic self-healing action without external stimuli. The non-autonomic self-healing exploits external stimuli mediated chemistry based on either dynamic covalent bond or non-covalent interactions.^{22,23} The self-healing material can also be classified into extrinsic and intrinsic based on the mechanism involved in the repair of the damage. Scheme 1.3 & Table 1.1 illustrate the key differences between them. Extrinsic self-healing system needs an external healing agents, either encapsulated in microcapsule or embedded in matrix network and the healing process is initiated in autonomic manner by the damage caused to the microcapsule or vascular network. The capsules or networks are made of polymer such as polyurethane (PU), poly(urea-formaldehyde) (PUF) *etc.* However, there are also some shortcomings of the microcapsule mediated extrinsic self-healing approach as multiple times healing is not possible and catalysts are usually expensive. On the contrary, intrinsic self-healing system utilizes non-covalent interactions or dynamic covalent chemistry. The non-covalent interactions employed are hydrogen bonding, host-guest complex, metal-ligand interaction *etc.* The reversible dynamic covalent interactions (DCC)

involve Diels-Alder reaction, imine chemistry, radical exchange and trans-esterification *etc.* The healing mechanism may be triggered by some external stimuli. Due to the reversible nature of the supramolecular interactions or DCC employed in the intrinsic self-healing system, healing of damaged area is possible multiple times. Thus, the current research goal is focused towards designing next generation materials capable of exhibiting intrinsic self-healing behavior.

(A) Intrinsically self-healing polymer systems with reversible chemical bonds



(B) Self-healing through exhaustion of healing agents



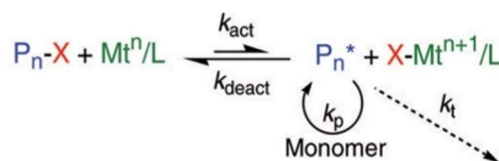
Scheme 1.3. Schematic illustration of intrinsically self-healing polymer systems with A) reversible chemical bonds and B) self-healing through exhaustion of healing agents. A) The self-healing of damages is realized by the reformation of chemical bonds at the fractured surfaces through supramolecular assembly. B) The self-healing is realized through exhaustion of liquid agents pre-embedded in the polymer matrix to fill in the ruptured space. Reprinted with permission from reference [23]. Copyright © 2017 WILEY-VCH Verlag GmbH & Co. KGaA, Weinheim

Table 1.1 Salient features of extrinsic and intrinsic self-healing materials Reprinted with permission from Reference [24]. Copyright © 2017 WILEY-VCH Verlag GmbH & Co. KGaA, Weinheim

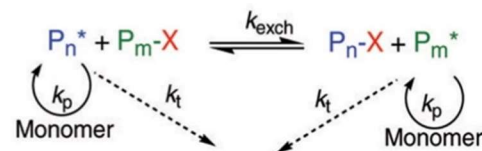
Parameters	Extrinsic	Intrinsic
Healing system	An external healing agent dispersed in capsules or vascular networks.	Non-covalent chemistry or dynamic covalent chemistry
Mechanism	Healing agent and a catalyst	Reformation of chemical bonds
Initiation	Triggered by external/internal damage/rupture.	Triggered by external stimuli <i>e.g.</i> pH change, light, temperature, pressure
Drawbacks	Expensive catalysts Multiple healing is not possible	Multiple healing is possible

1.2.3. Design strategies for self-healing polymeric materials: Exhibition of self-healing ability by polymers demands presence of some functionality which can undergo dimerization or couple other moieties. Such multifunctional and well-defined macromolecules needs a keen choice of a controlled polymerization technique coupled with functionalization strategies.^{25,26} Among all the polymerization techniques familiarized up till now, methods like atom transfer radical polymerization (ATRP), Reversible Addition Fragmentation Chain Transfer polymerization (RAFT) *etc.* are the most adaptable due to their exceptional features like controlled chain length, Poly Dispersity Index (PDI), tunable architecture, end group functionality (Scheme 1.4).

(A) **ATRP**
Transition metal activation (k_{act}) of a dormant species with a radically transferable atom



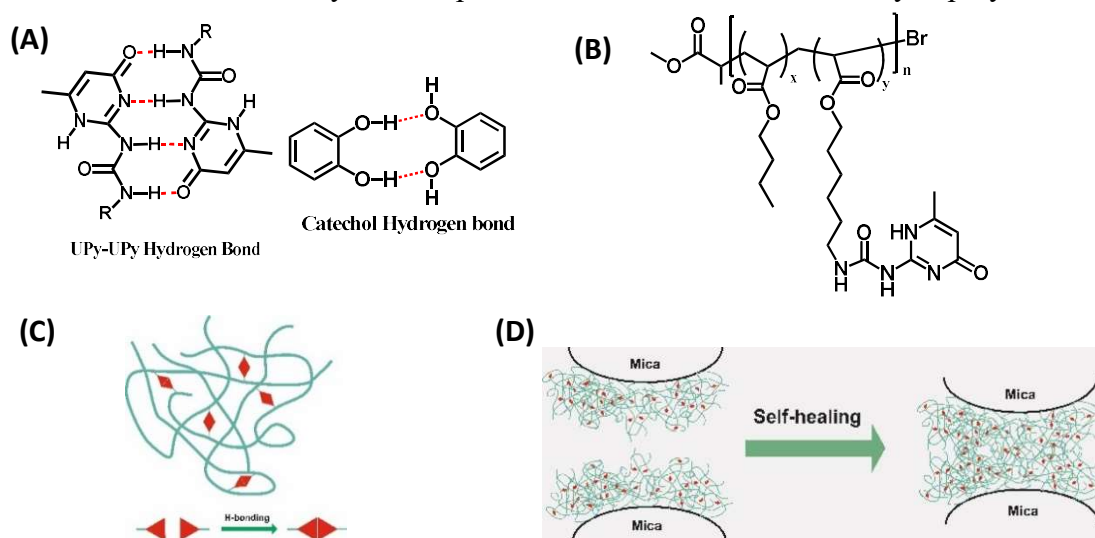
(B) **RAFT**
Majority of chains are dormant species that participate in transfer reactions (k_{exch}) with a low concentration of active radicals



Scheme 1.4. Mechanism of different control radical polymerisation like (A) ATRP and (B) RAFT. Reprinted with permission from reference [27]. Copyright © 2005 Elsevier Ltd.

1.2.3.1 Non-autonomic design strategies: In this, non-covalent interactions is an interesting concept as it renders thermodynamically stable polymers with reversibility and tunability. The supramolecular system can be tuned by changing reaction conditions (*e.g.*, temperature, polarity of solvent, concentration and pH) or by external stimulations. These interactions include hydrogen bonding, host-guest complex, metal-ligand complex, hydrophobic, π - π and ionic interactions. Recently, the strategy to incorporate strong and reversible hydrogen bonding motifs like ureido-pyrimidine^{28,29} catechol-quinone moiety³⁰ *etc.* into the polymeric structure to generate self-healing polymer has gained a lot of significance. As shown in Scheme 1.5, Sijbesma *et al.* reported a series of random copolymers with 2-ureido-4[1H]-

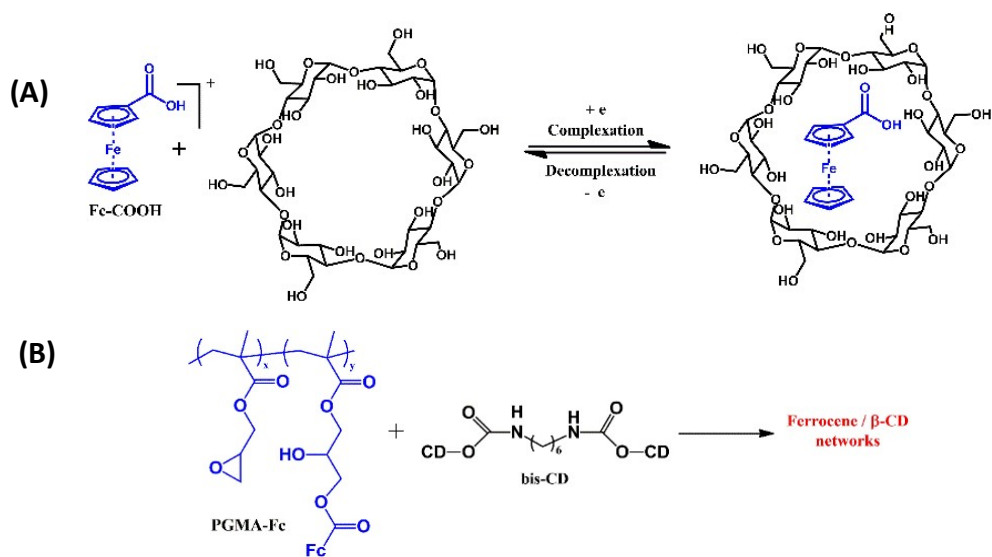
pyrimidinone (UPy) as functionality which was synthesized by means of living polymerization method such as atom transfer radical polymerization (ATRP).²⁸ The system showed formation of UPy dimer mediated by strong quadruple hydrogen bonding for designing highly thermally responsive supramolecular polymers. The poly (*n*-butyl acrylate) copolymer with UPy units (PBA-UPy) reported by Zeng *et al.* was spin coated on mica substrates to produce a uniform smooth polymer film with thickness of 100 nm (Scheme 1.5).²⁹ The enhanced surface energy of the polymer due to the strong intermolecular interaction among the strong hydrogen bonding UPy dimers provided adhesion properties that can traverse across the topological interface and the bulk viscoelasticity of the polymers and were sensitive to humidity and temperature. Thus, fractured PBA-UPy copolymer



Scheme 1.5. (A) Hydrogen bonding interaction in UPy dimers and catechol dimers, (B) chemical structure of poly(BAUPy) copolymer, (C) interchain hydrogen bonding among UPy groups and (D) self-healing mechanisms mediated by multiple hydrogen bonding polymers coated on mica surface. Adapted with permission from reference [29]. Copyright ©2014 WILEY-VCH Verlag GmbH & Co. KGaA, Weinheim.

films can fully recover to 100% of their self-adhesion strength in about 2 days under almost zero external load. Since non-specific interactions such as hydrogen bonding may lead to passivized self-healing, improvised strategy was developed utilising highly distinct and dynamic host guest interactions that involves binding of different guest molecules with cyclic macromolecules such as cyclodextrins (CD).

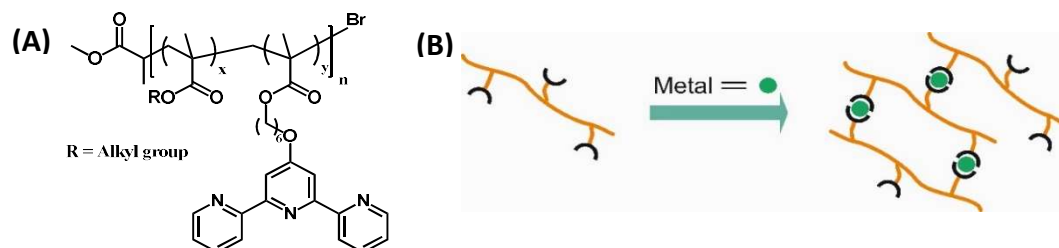
Chuo *et al.* reported an electrically driven self-healing polymeric material based on ferrocene-grafted poly(glycidyl methacrylate)(PGMA-Fc) and a bifunctional β -cyclodextrin derivative (**bis-CD**) (Scheme 1.6).³¹ Crosslinked PGMAFc/CD network was coated on a copper surface and was cut with a sharp knife to give a knife print of 80 μm in width which got reduced to 40 μm with an electrical treatment of 1.5 V \times 6 for 24 h. The redox triggered decomplexation reaction of the Fc/CD complexes provided self-healing which was improved with further thermal treatment at 85 $^{\circ}\text{C}$ for a day. The system was anticipated to be potential self-healing agent for commercial paint products. Further, inspired from the natural healing processes like mussel byssus threads, metal complexation interaction was also explored as a self-healing strategy.



Scheme 1.6. (A) Redox mediated reversible host-guest complex formation between β -cyclodextrins (CD) with ferrocene (Fc), (B) copolymer of Fc-grafted PGMA chains (PGMA-Fc) and difunctional β -cyclodextrins compound (bis-CD) for the construction of redox responsive intrinsic self-healing material network. Adapted with permission from reference [31]. Copyright \copyright 2013 Wiley Periodicals, Inc.

Schubert *et al.* demonstrated a cross-linked metallo polymeric system based on iron bis-terpyridine (metal-ligand) complex chemistry.³² The authors synthesized different polymers from terpyridine methacrylate monomers copolymerized with different methacrylate monomers *via* living polymerization technique in order to have a controlled loading (Scheme 1.7). Later, the copolymers with the terpyridine moiety as crosslinked with

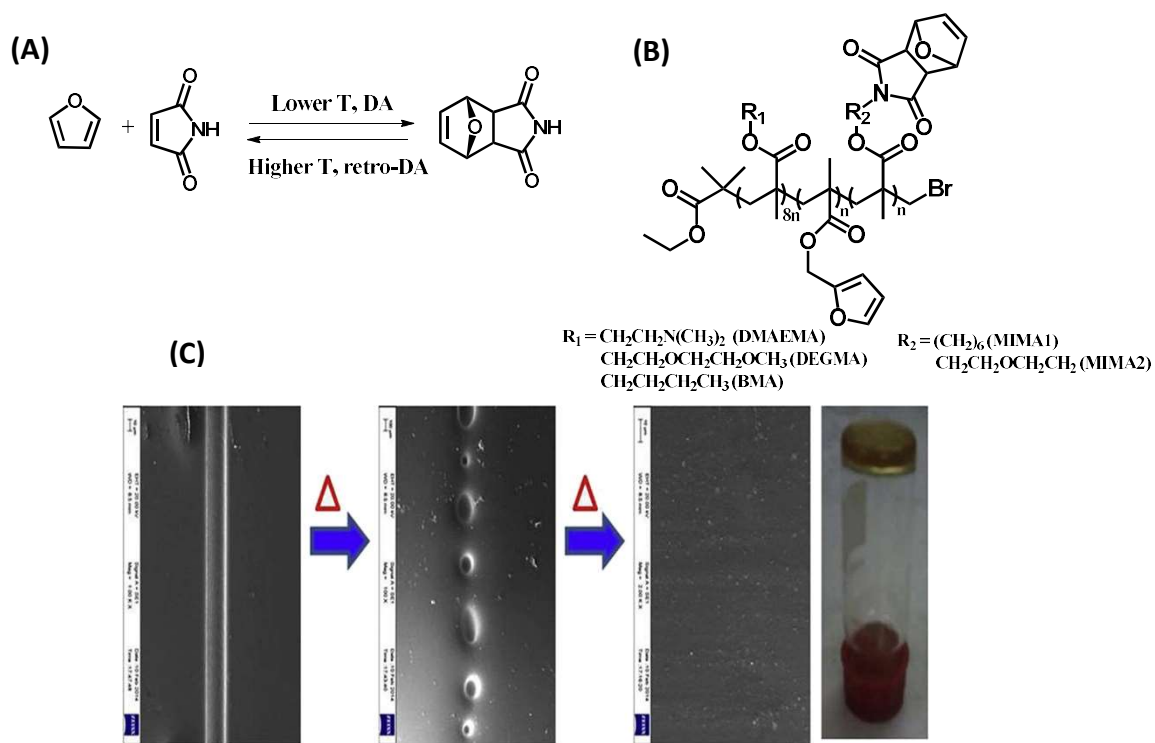
iron (II) sulfate resulted in the metallopolymers. Furthermore, the films out of these materials showed healing of larger and wider scratches that was correlated with mobility/flexibility of the copolymer backbone revealed on thermal studies.



Scheme 1.7. (A) Chemical structure of copolymer having terpyridine moiety, a potential binding site of the Fe(II) ion, (D) metal ion mediated formation of cross-linked polymer network. Adapted with permission from reference [32]. Copyright © 2013 WILEY-VCH Verlag GmbH & Co. KGaA, Weinheim.

Further, dynamic covalent interactions that has the combined effect of reversibility of non-covalent interactions as well strength of covalent bond were used to develop self-healing materials. One of the very adaptable chemistry in this category is [4+2] cycloaddition *via* Diels-Alder (DA) reaction, which has characteristic dynamic equilibrium between the DA and the retro DA reaction. The equilibrium constant of this reaction between a diene and dienophile can be controlled thermally, which is applicable in material and polymer science to achieve novel polymeric architectures with intrinsic self-healing behavior. Schubert *et al.* synthesized terpolymers functionalized with furan and maleimide groups and observed the effect of different polar and nonpolar co-monomers on self-healing performance on the basis of DA reversible crosslinking reaction. (Scheme 1.8)³³ The DA reactions between furan and maleimide suffer from a drawback of using high temperature (120 to 180 °C) for retro DA. Self-healing behavior of the polymers were investigated by thermal studies and copolymer with DEGMA as the co-monomer exhibited best self-healing behavior due to higher flexibility of the linker unit with reduction of healing temperature. N. Singha *et al.* also reported tailor-made copolymers of methacrylate monomers *via* RAFT polymerization technique and analysed the DA and retro-DA reaction between the furfuryl groups of PFMA part and a bismaleimide crosslinker.³⁴ DSC analysis was used to determine of the endothermic retro-DA reaction in copolymer-DA adduct. Self-healing property of the above cross-linked material was demonstrated by SEM *via* monitoring the repair of a scratch in the

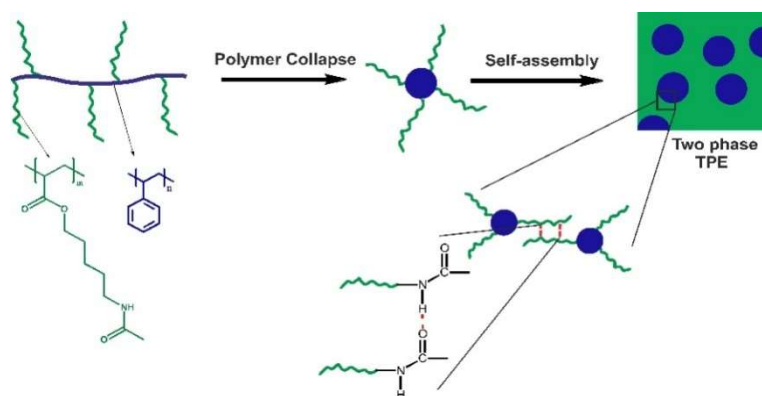
copolymer film upon heating and cooling. Further, self-healing strategies with dynamic covalent interactions like thiol-disulphide exchange chemistry³⁵ which was redox sensitive as well as acylhydrazone chemistry³⁶ which was temperature and pH responsive were also reported. Thus, most of the non-autonomic strategies rely on healing mediated by bulk exposure to external stimuli like temperature, redox conditions *etc.* to activate mechanism, so we cannot strictly call them as self-healing. Further, a smart look at nature and application of locally invasive stimuli like light or pure non-invasive stimuli will be a good lead in the future expansion of this area of knowledge.



Scheme 1.8. (A) Classical DA and retro-DA reactions between furan and maleimide moieties, (B) chemical structure of the terpolymers derived from maleimide methacrylate monomers copolymerized with different polar and nonpolar comonomers. (C) Monitoring healing of scratch by scanning electron microscopy upon heating. Adapted and reprinted with permission from references [33,34]. Copyright © 2015 Elsevier Ltd.

1.2.3.2. Thermoplastic elastomers as autonomous self-healing design: Nearly all strategies towards synthetic self-healing polymeric materials demand a stimulus such as heat, healing agents, plasticizer or solvent for initiating the process. Nowadays, an increasing number of research is being directed towards designing thermoplastic polymer materials that

show autonomic self-healing capability. Leibler *et al.* reported a set of synthetic supramolecular network from multi-topic fatty acid molecules with urea *via* complimentary H-bonding resembling self-healing thermoreversible rubber network.³⁷ Thermoplastic elastomer which consists of a soft rubbery matrix embedded with block or brush-copolymers as hard crystalline domain shows combined effect of high elastic modulus and toughness with spontaneous healing capability. Zhibin Guan and coworkers demonstrated a novel multiphase design of a thermoplastic elastomer system that incorporated rigidity and spontaneous healing.³⁸ As shown in Scheme 1.9, a dynamic healing motif integrated into the hard-soft multiphase thermoplastic elastomer with Polystyrene backbone (hard phase) and poly- acrylate amide (PA-amide) (soft phase). They collapsed to form a core-shell nanostructure having a hard polystyrene core and a soft PA-amide shell on treatment with a polar solvent. Reversible hydrogen bonding interaction among the PA-amide brushes result in dynamic micro-phase separated nanostructure with reduced glass transition temperature (T_g). The mechanical stability of the brush polymers was at par with the classical elastomers which was confirmed through static stress-strain and creep recovery test which displayed self-healing behavior at room temperature in the absence of any external agents or stimuli.



Scheme 1.9. Design of multiphase thermoplastic elastomeric self-healing brush polymer system. Polymer with polystyrene backbone and polyacrylate amide brush, collapse into core-shell nanostructures that self-assemble into a biphasic morphology of thermoplastic elastomer. The dynamic hydrogen bonds among the amides forms cluster of hydrogen bonding interactions to result in a molecular velcro. Adapted with permission from reference [38]. Copyright © 2012, Nature Publishing Group.

The polymer samples were cut into two fragments which were gently brought together to investigate the self-healing behavior mediated by the dynamic hydrogen bonding

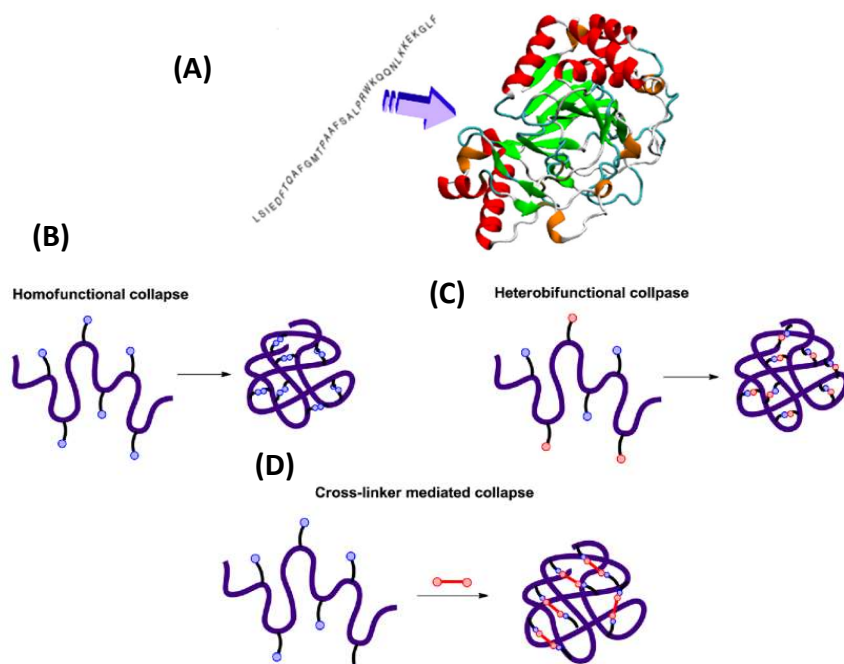
in the soft segment. The stress-strain tensile behavior of a cut sample and pristine sample showed comparable rate and performance for initial modulus, yield strength, and stress at 50% strain. The multiphase design for which the healing was because of the optimum balance of the hard–soft micro phases integrated the mechanical properties of thermoplastic polymer with thermoset (epoxy) and facilitated autonomic self-healing. Such single component self-healing system which forms flexorigid compartments and modulates its macroscopic property like flow ability can be promising autonomic healing prototypes.

1.3. Stimuli-responsive single chain polymeric nanoparticles

1.3.1. Mimicking self-folding in protein *via* chain collapse in synthetic polymers:

Nature's biochemistry consists of numerous interactive proteins that perform unique functions which are formed from only 20 different amino acids. The nature's way of creating such materials lies in its ability to control the length and sequence of its polypeptide chains. A specific polypeptide chain folds into a particular H-bonding patterns like alpha helices, beta sheets and perform a specific function *e.g.* in enzymes, the binding groove developed like this not only allows specific substrate binding but also high catalytic activity and efficacy. This structure function relationship between proteins and its functions been an inspiration for macromolecular science. *e.g.* chiral dendrimers and helical polymers were functionalized catalytically active sites to give selective catalyst functions.^{39–48} The formation of 3D structure of proteins is driven by not only H-bonding but also hydrophobic interactions and disulphide bonds. This can be mimicked by collapsing individual polymer chain into nanoparticle *via* intramolecular chain collapse.^{49–52} Although early examples showed such chain collapse *via* covalent reactions like “click” chemistry, radical coupling, dimerization, and cyclization reactions,^{53–62} however lack of reversibility affect the smart dynamic nature of the system in response to the stimuli. This can be achieved *via* the use of dynamic covalent and non-covalent interactions with few reports.^{63–68} The typical strategies used can also be classified according to the type of chemistry to generate the nanoparticle (Scheme 1.10): homo-functional cross-linking, where pendant functional groups react with each other to generate a dimerized bond, heterobifunctional chain collapse, where two complementary functionalities attached to the polymer chain react together, and the cross-

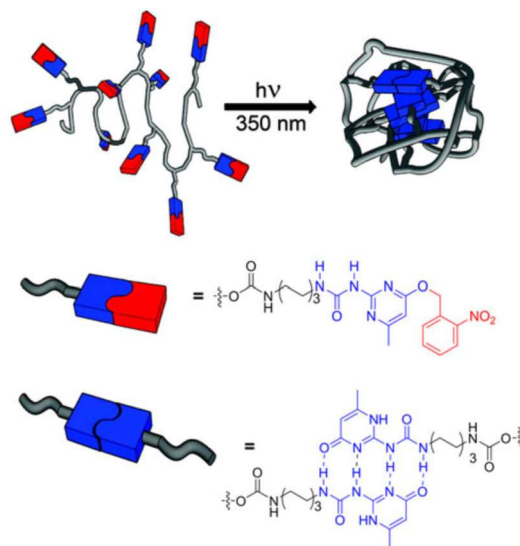
linker-mediated collapse, which uses a cross-linking molecule to bind two other guest functionalities in the polymer. Significantly, the overall structure and potential properties of the single-chain nanoparticle (SCNP) depends on the strategy used for the polymer collapse.



Scheme 1.10. Design of intramolecular chain collapse strategies for polymer inspired from (A) self-folding of protein. Reprinted with permission from reference [69]. Copyright © 2018 Elsevier Ltd. (B) homofunctional, (C) heterofunctional and (D) crosslinker mediated chain collapse. Reprinted with permission from reference [49]. Copyright © 2016 American Chemical Society.

a. Homo-functional chain collapse: The concept of distinct NPs based on intramolecular reaction of single polymer chains was suggested by Martin and Eichinger in 1980s.^{70,71} Later the synthesis of single chain polystyrene (PS) NPs was published by Davankov *et al.*⁷² with pendant chloromethylene groups on linear PS chains self-cross-linked *via* SnCl₄ (catalyst). A few years later, Mecerreyes *et al.* developed unimolecular particles from copolymers based on L,L-lactide, PMMA and PS that intramolecularly interacted in ultra-diluted solutions *via* a radical initiator such as 2,2-azo-bis-isobutyronitrile (AIBN). Later, analogous strategy based on AIBN-induced radical crosslinking of styrene groups was developed by Jiang and Thayumanavan.⁵³ The reactions were performed in ultra-dilute conditions (*ca.* 10⁻⁵ to 10⁻⁶ M) to avoid the favored and competing intermolecular reactions. Since the design of

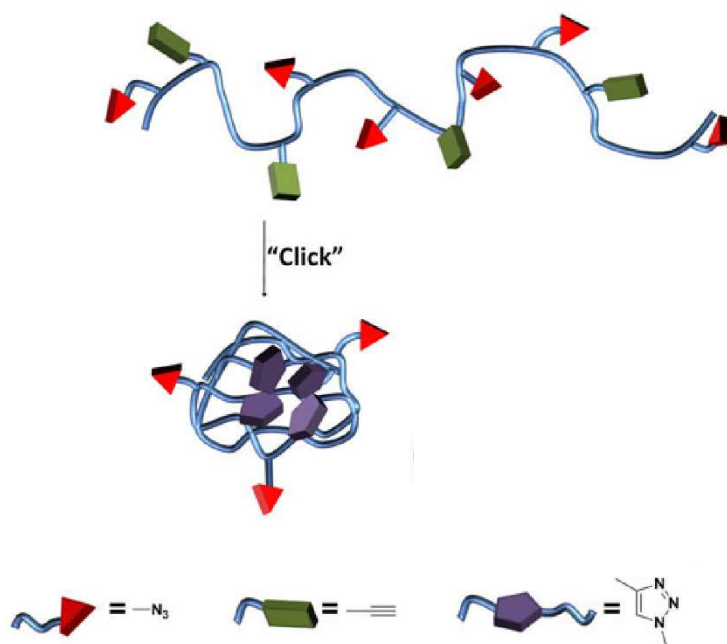
SCPNS *via* covalent bonds lacked dynamicity, supramolecular single-chain NP *via* non-covalent and dynamic covalent interactions were also employed. Such systems may give a better understanding of protein-folding processes despite the simple composition of synthetic polymers than natural polymers which can be used to mimic some of nature's sophisticated processes.



Scheme 1.11. Supramolecular cross-linking of the UPy-urethane sidegroups after protecting group removal via UV irradiation to render collapse of a single polymer chain into a NP. Reprinted with permission from reference [65]. Copyright © 2010 American Chemical Society.

Concerning this, the groups of Hawker and Kim⁷³ synthesized random PMMA copolymers having dendritic hydrogen-bonding self-complementary units. The collapse of the polymer coils was led by the formation of intramolecular H-bonds between the dendritic units, giving stable and discrete spherical SCPNs. In a more recent work, Meijer *et al.* developed a system that could be activated by UV radiation to induce the collapse of linear precursors by supramolecular interactions.⁶⁵ For this purpose, they decorated PMMA with 2-ureidopyrimidinone (UPy) units protected with a photocleavable group (Scheme 1.11). As soon as they were irradiated with UV light, the protecting group was released and each UPy unit could very efficiently form four H-bonds, collapsing the polymer chain to obtain the NP.

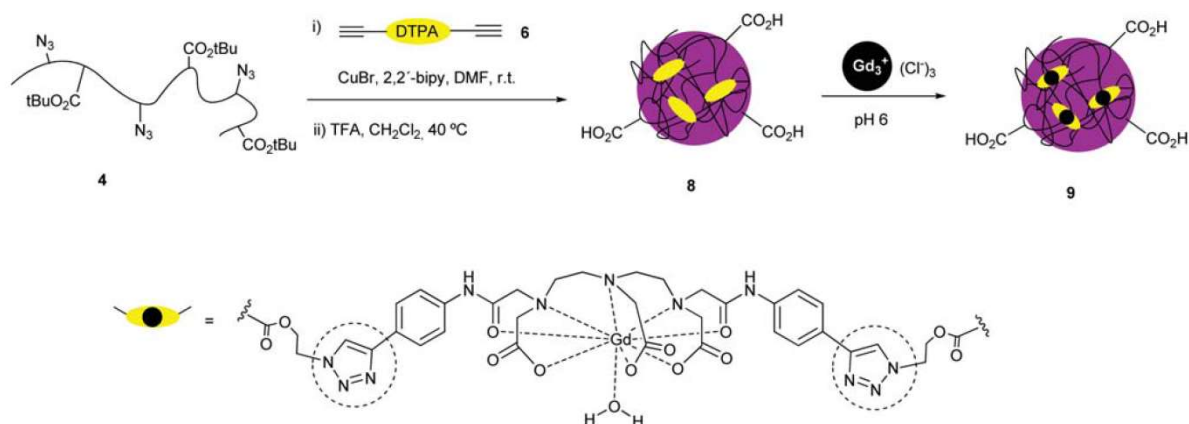
b. Hetero-bifunctional chain collapse: The fabrication of SCPNs can also be carried out with two different but complementary functional side groups pending from the same polymer backbone. Loinaz *et al.* have utilized a “click” reaction as a strategy to produce PMMA SCPNs.⁷⁴ Such “click” reaction was an intramolecular Cu(I)-catalyzed [3+2] cycloaddition that took place between azide and alkyne motifs present in the same polymer backbone at room temperature.⁷⁵ However, it is so often challenging to get a copolymer with two complementary reactive motifs randomly distributed over the backbone.



Scheme 1.12. SCPN formation by intramolecular “click” cycloaddition of self-complementary azide-alkyne group. Reprinted with permission from reference [76]. Copyright © 2012 Springer Nature Switzerland AG.

c. Cross-linker-mediated chain collapse: Difunctional cross-linker-mediated collapse of polymer chains is a very efficient and straightforward method for obtaining SCPNs. Hawker’s group introduced this synthetic approach using isocyanate functionalized acrylic polymers and adiamine cross-linker under mild, room-temperature conditions to generate unimolecular NPs.⁷⁷ They obtained different sets of NPs with controlled diameters ranging from 8 to 20 nm by altering the molecular weight and the percentage of isocyanate motifs in the precursor copolymer. Pomposo *et al.* reported a NP fabrication on “click” chemistry using a difunctional cross-linker. A solution of an aliphatic dialkyne was added very slowly

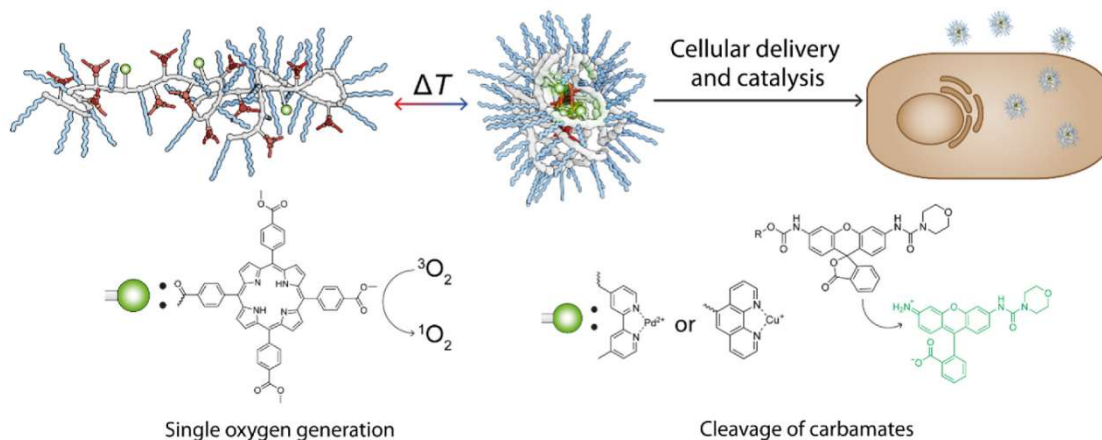
and with a constant rate aided with a syringe pump, to an azide containing copolymer of diverse nature.^{60,78} Following the same method, Odriozola *et al.* prepared water-soluble acrylic SCPNs utilizing a specific cross-linker based on a gadolinium(III) (Gd^{3+}) chelating unit (diethylenetriaminepentaacetic acid, DTPA) with two terminalalkyne functionalities (Scheme 1.13).⁷⁹



Scheme 1.13. Synthesis and deprotection of SCPNs, and loading with Gd^{3+} . The newly formed 1,2,3-triazole rings during the ‘‘click’’ cycloaddition. Reprinted with permission from reference [79]. Copyright © 2010 The Royal Society of Chemistry.

1.3.2. Single chain polymeric nanoparticles as catalytic nanocompartments: As a relatively new class of materials, single-chain polymer nanoparticles (SCNPs) entered the field of biomedical applications. With sizes of an order of magnitude smaller than conventional polymer nanoparticles, SCNPs are in the size regime of many proteins and viruses (1–20 nm) which is suitable for accessing biological barriers like blood brain barrier, blood retinal barrier *etc.* Further, this gives compartmental structures which can mimic protein functions like catalysis and can also be loaded with cargo molecules coupled with stimuli-responsive release of them in desired target environment. Liu *et al.*⁸⁰ introduced a modular post-functionalization approach to synthesize amphiphilic poly(acrylamide) polymers equipped with copper- or palladium-binding ligands (Scheme 1.14). Functionalization of the polymer with a porphyrin motif enabled the photo-induced production of singlet oxygen and the generated singlet oxygen was used to cleave an amino-acrylate linker, releasing a drug mimic from the nanoparticle. Interestingly, the catalytic reactions were performed in phosphate buffer at a physiological pH. Later, the catalytic

activity of the SCPNs studied at both the ensemble and individual level using single-molecule fluorescence microscopy. Recently, they had revealed that depropargylations were also possible using folded copolymers comprising Cu(I) and Pd(II) complexes in the presence of HeLa cells⁸¹

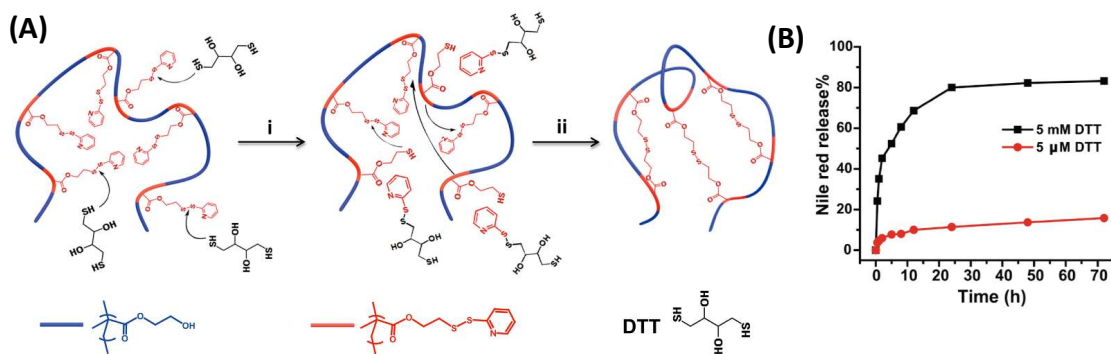


Scheme 1.14. Schematic representation of the folding of catalytically active copolymers, its cellular delivery, and Catalysis. Reprinted with permission from reference [52]. Copyright © 2019 Chinese Chemical Society

Later He *et al.* reported imidazole-functionalized copolymers of poly(methyl methacrylate-co-3-imidazolyl-2-hydroxy propyl methacrylate) which were used for intramolecular Cu-imidazole binding that triggered the self-folding of polymers⁸². Metal-containing single chain polymeric nanoparticles (SCPns) can be used as synthetic mimics of metalloenzymes mimicking monophenol hydroxylation reactions. Cu-containing SCPNs showed a high selectivity for the hydroxylation reaction of phenol to catechol, >80%, with a turnover frequency of >870 h⁻¹ at 60 °C.

In order to use polymer nanoparticles as drug delivery vehicles, drugs may be either covalently linked to the particle or encapsulated using non-covalent interactions. Dye molecules^{83,84} as well as therapeutic cargos have been encapsulated into SCPNs to evaluate the encapsulation process. The cargos are commonly directly added to the reaction mixture during the SCPN formation process and randomly entrapped, often supported by hydrophobic interactions. Solvatochromic properties of dyes, such as Nile red, are highly suited for monitoring hydrophilicity inside particles. Addition of the hydrophobic dye Nile

red to the self-folding PEG/BTA Amphiphilic random copolymers (ARPs) resulted in a blue shift in the emission spectrum that is evidence of the presence of hydrophobic pockets inside the folded ARPs.⁸³ Later on reports based on loading of a naphthalimide-based dye into ARP also appeared.^{81,85}



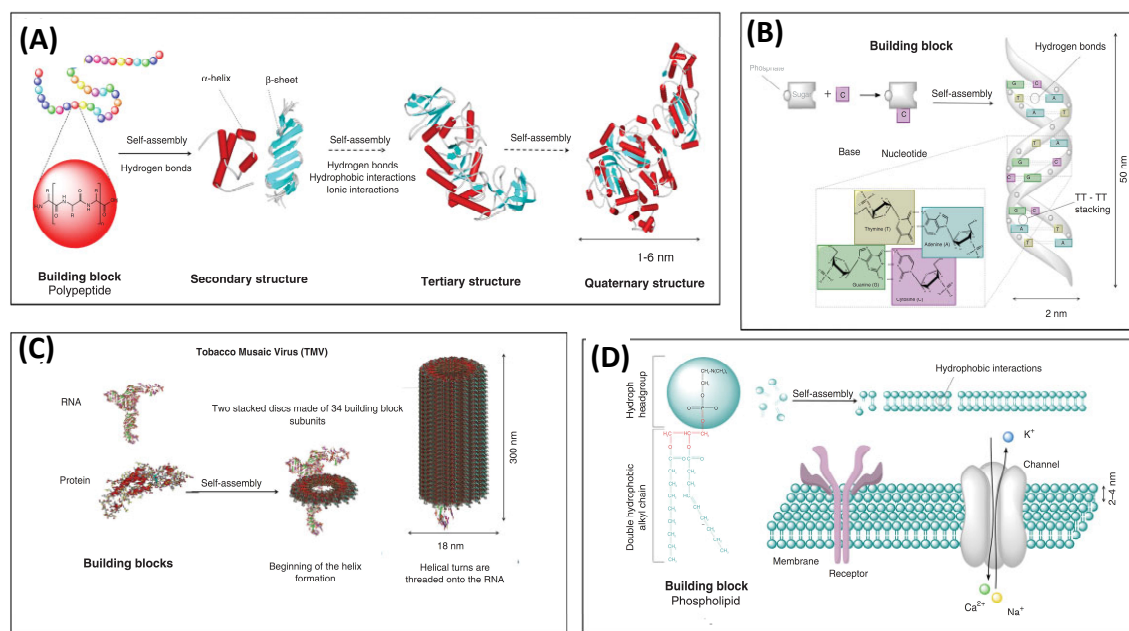
Scheme 1.15. Schematic representation of (A) SCNPs formation by thiol-disulfide exchange; (B) release from disulfide SCNPs of entrapped Nile red at different 5 μ M and 5mMDTT. Reproduced with permission from reference. [86]. Copyright © 2015The Royal Society of Chemistry.

The encapsulation of molecules inside ARPs has also been utilized to entrap drug molecules and drug models. Covalently cross-linked methacrylate SCNPs, containing 41 wt% of vitamin B9 (*i.e.* folic acid), were obtained by Michael addition crosslinking.⁸⁷ As these particles are not water-soluble, they were placed into water to release the entrapped drugs. Release took 5–6 h and comparison with the power law model specified release by Fickian diffusion.⁸⁸ Disulfide-linked SCNPs were loaded separately with Nile red.⁸⁶ Low amounts of DTT used to create free thiols for nanoparticle formation and the particles were stable up to 5 μ M DTT with no significant amount of Nile red releasing. However, at higher DTT concentrations (5 mM), disulfide bridges were cleaved, and Nile red was released when dialyzing the particles in water (Scheme 1.15). Later Cheng *et al.* reported loading of hydrophilic chemotherapeutic 5-fluorouracil into PEG U-DPy ARPs.⁸⁹ Drug loading of up to 19.6 wt% was achieved and a combination of high temperature and low pH was needed to break the U-DPy hydrogen bonds and thus to release the drug in water. Hence, release from SCNPs is not only limited to passive diffusion alone, but can also be in retort to changing chemical environment, or temperature conditions. Still more systematic study is

lacking in the system where controlled loading *via* difference in folded-unfolded morphology, multi cargo loading and delivery and feedback loop release control systems are yet to be explored.

1.4. Mimicking Nature’s precision with peptide self-assembly

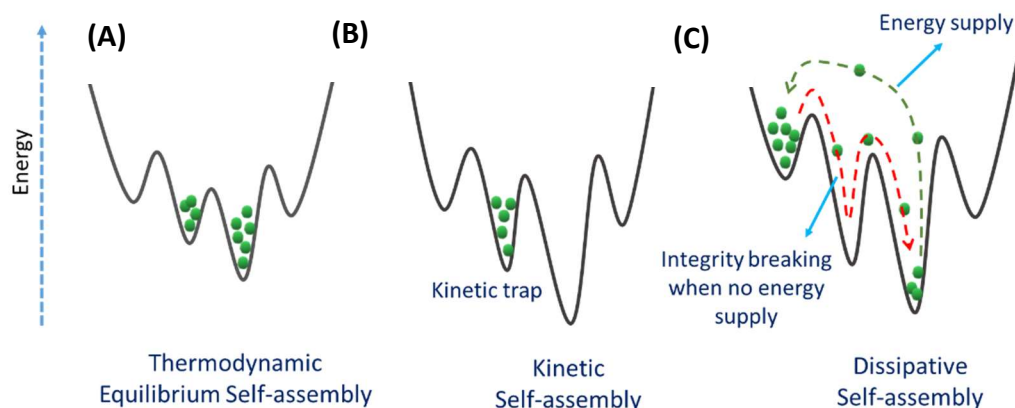
Molecular self-assembly is a ubiquitous process that results in formation of organized structures from small molecular building blocks *via* interplay of supramolecular interactions in its environment using a bottom-up approach. Self-assembly is of primary importance to life where it generates much of the functionality of the living cell with a variety of biological structures, ranging from proteins and nucleic acids to viruses and cell membranes (Scheme 1.16).



Scheme 1.16. Examples of biological self-assembled structures showing the building blocks and the relevant interactions involved in the self-assembly process. (A) Protein folding; (B) ds-DNA; (C) tobacco mosaic virus (TMV); and (D) cell membrane.. Reproduced with permission from reference. [90]. Copyright © 2013 Wiley Periodicals, Inc.

These structures possess a highly precise organization on the nanometer scale derived from its specific interactions at molecular level. Self-assembling systems play a significant role in performing physiological functions.

The common self-assembly process which can be mimicked easily in synthetic systems comes under thermodynamic control where molecules from the monomeric state can easily enter self-assembled systems and is reversible vice versa. Thermodynamically self-assembled structures are quite stable as they continue in the global energy minimum. However, the nature attains its precision in synthesis of architectures *via* adaptive kinetic self-assembly where self-assembled system results in a single structure that defines the property of the system which are momentarily stable and confined in the lower free-energy state that with either an activation energy or with incubation time changes to global energy minima or by dissipative self-assembly where system requires a continuous source of energy to maintain its dynamicity (Scheme 1.17).



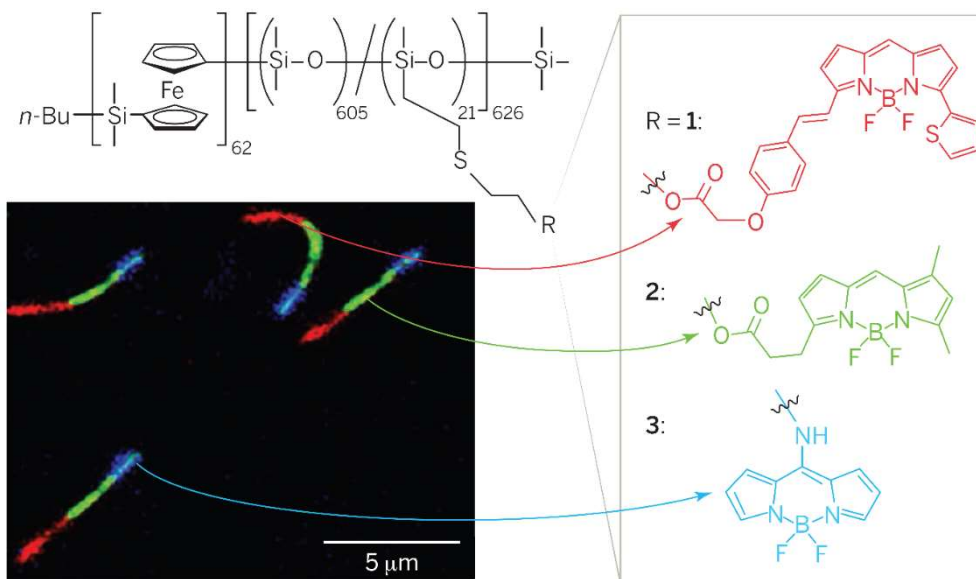
Scheme 1.17. A representative scheme illustrating the different routes of self-assembly. (A) Thermodynamic or equilibrium, (B) kinetic trap and (C) dissipative self-assembly. Reproduced with permission from reference. [91]. Copyright © 2015 Springer Nature Limited

Although self-assembly processes controlled by kinetic trap and energy dissipation were thought to be difficult to mimic in lab hitherto, recent reports shows it is possible by living supramolecular polymerization which renders such emergent self-assembly technique an exciting arena of research.

1.4.1. Living Supramolecular polymerization (LSP) and control over nanostructures:

In supramolecular polymerization, monomers bond through reversible noncovalent interactions like hydrogen bonds (H-bonds). Supramolecular polymerization typically

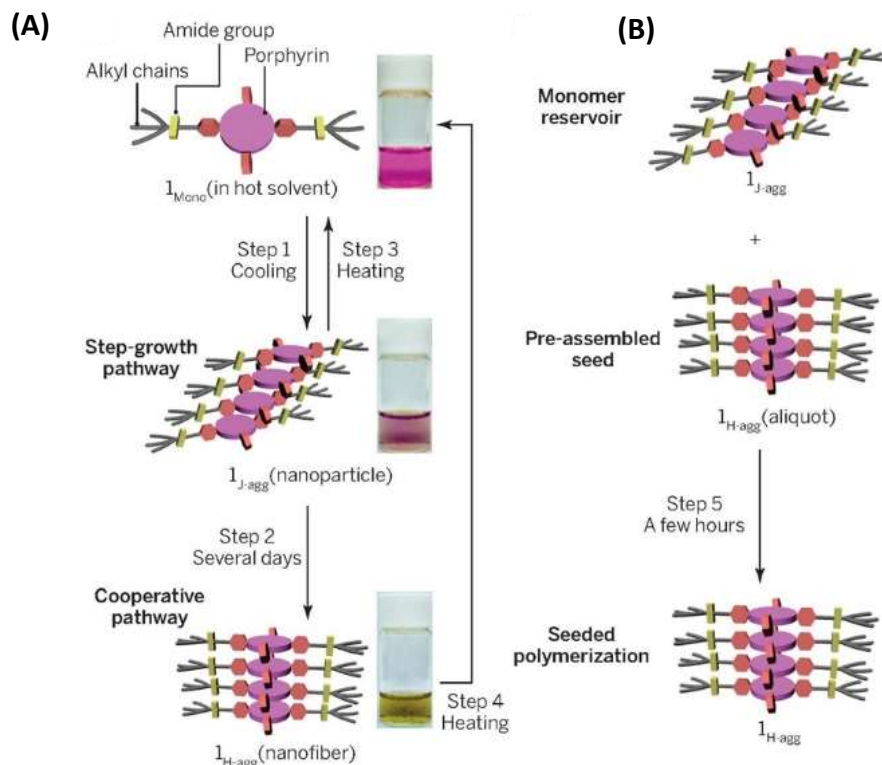
continues in step-growth fashions where the monomer which is reactive on both ends couples and many smaller fragments form before the appearance of long chain. Living polymerization presented in the 1950s,⁹² led to a broad development in covalent polymer synthesis area.⁹³ However, its supramolecular equivalent approach developed lately which gave better control and uniformity of chain growth and dispersity in supramolecular polymers. In living supramolecular polymerization (LSP), monomers undergo interaction in presence of an initiator to produce an active center or living end which regenerates on addition of further monomer and propagates along the polymer chain before chain transfer or termination which is in-fact removed from the system. The last monomer unit on a polymeric strand remains active giving provision for addition of another block.



Scheme 1.18. Laser scanning confocal microscopy image (scale bar, 5 μm) of self-assembled polyferrocenyl dimethylsilane block copolymer micelles functionalized with fluorescence tunable BODIPY derivatives. Reproduced with permission from reference [94]. Copyright © 2015, American Association for the Advancement of Science.

LSP is an efficient control on the degree of polymerization, the chain conformation, and its lifetime. An early effort on living supramolecular polymerization was made by Manners *et al.* by assembling polyferrocenyl dimethylsilane block copolymers in hydrocarbon solvents by crystallization driven self-assembly (Scheme 1.18). Addition of a

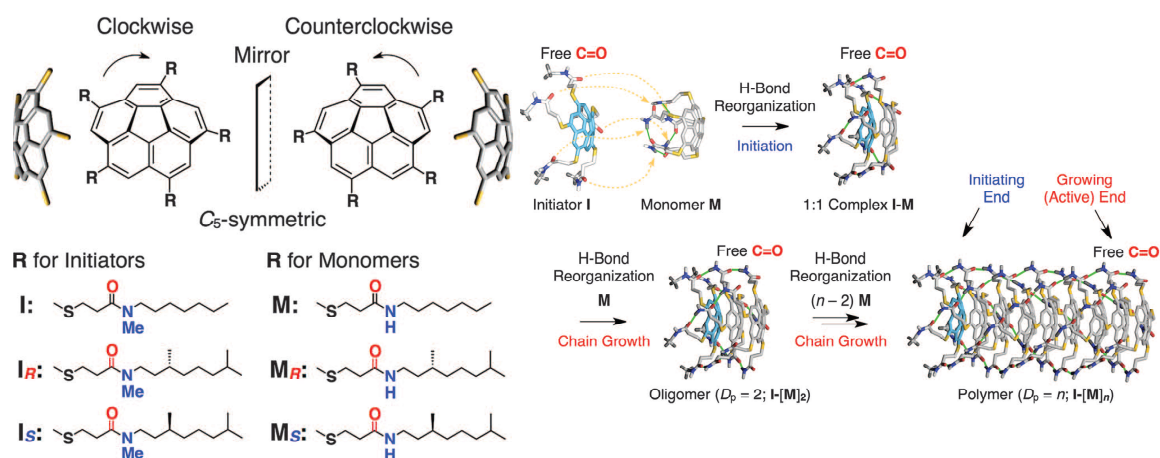
fresh feed of the polymer in a good solvent like tetrahydrofuran caused the nanosized cylindrical micelle seeds to grow up to micrometers in length.⁹⁵ They had also prepared hierarchical one-dimensional (1D) or 3D multiblock co-micelle structures by addition of different block copolymers to the preformed micellar seeds, which were stable both in solution and in solid state. Similarly, Aida and co-workers achieved a p-n hetero-junction through seeded growth of hexabenzocoronene derivatives into semiconducting nanotubes.⁹⁶ This paid a step ahead in the progress in the field which was already proven under thermodynamic control resulting in equilibrium structures. A massive mainstream of supramolecular polymers, formed *via* isodesmic or a cooperative mechanism, are examined in thermodynamic control.^{97–99} However, the concept of pathway complexity, synchronicity of multiple competitive pathways in self-assembly pave the way for a new archetype and way to control the destiny of supramolecular systems under a variety of conditions.^{91,100–103} E.W. Meijer *et al.* have reported S-chiral oligo(*p*-phenylenevinylene) (SOPV) system¹⁰⁰ that assembles to result right handed off-pathway metastable aggregate (*P*-SOPV) and left-handed on-pathway stable aggregate (*M*-SOPV) through nucleation elongation mechanism depending on the solvent systems (interplay of polar and apolar) and reaction conditions employed. It is vital to build a far-from-equilibrium condition by means of kinetically controlled self-assembly. A promising scheme to get switch over the kinetics of one-dimensional aggregation processes is living supramolecular polymerization. The living supramolecular polymerization has been attained using seed-mediated (SSP) as well as the initiator molecule facilitated strategy where either added seeds or properly designed molecules that function as initiators and is employed for the growth of monomers into one-dimensional non-covalently bound molecular aggregates. The kinetically trapped species generate an out-of-equilibrium scenario in which the nucleation of the monomers, prior to the subsequent elongation, is retarded. There are scarce examples of kinetically controlled supramolecular polymerization that proceeds through the formation of metastable species is scarce in literature. Sugiyasu, Takeuchi, and co-workers¹⁰⁴ showed the seeded controlled approach in systems undergoing self-assembly following a nucleation–elongation mechanism coupled with a kinetically controlled pre-equilibrium process.



Scheme 1.19. (A) Supramolecular seeded growth of nanofibers from molecule **1** proceeds slowly after first forming nanoparticles, but when these nanoparticles interact with existing nanofibers (B) living supramolecular polymerization occurs. Reproduced with permission from reference [104]. Copyright © 2014 Macmillan Publishers Limited.

The porphyrin-based molecule initially forms J-aggregates leading to metastable organic nanoparticles which after several days transformed into stable “H- aggregates” with nanofiber morphology *via* cooperative mechanism (Scheme 1.19). The nanofibers formed much more rapidly when an aliquot of nanofiber was added to the nanoparticle solution which served as porphyrin monomers through a living polymerization process. Lately, a smart molecular design by Würthner and co-workers¹⁰⁵ allowed a prolonged lag time in the self-assembly process of a perylene bisimide-based organogelator by locking the molecule in an inactive conformation *via* induced intramolecular H-bonding. A living polymerization process was achieved by introducing preassembled nanofibers of the organogelator as seeds. Later Miyajima, Aida, and co-workers¹⁰⁶ reported a unimolecular living polymerisation of a nonplanar bowl-shaped corannulene molecule attached with five amide-functionalized thio alkyl chains. This *C*₅-symmetric molecule did not undergo self-assembly *via* intermolecular

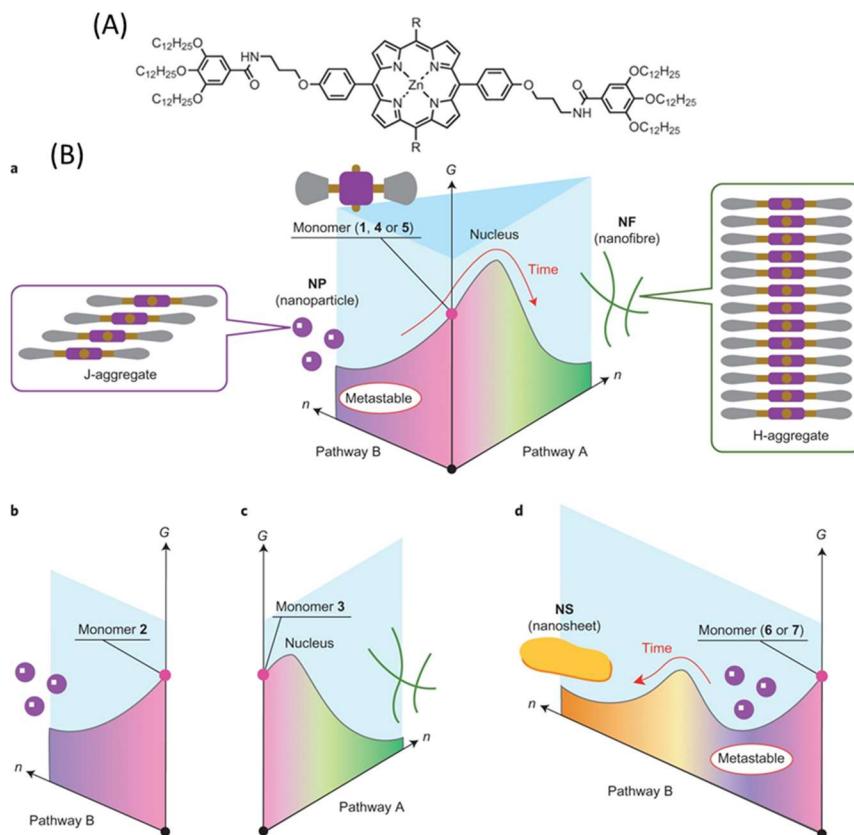
H-bonding in methylcyclohexane (MCH) (Scheme 1.20). However, upon heating, this metastable cage like monomer opened up to undergo a spontaneous 1D self-assembly. Once such assembly formed, it continued to grow with a fresh supply of the metastable monomer even at low temperatures. Further work by Aida *et al.* used corannulene molecules functionalized with methyl-substituted amides as the initiator for chain-growth polymerization and it served as suitable proton acceptors¹⁰⁷ when a caged corannulene molecule approaches. Polymerization was initiated only from one face of the monomer and promoted growth only in a particular direction.



Scheme 1.20. Unimolecular chain growth supramolecular polymerization proposed by Aida *et al.* Reproduced with permission from reference [107]. Copyright © 2015 American Association for the Advancement of Science

However, such control over dimension was limited only in 1D materials until recently, when Masayuki Takeuchi, Kazunori Sugiyasu, and coworkers have reported tweaking of the metastable porphyrin derivatives supramolecular assemblies to form 1D nanofiber *via* face-to-face H-aggregate and 2D nanosheet *via* route short-slipping J-aggregate as shown in Scheme 1.21. The interplay of molecular design, molecular recognition, and pathway complexity in the self-assembly exposed the energy landscape that showed kinetic behavior. Introducing more steric hindrance to the molecule promoted pathway B to result in nanosheet.¹⁰⁸ The interplay of dynamic covalent chemistry and self-replication was used by Otto *et al.* to grow kinetically controlled fibers in aqueous milieu from metastable macrocycles with an excellent length control.¹⁰⁹ Suhrit Ghosh *et al.* also

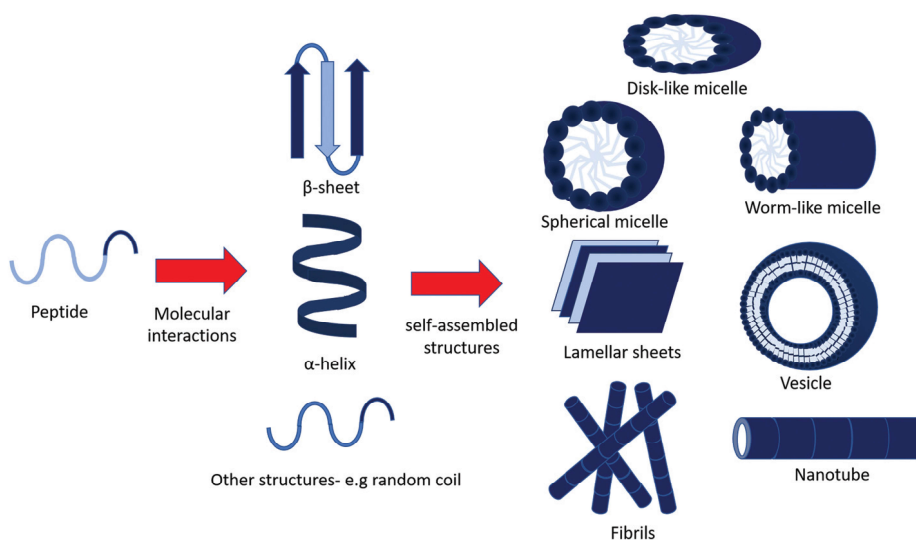
demonstrated supramolecular polymerization in naphthalene-diimide systems with perfect control by a chain-growth mechanism.^{110,111} Besides nucleation-elongation model in amyloid fibril formation, provides a vital cue to study the pathway complexity to get an insight of the fibrillation.^{112,113}



Scheme 1.21. (A) Chemical structure of the porphyrin derivative. (B) Self-assembly energy landscapes of porphyrin derivatives. (a-d) Self-assembled energy landscapes for a range of porphyrin derivatives. Red arrows show the transformation on time lag: (a) metastable nanoparticles are kinetically formed and they transformed into (a) nanofiber and (d) nanosheet after an incubation time period shown by Masayuki Takeuchi, Kazunori Sugiyasu and coworkers. Reprinted with permission from reference [108]. Copyright © 2017 Springer Nature.

1.4.2. Peptide as a building block for nanostructures: The fabrication of new materials using natural building blocks, such as phospho-lipids, oligosaccharides, oligonucleotides, proteins, and peptides, has become a subject of major interest.¹¹⁴ Among them, peptides have drawn important consideration due to their precise structure, good chemical and physical stability, morphological, sequential diversity and the possibility to produce them in large

amounts. In addition, peptides are known as exciting building blocks for generating self-assembled nanostructures in biomedical applications due to their inherent biocompatibility, biodegradability as well as ease of obtainability. Peptide amphiphiles are capable to self-assemble to effect in a range of hierarchical structures (Scheme 1.22). Recently Samuel I. Stupp and coworkers focused on supramolecular chemistry and materials science, learning towards the functional aspect of the designed bio-material.¹¹⁵

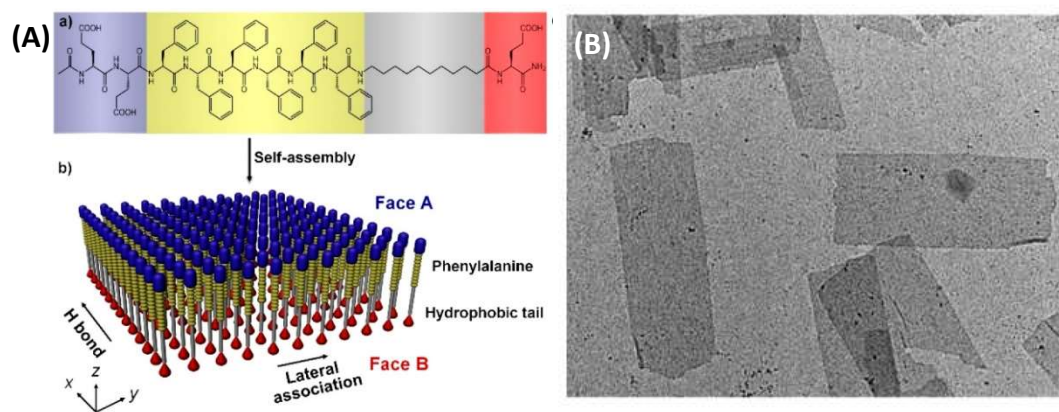


Scheme 1.22. Peptide undergo self-assembly to give a range of supramolecular nanostructures. Reprinted with permission from reference [116]. Copyright © 2017 The Royal Society of Chemistry.

Pol Besenius and coworkers demonstrated the synthesis of peptide-based copolymers that self-assembled to form nanorods in water. They described that the oxidative disassembly of charged ampholytic copolymers is up to two times faster as compared to neutrally charged homopolymers. This work finds its importance in view of tuning the oxidation induced disassembly which tends to be extremely slow and requires high concentrations of reactive oxygen species and acidic media.¹¹⁷ Further, they reported pH-responsive self-assembly of peptide-based copolymer systems using diethoxy substituted naphthalene diimide (NDI). The study demonstrated the importance of molecular design on their structure that directs the functional properties.¹¹⁸

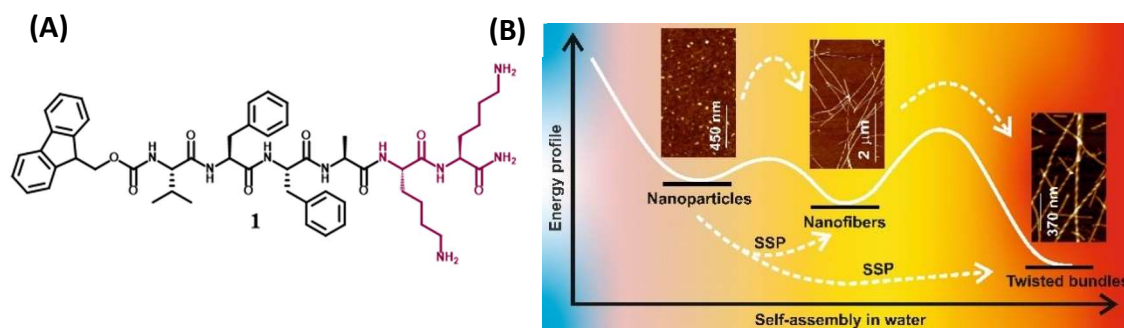
Recently, M. Stevens *et al.* reported the thermodynamically controlled growth of solution-processable and free-standing nanosheets *via* peptide assembly in two dimensions.

Self-assembly of F6C11 peptide amphiphile containing hexa-phenylalanine, a hydrophobic tail, and glutamic acids to the formation of Janus 2D structures with single-layer thickness *via* self-sorting between peptide β -strands and hydrocarbon chains is demonstrated which enable a predetermined surface heterofunctionalization (Scheme 1.23).¹¹⁹ A controlled 2D-to-1D morphological transition was achieved by subtly adjusting the intermolecular forces. These nanosheets provide an ideal substrate for the engineering of guest components (*e.g.*, proteins and nanoparticles), where enhanced enzyme activity was observed. Thus it was anticipated that sequence-specific programmed peptides will offer promise as design elements for 2D assemblies with face-selective functionalization.



Scheme 1.23. (A) Schematic of **F6C11** self-assembly into Janus nanosheets following self-sorting between phenylalanine (blue) and hydrocarbon tails (red) and resultant nanosheets as seen in TEM. Reprinted with permission from reference [119]. Copyright © 2017 American Chemical Society.

Recently in our group by Singh *et al.* also demonstrated a peptide amphiphile **1** inspired by the β -amyloid nucleating core of A β 42 based short peptide sequence VFFAKK (Scheme 1.24) which demonstrated step-wise self-assembly in water.¹²⁰ Variation of temperature or solvent composition arrests the self-assembly to result metastable nanoparticles which on gradual increase in temperature produce kinetically controlled nanofibers at 25°C and eventually thermodynamically stable twisted helical bundles at 80 °C. Mechanical agitation of the fibers is performed to furnish short seeds with narrow polydispersity index, which by mediation of seeded supramolecular polymerization established length precision of the nanofibers.



Scheme 1.24. (A) Chemical structure of the peptide amphiphile **1** and (B) pathway driven self-assembly to produced different nanostructures. Reprinted with permission from reference [120]. Copyright © 2018 Royal Society of Chemistry.

Thus, we believe that a deep understanding into the fundamentals of this self-assembly process to give multi-ordered nanostructures which helps in designing peptides for functional applications like hydrogel formation, catalysis *etc.*

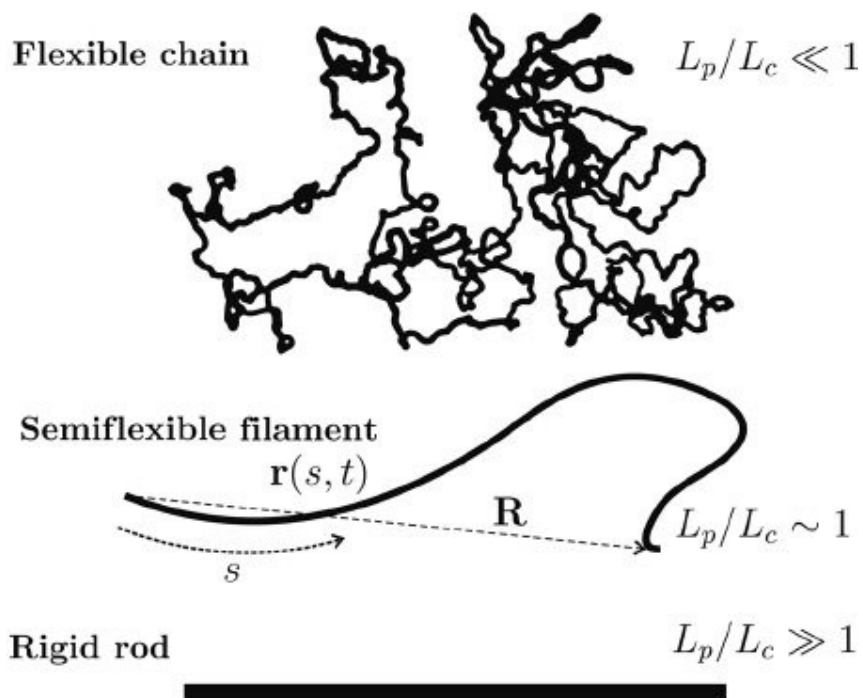
1.5. Mimicking strain-stiffening in peptide-polymer networks

1.5.1. Strain-stiffening in fibrous protein networks: Cells and connective tissues in our body are exposed to various stimuli of deformations like shear force due to blood flow, tensile stress on epithelium *etc.*¹²¹ In this realm, assembled fibrous protein networks are crucial factors that helps in maintenance of mechanical strength and structural integrity of body organs in a dynamic manner.¹²² Three distinct types of fibrillar structures found in cells are actin, tubulin and intermediate filaments which synergistically act in combination with a numerous crosslinking and motor proteins which facilitates cell motility to mechano-responsiveness.^{123,124} In contrast to the cytoskeleton (CSK), the static extracellular matrix (ECM) contains fibrin and collagen fibers. Fibrin is actively involved in the formation of blood clots and plays a major role in wound healing,¹²⁵ whereas collagen is the most abundant acting as the main load-bearing component in tissues.¹²⁶ The critical morphological features seen on comparing CSK and ECM networks are rigid-to-semi-flexible polymer bundles and large mesh network. Thus, it exhibit an amazing tendency to stiffen in response to mechanical stimuli. Such process is referred to as strain-stiffening and is critically

implicated in maintaining tissue and cell integrity under external and internal forces. The physical origins of nonlinearity in these systems is dependent on the structural and morphological characteristics of the constituent biopolymers.

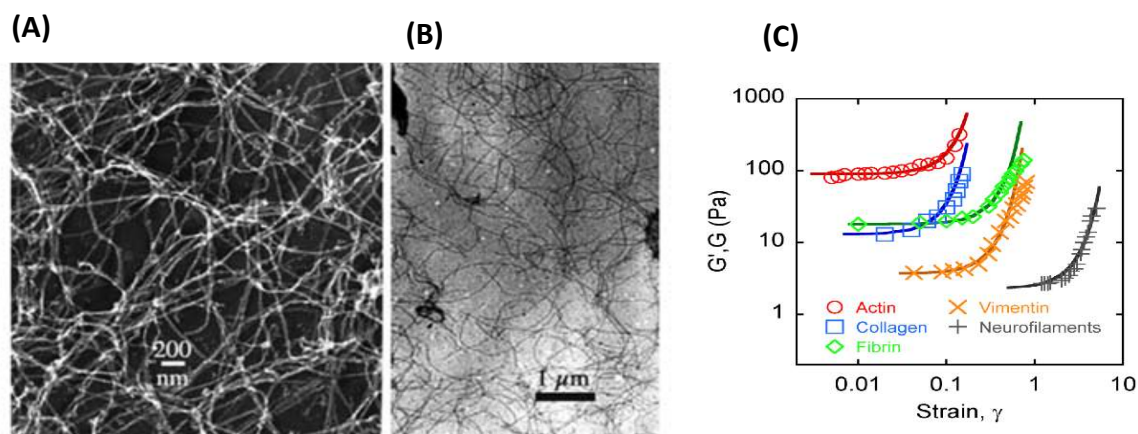
1.5.2. Physical origin of strain-stiffening: The structural heterogeneity and complexity intrinsic to biological systems often hinders an explicit understanding of the strain-stiffening behavior. Therefore, rheology and theory on reconstituted gels from isolated extracellular or cytoskeletal proteins have become prevalent complementary strategies. Such *in vitro* studies capture some of the features measured such as strain-stiffening and negative normal force.¹²⁷ The rigidity of a polymer backbone determines how an individual polymer chain responds to an external loading. A flexible polymer chain sustain large deformations without any significant resistance before reaching full elongation. On the other hand, semi-flexible and rigid polymers access their non-linear extensional regimes even small strains. The onset of non-linear regime is directly related to persistence length L_p . L_p is defined as the characteristic length of tangent to tangent correlation where thermal fluctuations $k_B T$ are adequate to inverse the course of the filament. In a semi-flexible polymer, L_p is comparable to its contour length L_c (*i.e.* the length at full extension) where $L_p/L_c \sim 1$. Besides semi-flexible polymers, two additional regimes can be illustrated (Scheme 1.25), one of it is rigid rods ($L_p/L_c \gg 1$), corresponding to a nearly fully expanded conformation of the backbone where nonlinear elasticity arises from pulling of molecular bonds along the filament axis. (2) Flexible chain ($L_p/L_c \ll 1$), wherein thermal energy bends the filament to orient as a random coil and most synthetic polymers fall within this group.

Ultimately, the elastic behavior in these materials is governed by the resistance to bending and stretching of the semi-flexible filaments. Filament stretching gives an affine-type of deformation (*i.e.* the local strains are uniformly distributed within the material and follow the imposed macroscopic strain), whereas filament bending shows signatures of non-affinity.

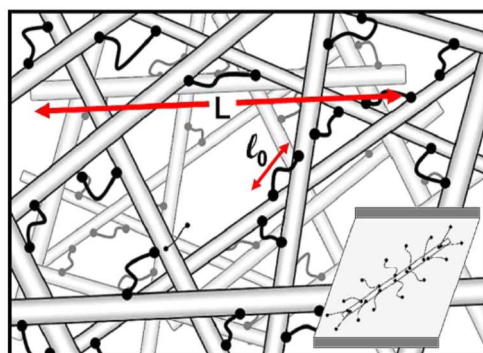


Scheme 1.25. Classification of polymers based on backbone stiffness: flexible chains adopt a random coil conformation, semi-flexible filaments are nearly straight with thermal folds, and rigid rods are not influenced by thermal energy. Reprinted with permission from reference [128]. Copyright © 2014, Royal Society of Chemistry.

1.5.3. Theoretical models for synthetic systems: The early theoretical work suggests that strain-stiffening is inherent to any connected meshwork of semi-flexible polymers by Storm *et al.*¹²⁹ (Scheme 1.26). Here a molecular theory was reported that showed strain-stiffening in a range of reconstituted gels formed from cytoskeletal and extracellular proteins and revealed universal stress–strain relations ranging from low to intermediate strains. With the input of force extension for semi-flexible filaments as well as with the model of homogeneous, isotropic, and have uniform straining, they showed that systems of filamentous proteins arranged in an open mesh network stiffen at low strains without any external crosslinker. Later it was shown that strain-stiffening is also possible in a flexibly cross-linked stiff polymer network where randomly oriented stiff filaments or rods are interconnected by relatively short but highly flexible cross-linkers (Scheme 1.27).



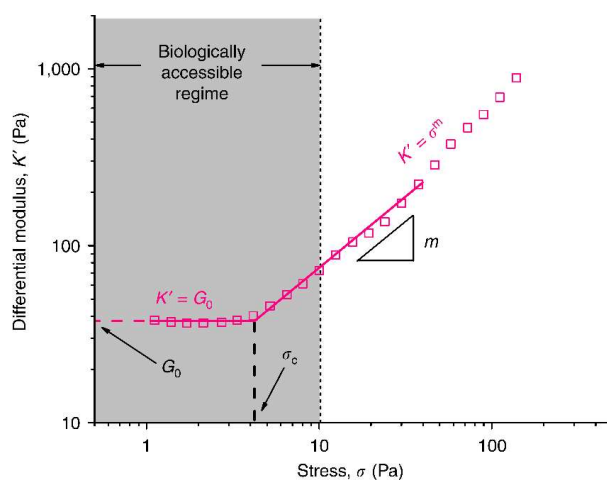
Scheme 1.26. Neurofilament and fibrin protofibril networks. (A) Metal shadowed neurofilaments, and (B) uranyl acetate-stained fibrin protofibrils. (C) Dynamic shear storage moduli measured at different strain amplitudes for a series of crosslinked biopolymer networks. Reprinted with permission from reference [129]. Copyright © 2005 Nature Publishing Group.



Scheme 1.27. Schematic figure of an isotropic stiff polymer network with highly compliant cross-linkers. The inset illustrates the proposed non-uniform deformation of the crosslinkers on a single filament in a sheared background medium. Reprinted with permission from reference [130]. Copyright © 2008 The American Physical Society.

1.5.4. Measurement of non-linear elasticity: The nonlinear elasticity of hydrogels can be measured using oscillatory shear rheology. In a conventional strain-controlled rheometer apparatus, the gel is placed (or formed *in situ*) between two plates. While the lower plate remains stationary, the upper plate imposes a sinusoidal strain on the gel of the form $\gamma = \gamma_0 \sin(\omega t)$ and the shear stress σ needed to induce such deformation is measured. The output stress is also recorded in the form of a sinusoidal function with an associated phase shift (ϕ)

such that $\sigma = \sigma_0 \sin(\omega t + \varphi)$. The elasticity of the gel, given by its storage modulus G' , is obtained from the part of stress that oscillates in phase with the imposed strain, where $G' = \sigma_0 \gamma_0^{-1} \cos(\omega t)$. Concurrently, the out-of-phase stress yields the viscous contribution given by its loss modulus G'' , whereby $G'' = \sigma_0 \gamma_0^{-1} \sin(\omega t)$. As a simple sinusoidal function cannot describe biopolymer network accurately because of non-linear relationship with applied strain, constant pre-stress σ is applied to the material in parallel superposition with a low-amplitude oscillatory stress that gives differential modulus $K' = \delta\sigma/\delta\gamma$ (*i.e.* the derivative of the stress-strain curve) which is a perfect description of the modulus in its stressed state.^{131,132} As described by rubber elasticity theory, the stiffness of most synthetic gels with individual flexible polymers is characterized by a linear regime where K' is independent of applied stress (or strain), followed by a non-linear extensional regime at a particular critical point dominated by entropic elasticity.¹³³ In practice, however, probing non-linear regime for such synthetic materials is difficult owing to the detachment of the gel from the rheometer plates at higher strains.¹³⁴ The onset of non-linearity of most biopolymer gels called critical stress σ_c , is attained at much smaller stresses—typically in the range of 1-10 Pa in range of the cell traction forces within their contiguous matrix.¹³⁵ Thus the two distinct regimes on stressing the material are a linear, low-stress regime where K' is defined by the plateau storage modulus ($K' = G'_0$) and a stress-stiffening regime beyond σ_c where



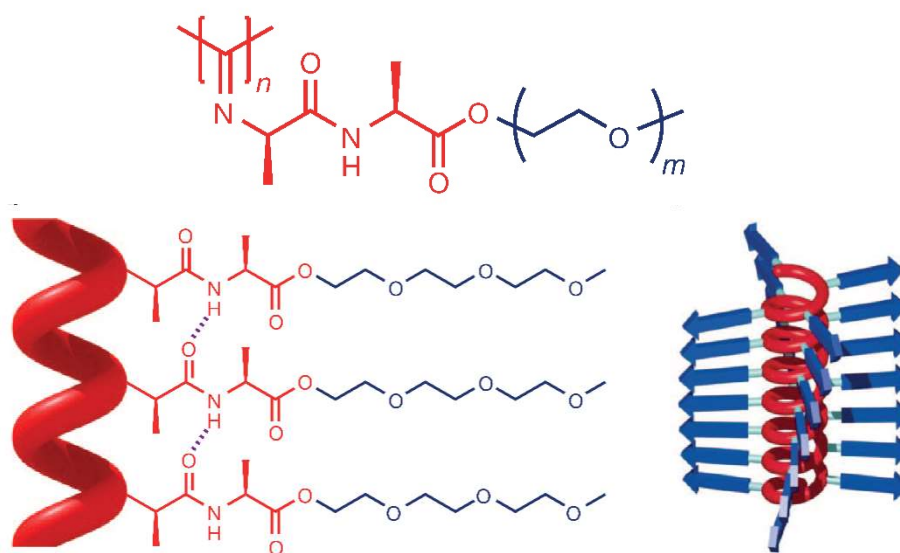
Scheme 1.28. Differential modulus K' plotted against stress σ for ethyleneglycol functionalised Polyisocyanopeptide gels. Reprinted with permission from reference [136]. Copyright © 2014 Macmillan Publishers Limited.

the magnitude of K' increases as a power law $K' = \sigma^m$. The index m , known as the stiffening exponent, yields a direct measure of the degree of mechanical responsiveness, reaching an upper limit $m = 3/2$ at large stresses ascribed to the stretching out of thermal undulations that corresponds to the terminal scaling predicted by the theory of semi-flexible networks.¹³² These parameters determined in combination provides a direct measure of sensitivity and mechanical response and sensitivity of gel towards applied stress (Scheme 1.28).

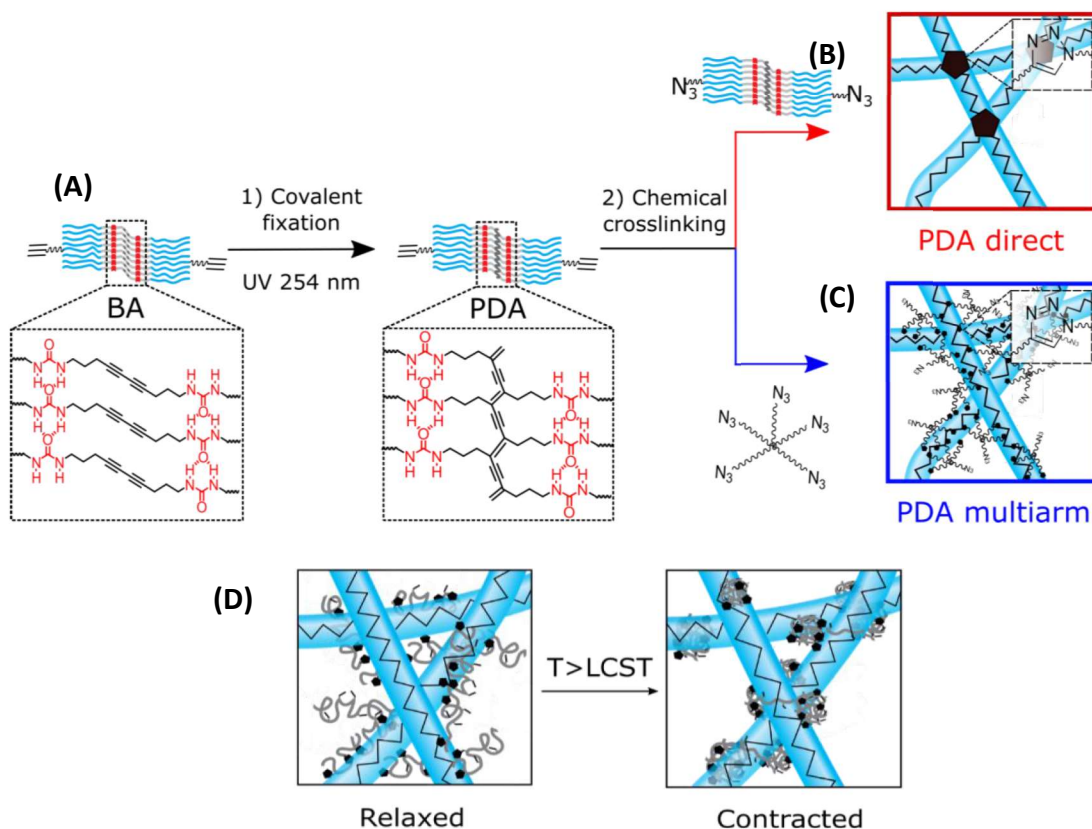
1.5.5. Biomimetic strain-stiffening hydrogels: Recently, strain-stiffening has been identified to improve cell spreading and cell differentiation in soft scaffold substrates.^{137–140} Thus, designing strain-stiffening hydrogels which are biomimetic holds promise in biomedicine. In pursuit of this, Rowan and co-workers introduced a major breakthrough in this area with the design of polyisocyanopeptides (PICs) polymers grafted with short oligo(ethylene glycol) (OEG) blocks¹⁴¹ PICs fold to β -helices which is stabilised through intramolecular hydrogen-bonds in parallel to the polymer backbone (Scheme 1.29). These protein mimics undergoes a sol to gel conversion on heating beyond the lower critical solution temperature (LCST) of the peripheral OEG that gives a transparent hydrogel at low polymer concentration. The gelation process relies on physical aggregation of individual PIC chains forming bundles of well-defined dimensions in which, the helical architecture of the polymer backbone regulate the assembly process, such that, an increase of polymer length and/or concentration does not increase the aggregation number. Mechanically, PIC networks share vital metrics with gels from neurofilament fibers for example, the upper limit of $m = 3/2$ at high stresses consistent with both networks. Moreover, PICs were recently united with flexible, semi-flexible and rigid elements to form composites that exhibited more biomimetic synergy between cytoskeleton and extracellular subsystems.¹⁴³

Sijbesma *et al.* later demonstrated biomimetic, strain-stiffening materials made through self-assembly and covalent fixation of small building blocks to form fibrous hydrogels that are able to stiffen by an order of magnitude in response to applied stress^{144–146} (Scheme 1.30). The gels consisted of semiflexible rod like micelles of bisurea bolaamphiphiles with oligo(ethylene oxide) (EO) outer blocks and a polydiacetylene (PDA) backbone. A gelation method based on Cu-catalyzed azide-alkyne cycloaddition (CuAAC),

was developed and shown to lead to strain-stiffening hydrogels with unusual, yet universal, linear and nonlinear stress-strain response. Crosslinking the fibers with direct arm, multiarm crosslinkers displayed strain-stiffening and self-healing hydrogels that closely mimic the mechanics of biological networks. Further, the chemical crosslinking of a fibrous matrix with thermoresponsive poly(*N*-isopropylacrylamide) (PNIPAM) produces internal stress by induction of a coil-to globule transition upon crossing the lower critical solution temperature of PNIPAM, resulting in a unique stiffening response that spans more than three orders of magnitude in modulus. Moreover, rigidified networks dramatically stiffen in response to applied shear stress featuring power-law rheology with exponents that match those of reconstituted collagen and actomyosin networks pre-stressed by molecular motors.



Scheme. 1.29. Molecular structure of PICs depicting the β -sheet helical backbone stabilised *via* peptidic intra-chain dialanyl hydrogen bonds (dotted lines). PICs consist of a stiff polymer backbone (red) grafted with flexible oligo(ethylene glycol) chains of varying lengths (blue). Reprinted with permission from reference [142]. Copyright©2013 Macmillan Publishers Limited. All rights reserved.



Scheme 1.30: (A) Hierarchical self-assembly through intermolecular H-bonding and hydrophobic interactions of diacetylene bisurea bolaamphiphiles followed by topochemical polymerization of the stacked diacetylenes. Aggregation of 9-10 ribbons into semi-flexible fibres followed by covalent crosslinking into strain-stiffening networks and Photo-polymerization of the assembled diacetylene groups (i.e. covalent fixation) and the resulting PDAs. Further crosslinking with (B) direct arm, (C) multi arm and (D) PNIPAM crosslinker. Reprinted with permission from reference [144,146]. Copyright©2018, 2019 American Chemical Society

Designing biomimetic polymeric system possessing a similar biomechanical nature is still an open area with much to be explored. Unlike the reported synthetic systems, peptide fibers formed by pathway dependant self-assembly crosslinked to form network may be a good candidate in terms of close mimic to a natural biological system.

1.6. Scope of research

Thus, there are excellent opportunities to design stimuli-responsive materials using polymer and peptide as building blocks. The materials can be tailor-made to create complex

nanostructures in precise way to understand the working principle of natural materials and to utilize that knowledge for functional applications.

In this regard, Chapter 2 is devoted to the photo-responsive chain collapse of flexible polymer to give versatile nanostructures from globular nanoparticles to polymer networks that has autonomous self-healing ability and can be modulated by external stimuli *e.g.* light.

Chapter 3 demonstrates the intramolecular chain collapse of amphiphathic random graft polymers having thermo-responsive back bone and photo-responsive functionality in it to nanoparticle *via* dual response *i.e.* photodimerization and host-guest interaction. The system shows excellent tunability and fidelity as nanocompartments which was utilized for loading and release of cargo under thermo-responsive trigger.

In chapter 4, photoresponsive short amyloid peptide-based self-assembled pathway dependent divergent nanostructures such as fibers and sheets are formed *via* self-assembly. The nanostructures show excellent control in growth in terms of length and area and was utilized for functional applications.

In chapter 5, strain-stiffening behavior which is commonly seen in natural biopolymers is mimicked in a network of the nanofibers from short amyloid peptide and thermo-responsive PNIPAM polymer crosslinker. Later, the nanofibers are covalently fixated and shown excellent enhancement in strain-stiffening behavior.

1.7. Objectives of the present thesis:

The thesis consists of broad section of stimuli-responsive material synthesis, physical studies and their applications. The platforms for the materials are both polymer and peptides. The overall objectives of the thesis are as follows:

1. Design and synthesis of stimuli responsive polymers *via* controlled living polymerisation *e.g.* ATRP, RAFT *etc.* Designing a library of polymers with control over molecular weight and functionality. Monitoring the chain collapse of the polymers *via* different techniques such as spectroscopic, scattering and microscopic techniques.

2. Functional applications of the polymer in modulation of self-healing behavior in synthetic systems, controlled loading and delivery of cargo molecules.

3. Development of stimuli-responsive bio-inspired peptide molecules and monitoring their self-assembly in water to form a plethora of hierarchical structures such as 1D nanofibers, 2D nanosheets. Developing control over the dimensions of such structures through living supramolecular polymerisation.

4. Finally, developing bio-inspired peptide–polymer conjugates to mimick strain-stiffening behavior in biopolymer networks.

1.8. References:

- 1 J. Li, M. Stachowski and Z. Zhang in *Switchable and Responsive Surfaces and Materials for Biomedical Applications* (Ed: Z Zhang), Elsevier Ltd, 2015, pp 259-298
- 2 D. Wang, M. D. Green, K. Chen, C. Daengngam and Y. Kotsuchibashi, *Int. J. Polym. Sci.*, 2016, 2–4.
- 3 I. Y. Galaev and B. Mattiasson, *Trends in Biotechnology*, 1999, **20**, 305–311.
- 4 A. Kumar, A. Srivastava, I. Y. Galaev and B. Mattiasson, *Prog Polym Sci*, 2007, **32**, 1205–1237.
- 5 E. Cabane, X. Zhang, K. Langowska, C. G. Palivan and W. Meier, *Biointerphases*, 2012, **7**, 1–27.
- 6 S. Talebian, M. Mehrali, N. Taebnia, C. P. Pennisi, F. B. Kadumudi, J. Foroughi, M. Hasany, M. Nikkhah, M. Akbari, G. Orive and A. Dolatshahi-Pirouz, *Adv. Sci.*, 2019, **6**, 1801664.
- 7 M. Delcea, H. Möhwald and A. G. Skirtach, *Adv Drug Deliv Rev*, 2011, **63**, 730–747.
- 8 E. S. Gil and S. M. Hudson, *Prog. Polym. Sci.*, 2004, **29**, 1173–1222.
- 9 W. B. Liechty, D. R. Kryscio, B. V. Slaughter and N. A. Peppas, *Annu Rev Chem Biomol Eng*, 2010, **1**, 149–173.
- 10 A. L. Shigo, *Ann. Rev. Phytopath.*, 1984, **22**, 189–214.
- 11 W. K. Stadelmann, A. G. Digenis and G. R. Tobin, *Am. J. Surg.*, 1998, **176**, 26S-38S.
- 12 J. Teyssier, S. V. Saenko, D. Van Der Marel and M. C. Milinkovitch, *Nat. Commun.*, 2015, **6**, 1–7.
- 13 Jpbarrass., Series of photographs: Abrasion caused by sliding fall on concrete. Wikimedia, 2008; https://en.wikipedia.org/wiki/Wound_healing (accessed Feb 25,

- 2018).
- 14 Ho-H. Chou, A. Nguyen, A. Chortos, J. W.F. To, C. Lu, J. Mei, T. Kurosawa, W- G. Bae, J. B.-H. Tok, Z. Bao, *Nat. Commun.*, 2015, **6**, 8011.
 - 15 Y. Zhang, A. A. Broekhuis and F. Picchioni, *Macromolecules*, 2009, **42**, 1906–1912.
 - 16 Y. L. Liu and T. W. Chuo, *Polym. Chem.*, 2013, **4**, 2194–2205.
 - 17 M. Vatankhah-Varnoosfaderani, S. Hashmi, A. Ghavaminejad and F. J. Stadler, *Polym. Chem.*, 2014, **5**, 512–523.
 - 18 M. Bag, S. Banerjee, R. Faust and D. Venkataraman, *Sol. Energy Mater. Sol. Cells*, 2016, **145**, 418–422.
 - 19 D. G. Shchukin, *Polym. Chem.*, 2013, **4**, 4871–4877.
 - 20 K. S. Toohey, N. R. Sottos, J. A. Lewis, J. S. Moore and S. R. White, *Nat. Mater.*, 2007, **6**, 581–585.
 - 21 S. R. White, N. R. Sottos, P. H. Geubelle, J. S. Moore, M. R. Kessler, S. R. Sriram, E. N. Brown and S. Viswanathan, *Nature*, 2001, **409**, 794–797.
 - 22 X. Chen, F. Wudl, A. K. Mal, H. Shen and S. R. Nutt, *Macromolecules*, 2003, **36**, 1802–1807.
 - 23 D. Chen, D. Wang, Y. Yang, Q. Huang, S. Zhu and Z. Zheng, *Adv. Energ. Mat.*, 2017, **7**, 27–31
 - 24 J. P. Joseph, A. Singh and A. Pal, in *Smart Polymer Nanocomposites Energy Harvesting, Self-Healing and Shape Memory Applications*, ed. M. A. A. Ponnamma, D., Sadasivuni, K.K., Cabibihan, J.-J., Al-Maadeed, Springer, 2017, pp. 181–218.
 - 25 B. Saikia, J. Das, P. Gogoi and S. K. Dolui, in *Industrial Applications for Intelligent Polymers and Coatings*, ed. Hosseini M., Makhlof A., Springer International Publishing 2016, pp 271-291
 - 26 K. Matyjaszewski and N. V. Tsarevsky, *Nat. Chem.*, 2009, **1**, 276-288.
 - 27 K. Matyjaszewski and J. Spanswick, *Mat. Today*, 2005, 26–33.
 - 28 A. T. Ten Cate and R. P. Sijbesma, *Macromol. Rapid Commun.*, 2002, **23**, 1094–1112.
 - 29 A. Faghijnejad, K. E. Feldman, J. Yu, M. V. Tirrell, J. N. Israelachvili, C. J. Hawker, E. J. Kramer and H. Zeng, *Adv. Funct. Mater.*, 2014, **24**, 2322–2333.

- 30 B. K. Ahn, D. W. Lee, J. N. Israelachvili and J. H. Waite, *Nat. Mater.*, 2014, **13**, 867–872.
- 31 T. W. Chuo, T. C. Wei and Y. L. Liu, *J. Pol. Sci, Part A: Pol. Chem.*, 2013, **51**, 3395–3403.
- 32 S. Bode, L. Zedler, F. H. Schacher, B. Dietzek, M. Schmitt, J. Popp, M. D. Hager and U. S. Schubert, *Adv. Funct. Mater.*, 2013, **25**, 1634–1638.
- 33 J. Kötteritzsch, M. D. Hager and U. S. Schubert, *Polymer*, 2015, **69**, 321–329.
- 34 N. B. Pramanik, G. B. Nando and N. K. Singha, *Polymer*, 2015, **69**, 349–356.
- 35 J. A. Yoon, J. Kamada, K. Koynov, J. Mohin, R. Nicolaÿ, Y. Zhang, A. C. Balazs, T. Kowalewski and K. Matyjaszewski, *Macromolecules*, 2012, **45**, 142–149.
- 36 N. Kuhl, S. Bode, R. K. Bose, J. Vitz, A. Seifert, S. Hoepfener, S. J. Garcia, S. Spange, S. Van Der Zwaag, M. D. Hager and U. S. Schubert, *Adv. Funct. Mat.*, 2015, **25**, 3295–3301.
- 37 P. Cordier, F. Tournilhac, C. Soulié-Ziakovic, L. Leibler, *Nature*, 2008, **451**, 977–980.
- 38 Y. Chen, A. M. Kushner, G. A. Williams and Z. Guan, *Nat. Chem.*, 2012, **4**, 467–472.
- 39 Y. Chi, S. T. Scroggins and J. M. J. Fréchet, *J. Am. Chem. Soc.*, 2008, **130**, 6322–6323.
- 40 Y. Zhao, F. Sakai, L. Su, Y. Liu, K. Wei, G. Chen and M. Jiang, *Adv. Mater.*, 2013, **25**, 5215–5256.
- 41 M. T. De Martino, L. K. E. A. Abdelmohsen, F. P. J. T. Rutjes and J. C. M. Van Hest, *Beilstein J. Org. Chem.*, 2018, **14**, 716–733.
- 42 M. Raynal, P. Ballester, A. Vidal-Ferran and P. W. N. M. Van Leeuwen, *Chem. Soc. Rev.*, 2014, **43**, 1734–1787.
- 43 X. Fan, Z. Li and X. J. Loh, *Polym. Chem.*, 2016, **7**, 5898–5919.
- 44 A. W. Bosman, H. M. Janssen and E. W. Meijer, *Chem. Rev.*, 1999, **99**, 1665–1688.
- 45 D. A. Tomalia and J. M. J. Fréchet, *J. Pol. Sci, Part A: Pol. Chem.*, 2002, **40**, 2719–2728.
- 46 E. A. C. Davie, S. M. Mennen, Y. Xu and S. J. Miller, *Chem. Rev.*, 2007, **107**, 5759–5812.

- 47 T. Nakano and Y. Okamoto, *Chem. Rev.*, 2001, **101**, 4013–4038.
- 48 G. Guichard and I. Huc, *Chem. Comm.*, 2011, **47**, 5933–5941.
- 49 S. Mavila, O. Eivgi, I. Berkovich and N. G. Lemcoff, *Chem. Rev.*, 2016, **116**, 878–961.
- 50 C. K. Lyon, A. Prasher, A. M. Hanlon, B. T. Tuten, C. A. Tooley, P. G. Frank and E. B. Berda, *Polym. Chem.*, 2015, **6**, 181–197.
- 51 M. Huo, N. Wang, T. Fang, M. Sun, Y. Wei and J. Yuan, *Polymer*, 2015, **66**, A11–A21.
- 52 G. M. ter Huurne, A. R. A. Palmans and E. W. Meijer, *CCS Chemistry*, 2019, 64–82.
- 53 J. Jiang and S. Thayumanavan, *Macromolecules*, 2005, **38**, 5886–5891.
- 54 C. Heiler, J. T. Offenloch, E. Blasco and C. Barner-Kowollik, *ACS Macro Letters*, 2017, **6**, 56–61.
- 55 C. Heiler, S. Bastian, P. Lederhose, J. P. Blinco, E. Blasco and C. Barner-Kowollik, *Chem. Comm.*, 2018, **54**, 3476–3479.
- 56 T. K. Claus, J. Zhang, L. Martin, M. Hartlieb, H. Mutlu, S. Perrier, G. Delaittre and C. Barner-Kowollik, *Macromol. Rapid Commun.*, 2017, **38**, 1700264.
- 57 S. Babaoglu, D. Karaca Balta and G. Temel, *J. Pol. Sci, Part A: Pol. Chem.*, 2017, **55**, 1998–2003.
- 58 K. Watanabe, R. Tanaka, K. Takada, M. J. Kim, J. S. Lee, K. Tajima, T. Isono and T. Satoh, *Polym. Chem.*, 2016, **7**, 4782–4792.
- 59 R. Lambert, A. L. Wirotius and D. Taton, *ACS Macro Letters*, 2017, **6**, 489–494.
- 60 A. R. De Luzuriaga, I. Perez-Baena, S. Montes, I. Loinaz, I. Odriozola, I. García and J. A. Pomposo, *Macromolecular Symposia*, 2010, **296**, 303–310.
- 61 A. P. P. Kröger, R. J. E. A. Boonen and J. M. J. Paulusse, *Polymer*, 2017, **120**, 119–128.
- 62 A. Sanchez-Sanchez, I. Pérez-Baena and J. A. Pomposo, *Molecules*, 2013, **18**, 3339–3355.
- 63 H. Frisch, J. P. Menzel, F. R. Bloesser, D. E. Marschner, K. Mundsinger and C. Barner-Kowollik, *J. Am. Chem. Soc.*, 2018, **140**, 9551–9558.
- 64 B. T. Tuten, D. Chao, C. K. Lyon and E. B. Berda, *Polym. Chem.*, 2012, **3**, 3068–

3071.

- 65 E. B. Berda, E. J. Foster and E. W. Meijer, *Macromolecules*, 2010, **43**, 1430–1437.
- 66 O. Altintas, J. Willenbacher, K. N. R. Wuest, K. K. Oehlenschlaeger, P. Krolla-Sidenstein, H. Gliemann and C. Barner-Kowollik, *Macromolecules*, 2013, **46**, 8092–8101.
- 67 A. M. Hanlon, I. Martin, E. R. Bright, J. Chouinard, K. J. Rodriguez, G. E. Patenotte and E. B. Berda, *Polym. Chem.*, 2017, **8**, 5120–5128.
- 68 E. A. Appel, J. Dyson, J. del Barrio, Z. Walsh and O. A. Scherman, *Angew. Chem. Int. Ed.*, 2012, **124**, 4261–4265.
- 69 A. V. Melkikh and D. K. F. Meijer, *Prog. Biophy. Mol. Biol.*, 2018, **132**, 57–79.
- 70 J. E. Martin and B. E. Eichinger, *Macromolecules*, 1983, **16**, 1350–1358.
- 71 J. E. Martin and B. E. Eichinger, *Macromolecules*, 1983, **16**, 1345–1350.
- 72 V. A. Davankov, M. M. Ilyin, M. P. Tsyurupa, G. I. Timofeeva and L. V. Dubrovina, *Macromolecules*, 1996, **29**, 8398–8403.
- 73 M. Seo, B. J. Beck, J. M. J. Paulusse, C. J. Hawker and S. Y. Kim, *Macromolecules*, 2008, **41**, 6413–6418.
- 74 A. R. De Luzuriaga, N. Ormategui, H. J. Grande, I. Odriozola, J. A. Pomposo and I. Loinaz, *Macromol. Rapid Commun.*, 2008, **29**, 1156–1160.
- 75 E. Harth, B. Van Horn, V. Y. Lee, D. S. Germack, C. P. Gonzales, R. D. Miller and C. J. Hawker, *J. Am. Chem. Soc.*, 2002, **124**, 8653–8660.
- 76 M. K. Aiertza, I. Odriozola, G. Cabañero, H. J. Grande and I. Loinaz, *Cell. Mol. Life Sci.*, 2012, **69**, 337–346.
- 77 J. B. Beck, K. L. Killops, T. Kang, K. Sivanandan, A. Bayles, M. E. Mackay, K. L. Wooley and C. J. Hawker, *Macromolecules*, 2009, **42**, 5629–5635.
- 78 L. Oria, R. Aguado, J. A. Pomposo and J. Colmenero, *Adv. Mater.*, 2010, **22**, 3038–3041.
- 79 I. Perez-Baena, I. Loinaz, D. Padro, I. García, H. J. Grande and I. Odriozola, *J. Mater. Chem.*, 2010, **20**, 6916–6922.
- 80 Y. Liu, T. Pauloehrl, S. I. Presolski, L. Albertazzi, A. R. A. Palmans and E. W. Meijer, *J. Am. Chem. Soc.*, 2015, **137**, 13096–13106.

- 81 Y. Liu, S. Pujals, P. J. M. Stals, T. Paulöhr, S. I. Presolski, E. W. Meijer, L. Albertazzi and A. R. A. Palmans, *J. Am. Chem. Soc.*, 2018, **140**, 3423–3433.
- 82 S. Thanneeru, S. S. Duay, L. Jin, Y. Fu, A. M. Angeles-Boza and J. He, *ACS Macro Lett.*, 2017, **6**, 652–656.
- 83 M. Artar, T. Terashima, M. Sawamoto, E. W. Meijer and A. R. A. Palmans, *J. Pol. Sci., Part A: Pol. Chem.*, 2014, **52**, 12–20.
- 84 T. Terashima, T. Sugita, K. Fukae and M. Sawamoto, *Macromolecules*, 2014, **47**, 589–600.
- 85 Y. Hirai, T. Terashima, M. Takenaka and M. Sawamoto, *Macromolecules*, 2016, **48**, 5084–5091.
- 86 C. Song, L. Li, L. Dai and S. Thayumanavan, *Polym. Chem.*, 2015, **6**, 4828–4834.
- 87 A. Sanchez-Sanchez, S. Akbari, A. Etxeberria, A. Arbe, U. Gasser, A. J. Moreno, J. Colmenero and J. A. Pomposo, *ACS Macro Lett.*, 2013, **2**, 491–495.
- 88 L. L. Lao, N. A. Peppas, F. Y. C. Boey and S. S. Venkatraman, *Inter. J. Pharm.*, 2011, **418**, 28–41.
- 89 C. C. Cheng, D. J. Lee, Z. S. Liao and J. J. Huang, *Polym. Chem.*, 2016, **7**, 6164–6169.
- 90 A. C. Mendes, E. T. Baran, R. L. Reis and H. S. Azevedo, *Wiley Interdisciplinary Reviews: Nanomedicine and Nanobiotechnology*, 2013, **5**, 582–612.
- 91 E. Mattia and S. Otto, *Nat. Nanotechnol.*, 2015, **10**, 111–119.
- 92 M. Szwarc, M. Levy and R. Milkovich, *J. Am. Chem. Soc.* 1956, **78**, 2656–2657.
- 93 G. Odian and F. Group, *Principles of Polymerization, 4th Edition*, 2004.
- 94 R. D. Mukhopadhyay and A. Ajayaghosh, *Science*, 2015, **349**, 241–242.
- 95 X. Wang, G. Guerin, H. Wang, Y. Wang, I. Manners, M. A. Winnik, *Science*, 2007, **317**, 644–647
- 96 W. Zhang, W. Jin, T. Fukushima, A. Saeki, S. Seki and T. Aida, *Science*, 2011, **334**, 340–343.
- 97 L. Brunsveld, B. J. B. Folmer, E. W. Meijer and R. P. Sijbesma, *Chem. Rev.*, 2001, **101**, 4071–4097.
- 98 T. Aida, E. W. Meijer and S. I. Stupp, *Science*, 2012, **335**, 813–817.

- 99 C. Rest, R. Kandanelli and G. Fernández, *Chem. Soc. Rev.s*, 2015, **44**, 2543–2572.
- 100 P. A. Korevaar, S. J. George, A. J. Markvoort, M. M. J. Smulders, P. A. J. Hilbers, A. P. H. J. Schenning, T. F. A. De Greef and E. W. Meijer, *Nature*, 2012, **481**, 492–496.
- 101 P. A. Korevaar, C. J. Newcomb, E. W. Meijer and S. I. Stupp, *J. Am. Chem. Soc.*, 2014, **136**, 8540–8543.
- 102 A. Sorrenti, J. Leira-Iglesias, A. J. Markvoort, T. F. A. De Greef and T. M. Hermans, *Chem. Soc. Rev.*, 2017, **46**, 5476–5490.
- 103 J. S. Valera, R. Gómez and L. Sánchez, *Small*, 2018, **14**, 1870012.
- 104 S. Ogi, K. Sugiyasu, S. Manna, S. Samitsu and M. Takeuchi, *Nat. Chem.*, 2014, **6**, 188–195.
- 105 S. Ogi, V. Stepanenko, K. Sugiyasu, M. Takeuchi and F. Würthner, *J. Am. Chem. Soc.*, 2015, **137**, 3300–3307.
- 106 J. Kang, D. Miyajima, Y. Itoh, T. Mori, H. Tanaka, M. Yamauchi, Y. Inoue, S. Harada and T. Aida, *J. Am. Chem. Soc.*, 2014, **136**, 10640–10644.
- 107 J. Kang, D. Miyajima, T. Mori, Y. Inoue, Y. Itoh and T. Aida, *Science*, 2015, **347**, 646–651.
- 108 T. Fukui, S. Kawai, S. Fujinuma, Y. Matsushita, T. Yasuda, T. Sakurai, S. Seki, M. Takeuchi and K. Sugiyasu, *Nat. Chem.*, 2017, **9**, 493–499.
- 109 A. Pal, M. Malakoutikhah, G. Leonetti, M. Tezcan, M. Colomb-Delsuc, V. D. Nguyen, J. van der Gucht and S. Otto, *Angew. Chem. Int. Ed.*, 2015, **54**, 7852–7856.
- 110 D. S. Pal, H. Kar and S. Ghosh, *Chem. Comm.*, 2018, **54**, 928–931.
- 111 G. Ghosh, P. Dey and S. Ghosh, *Chem. Comm.*, 2020, **56**, 6757–6769
- 112 P. N. Cheng, C. Liu, M. Zhao, D. Eisenberg and J. S. Nowick, *Nat. Chem.*, 2012, **4**, 927–933.
- 113 I. V. Baskakov, G. Legname, M. A. Baldwin, S. B. Prusiner and F. E. Cohen, *J. Biol. Chem.*, 2002, **277**, 21140–21148.
- 114 G. M. Whitesides, J. P. Mathias and C. T. Seto, *Science*, 1991, **254**, 1312–1319.
- 115 M. P. Hendricks, K. Sato, L. C. Palmer, S. I. Stupp, *Acc. Chem. Res.* **2017**, *50*, 2440.
- 116 C. J. C. Edwards-Gayle and I. W. Hamley, *Org. Biomol. Chem.*, 2017, **15**, 5867–5876.
- 117 C. M. Berac, L. Zengerling, D. Straßburger, R. Otter, M. Urschbach and P. Besenius,

- Macromol. Rap. Commun.*, 2020, **41**, 1900476.
- 118 A. Sarkar, J. C. Kölsch, C. M. Berač, A. Venugopal, R. Sasmal, R. Otter, P. Besenius and S. J. George, *ChemistryOpen*, 2020, **9**, 346–350.
- 119 Y. Lin, M. R. Thomas, A. Gelmi, V. Leonardo, E. T. Pashuck, S. A. Maynard, Y. Wang and M. M. Stevens, *J. Am. Chem. Soc.*, 2017, **139**, 13592–13595.
- 120 A. Singh, J. P. Joseph, D. Gupta, I. Sarkar and A. Pal, *Chem. Comm.*, 2018, **54**, 10730–10733.
- 121 C. R. White and J. A. Frangos, *Philos. Trans. R. Soc. B Biol. Sci.* 362, 2007, **362**, 1459–1467.
- 122 T. Lecuit and P. F. Lenne, *Nat. Rev. Mol. Cell Biol.*, 2007, **8**, 633–644.
- 123 B. M. Chung, J. D. Rotty and P. A. Coulombe, *Curr. Opin. Cell Biol.*, 2013, **25**, 600–612.
- 124 O. C. Rodriguez, A. W. Schaefer, C. A. Mandato, P. Forscher, W. M. Bement and C. M. Waterman-Storer, *Nat. Cell Biol.*, 2003, **5**, 599–609.
- 125 N. Laurens, P. Koolwijk and M. P. de Maat, *J. Thromb. Haemost.*, 2006, **4**, 932–936.
- 126 K. Gelse, E. Pöschl and T. Aigner, *Adv. Drug Deliv. Rev.*, 2003, **55**, 1531–1546.
- 127 L. Martikainen, K. Bertula, M. Turunen and O. Ikkala, *Macromolecules*, 2020, **53**, 9983–9992.
- 128 R. H. Pritchard, Y. Y. Shery Huang and E. M. Terentjev, *Soft Matter*, 2014, **10**, 1864–1884.
- 129 C. Storm, J. J. Pastore, F. C. MacKintosh, T. C. Lubensky and P. A. Janmey, *Nature*, 2005, **435**, 191–194.
- 130 C. P. Broedersz, C. Storm and F. C. MacKintosh, *Phys. Rev. Lett.*, 2008, **101**, 1–4.
- 131 C. P. Broedersz, K. E. Kasza, L. M. Jawerth, S. Münster, D. A. Weitz and F. C. MacKintosh, *Soft Matter*, 2010, **6**, 4120–4127.
- 132 M. L. Gardel, J. H. Shin, F. C. MacKintosh, L. Mahadevan, P. Matsudaira and D. A. Weitz, *Science*, 2004, **304**, 1301–1305.
- 133 K. S. Anseth, C. N. Bowman and L. Brannon-Peppas, *Biomaterials*, 1996, **17**, 1647–1657.
- 134 A. Basu, Q. Wen, X. Mao, T. C. Lubensky, P. A. Janmey and A. G. Yodh,

- Macromolecules*, 2011, **44**, 1671–1679.
- 135 W. R. Legant, J. S. Miller, B. L. Blakely, D. M. Cohen, G. M. Genin and C. S. Chen, *Nat. Methods*, 2010, **7**, 969–971.
- 136 M. Jaspers, M. Dennison, M. F. J. Mabesoone, F. C. MacKintosh, A. E. Rowan and P. H. J. Kouwer, *Nat. Commun*, 2014, **5**, 5808.
- 137 R. K. Das, V. Gocheva, R. Hammink, O. F. Zouani and A. E. Rowan, *Nat. Mater.*, 2016, **15**, 318–325.
- 138 Q. Wen and P. A. Janmey, *Exp. Cell Res.*, 2013, **319**, 2481–2489.
- 139 J. P. Winer, S. Oake and P. A. Janmey, *PLoS one*, , 2009, **4**, e6382.
- 140 A. J. Engler, S. Sen, H. L. Sweeney and D. E. Discher, *Cell*, 2006, **126**, 677–689.
- 141 J. J. L. M. Cornelissen, J. J. J. M. Donners, R. De Gelder, W. S. Graswinckel, G. A. Metselaar, A. E. Rowan, N. A. J. M. Sommerdijk and R. J. M. Nolte, *Science*, 2001, **293**, 676–680.
- 142 P. H. J. Kouwer, M. Koepf, V. A. A. Le Sage, M. Jaspers, A. M. Van Buul, Z. H. Eksteen-Akeroyd, T. Woltinge, E. Schwartz, H. J. Kitto, R. Hoogenboom, S. J. Picken, R. J. M. Nolte, E. Mendes and A. E. Rowan, *Nature*, 2013, **493**, 651–655.
- 143 M. Jaspers, S. L. Vaessen, P. Van Schayik, D. Voerman, A. E. Rowan and P. H. J. Kouwer, *Nat. Commun*, 2017, **8**, 1–10.
- 144 M. Fernández-Castaño Romera, X. Lou, J. Schill, G. Ter Huurne, P. P. K. H. Fransen, I. K. Voets, C. Storm and R. P. Sijbesma, *J. Am. Chem. Soc*, 2018, **140**, 17547–17555.
- 145 M. Fernandez-Castano Romera, R. P. M. Lafleur, C. Guibert, I. K. Voets, C. Storm and R. P. Sijbesma, *Angew. Chem. Int. Ed.*, 2017, **56**, 8771–8775.
- 146 M. Fernández-Castano Romera, R. Göstl, H. Shaikh, G. Ter Huurne, J. Schill, I. K. Voets, C. Storm and R. P. Sijbesma, *J. Am. Chem. Soc*, 2019, **141**, 1989–1997.

Chapter 2

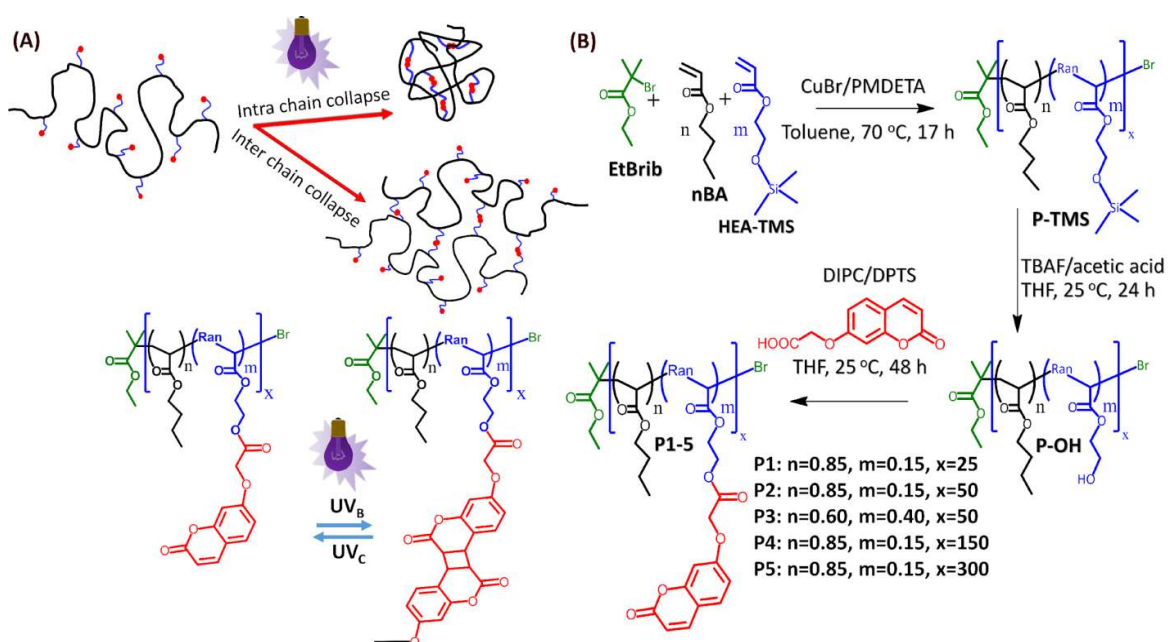
Photoresponsive Chain Collapse In Flexo-Rigid Functional Copolymer To Modulate Self-Healing Behavior

*In this chapter, photoresponsive polymers **P1-P5** containing pendant coumarin moieties are designed that undergo intra or inter-chain collapse to form diverse nanostructures. The shape and dimension of the nanostructures can be efficiently controlled by concentration, solvent compatibility and characteristics of the polymers. Photodimerization of coumarin moieties transforms the extended coiled chain of the polymer to uniform sized nanoparticles in dilute condition, while in the crowded macromolecular concentration regime, the polymer folds in nanostructures with polydisperse topologies that are far from condensed globule or partially swollen globule conformation. Scaling law exponents for polymer chain compaction suggests interchain collapse with rigid compact segments connected by flexible polymer chains and draws its analogy with the elastomers. Such hardening of the rigid segment as a consequence of photodimerization renders significant increase in the glass transition temperature (T_g) that can be reversibly controlled upon decrosslinking. Lastly, the structural variation of this class of polymers over self-healing is explored and crosslinked polymers shows photo-triggered nonautonomic & intrinsic self-healing behavior at ambient condition. This is an interesting approach to access photo-modulated self-healing system in low T_g polymers that shows coexistence of autonomic and non-autonomic self-healing pathways and may find its application in designing smart coating of the photovoltaic device.*

2.1. Introduction

Design of smart and adaptable stimuli-responsive systems in nanoscience owes its fascination in mimicking the nature's ability to produce intelligent self-repairing biomaterials as employed in natural processes *e.g.* in blood clotting, tissue regeneration, *etc.*¹⁻³ Such self-healing materials that autonomically mends *in situ* at the microscopic level as a response to macroscopic damages, are currently envisaged as sustainable and long-lasting materials for applications in electronics, energy, transportation and coatings.⁴⁻⁶ As compared to the extrinsic self-healing materials having healing catalyst encapsulated in microcapsules,^{7,8} the materials with intrinsic mechanism have recently gained significant attention owing to the reasons such as reduced cost, multiple cycle of healing *etc.*^{9,10} Such mechanism to heal damage demands reversible chemical interactions *e.g.* hydrogen bonding,¹¹⁻¹⁴ host-guest interactions,¹⁵⁻¹⁷ metal-ligand complexations,¹⁸⁻²⁰ ionic interactions,^{21,22} π - π stacking interactions^{23,24} and dynamic covalent bonds.^{25,26} While a number of thermoplastic elastomers having hard-soft multiphasic domains in noncovalent supramolecular matrix show autonomic self-healing,²⁷⁻²⁹ a number of external triggers *e.g.* thermal, light, electrical stimuli render the systems nonautonomic. Among the stimuli-triggered self-healing examples, thermally controlled Diels-Alder reactions pose challenges owing to the high temperature required for mending the damages thereby hampering polymer stability,^{30,31} paving way to the emergence of photo-triggered healing that shows advantages with respect to ambient operating temperature and locally selected area for the healing process. Light mediated cycloaddition reaction in coumarin, anthracene, cinnamate moieties endow excellent dynamic and reversible photoresponsive systems.³²⁻³⁶ However, design of functional polymers for self-healing coating applications in automobile industry, photovoltaic devices demands optimization of a number of crucial parameters *e.g.* ease of processing and crosslinking ability, flexibility vs rigidity, architectural control, tacticity in a multiphase, compartmentalized polymer network. In that regard, a rational design inspired by the natural system that addresses multiple structural control over the nanostructures and

subsequent alteration of macroscopic self-healing properties at ambient temperature is not well explored. Thus, a bottom-up assembly of polymer building blocks, that can be reversibly photofixated with control over its nanostructures might be a suitable approach for designing self-healing materials.³⁷ Moreover, the concentration dependent polymer chains collapse may provide useful insight to the nanostructure formation, ranging from single chain polymeric nanoparticles^{38–43} (SCPN) to hierarchical polymer network with selective hardening of the rigid segment in the hard-soft multiphasic domain of the functional copolymers.



Scheme 2.1. (A) Schematic representation demonstrating homo-functional intra and inter chain collapse by means of reversible photodimerization of coumarin in presence of UV_B and UV_C light with the chemical structure of coumarin functionalized single chain polymers (P1-P5) possessing different percentage functionalities and degree of polymerizations. (B) Synthetic scheme for the coumarin functionalized polymers

Herein, we present a simple yet elegant design of functional polymers incorporating photo-responsive coumarin moieties in a linear chain of butyl acrylate based graft copolymers, P1-P5 (Scheme 2.1). Such polymers undergo transformation from extended coiled chain structure to globular nanoparticle, mediated by preorganization of polymer with subsequent collapse under UV_B light ($\lambda_{\text{max}} = 320 \text{ nm}$). The efficacy and kinetics of the transformation can be controlled through the modulation of percentage functionality,

concentration and molecular weight of the polymer. Photo-fixation of such systems, especially in dilute and crowded macromolecular condition, renders diverse nanostructures, ranging from globular nanoparticles to higher order structures with locally compact portions of polymer chains connected together akin to the structural features displayed by thermoplastic elastomers. Such strategy and understanding of the domain specific flexible-rigid segments that can be further photo-fixated, are efficiently exploited to modulate the self-healing behavior of the polymer films. Thus, we show a smart design of functional polymer that showed photo-modulated interconversion of autonomic and non-autonomic self-healing behavior at ambient condition.

2.2. Result and Discussion

2.2.1. Synthesis and characterization of photoresponsive polymers: The polymers (**P1-P5**) with pendant coumarin functionalities were synthesized by controlled living atom transfer radical polymerization (ATRP) followed by post-functionalization with reactive functional units (Scheme 2.1B). First, a number of copolymers of *n*-butyl acrylate (BA) and trimethylsilyloxyethyl acrylate (HEA-TMS) were synthesized with different grafting percentage of HEA-TMS and degree of polymerization. Subsequently, the TMS groups were de-protected to result in free hydroxyl groups which were further functionalized with coumarin acid derivatives using DIPC/DPTS strategy to render photoresponsive polymers.⁴⁴ The formation of the polymers was confirmed by the characteristic ¹H-NMR peaks of the coumarin groups at δ 7.57, 7.33, 6.84, 6.18 ppm that indicated the incorporation of coumarin moieties into the polymer side chains with different grafting percentages (*cf* Experimental section). Size exclusion chromatographic (SEC) analyses indicated the control over molecular weight of the polymers with reasonably good polydispersity indices (PDI) PDI, although tethering of the functional groups rendered the PDI in the range of 1.16-1.47.^{45,46} Table 2.1 summarizes the characteristic details of the polymers including the percentage grafting as obtained from ¹H-NMR, molecular weight, calculated hydrodynamic radii (R_H^{CAL} and R_H^{VIS}) of the polymers (IV) from SEC analyses. The hydrodynamic radii of the single chain polymers (R_H^{CAL}) were calculated according to the equation $R_{HO}^{CAL} = 1.44 \times 10^{-}$

$2 \times M_w^{0.561}$ and compared with R_{HO}^{VIS} as determined utilizing the viscometer signal from SEC analysis in THF.^{47,48}

Table 2.1: Characterization details of the synthesized photoresponsive polymers

Polymer	% Functionality ^a	M_n (Da) ^b	M_w (Da) ^b	R_H^{0CAL} (nm) ^c	R_H^{0VIS} (nm) ^d	R_H^{0DLS} (nm) ^e
P1	9.6%	6299	8861	2.4	2.1	4.5 ± 0.3
P2	12%	9597	11169	2.7	2.6	10 ± 0.7
P3	28%	11009	13509	3.0	2.5	6 ± 0.4
P4	14%	22586	32509	4.9	6.0	30 ± 2
P5	4%	32453	47852	6.2	13.0	52 ± 3.5

^aDetermined by ¹H NMR. ^bDetermined by SEC analysis in THF using polystyrene as standard. ^cFor the polymer, hydrodynamic radii (R_H^{0CAL}) as calculated according to the formula $R_H^{0CAL}(\text{nm}) = 1.44 \times 10^{-2} M_w^{0.561}$.^{47,48} ^dHydrodynamic radii (R_H^{0VIS}) as determined by using viscometer detector in SEC. ^e R_H^{DLS} as determined by the dynamic light scattering studies. Polymer concentration = 6 mg/mL in THF

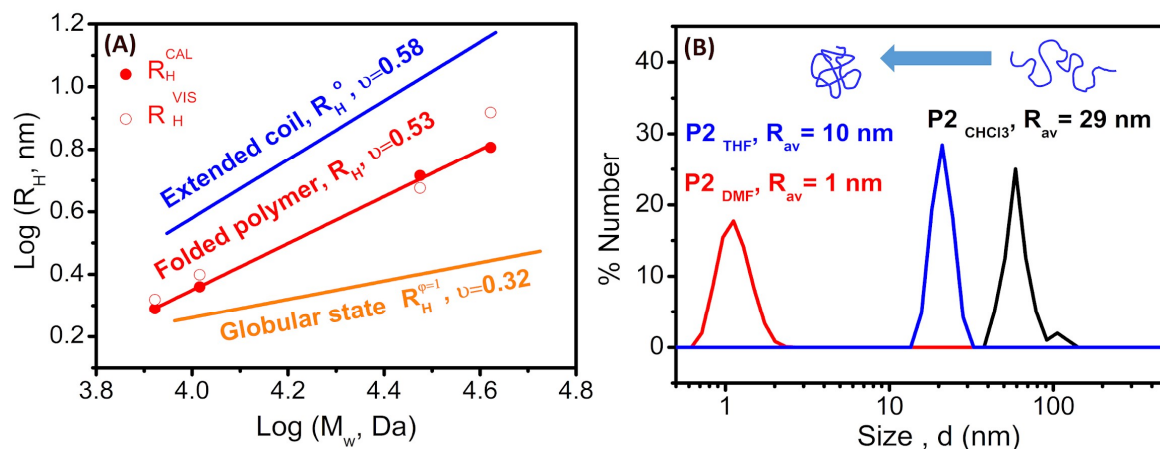


Figure 2.1. Illustration of the $R_H = KM_w^\nu$ scaling law for polymers **P1**, **P2**, **P4**, **P5** based on hydrodynamic radii (R_H) and weight average molecular weights (M_w). Closed blue circles represent calculated hydrodynamic radii (R_H^0) of the precursor polymers according to the formula $R_{HO}^{CAL}(\text{nm}) = 1.44 \times 10^{-2} M_w^{0.561}$. The blue line is a fit of calculated hydrodynamic radii (R_H^0) of precursor polymers giving exponent value of $\nu = 0.58$ denoting extended coil state of polymer. Closed red circles represent calculated hydrodynamic radii (R_H^{CAL}) of photodimerized polymer according to the formula $R_H^{CAL}(\text{nm}) = R_H^0 (1-f)^{0.6}$. A linear fit (red line) of calculated hydrodynamic radii (R_H^{CAL}) of photodimerized polymer gives exponent value of $\nu = 0.53$ denoting folded state of polymer. Open red circles represent R_H values (R_H^{VIS}) as determined from viscometer signal in SEC measurements, that also shows similar folding states. Closed orange circles represent calculated hydrodynamic radii ($R_H^{\phi=1}$) of compact globular conformation of the polymer calculated according to the formula: $R_H^{\phi=1} = [3M_w / (4\pi\phi\rho N_A)]^{1/3}$ with $\phi = 1$ and $\rho = 1.05 \text{ g/cm}^3$. The orange solid lines shows linear fit of calculated hydrodynamic radii (R_H^{ϕ}) of complete ($R_H^{\phi=1}$) globular state of polymers with exponent value of $\nu = 0.32$. (B) Dynamic light scattering studies of the polymer **P2** showing hydrodynamic radii in THF, chloroform and DMF.

Fitting the hydrodynamic radii in the power law relation $R_H \propto M_w^\nu$ the native polymer renders an exponent value of *ca.* $\nu = 0.58$ (Figure 2.1A), that indicates an expanded coil state of the polymer chain in good solvent such as THF (Flory exponent, $\nu_F = 0.59$). Dynamic light scattering (DLS) studies also exhibited higher hydrodynamic radii of the native polymers, *e.g.* **P2** in THF and CHCl₃ relative to that in DMF (Figure 2.1 B).

2.2.2. Monitoring photodimerization: The polymers **P1-P5** exhibited characteristic UV absorption bands of the coumarin groups in the wavelength range of 280-350 nm. Upon increasing time of UV_B irradiation, the bands gradually diminished as a result of photodimerization of the coumarin moieties. Dilute solutions of the polymer **P2** in THF, CHCl₃, DMF (0.01 mM) were exposed to UV_B light ($\lambda_{\max} = 320$ nm) that showed a gradual decrease in the characteristic absorption of the coumarin peaks within 90 min (Figure 2.2 A-D). However, the polymers showed retrieval of the absorbance upon irradiation of UV_C light ($\lambda_{\max} = 254$ nm) within 30 min indicating the photoreversible nature of the photodimerization process. The photodimerization degree (% PD) of the polymers exhibited solvent dictated kinetics of photodimerization as the nonpolar side chains *e.g.* butyl acrylate chains show variable interactions with the solvents. Polymers and solvents with a similar value of Hildebrand solubility parameters (δ) are likely to engage in a maximal degree of interaction and denoted as good solvents, while solvents with solubility parameters far away from the limit of polymer promotes minimal interactions and are denoted as bad solvents.^{49,50} The Hildebrand solubility parameter (δ) for butyl acrylate chains has a value of 17.9 MPa^{1/2} which is comparable to that of THF (18.5 MPa^{1/2}) and CHCl₃ (18.7 MPa^{1/2}) leading to high volume of chain interactions and effective exposure of functional groups in an expanded coil chain structures. Thus, the polymer (**P2**) exhibited faster photodimerization kinetics leading to saturation at higher PD (80%) in THF; however in DMF ($\delta = 24.7$ MPa^{1/2}), it showed slower kinetics and poor photodimerization degree even after 90 min (Figure 2.2 E-F). In corroboration with the Hildebrand solubility parameters, the trend of photodimerization degree and kinetics of **P2** solution exhibited the order PD_{THF} > PD_{CHCl₃} > PD_{DMF}. Upon comparing the polymers **P1-P5** differing in chain length and % functionality, we found that

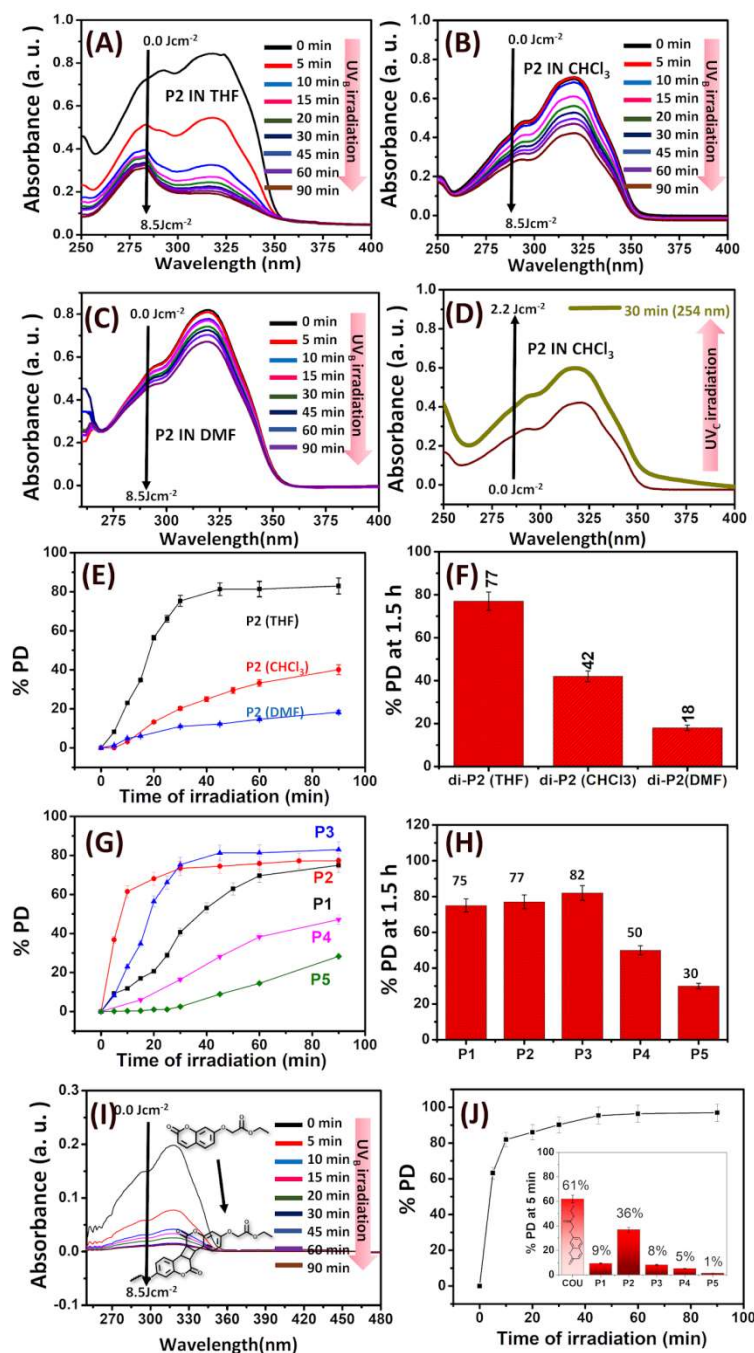


Figure 2.2. Photodimerization study of the polymer **P1-5** using UV spectroscopy. Gradual decrease in UV absorbance with time of irradiation for the polymer **P2** (A) in THF and (B) in CHCl₃ & (C) in DMF (D) Retrieval of absorbance for **P2** in the range of 300-350 nm after UV_C irradiation (E) Kinetics of photodimerization for the polymer **P2** in THF, CHCl₃, DMF. (F) Photodimerization degree of **P2** polymer in different solvents *e.g.* THF, CHCl₃ and DMF after UV_B irradiation for 1.5 h. (G) Kinetics of photodimerization for the **P1-5** in THF (H) Photodimerization degree of **P1-5** after UV irradiation for 1.5 h. (I) Photodimerization of the coumarin ethyl acetate ester (Small molecule analogue) (J) Kinetics of photodimerization for coumarin ethyl acetate ester in THF (Inset showing % PD_{5 min} of the polymers with coumarin ester (2x8 W UV_B lamp, λ_{\max} = 320 nm, concentration = 0.01 mM).

the polymers **P1-P2** with smaller chain length showed faster photodimerization (PD = 75-77%, in 90 min) with higher second order rate constants as compared to their longer chain analogues, **P4** (50%) and **P5** (30%) with much higher hydrodynamic radii (Figure 2.2 G-H, Table 2.2). Similarly, the small molecular analogue of coumarin *e.g.* ethyl ester of coumarin showed much faster kinetics of photodimerization (60% PD in 5 min) compared to the coumarin grafted polymers (Figure 2.2 I-J), indicating the role of polymer chain mobility in the photodimerization reaction. The polymer chain reptation time depends on the polymer molecular weight ($\tau \propto M^3$) rendering slower photodimerization for **P4** and **P5** with longer polymer chains.^{51,52} Moreover, increase in the % functionality promoted faster photodimerization for environment, chain length of the polymer, amount of functionality played vital role in the kinetics of photodimerization and demonstrated eventual folding of the polymers.

Table 2.2. Rate constant and Regression co-efficient for second order kinetics of photodimerization in THF

	Rate constant, $k_2 \times 10^2$ (mM ⁻¹ min ⁻¹)	R^2
P1	3.2	0.98528
P2	4.9	0.93634
P3	6.7	0.95813
P4	1	0.99803
P5	0.3	0.99716
Coumarin ester	39	0.98032

The photodimerization was also studied by recording ¹H NMR of the polymer solution before and after UV irradiation *albeit* at a relatively higher concentration. The aromatic protons (marked p and q) of the coumarin moieties in the **P2** polymer gradually diminished in intensity suggesting $[2\pi+2\pi]$ cyclodimerization triggered by UV light ($\lambda_{\max} = 320$ nm) (Figure 2.3A) and rendered a PD value of 50% (Figure 2.3B) after 10 h of irradiation. Additionally, ¹H NMR characterization of the new peaks of the cyclobutane adduct indicated the resulting stereoisomer among all the possible products: *syn* head-to-head dimer (*syn*-HH), *anti* head-to-head dimer (*anti*-HH) and *syn* head- to-tail dimer (*syn*-HT). The gradual appearance of the characteristic NMR signal of the cyclobutyl protons at δ 3.3-3.6 ppm (Figure 2.3C) with irradiation of the polymer (**P2**) solution suggested the formation of the *anti*-HH dimer as corroborated with literature.^{53,54} Such stereo-selectivity

of the photodimerization also validated the influence of the nonpolar solvent environment and nonpolar butyl acrylate polymer backbones.

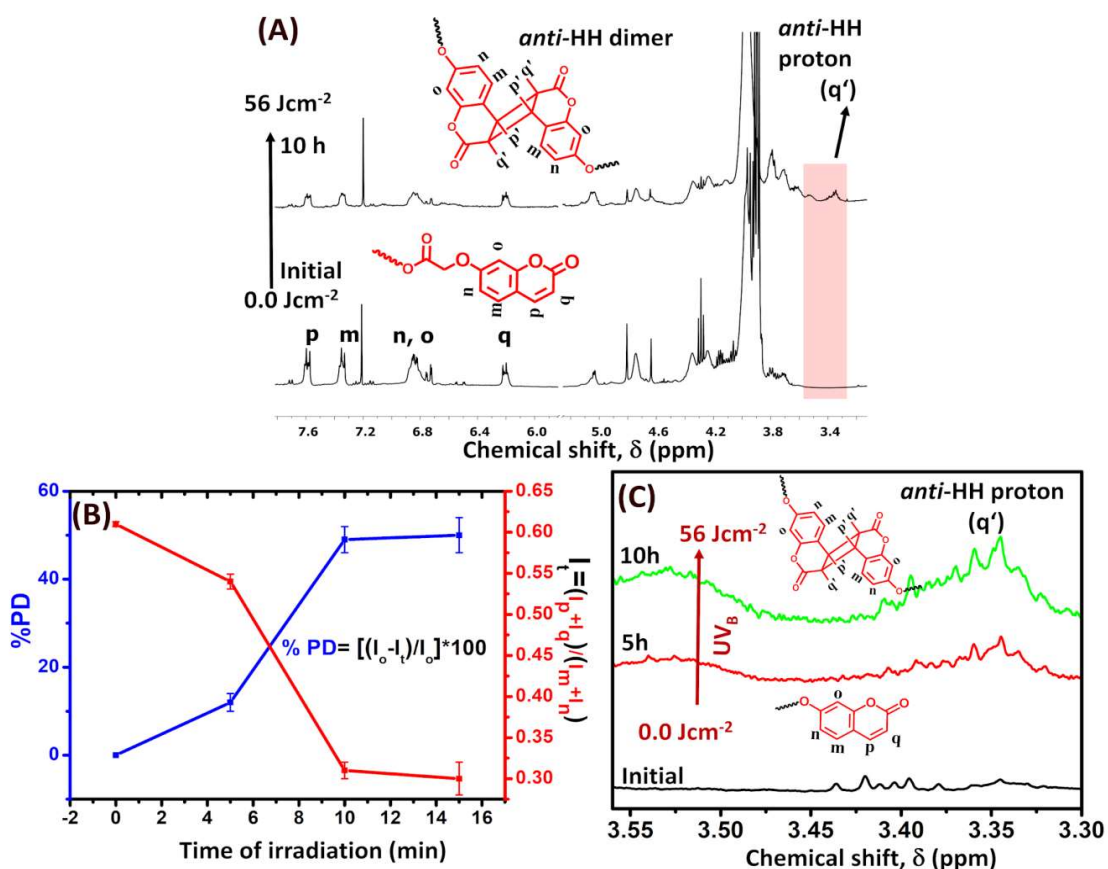


Figure 2.3. (A) Partial stacked ^1H NMR spectra of the polymer **P2** before and after 10 h irradiation. (B) Graph showing the decrease in integral ratio of the protons at photodimerization site of coumarin (Red line) with concomitant increase in the photodimerization degree with time course of irradiation (Blue line). (C) Expanded region of ^1H NMR spectra showing increase in anti-HH dimer proton signal at δ 3.30-3.6 ppm. ^1H -NMR studies in CDCl_3 , UV irradiation at 1 mM concentration in THF (2x8W UV_B lamp, $\lambda_{\text{max}} = 320 \text{ nm}$)

2.2.3. Monitoring chain collapse and nanostructure formation: The transition from extended coil chain to particle shape upon photodimerization was further investigated using DLS and SEC analyses. The viscometer signal of the polymers **P1-P5** shifted to a larger retention volume on the course of UV irradiation (Figure 2.4A-C), indicating gradual decrease in the hydrodynamic size. Table 2.3 summarizes the experimental and calculated R_H values obtained by folding of the polymer chain upon UV irradiation for 4 h. As

compared to R_H of the extended coil chain of the polymers (**P1-P5**) in THF, the photodimerization mediated chain collapse of the polymers to form **di-P1-P5** decreased hydrodynamic radii and corroborated with the calculated radii, as given by the equation $R_H^{CAL} = R_{HO}^{CAL} (1 - f)^{0.6}$, where f represents a fraction of functional groups responsible for intrachain folding of the polymer chain.^{47,48} Fitting in the aforementioned power law equation, we found an exponent value of *ca.* $\nu = 0.53$ (Figure 2.1A). In order to understand the compactness of the folded chain, we calculated the limiting hydrodynamic radii for possible condensed globules using the equation: $R_H^\phi = [3M_w / (4\pi\phi\rho N_A)]^{1/3}$ and obtained exponent value of *ca.* $\nu = 0.32$, where ϕ is the segment volume fraction in a spherical globule ($\phi = 1$ for compact globules; ρ is the density of polystyrene standard (1.05 g/cm³), N_A is Avogadro's number and M_w is the apparent molecular weight of the precursor polymers. Therefore, $\nu = 0.53$ for the irradiated polymer samples suggested an intermediate folding state (Θ state) for di-**P1-P4**, that is far from the value with respect to that of a compact globular conformation.

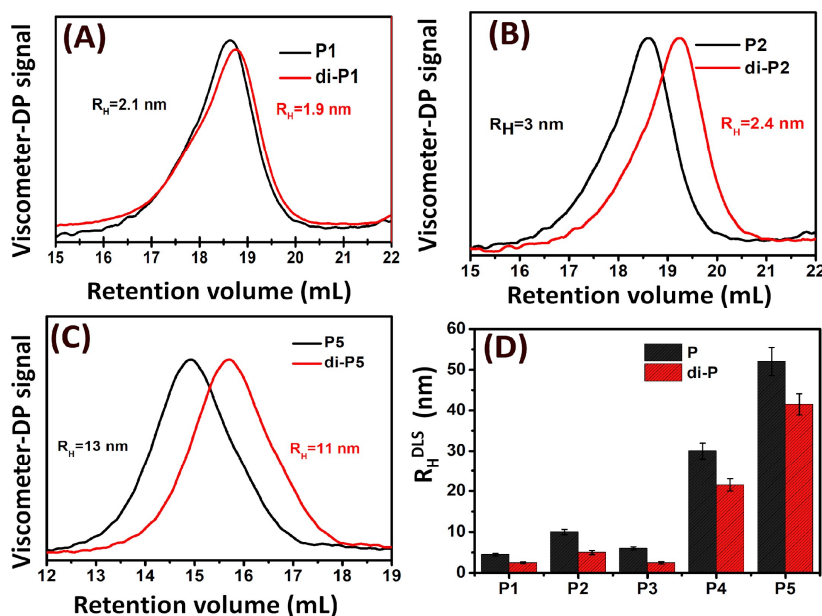


Figure. 2.4. SEC analyses showing delay in retention volume upon UV irradiation of polymer sample (A) **P1** (B) **P2** (C) **P5** (D) DLS data showing hydrodynamic radii (R_H^{DLS}) for all the polymer samples before and after irradiation. (Irradiation of sample solution (conc = 6 mg/mL) in THF with 2x8W UV_B lamp, 8h)

Table 2.3. Characterization details of folded polymeric nanoparticles after UV irradiation

Polymer	M_w^{app} (Da) ^a	R_H^{CAL} (nm) ^b	R_H^{VIS} (nm) ^c	$R_H^{\phi=1}$ (nm) ^d	R_H^{DLS} (nm) ^e	% compaction ^{DLS}	Radii _{AFM} ^f (R _{AFM} , nm)	Radii spherical ^g (R _s , nm)
di-P1	8368	2.2	1.9	1.7	2.5 ± 0.2	44	22 ± 1	11
di-P2	10368	2.4	2.4	1.9	5 ± 0.5	50	48 ± 3	23
di-P3	11213	2.2	2.3	2.0	2.5 ± 0.3	58	33 ± 2.5	16
di-P4	29844	4.4	5.4	2.7	22.5 ± 1.5	28	115 ± 5	54
di-P5	41895	5.2	11.0	3.0	41.5 ± 2.6	20	214 ± 7	83

^aDetermined by SEC analysis in THF solvent using polystyrene as standard. ^bFor the polymer, hydrodynamic radii (R_H^{CAL}) as calculated according to the formula $R_H^{CAL}(nm) = R_H^{CAL} (1-f)^{0.6}$.¹⁸ ^cHydrodynamic radii (R_H^{VIS}) as determined by viscometer detector using SEC. ^dCompact globules: $R_H^{\phi=1} = [3M_w / (4\pi\phi\rho N_A)]^{1/3}$ with $\phi = 1$ and $\rho = 1.05$ g/cm³. N_A is Avogadro's number. ^e R_H^{DLS} as determined by the Dynamic light scattering studies. ^fDiameter and height determined from analysis of the AFM images. ^gSpherical diameter as determined from the ellipsoid particle adsorbed on silicon surface. UV irradiation ($\lambda_{max} = 320$ nm) for 6 mg/mL polymer in THF with 2x8W UV_B lamp, 4 h)

However, the deviation of *di-P5* polymers from the boundary condition could be ascribed to the lower percentage functionality with respect to the long polymer chain length. Thus, compaction efficiency of the coiled chain polymers as a result of photodimerization mediated chain collapse led to formation of an intrinsically disordered domain. Also, comparison of DLS data for **P1-P5** and *di-P1-P5* polymers in THF (Figure 2.4D) showed the highest (58%) and lowest (20%) compaction of the hydrodynamic radii for the irradiated polymers of *di-P3* and *di-P5* respectively owing to difference in the % of coumarin functionality.

Next, the nanostructure formation as a result of the polymer folding was investigated by Atomic force microscopy. The pre-assembled polymer structures showed a clear distinction in morphology in the different solvent environments. The polymer **P2** showed larger nanoparticles in solvents *e.g.* THF and CHCl₃ whereas smaller nanoparticles were observed in DMF environment, which is in accordance with the DLS results and compatibility obtained from Hildebrand solubility parameters for extended coil conformation (Figure 2.1B, 2.5). Upon UV exposure, the photoresponsive polymers showed formation of different nanostructures at different concentration regime. At dilute regime (10⁻³ mg/mL) of *di-P1-P5*, the chain folding led to formation of hemiellipsoidal nano objects in the size range of 22 nm, 48 nm, 33 nm, 115 nm, 214 nm respectively (Figure 2.6 A-E) indicating the extended coil to globule transition, that mimic the folded polymer chains with exponent values of $\nu = 0.32$.^{55,56} Histogram analyses exhibited excellent polydispersity index

(PDI) for the size of the nanoparticles suggesting control over the size, that is dependent on the polymer chain length. Comparison of **di-P2** and **di-P3** with comparable DP yet different % of functionalities revealed further compaction of the nanoparticles from 48 nm to 33 nm.

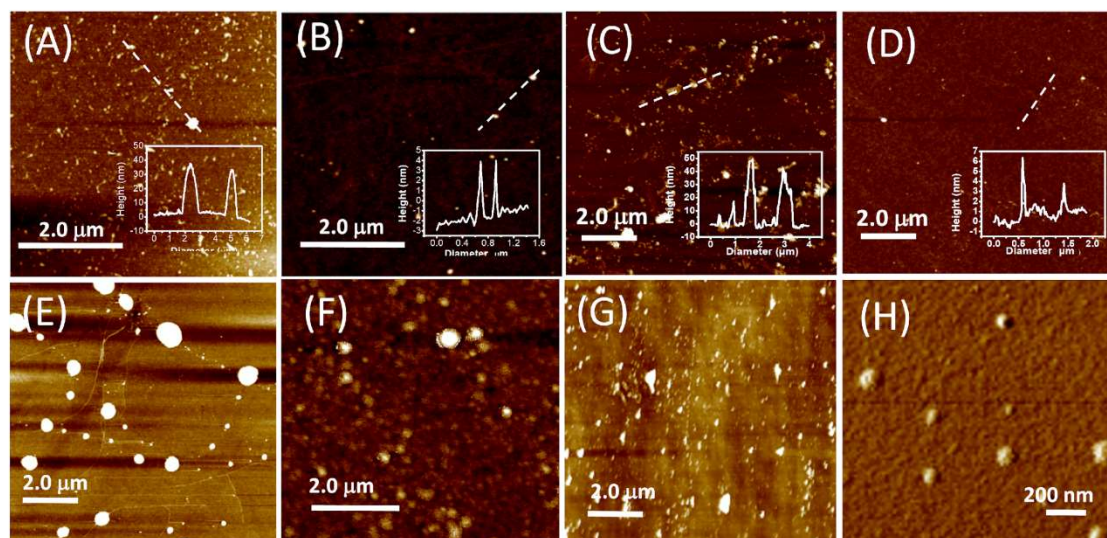


Figure 2.5. AFM Height images of polymer **P1** (A) before and (B) after, polymer **P2** (C) before and (D) after, UV_B irradiation in THF (Inset has corresponding height profiles of corresponding nanostructures) AFM Height images of polymer **P2** (E) before and (F) after 3h of UV_B irradiation in CHCl₃. (G) AFM Height images of native polymer **P2** ($c = 10^{-3}$ mg/mL) in DMF solvent. (H) AFM phase images of selected zoomed area of **di-P1** in THF (Irradiation of all the samples were conducted at a concentration of 10^{-3} mg/mL using 2 UV_B lamps for 3h.)

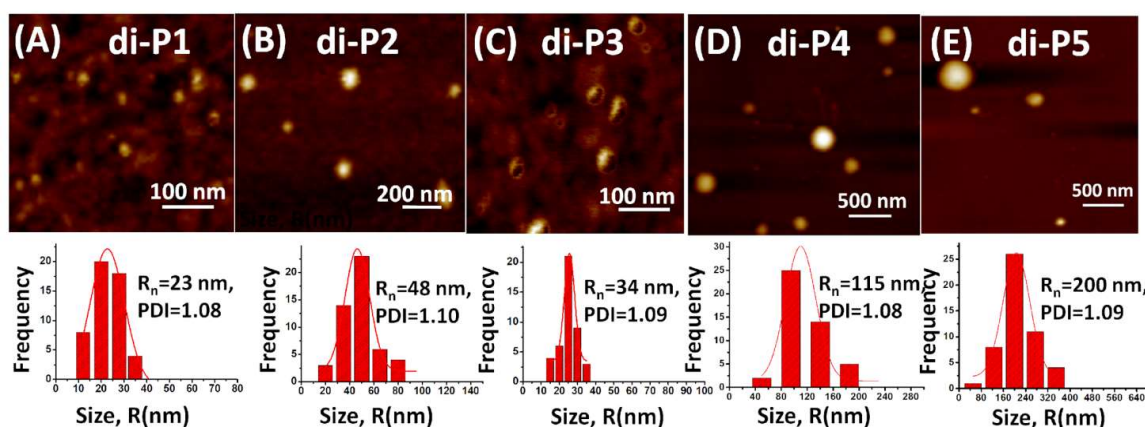


Figure 2.6. AFM images of irradiated samples and their corresponding histogram analyses from (A) **di-P1**, (B) **di-P2** and (C) **di-P3**, (D) **di-P4**, (E) **di-P5** in THF. (Irradiation of sample solution (conc = 10^{-3} mg/mL) in THF with 2x8W UV_B lamp, 3 h.

This clearly indicated involvement of greater number of chain collapse sites in **P3** during chain collapse process. Since drop-casting of the nanoparticle solution onto a silicon surface results in the flattening of the soft particle to a hemiellipsoidal geometry, the radii of the spherical nanoparticles were estimated by comparing the volume of hemiellipsoid and sphere.⁵⁷ In correlation with the hydrodynamic radii obtained from DLS analyses, the estimated spherical radii from AFM depends on the polymer chain length and % of functionality. However, they were found to be higher than the hydrodynamic radii that might be attributed to underestimation of the formation of aggregates during the sample preparation. Irradiation performed for polymer samples at higher concentration clearly showed the presence of higher order supramolecular self-assembled nanostructures of the polymer (Figure 2.7). While *di*-**P1**, **P2**, **P3** in THF at dilute condition (10^{-3} mg/mL) exhibited presence of uniform nanoparticles (radius 11 nm) presumably due to the intrachain collapse, at higher concentration (1 mg/mL) they showed supramolecular fiber formation owing to the interchain polymer collapse. UV irradiation at intermediate concentration regime (0.1 mg/mL) showed the onset of transition from intrachain to interchain photodimerization to render toroid or nanofibers that accounts for the intermediate folded states.^{58,59} The relatively rigid polymers with higher % functionality showed strong interchain interactions and collapse into conformations with toroid or rod shaped nanostructures. However, relatively flexible polymers (**P4** and **P5**) with longer reptation time, rather showed aggregated globules upon increasing the macromolecular crowding. Therefore, the polymer chain in extended coil conformation could be directed to form compact/globular nanoparticles in dilute regime or higher order structures *e.g.* toroid, nanofibers in crowded polymer concentration based on a number of parameters.

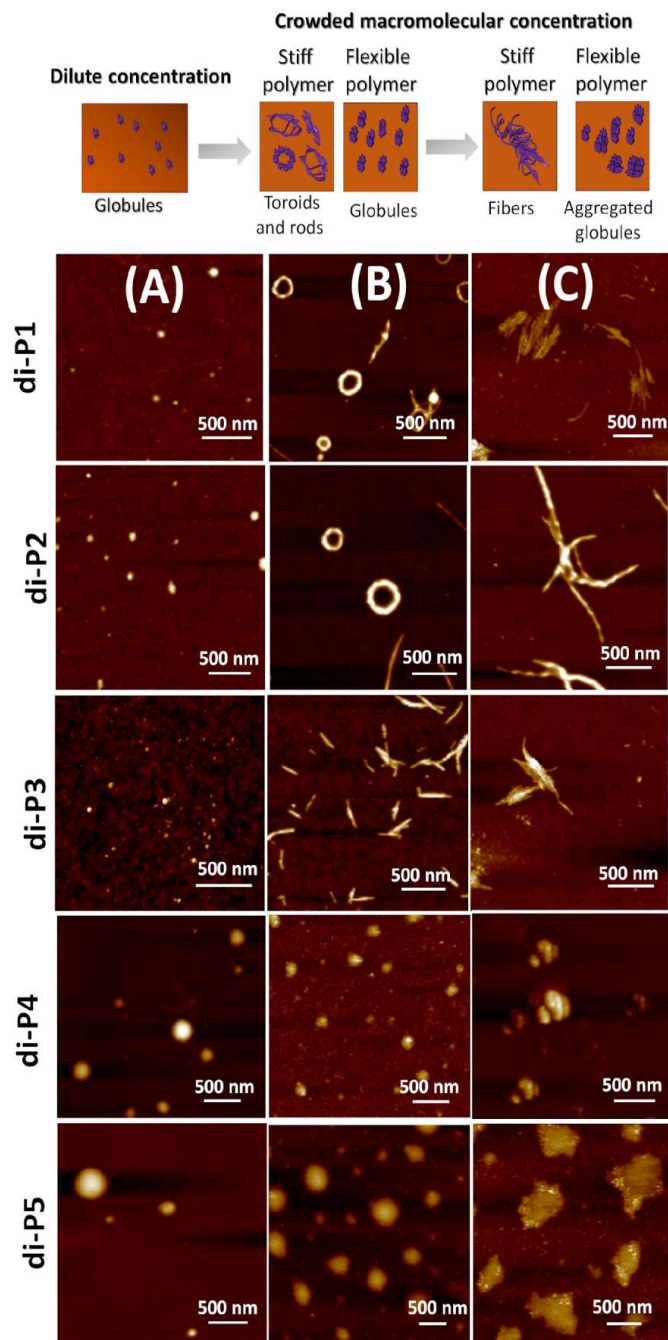


Figure 2.7. Scheme depicting concentration dependent nanostructures formation as a result of crowding of polymer chains. Diverse nanostructures as observed from AFM images of the polymers **di-P1**-(A) 0.001 mg/mL, (B) 0.1 mg/mL and (C) 1 mg/mL in THF (left to right).

2.2.4. Monitoring influence of crosslinking over thermal properties: Further the thermal properties of the polymers were investigated by Differential Scanning Calorimetric (DSC)

studies in the context of flexible-rigid domain of the copolymer chains. The glass transition temperature (T_g), indicating the switch over from the hard glassy nature to soft rubbery material plays a pivotal role in the thermal self-healing process of the thermoplastic elastomers.

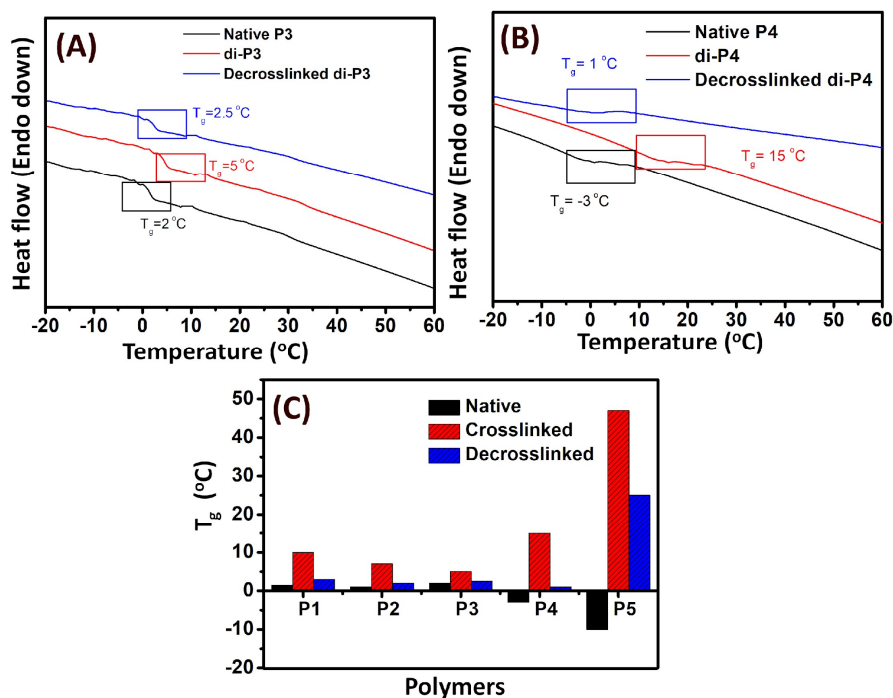


Figure 2.8. Representative differential Scanning Calorimetry (DSC) traces showing effect of photodimerization on the glass transition temperature of the polymer films (20 mg/mL) of (A) **P3** (B) **P4** casted on a glass substrate and (C) the glass transition temperatures for **P1-P5** from DSC studies in native, crosslinked and decrosslinked form of the polymers. 2x8W UV_B Lamps and 2x8W UV_C Lamps were used for crosslinking and decrosslinking respectively.

Table 2.4. DSC data of different polymers of **P1-P5**

Polymer	T_g Native (°C)	T_g crosslinked (°C)	T_g decrosslinked (°C)
P1	1.5	10	3
P2	1	8	2
P3	2	5	2.5
P4	-3	15	1
P5	-10	47	25

The polybutyl acrylate polymer chain shows a typical low glass transition temperature ($T_g = -54$ °C) owing to its inherent flexibility, however grafting of the relatively rigid comonomers hydroxyl ethyl acrylate and coumarin moieties in the polymers **P1-P5** increased

the T_g values to a range of 2 to -10 °C (Figure 2.8 and Table 2.4). This was evident from the highest T_g value (2 °C) of **P3** with 28% of rigid comonomers, while **P5** (4% rigid comonomers) exhibited the lowest T_g value (-10 °C) among all the polymers. Upon UV mediated covalent photodimerization for 10 h, all the polymers **di-P1-P5** exhibited an upward shift in the T_g values presumably due to the loss of mobility of the polymer chains resulting from network stiffness.^{20b} The change of T_g was found to be the highest for **di-P5** ($\Delta T_g = +47$ °C) with longest polymer chain and least percentage of rigid comonomers, while **di-P3** with highest percentage (28%) of rigid coumarin and HEA functionalities showed minimal ΔT_g response ($+3$ °C). It is worthwhile to note that **di-P3** showed maximum chain

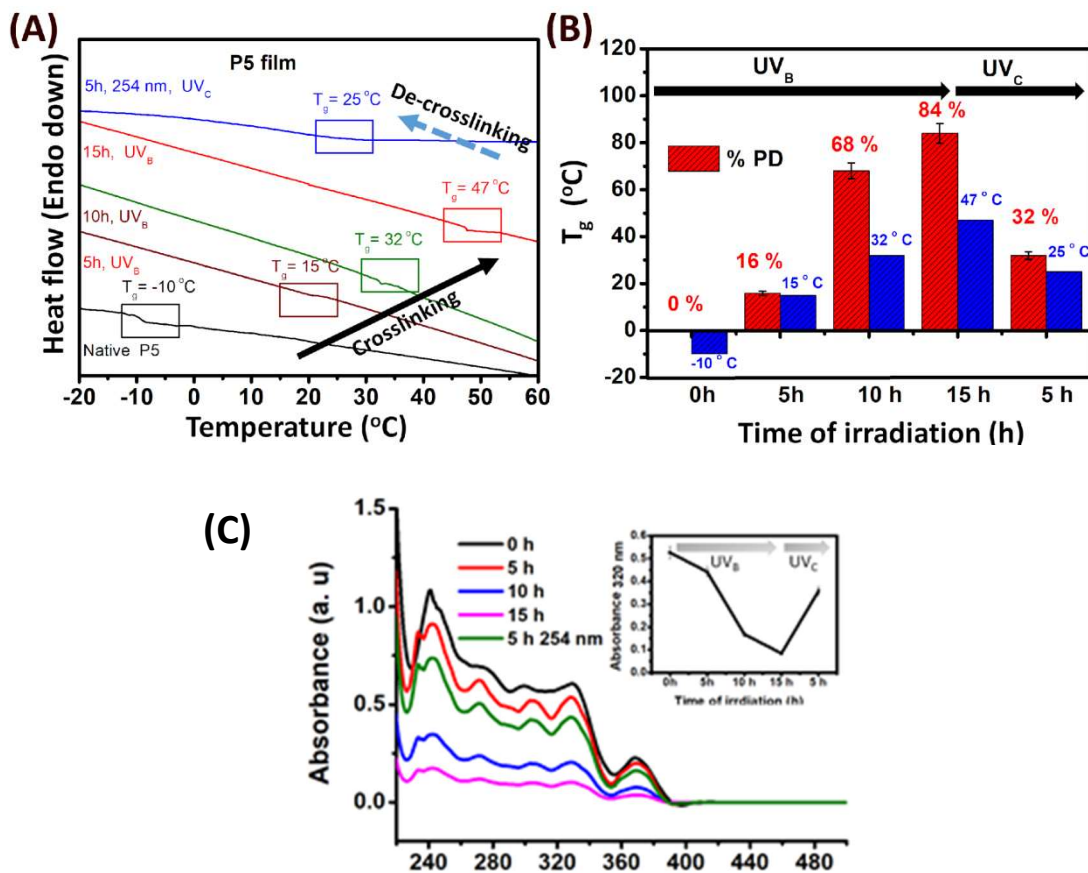


Figure 2.9. (A) DSC traces showing effect of photodimerization on the glass transition temperature of the **P5** polymer film. (B) Bar graph showing % PD and glass transition temperature of the polymer film (**P5**) with increasing time of UV_B and UV_C irradiation. (C) UV Spectra showing photodimerization of **P5** polymer film with increase in time of irradiation.

compaction owing to highest % PD in solution; however, in solid state increased amount of coumarin moieties contributed towards the rigidity of the original polymer itself and resulted in minimal changes upon photocrosslinking.

Furthermore, the polymers showed reversal of the T_g values upon irradiating the cross-linked polymer sample with UV_c light ($\lambda_{\text{max}} = 254 \text{ nm}$) for 5 h indicating the dynamic nature of reversible covalent bond in the cyclobutane adducts. In addition, an increase in the % PD values with time of irradiation for the solid film of **P5** rendered a gradual increase in T_g values, thereby indicating photodimerization degree as a crucial factor in the rigidification of the polymers (Figure 2.9). Such a control over the glass transition temperature owing to the photo-crosslinkable behavior and balance of flexible-rigid segments prompted us to investigate the self-healing properties for this class of polymer at ambient conditions.

2.2.5. Investigation of self-healing property: The transparent polymers were investigated for micron level crack healing that exhibited autonomic and intrinsic self-healing as it requires no external intervention. Also, the gradient of the T_g values in the bulk and new interface is expected to promote the interdiffusion of the chains leading to healing of the cracks. In that regards, low T_g , high ΔT_g values upon photo-crosslinking and good film forming ability of **P5** encouraged us to select these two polymers for investigating the self-healing behavior as these parameters are crucial to modulate the mobility of the crosslinked and decrosslinked polymer chains. The polymers (20 mg/mL in THF) were drop-casted on a glass substrate and dried to render stable films. A surgical blade was used to make a cut on the surface of the film and investigated for healing at room temperature with the aid of a bright field microscope. The optical microscopic images of the native **P5** film with time (Figure 2.10 A) showed fast healing of the scratch within a few minutes for the native polymers without any outside intervention, suggesting autonomic and intrinsic nature of the self-healing behavior. **P5** showed complete healing within 3 minutes, while **P4** exhibited 80% healing of the original scratch after 15 minutes. The scratch in **P3** film did not show any detectable healing even after 30 min. This is presumably due to relatively less diffusion of the polymer chains as a consequence of higher % of rigid functionality in **P4** and **P3** in

accordance with the T_g values, thus overshadowing the effect of flexible butyl acrylate segments.

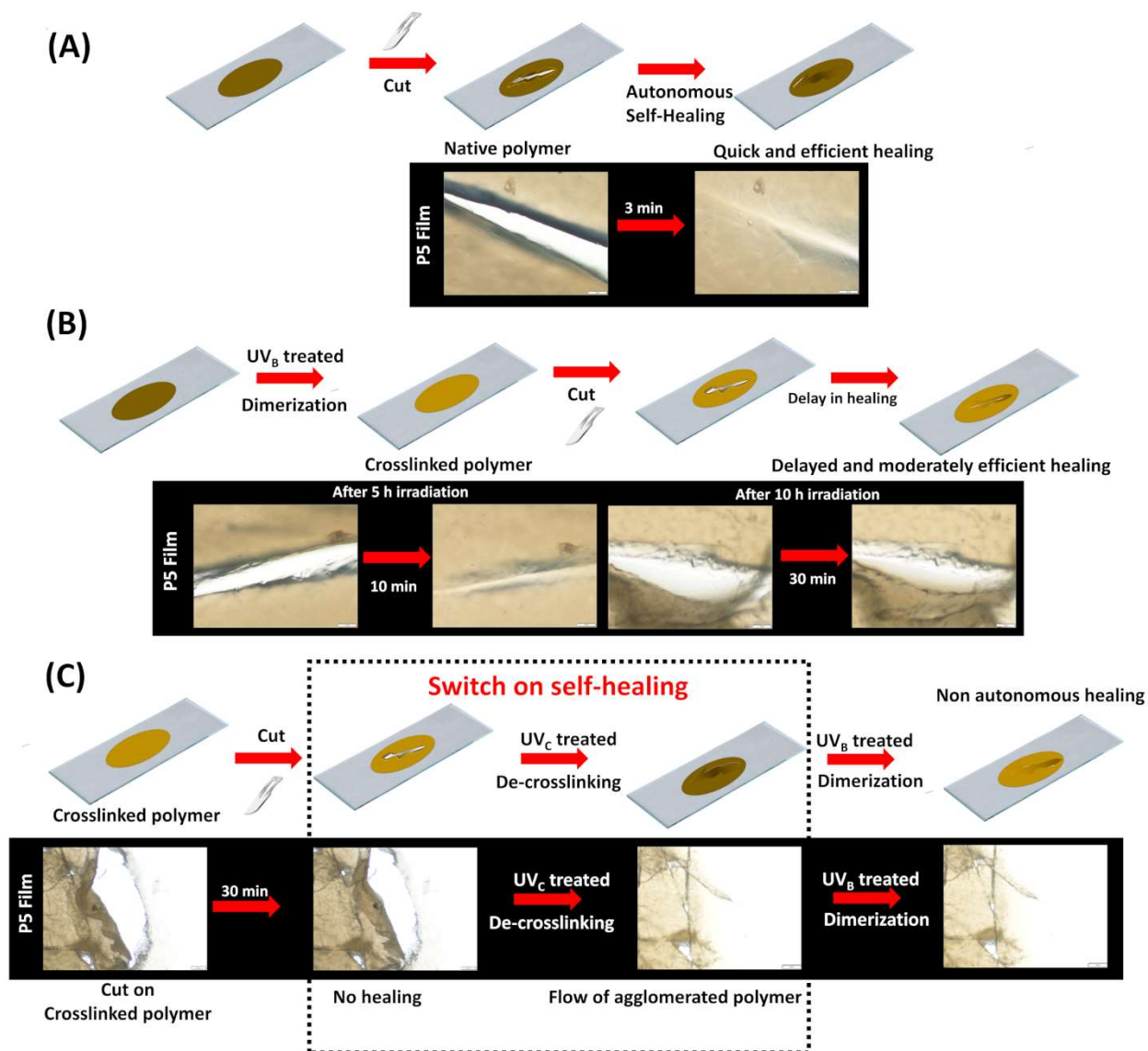


Figure 2.10. Self-healing pathways with corresponding optical microscopy images depicting autonomic and nonautonomic route of healing. (A) Film of native polymer **P5** shows complete autonomic healing of a cut of average width $\sim 80 \mu\text{m}$ within 3 min. (B) Photo-crosslinked film of polymer **di-P5** exhibits delayed and inefficient autonomic healing of a cut on the film (average width $\sim 110 \mu\text{m}$). Photoirradiation of the film for 5 h and 10 h (2 x 8W UV_B Lamp) resulted crosslinked films that show 90% healing within 6-7 min and 20% healing even after 20 min. (C) Non autonomic pathway of healing *via* UV_C irradiation. (1 x 8W UV_C Lamp)

However, a cut in the photocrosslinked **di-P5** polymer films exhibited a delay in the healing process (up to 30 min) owing to the rigidification in the hard segments. Thus, increasing % PD of the film resulted in an increase in the T_g values that rendered a significant delay in the self-healing for *di-P5* films (Figure 2.10B). This correlates the DSC data showing photocrosslinking mediated maximal change (ΔT_g) and subsequent reduction in the mobility of the polymer chains akin to the reported multiphase design of thermoplastic elastomers.²⁸ Further, **di-P4** and **di-P3** polymer with 14% and 28% rigid functional groups exhibited slower healing kinetics with 55% healing and no apparent healing even after long time (1h) respectively. This, in turn, indicated requirement of an optimum balance of % functionality in the rigid segment along with the polymer molecular weights for effective modulation of the self-healing behavior. Thus, the healing response of the polymer film could be photo-triggered using UV_C light as an external stimuli. Thus, the crosslinked film of **di-P5** upon irradiation with UV_C light resulted in photocleavage of cyclobutane moieties resulting a significant reduction in T_g values with subsequent viscoelastic mobility. This, in turn, increase the diffusional flow of the polymer chains rendering them closer, that is sufficient to switch on the self- healing of the film (Figure 2.10 C). Such photo-triggered self-healing is non-autonomic, and can be repeated for multiple cycles.

2.3. Conclusion

In summary, we demonstrated a smart design of a series of nonpolar polymers decorated with photodimerizable coumarin moieties that undergo intrachain or interchain collapse with UV irradiation to form diverse nanostructures. The polymers **P1-P5** assumed to have an extended coil state ($\nu = 0.58$) in good solvent conditions. A number of factors such as concentration, molecular weight of the polymer, percentage functionality of the photoactive coumarin moieties and solvent environment play a deciding role in controlling degree of photodimerization and resulted chain collapse mediated folding of the polymers. At lower concentration single chain polymers undergo transition from extended coil to globular nanoparticle mediated by intrachain collapse while interchain photocrosslinking of the rigid

coumarin moieties of the polymers rendered folding and compaction far from a condensed globular state at higher polymer concentration. This indicated the crosslinked network of polymer with locally compact portions of polymers connected together by photodimerized coumarin moieties possess structural analogy with flexo-rigid thermoplastic elastomeric system. Tweaking the balance of the flexible vs rigid moieties in the polymer chain especially, utilizing the photo irradiation resulted in a significant change in the glass transition temperature that played a pivotal role in controlling the efficacy and nature of the self-healing behavior. The native polymers showed intrinsic and autonomic healing behavior at ambient temperature. However, covalent crosslinking harden the polymer and delayed the healing process. The crosslinked polymer film could be photo-triggered to break the cyclobutane rings thereby endowing the chain mobility and switching on a non-autonomic and intrinsic self-healing behavior at ambient conditions. Such a rational design of the photo-modulated self-healing system showed coexistence of autonomic and non-autonomic self-healing pathways, that can be modulated by photocrosslinking. Such photo-tunable self-healing behavior might justify its potential application in smart coating of photovoltaic device and designing flexographic imaging plate materials in future.

2.4. Experimental Section

2.4.1. Materials:

Solvents used in the syntheses were of reagent grade. Acetone, chloroform, THF, 1,4-dioxane were dried as per literature protocol.⁶⁰ The reagents, ethyl bromoacetate, tetra-*n*-butylammonium fluoride (TBAF), triethyl amine were purchased from Alfa-aeser and used without further purification. Glacial acetic acid was purchased from SD fine. The chemicals 7-hydroxy-4-methyl coumarin, pentamethyl diethyl triamine (PMDETA), Cu(I)Br were purchased from Sigma-Aldrich, USA. The reagents ethyl bromo isobutyrate (EtBriB), *N,N'*-diisopropylcarbodiimide (DIPC) (99%) were purchased from TCI and were used without further purification. 4-(Dimethylamino)pyridinium 4-toluenesulfonate (DPTS) was prepared according to a reported procedure.⁶¹ The monomers 2-hydroxy ethyl acrylate (HEA), butyl acrylate (*n*-BA) were purchased from TCI and were passed through basic alumina (to remove

inhibitor MEHQ) before using them for ATRP. 2-(Trimethylsilyloxy)ethyl acrylate (TMS-HEA) was prepared according to a literature procedure.⁶²

2.4.2. Instrumentations:

NMR spectra were acquired on a 400 MHz Bruker machine. The chemical shifts were reported in ppm with downfield of tetramethylsilane using the resonance of the deuterated solvent as internal standard. Splitting patterns were designated as singlet (s), doublet (d), triplet (t) and multiplet (m). % of functionality was calculated using the formula, %Functionality = $\{(I_p)/(I_p+I_e)\} \times 100$ where, I_p is integral per proton of corresponding functional group, I_e is integral proton of end group (e. g. methyl group of butyl acrylate chain). Size exclusion chromatography (SEC) was performed on a Malvern Viscotek instrument having RI, right angle light scattering (RALS), viscometer detector using T_{6000M}-T₃₀₀₀ columns in series with THF as eluent at 35 °C with a flow rate of 1 mL/min. The results were analysed by using Omniseq software. The sample peaks were analysed for M_n , M_w , PDI , intrinsic viscosity (IV) as well as R_H by means of conventional and triple detector universal calibration method obtained using polystyrene standards. Samples were prepared by filtering solutions through a 0.2 µm PTFE-filter into a 2 mL GPC glass vial. Dynamic light scattering measurements were done on Malvern Zetasizer Nano ZS ZEN3600 equipped with a Helium–Neon laser (wavelength, $\lambda = 633$ nm with backscattering angle of 173°). Samples were prepared by filtering solutions through a 0.2 µm PTFE-filter into a glass cuvette. UV crosslinking was performed using an UV chamber equipped with 2* 8W UV_B lamp ($\lambda_{max} = 320$ nm, Intensity at 15 cm = 790 µW/cm²) and 1*8W UV_C lamp ($\lambda_{max} = 254$ nm, Intensity at 15 cm = 820 µW/cm²) and the sample in liquid state or solid film was kept at a distance of 15 cm for irradiation. Luminous intensity of irradiation at time t was determined in J/cm² by the formula $[(\mu\text{W}/\text{cm}^2)/10^6] * t$ (s). UV spectra were recorded using Shimadzu UV 6000 UV-vis spectrophotometer in a wavelength range of 800 to 200 nm. The samples were drop-casted on silicon wafer and AFM height images were recorded using tapping mode on a Bruker multimode 8 scanning probe microscope with silicon cantilever. Thermal studies of polymer samples were performed on Perkin Elmer Differential Scanning Calorimeter DSC 8000 model and the samples were heated from -80 to 150 °C at a heating

rate of 10 °C/min. Optical microscopy images of the self-healing polymer films were recorded on Olympus BX53 model upright fluorescent microscope equipped with sCCD camera.

2.4.3. Methods:

2.4.3.1. Synthesis and characterization of the polymers:

General procedure for random copolymerization of 2(Trimethylsilyloxy)ethyl acrylate (HEA-TMS) with *n*-butyl acrylate (*n*-BA) by ATRP method followed by deprotection of the TMS and post-functionalization of polymer with coumarin moieties.

ATRP polymerization was performed with *n*-BA and HEA-TMS as co-monomers followed by deprotection of TMS group (Scheme 1). Coumarin carboxylic acid was then tethered to the resulting copolymers using esterification. The detailed synthetic procedures of **P1-P5** are described as follows.

Random copolymerization by ATRP:

Cu(I)Br, *n*-BA, HEA-TMS, initiator (EtBriB), and toluene were placed in a schlenk tube capped with a rubber septum followed by degassing using freeze-thaw-pump cycles (three times). PMDETA was then added to the mixture and was degassed again. The reaction mixture was placed in an oil bath for stirring at 70 °C for around 17 hours. Then it was cooled to room temperature and diluted with THF. The solution was filtered through neutral alumina to trap the copper catalyst with subsequent removal of unreacted monomers and solvents in vacuum at 50 °C to yield the TMS protected copolymer. NMR and GPC analysis confirmed the polymer with the percentage of comonomers and M_w , M_n , PDI .

P-TMS-1. Random copolymer of butyl acrylate and 2(Trimethylsilyloxy)ethyl acrylate (intended % functionality = 15%, DP = 25): Cu(I)Br (0.32 mmol), *n*-BA (3.4 mmol), HEA-TMS (0.6 mmol), initiator (EtBriB) (0.16 mmol), and toluene (1 ml) were placed in a schlenk tube capped with a rubber septum followed by degassing using freeze-thaw-pump cycles (three times). PMDETA (0.32 mmol) was then added to the mixture and was again degassed. The reaction mixture was placed in an oil bath for stirring at 70 °C for around 17 hours. Then it was cooled to room temperature and diluted with THF. The solution was filtered through neutral alumina to trap the copper catalyst with subsequent removal of

unreacted monomers and solvents in vacuum at 50 °C to yield the TMS protected copolymer. ¹H NMR (400 MHz, CDCl₃): δ (ppm) 4.06– 3.99 (m, 5H, OCH₂), 3.83-3.70 (m, 1H, OCH₂CH₂O), 2.41–2.23 (m, 3H, CH₂), 1.98-1.90 (m, 1H, CH₂), 1.66-1.55 (m, 12H, CH₂), 1.43-1.38 (m, 9H, OCH₂CH₂CH₂CH₃), 0.95–0.92 (t, 8H, OCH₂CH₂CH₂CH₃), 0.13-0.05 (m, 2H, Si (CH₃)₃). %Functionality = 10%, SEC analysis (THF, polystyrene standards): $M_n = 3000$ g/mol; $M_w/M_n = 1.11$.

P-TMS-2. Random copolymer of butyl acrylate and 2(Trimethylsilyloxy)ethyl acrylate (intended % functionality = 15%, DP = 50): Cu(I)Br (0.16 mmol), BA (3.4 mmol), HEA-TMS (0.6 mmol), initiator (EtBriB) (0.08 mmol), and toluene (1 ml) were placed in a schlenk tube capped with a rubber septum followed by degassing using freeze-thaw-pump cycles (three times). PMDETA (0.16 mmol) was then added to the mixture and was again degassed. The reaction mixture was placed in an oil bath for stirring at 70 °C for around 17 hours. Then it was cooled to room temperature and diluted with THF. The solution was filtered through neutral alumina to trap the copper catalyst with subsequent removal of unreacted monomers and solvents in vacuum at 50 °C to yield the TMS protected copolymer. ¹H NMR (400 MHz, CDCl₃): δ (ppm) 4.31– 4.27 (m, 6H, OCH₂CH₂O), 3.98-3.90 (m, 20H, OCH₂), 3.68-3.72 (m, 5H,), 2.46–2.40 (m, 7H, CH₂), 2.24-2.18 (m, 15H, CH₂), 1.86-1.83(m, 11H, CH₂), 1.58-1.53 (m, 30H, OCH₂CH₂CH₂CH₃), 1.34-1.29 (m, 20H, OCH₂CH₂CH₂CH₃), 0.89–0.85 (t, 29H, OCH₂CH₂CH₂CH₃), 0.15–0.09 (m, 11 H, Si (CH₃)₃). %age Functionality = 12%. SEC analysis (THF, polystyrene standards): $M_n = 5437$ g/mol; $M_w/M_n = 1.23$.

P-TMS-3. Random copolymer of butyl acrylate and 2(Trimethylsilyloxy)ethyl acrylate (intended % functionality = 40%, DP = 50): Cu(I)Br (0.16 mmol), BA (2.4 mmol), HEA-TMS (1.6 mmol), initiator (EBriB) (0.08 mmol), and toluene (1 ml) were placed in a schlenk tube capped with a rubber septum followed by degassing using freeze-thaw-pump cycles (three times). PMDETA (0.16 mmol) was then added to the mixture and was again degassed. The reaction mixture was placed in an oil bath for stirring at 70 °C for around 17 hours. Then it was cooled to room temperature and diluted with THF. The solution was filtered through neutral alumina to trap the copper catalyst with subsequent removal of unreacted monomers and solvents in vacuum at 50 °C to yield the TMS protected copolymer. ¹H NMR (400 MHz, CDCl₃): δ (ppm) 4.25– 4.04 (m, 10H, OCH₂CH₂O), 3.78-3.74 (m, 4H, OCH₂CH₂O &

OCH₂), 2.4–2.19 (m, 6H, CH₂), 2.02–1.90 (m, 3H, CH₂), 1.79–1.54 (m, 15H, CH₂), 1.22–1.43 (m, 6H, OCH₂CH₂CH₂CH₃), 0.98–0.89 (t, 9H, OCH₂CH₂CH₂CH₃), 0.16–0.07 (m, 11H, Si (CH₃)₃). %Functionality = 29%. SEC analysis (THF, polystyrene standards): $M_n = 6000$ g/mol; $M_w/M_n = 1.26$.

P-TMS-4. Random copolymer of butyl acrylate and 2(trimethylsilyloxy)ethyl acrylate (intended % functionality = 15%, DP = 150): Cu(I)Br (0.16 mmol), BA (10.2 mmol), HEA-TMS (1.8 mmol), initiator (EtBriB) (0.08 mmol), and toluene (1 ml) were placed in a schlenk tube capped with a rubber septum followed by degassing using freeze-thaw-pump cycles (three times). PMDETA (0.16 mmol) was then added to the mixture and was again degassed. The reaction mixture was placed in an oil bath for stirring at 70 °C for around 17 hours. Then it was cooled to room temperature and diluted with THF. The solution was filtered through neutral alumina to trap the copper catalyst with subsequent removal of unreacted monomers and solvents in vacuum at 50 °C to yield the TMS protected copolymer. ¹H NMR (400 MHz, CDCl₃): δ (ppm) 4.05– 3.98 (m, 5H, OCH₂), 3.83-3.70 (m, 1H, OCH₂CH₂O), 2.41–2.23 (m, 3H, CH₂), 1.98-1.90 (m, 2H, CH₂), 1.66-1.55 (m, 9H, CH₂), 1.43-1.38 (m, 5H, OCH₂CH₂CH₂CH₃), 0.95–0.92 (t, 5H, OCH₂CH₂CH₂CH₃), 0.13-0.05 (m, 3H, Si (CH₃)₃). %Functionality = 14%. SEC analysis (THF, polystyrene standards): $M_n = 19718$ g/mol; $M_w/M_n = 1.12$.

P-TMS-5. Random copolymer of butyl acrylate and 2(trimethylsilyloxy)ethyl acrylate (intended % functionality = 15%, DP = 300): Cu(I)Br (0.16 mmol), BA (20.4 mmol), HEA-TMS (3.6 mmol), initiator (EtBriB) (0.08 mmol), and toluene (1 ml) were placed in a schlenk tube capped with a rubber septum followed by degassing using freeze-thaw-pump cycles (three times). PMDETA (0.16 mmol) was then added to the mixture and was again degassed. The reaction mixture was placed in an oil bath for stirring at 70 °C for around 17 hours. Then it was cooled to room temperature and diluted with THF. The solution was filtered through neutral alumina to trap the copper catalyst with subsequent removal of unreacted monomers and solvents in vacuum at 50 °C to yield the TMS protected copolymer. ¹H NMR (400 MHz, CDCl₃): δ (ppm) 4.06– 3.99 (m, 5H, OCH₂), 3.83-3.70 (m, 1H, OCH₂CH₂O), 2.41–2.23 (m, 3H, CH₂), 1.98-1.90 (m, 1H, CH₂), 1.66-1.55 (m, 10H, CH₂), 1.43-1.38 (m, 6H, OCH₂CH₂CH₂CH₃), 0.95–0.92 (t, 6H, OCH₂CH₂CH₂CH₃), 0.13-0.05 (m,

3H, Si (CH_3)₃). %Functionality = 12%. SEC analysis (THF, polystyrene standards): $M_n = 33640$ g/mol; $M_w/M_n = 1.13$.

Deprotection of TMS group:

The copolymer was treated with TBAF and acetic acid and stirred at room temperature for 24 hours. Then the reaction mixture was diluted with methanol-water (9:1) and the deprotected polymers were obtained by precipitation.

P-OH-1. Random copolymer of butyl acrylate and hydroxy ethyl acrylate (intended

%functionality = 15%, DP = 25): The deprotection of TMS was achieved by stirring the polymer **P-TMS-1** (0.027 mmol) with 0.54 mmol of TBAF and 3.3 mmol of acetic acid at room temperature for 24 hours. Precipitation from methanol-water (9:1) followed by drying under P_2O_5 in vacuum furnished the polymer **P-OH-1**. ^1H NMR (400 MHz, CDCl_3): δ (ppm) 4.35–4.25 (m, 5H, OCH_2), 3.75–3.69 (m, 1H, $\text{OCH}_2\text{CH}_2\text{O}$), 3.15 (s, 1H, OH), 2.37–2.20 (m, 3H, CH_2), 1.90–1.89 (m, 1H, CH_2), 1.65–1.53 (m, 12H, CH_2), 1.46–1.35 (m, 8H, $\text{OCH}_2\text{CH}_2\text{CH}_2\text{CH}_3$), 0.98–0.94 (t, 8H, $\text{OCH}_2\text{CH}_2\text{CH}_2\text{CH}_3$). % Functionality = 10%. SEC analysis (THF, polystyrene standards): $M_n = 2730$ g/mol; $M_w/M_n = 1.27$.

P-OH-2. Random copolymer of butyl acrylate and hydroxy ethyl acrylate (intended

%functionality = 15%, DP = 50): The deprotection of TMS was achieved by stirring the polymer **P-TMS-2** (0.014 mmol) with 0.28 mmol of TBAF and 1.7 mmol of acetic acid at room temperature for 24 hours. Precipitation from methanol-water (9:1) followed by drying under P_2O_5 in vacuum furnished the polymer **P-OH-2**. ^1H NMR (400 MHz, CDCl_3): δ (ppm) 4.37–4.19 (m, 24H, OCH_2), 3.95–3.79 (m, 5H, $\text{OCH}_2\text{CH}_2\text{O}$), 3.30 (s, 2H, OH), 2.15–1.92 (m, 13H, CH_2), 1.61–1.58 (m, 39H, CH_2), 1.38–1.25 (m, 23H, $\text{OCH}_2\text{CH}_2\text{CH}_2\text{CH}_3$), 0.95–0.88 (t, 29H, $\text{OCH}_2\text{CH}_2\text{CH}_2\text{CH}_3$). %Functionality = 12%. SEC analysis (THF, polystyrene standards): $M_n = 4888$ g/mol; $M_w/M_n = 1.21$.

P-OH-3. . Random copolymer of butyl acrylate and hydroxy ethyl acrylate (intended

%functionality = 40%, DP = 50): The deprotection of TMS was achieved by stirring the polymer **P-TMS-3** (0.013 mmol) with 0.26 mmol of TBAF and 2.5 mmol of acetic acid at room temperature for 24 hours. Precipitation from methanol-water (9:1) followed by drying under P_2O_5 in vacuum furnished the polymer **P-OH-3**. ^1H NMR (400 MHz, CDCl_3): δ (ppm) 4.32–4.15 (m, 8H, OCH_2), 3.84–3.74 (m, 5H, $\text{OCH}_2\text{CH}_2\text{O}$), 2.37–2.23 (m, 5H,

CH_2), 1.99-1.93 (m, 3H, CH_2), 1.68-1.60 (m, 20H, CH_2), 1.42-1.35 (m, 11H, $\text{OCH}_2\text{CH}_2\text{CH}_2\text{CH}_3$), 0.96–0.92 (t, 9H, $\text{OCH}_2\text{CH}_2\text{CH}_2\text{CH}_3$). %Functionality = 29%. SEC analysis (THF, polystyrene standards): $M_n = 4552$ g/mol; $M_w/M_n = 1.31$.

P-OH-4. Random copolymer of butyl acrylate and hydroxy ethyl acrylate (intended %functionality = 15%, DP = 150): The deprotection of TMS was achieved by stirring the polymer **P-TMS-4** (0.048 mmol) with 2.88 mmol of TBAF and 18 mmol of acetic acid at room temperature for 24 hours. Precipitation from methanol-water (9:1) followed by drying under P_2O_5 in vacuum furnished the polymer **P-OH-4**. ^1H NMR (400 MHz, CDCl_3): δ (ppm) 4.32– 4.15 (m, 26H, OCH_2), 3.84-3.74 (m, 11H, $\text{OCH}_2\text{CH}_2\text{O}$), 3.35(s, 1H, OH), 2.37–2.23 (m, 14H, CH_2), 1.99-1.93 (m, 5H, CH_2), 1.68-1.60 (m, 47H, CH_2), 1.42-1.35 (m, 35H, $\text{OCH}_2\text{CH}_2\text{CH}_2\text{CH}_3$), 0.96–0.92 (t, 45H, $\text{OCH}_2\text{CH}_2\text{CH}_2\text{CH}_3$). %Functionality = 18%. SEC analysis (THF, polystyrene standards): $M_n = 18076$ g/mol; $M_w/M_n = 1.27$.

P-OH-5. Random copolymer of butyl acrylate and hydroxy ethyl acrylate (intended %functionality = 15%, DP = 300): The deprotection of TMS was achieved by stirring the polymer **P-TMS-5** (0.048 mmol) with 2.88 mmol of TBAF and 18 mmol of acetic acid at room temperature for 24 hours. Precipitation from methanol-water (9:1) and subsequent drying under P_2O_5 in vacuum furnished the polymer **P-OH-5**. ^1H NMR (400 MHz, CDCl_3): δ (ppm) δ (ppm) 4.32– 4.15 (m, 27H, OCH_2), 3.84-3.74 (m, 10H, $\text{OCH}_2\text{CH}_2\text{O}$), 3.35(s, 1H, OH), 2.37–2.23 (m, 13H, CH_2), 1.99-1.93 (m, 5H, CH_2), 1.68-1.60 (m, 46H, CH_2), 1.42-1.35 (m, 34H, $\text{OCH}_2\text{CH}_2\text{CH}_2\text{CH}_3$), 0.96–0.92 (t, 55H, $\text{OCH}_2\text{CH}_2\text{CH}_2\text{CH}_3$). %Functionality = 12%. SEC analysis (THF, polystyrene standards): $M_n = 30640$ g/mol; $M_w/M_n = 1.35$.

Grafting of photoresponsive moieties on the polymers:

The synthesis of coumarin carboxylic acid was performed according to the literature procedure.⁶³ The polymer solution was added to a stirred solution of coumarin carboxylic acid with DPTS and DIPC. The solution was stirred under N_2 environment at 25 °C for 48 hours. Then the solvent was evaporated and the solid was precipitated from methanol-water (20 mL, 9:1 v/v) three times to purify the desired polymer.⁶⁴ The resultant polymer was subsequently dried under P_2O_5 in vacuum furnished the polymer **P1-P5**.

Polymer P1: The solution of polymer **P-OH-1** in THF (14.2 μmol) was added to a stirred solution of coumarin carboxylic acid (568 μmol) with DPTS (142 μmol) and DIPC (837.8

μmol) under N_2 environment. The solution was stirred under N_2 environment at $25\text{ }^\circ\text{C}$ for 48 hours. Precipitation from methanol-water (9:1) and subsequent drying under P_2O_5 in vacuum furnished the polymer **P1**. ^1H NMR (400 MHz, CDCl_3): δ (ppm) 7.60-7.57 (m, 1H, $>\text{C}=\text{CH}-$), 7.36-7.32 (m, 1H, $>\text{C}=\text{CH}-$), 6.89-6.77 (m, 2H, $=\text{CH}-\text{CH}=\text{C}-\text{CH}=\text{}$), 6.22-6.17 (m, 1H, $=\text{CH}-\text{CO}-\text{O}-$), 4.75-4.62 (m, 1.23H, $\text{OCH}_2\text{CO}-\text{O}$), 4.36-4.06 (m, 4H, $\text{OCH}_2\text{CH}_2\text{O}$) 3.95-3.66 (m, 19H, OCH_2), 2.37-2.12 (m, 12H, CH_2), 1.85-1.79 (m, 11H, CH_2), 1.46-1.31 (m, 41H, CH_2), 1.24-1.13 (m, 23H, $\text{OCH}_2\text{CH}_2\text{CH}_2\text{CH}_3$), 0.88-0.85 (t, 30H, $\text{OCH}_2\text{CH}_2\text{CH}_2\text{CH}_3$). %Functionality = 9.6%. SEC analysis (THF, polystyrene standards): $M_n = 6299\text{ g/mol}$; $M_w/M_n = 1.40$.

Polymer P2: The solution of polymer **P-OH-2** in THF ($7.1\text{ }\mu\text{mol}$) was added to a stirred solution of coumarin carboxylic acid (CA) ($192\text{ }\mu\text{mol}$) with DPTS ($48\text{ }\mu\text{mol}$) and DIPC ($292\text{ }\mu\text{mol}$) under N_2 environment. The solution was stirred under N_2 environment at $25\text{ }^\circ\text{C}$ for 48 hours. Precipitation from methanol-water (9:1) and subsequent drying under P_2O_5 in vacuum furnished the polymer **P2**. ^1H NMR (400 MHz, CDCl_3): δ (ppm) 7.60-7.55 (m, 1H, $>\text{C}=\text{CH}-$), 7.35-7.33 (m, 1H, $>\text{C}=\text{CH}-$), 6.85-6.80 (m, 2H, $=\text{CH}-\text{CH}=\text{C}-\text{CH}=\text{}$), 6.20-6.15 (m, 1H, $=\text{CH}-\text{CO}-\text{O}-$), 4.75-4.70 (m, 2H, $\text{OCH}_2\text{CO}-\text{O}$), 4.35-4.24 (m, 4H, $\text{OCH}_2\text{CH}_2\text{O}$) 3.98-3.90 (m, 15H, OCH_2), 2.24-2.20 (m, 8H, CH_2), 1.98-1.84 (m, 4H, CH_2), 1.53-1.50 (m, 26H, CH_2), 1.38-1.36 (m, 16H, $\text{OCH}_2\text{CH}_2\text{CH}_2\text{CH}_3$), 0.88-0.85 (t, 21H, $\text{OCH}_2\text{CH}_2\text{CH}_2\text{CH}_3$). %Functionality = 12%. SEC analysis (THF, polystyrene standards): $M_n = 9597\text{ g/mol}$; $M_w/M_n = 1.16$.

Polymer P3: The solution of polymer **P-OH-3** in THF ($5.7\text{ }\mu\text{mol}$) was added to a stirred solution of coumarin carboxylic acid (CA) ($228\text{ }\mu\text{mol}$) with DPTS ($57\text{ }\mu\text{mol}$) and DIPC ($336\text{ }\mu\text{mol}$) under N_2 environment. The solution was stirred under N_2 environment at $25\text{ }^\circ\text{C}$ for 48 hours. Precipitation from methanol-water (9:1) and subsequent drying under P_2O_5 in vacuum furnished the polymer **P3**. ^1H NMR (400 MHz, CDCl_3): δ (ppm) 7.60-7.57 (m, 1H, $>\text{C}=\text{CH}-$), 7.35-7.33 (m, 1H, $>\text{C}=\text{CH}-$), 6.85-6.80 (m, 2H, $=\text{CH}-\text{CH}=\text{C}-\text{CH}=\text{}$), 6.28-6.20 (m, 1H, $=\text{CH}-\text{CO}-\text{O}-$), 5.01-4.75 (m, 2H, $\text{OCH}_2\text{CO}-\text{O}$), 4.41-4.19 (m, 4H, OCH_2) 3.80-3.65 (m, 6H, $\text{OCH}_2\text{CH}_2\text{O}$), 2.30-2.21 (m, 4H, CH_2), 2.10-1.93 (m, 3H, CH_2), 1.70-1.50 (m, 12H, CH_2), 1.43-1.24 (m, 8H, $\text{OCH}_2\text{CH}_2\text{CH}_2\text{CH}_3$), 0.92-0.90 (t, 8H, $\text{OCH}_2\text{CH}_2\text{CH}_2\text{CH}_3$).

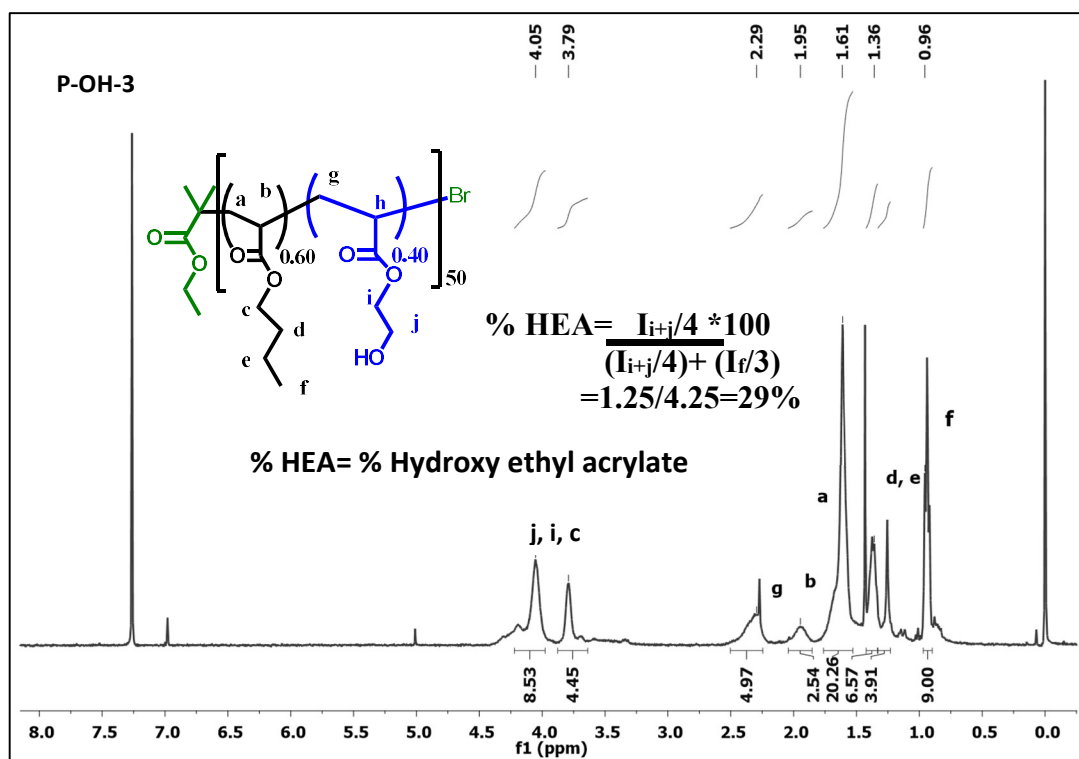
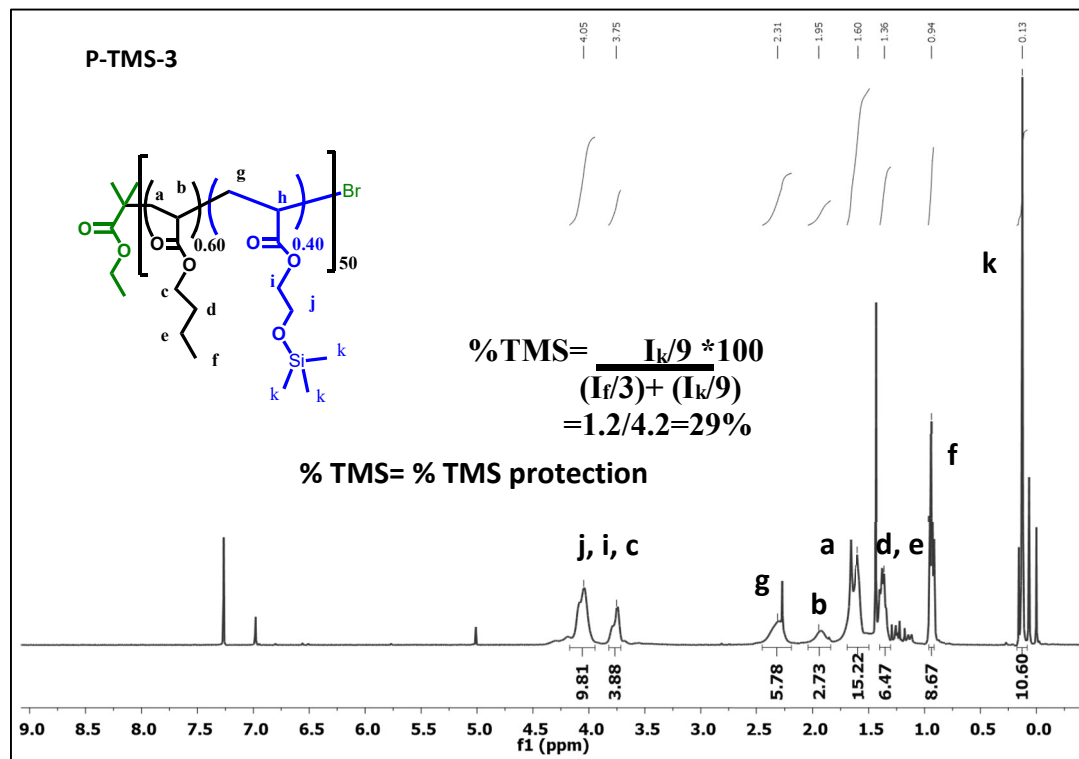
%Functionality = 28%. SEC analysis (THF, polystyrene standards): $M_n = 11009$ g/mol; $M_w/M_n = 1.23$.

Polymer P4: The solution of polymer **P-OH-4** in THF (5.1 μmol) was added to a stirred solution of coumarin carboxylic acid (CA) (316 μmol) with DPTS (75 μmol) and DIPC (450 μmol) under N_2 environment. The solution was stirred under N_2 environment at 25 °C for 48 hours. Precipitation from methanol-water (9:1) and subsequent drying under P_2O_5 in vacuum furnished the polymer **P4**. ^1H NMR (400 MHz, CDCl_3): δ (ppm) 7.60-7.55 (m, 1H, $>\text{C}=\text{CH-}$), 7.35-7.33 (m, 1H, $>\text{C}=\text{CH-}$), 6.85-6.80 (m, 2H, $=\text{CH}-\text{CH}=\text{C}-\text{CH}=\text{}$), 6.20-6.15 (m, 1H, $=\text{CH}-\text{CO}-\text{O-}$), 4.75-4.70 (m, 2H, $\text{OCH}_2\text{CO}-\text{O}$), 4.35-4.24 (m, 4H, $\text{OCH}_2\text{CH}_2\text{O}$) 3.98-3.90 (m, 9H, OCH_2), 2.24-2.20 (m, 7H, CH_2), 1.98-1.84 (m, 4H, CH_2), 1.53-1.50 (m, 15H, CH_2), 1.38-1.36 (m, 8H, $\text{OCH}_2\text{CH}_2\text{CH}_2\text{CH}_3$), 0.88-0.85 (t, 16H, $\text{OCH}_2\text{CH}_2\text{CH}_2\text{CH}_3$). %Functionality = 14%. SEC analysis (THF, polystyrene standards): $M_n = 22586$ g/mol; $M_w/M_n = 1.44$.

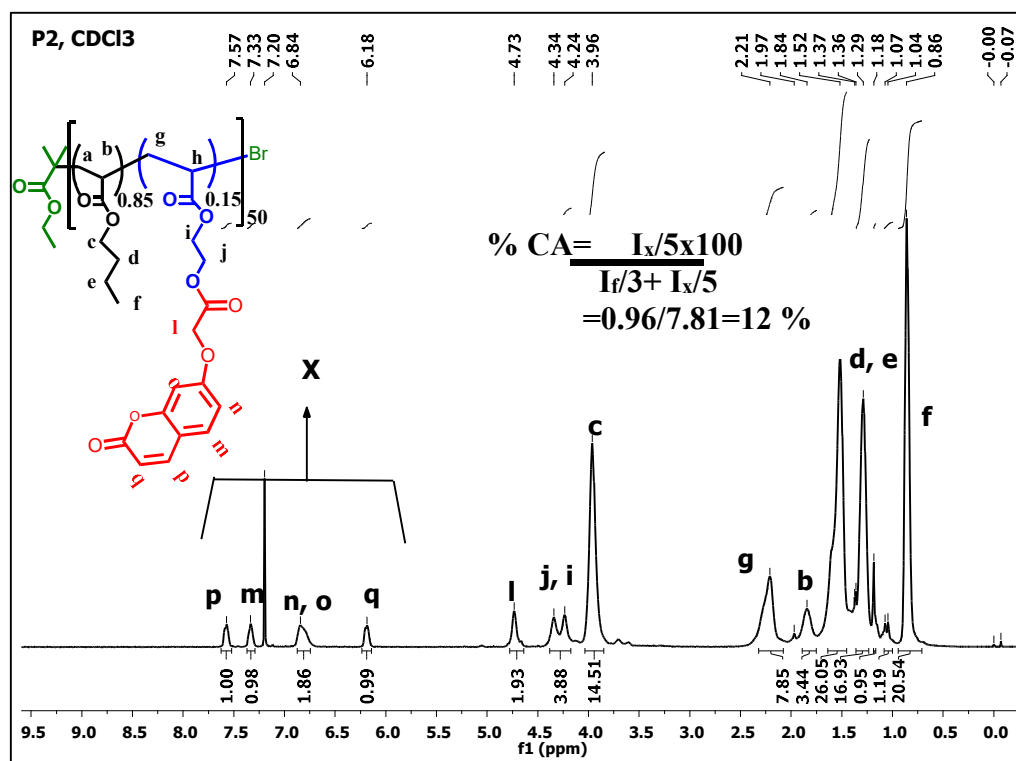
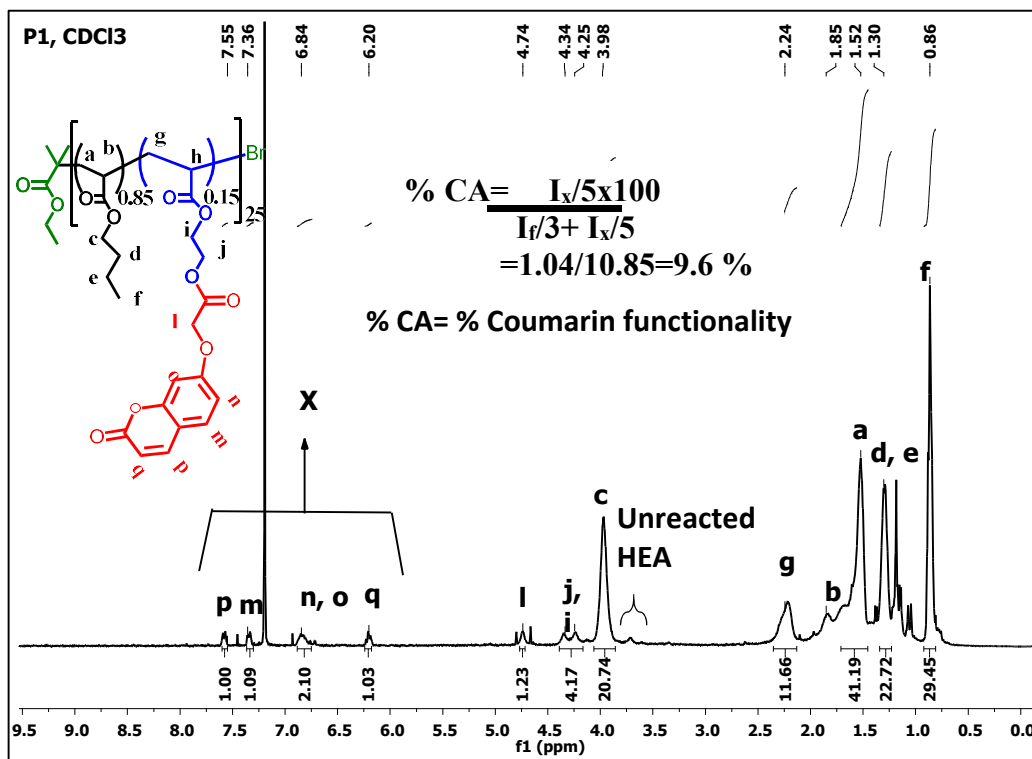
Polymer P5: The solution of polymer **P-OH-5** in THF (1.3 μmol) was added to a stirred solution of coumarin carboxylic acid (CA) (79 μmol) with DPTS (20 μmol) and DIPC (120 μmol) under N_2 environment. The solution was stirred under N_2 environment at 25 °C for 48 hours. Precipitation from methanol-water (9:1) and subsequent drying under P_2O_5 in vacuum furnished the polymer **P4**. ^1H NMR (400 MHz, CDCl_3): δ (ppm) 7.60-7.55 (m, 1H, $>\text{C}=\text{CH-}$), 7.35-7.33 (m, 1H, $>\text{C}=\text{CH-}$), 6.85-6.80 (m, 2H, $=\text{CH}-\text{CH}=\text{C}-\text{CH}=\text{}$), 6.20-6.15 (m, 1H, $=\text{CH}-\text{CO}-\text{O-}$), 4.75-4.70 (m, 5H, $\text{OCH}_2\text{CO}-\text{O}$), 4.35-4.24 (m, 7H, $\text{OCH}_2\text{CH}_2\text{O}$) 3.98-3.90 (m, 53H, OCH_2), 2.24-2.20 (m, 16H, CH_2), 1.98-1.84 (m, 41H, CH_2), 1.53-1.50 (m, 92H, CH_2), 1.38-1.36 (m, 33H, $\text{OCH}_2\text{CH}_2\text{CH}_2\text{CH}_3$), 0.88-0.85 (t, 69H, $\text{OCH}_2\text{CH}_2\text{CH}_2\text{CH}_3$). % Functionality = 4%. SEC analysis (THF, polystyrene standards): $M_n = 32453$ g/mol; $M_w/M_n = 1.47$.

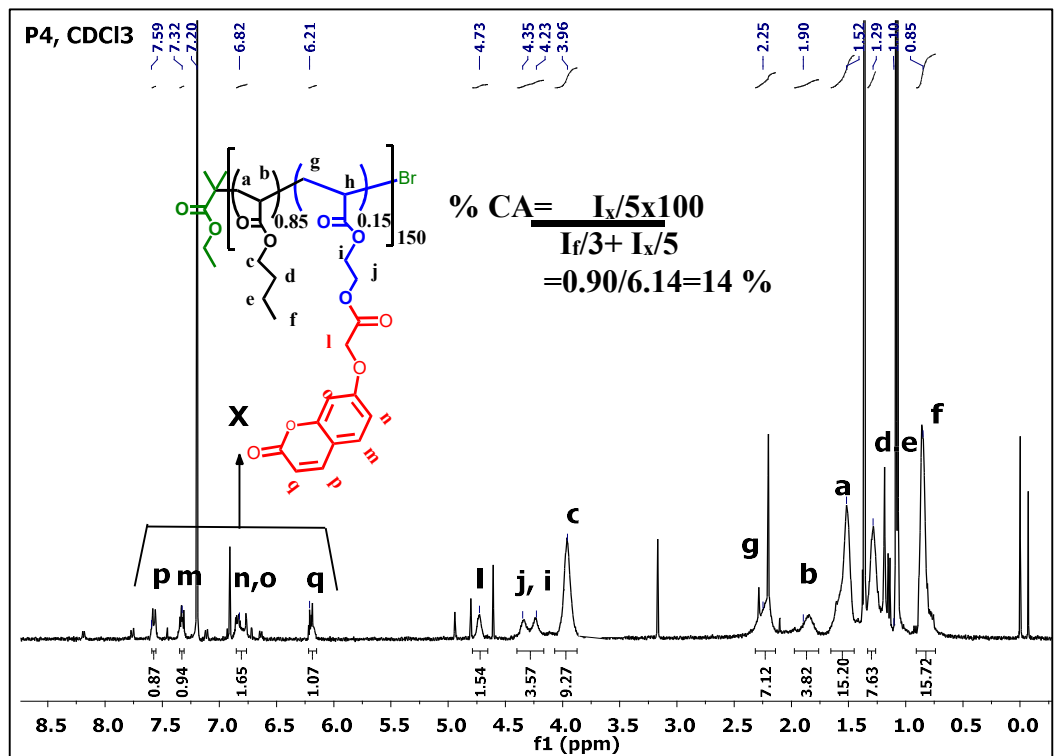
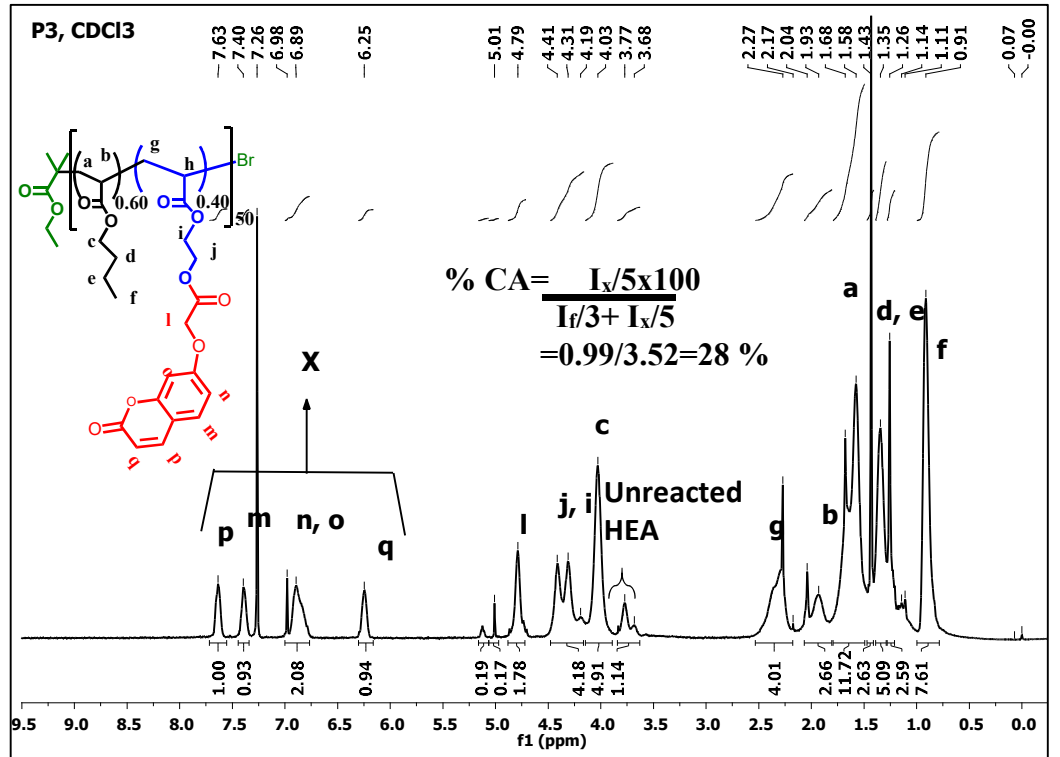
2.4.3.2. ¹H NMR characterization of polymers (CDCl₃, 400MHz)

a. Representative precursor polymers



b. Final polymers





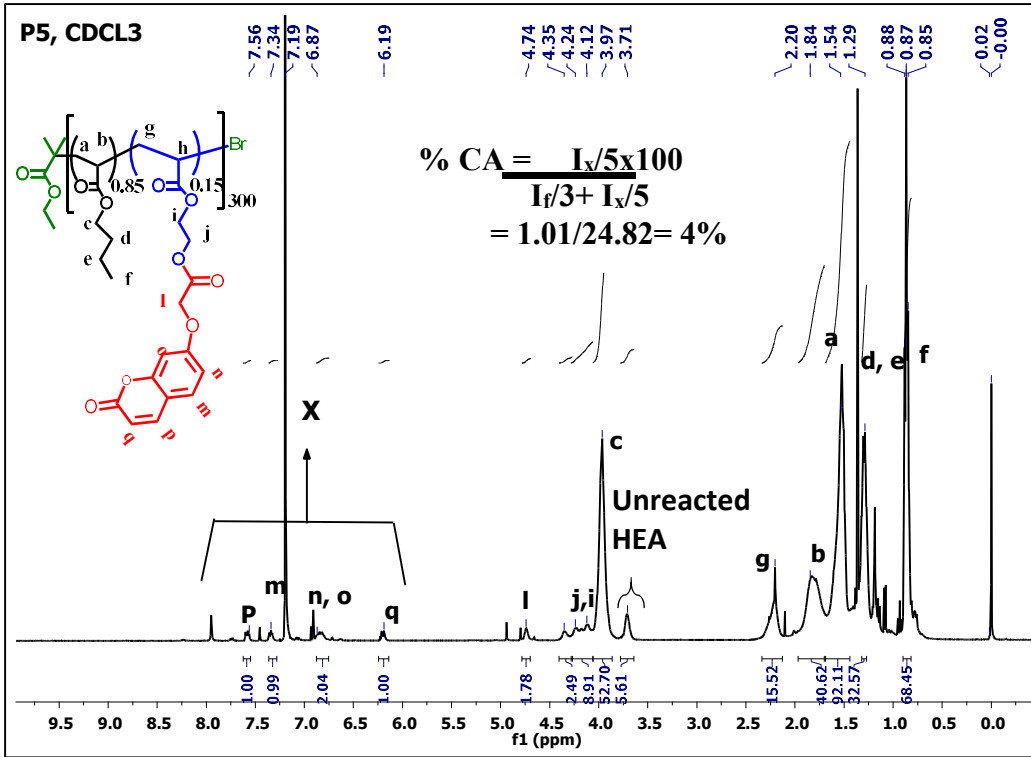


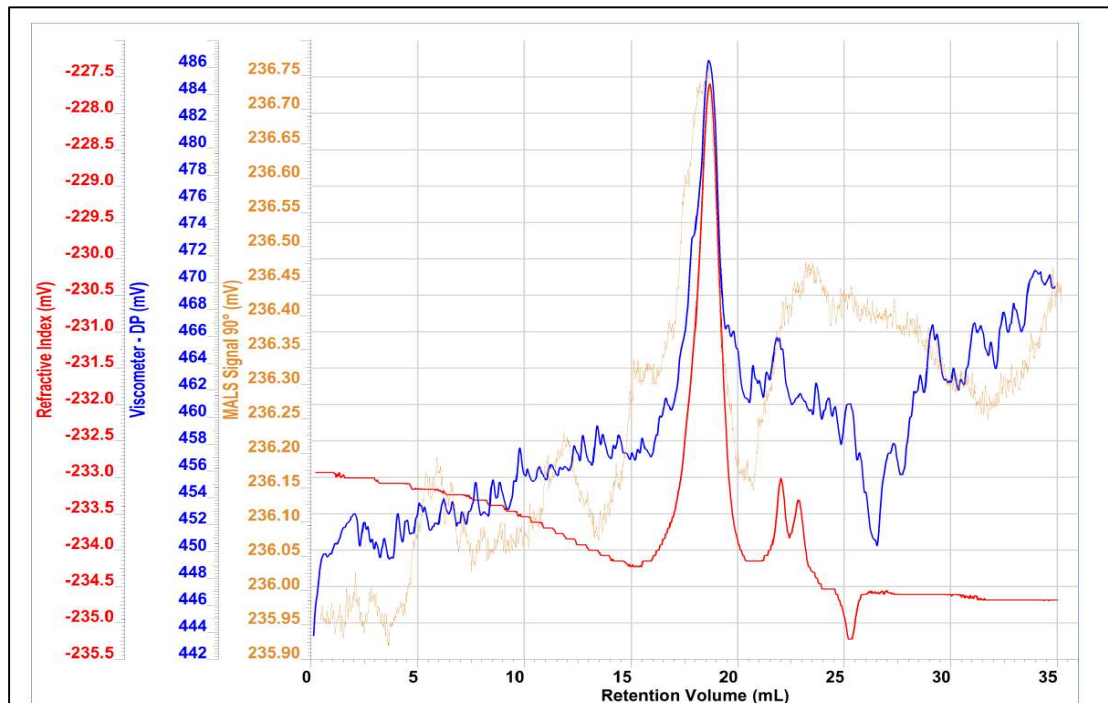
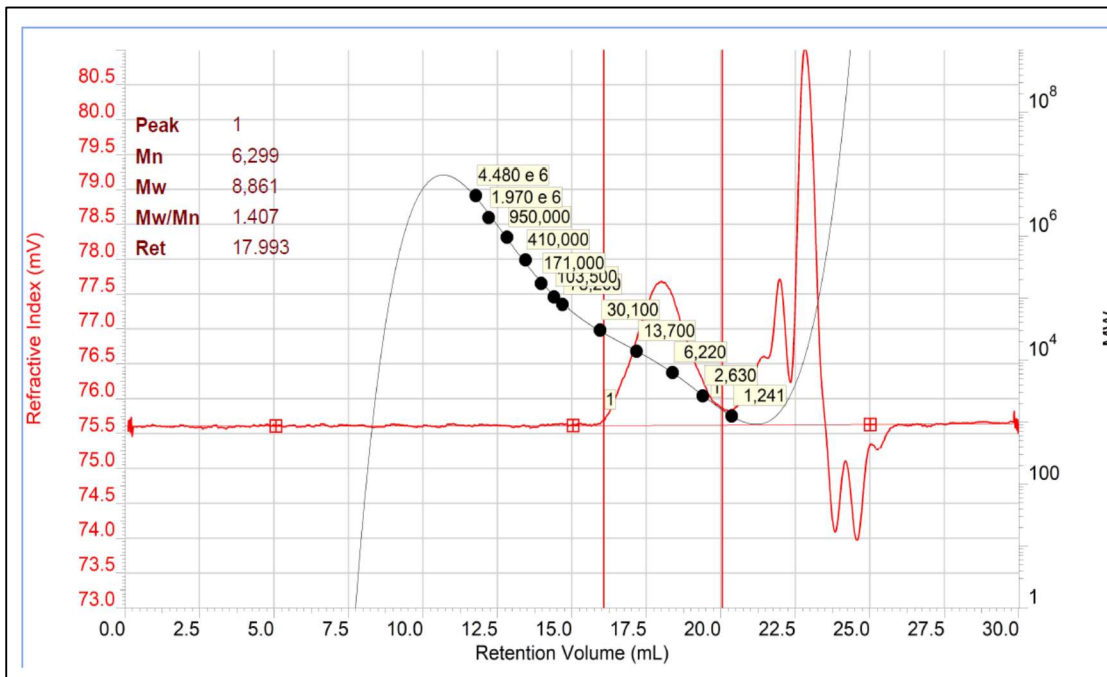
Table 2.5. Calculation of % functionality of polymers from integral area of ^1H NMR

TMS Protected	I_k	I_f	$I_k/9$	$I_f/3$	% TMS
P-TMS-1	2	6	0.22	2	10
P-TMS-2	10.8	28.5	1.2	9	12
P-TMS-3	10.8	9	1.2	3	29
P-TMS-4	2.5	5	0.28	1.6	15
P-TMS-5	2.5	6	0.27	2	12
After deprotection	I_{j+i}	I_f	$I_{j+i}/4$	$I_f/3$	% HEA
P-OH-1	1.3	8	0.32	2.67	10
P-OH-2	5	28.5	1.25	9.5	12
P-OH-3	5	9	1.25	3	29
P-OH-4	11	45	2.75	15	15
P-OH-5	10	55	2.5	18	12
Final polymers	I_x	I_f	$I_x/5$	$I_f/3$	% CA
P1	5.21	29.5	1.04	9.81	9.6
P2	5.73	20.5	0.96	6.83	12
P3	4.95	7.61	0.99	2.53	28
P4	4.53	15.7	0.90	5.24	14
P5	5.03	68.5	1	23.82	4

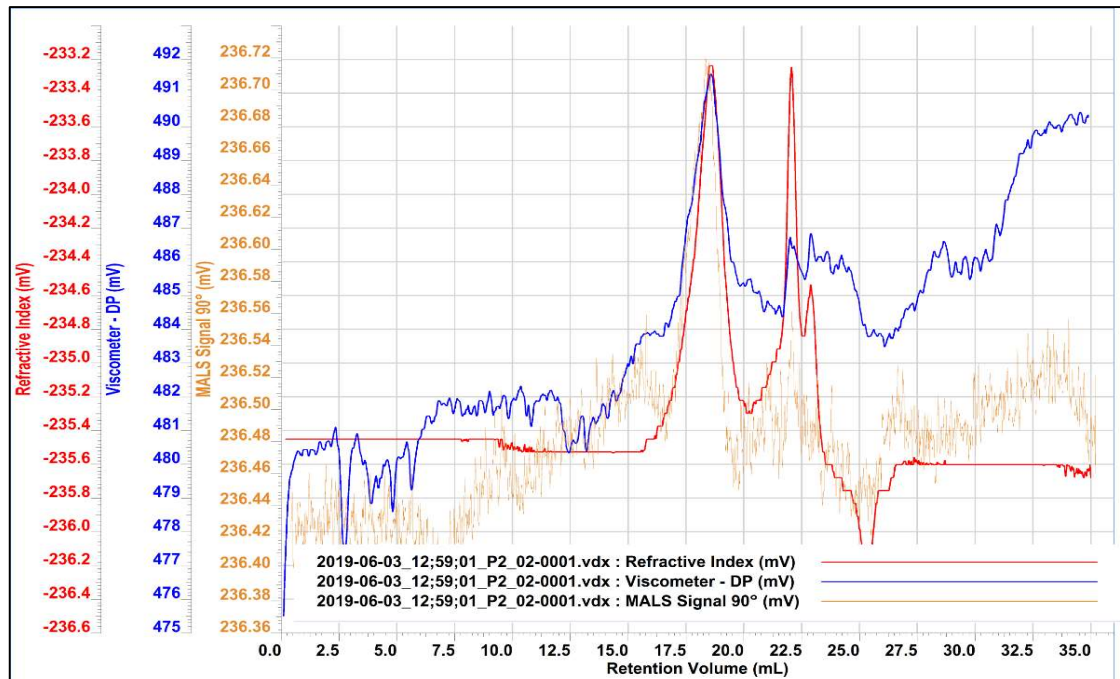
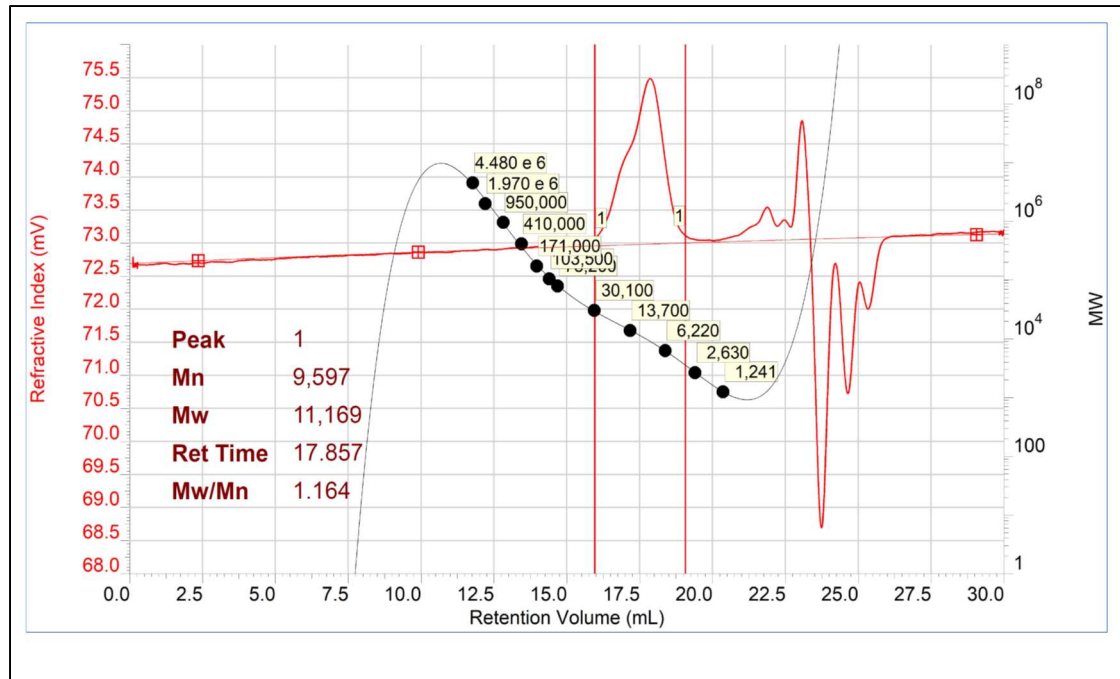
2.4.3.3. Size Exclusion Chromatography of the polymers

SEC measurement was performed on Malvern Viscotek instrument having RI, Right angle Light scattering (RALS), viscometer detector using T_{6000M}-T₃₀₀₀ column with THF as eluent at 35 °C at a flow rate of 1 mL/min. The results were analysed by using Omniseq software. The sample peaks were analysed for M_n , M_w , PDI , IV as well as R_H by means of conventional calibration as well as triple detector universal calibration using polystyrene standards. All the polymer samples were dissolved at a concentration of 5 mg/mL in THF and were shaking for 2-3 hours in order to ensure complete solubility of the polymers. The sample solution was then filtered through PTFE syringe while adding to the vial. 100 μL of the samples were injected and run at a flow rate of 1 mL/min for 35 min.

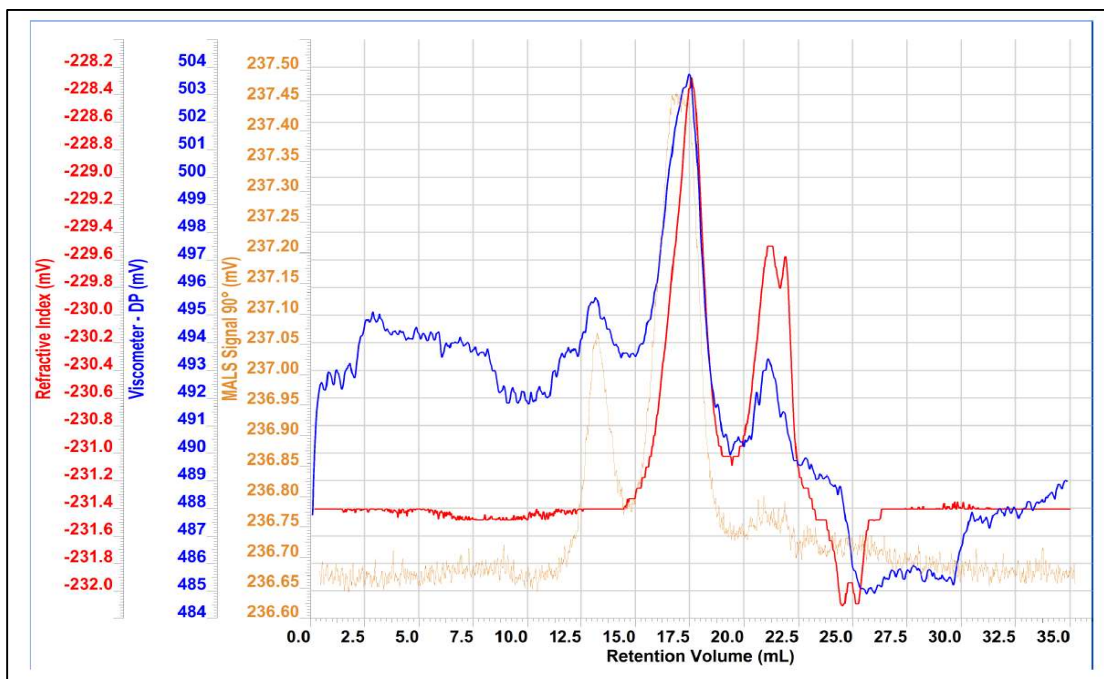
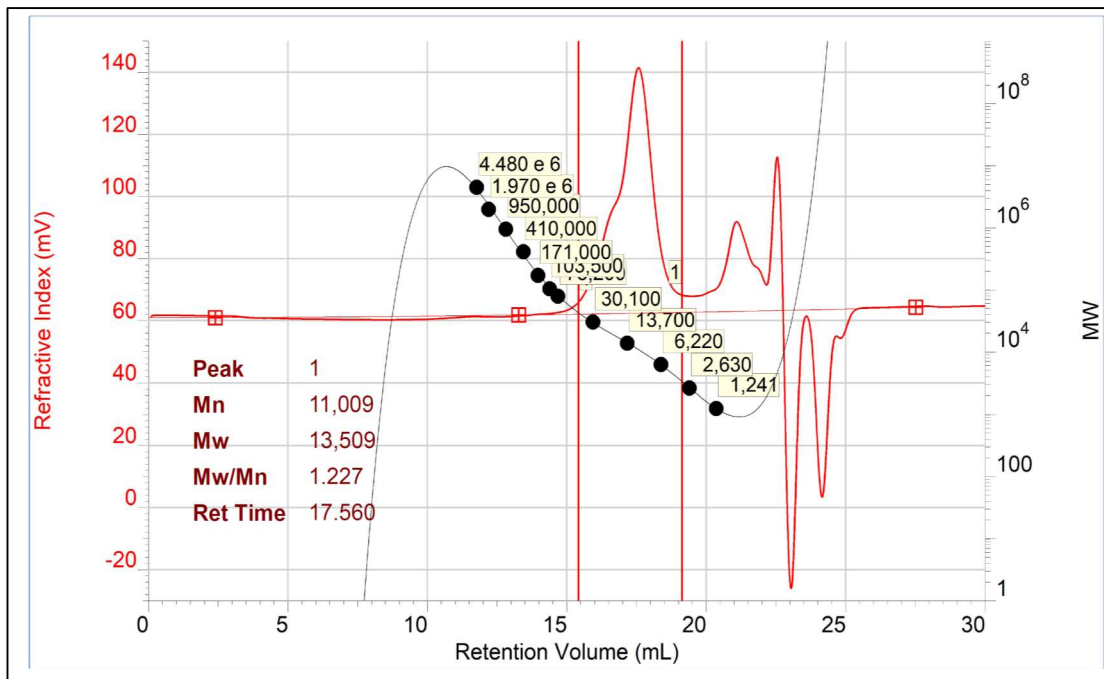
a. SEC curve of polymer P1:



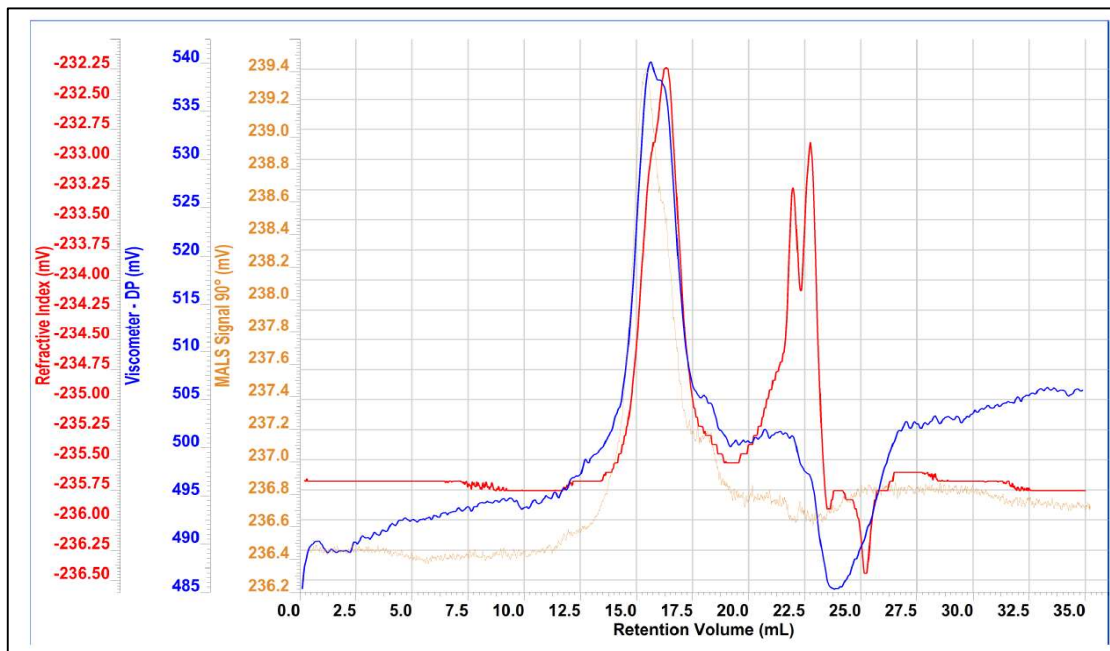
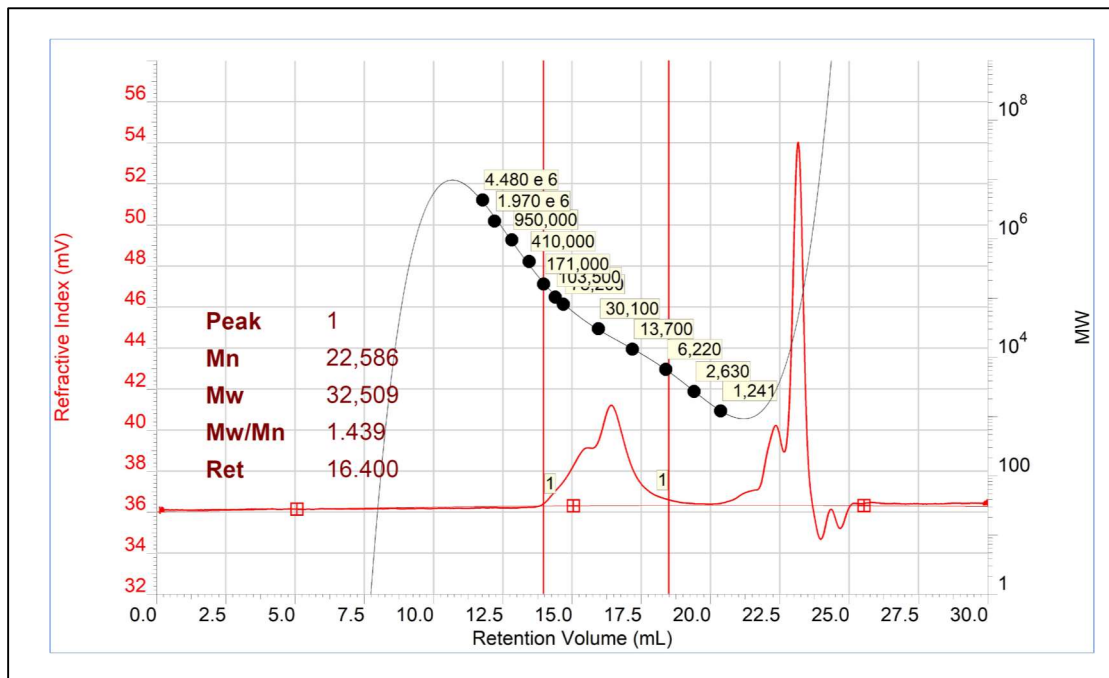
b. SEC curve of polymer P2:



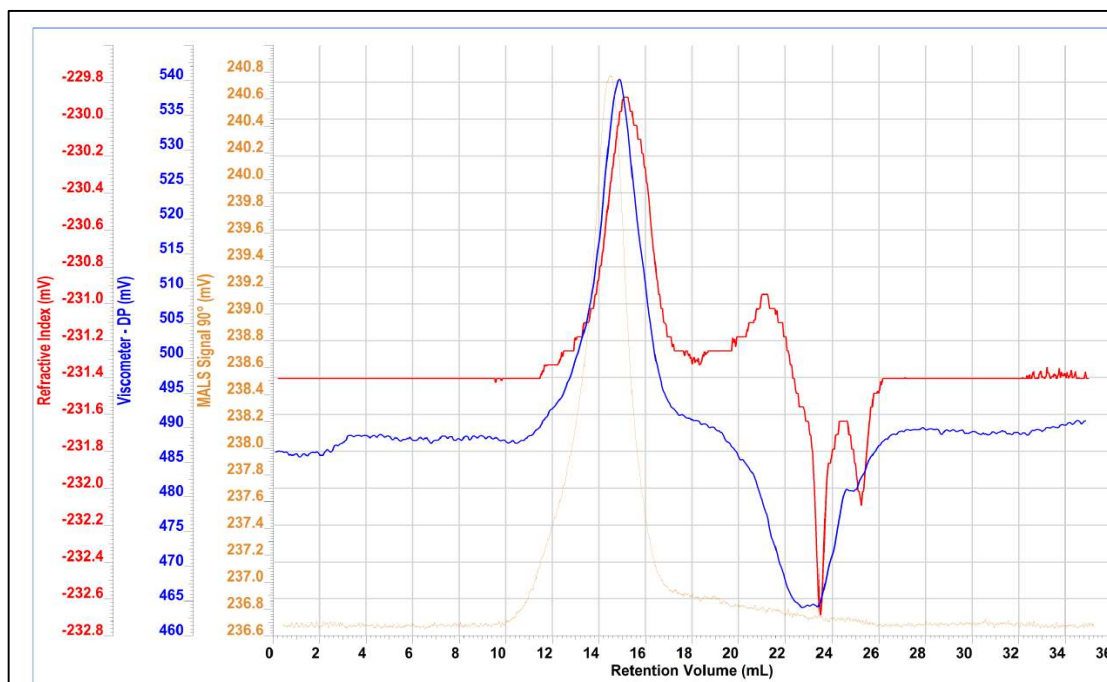
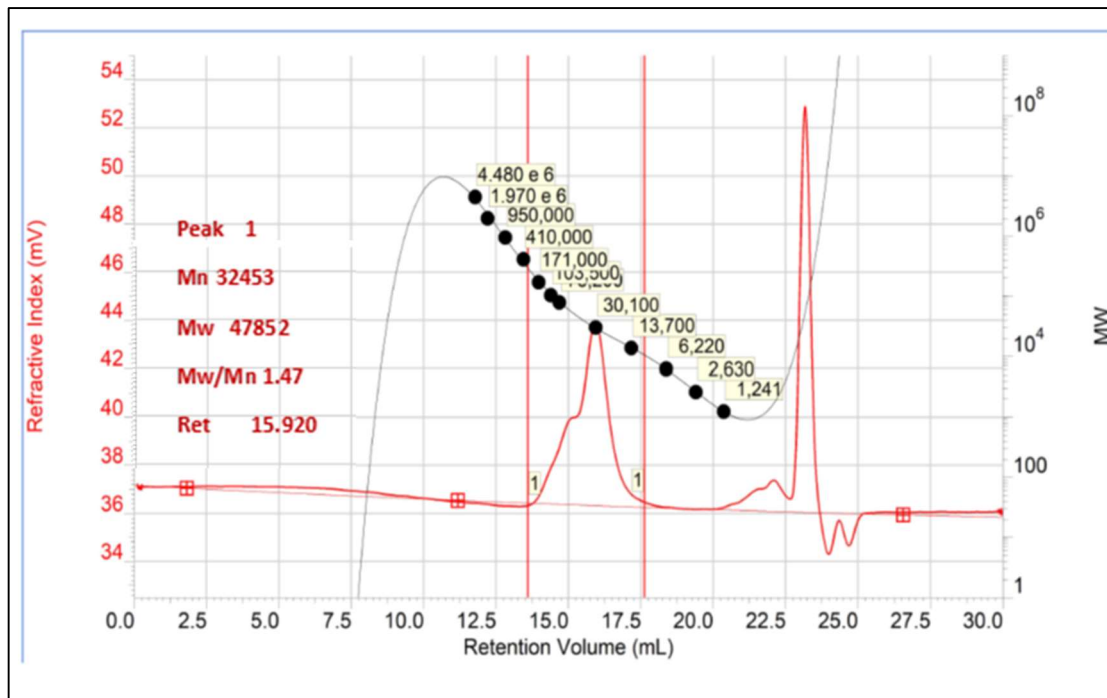
c. SEC curve of polymer P3:



d. SEC curve of polymer P4:



e. SEC curve of polymer P5:



2.4.3.4. Monitoring photodimerization by UV and ¹H-NMR: The polymers were dissolved in THF, CHCl₃ and DMF and monitored for a decrease in absorbance at 300 to 350 nm with an increase in exposure to UV_B irradiation at 320 nm with different time of exposure. Photodimerization Degree, $PD = (A_o - A_t)/A_o$, %PD = $(A_o - A_t)/A_o * 100$ where A_t is the absorbance at time t and A_o is initial absorbance. 1 mM solution of the polymer was prepared in CDCl₃ and ¹H NMR spectra was recorded. Further, the solution was exposed to UV_B irradiation in NMR tube and spectra were recorded at different time intervals (5h, 10, 15h). % Photodimerization degree (% PD) was calculated according to the formula $\% PD = \{(I_o - I_t)/I_o\} \times 100$, $I_t = I_{(p+q)}/I_{(m+n)}$, where I_{p+q} and I_{m+n} is the integral area of p, q, m, n protons, It is the ratio of integral area of $p+q$ with $m+n$ protons at a specific time of irradiation (t). I_o is the ratio of integral area of $p+q$ with $m+n$ protons for the native polymers.

2.4.3.5. Monitoring photodimerization by SEC: 100 μL of 6 mg/ml solution of **P2** in THF was injected and run at a flow rate of 1 mL/min using THF as eluent at 35 °C. The same sample was irradiated with UV_B light (2x8W) and was analysed by SEC after different times of irradiation (2, 4, 6, 8h). The SEC traces (normalised RALS signals) showed an increase in retention time corresponding to compaction of size of the polymer structure which directly corresponds to chain collapse due to photodimerization.

2.4.3.6. Monitoring chain collapse by DLS: Dynamic light scattering measurements were done on Malvern Zetasizer Nano ZS ZEN3600 equipped with a Helium-Neon laser (wavelength, $\lambda = 633$ nm with backscattering angle of 173°. 6 mg/mL solution of **P1-P5** in THF (2 mL) and was filtered through a 0.2 μm PTFE-filter in a glass cuvette with a path length of 1 cm. The same samples were irradiated with UV_B light (2x8W) and were analysed by DLS after 4 h of irradiation.

2.4.3.7. Microscopic analysis: 10 μL of the diluted samples (10⁻⁴ mg/mL) were drop-casted on silicon wafer followed by washing with the same solvent and dried overnight. AFM height images were recorded by tapping mode on a Bruker Multimode 8 scanning probe microscope with silicon cantilever (Bruker) and analysed using the software NanoScope

Analysis 1.5. The size distributions of the nanoparticles were analyzed using image-J software, from the U.S. National Institutes of Health. 50 random nanoparticles were selected from different areas of the images and a histogram was generated by choosing bin and frequency in Microsoft Excel. The number average radius (R_n), weight average radius (R_w), and PDI were estimated by using the equation. 1-3, where N_i is the number of nanoparticles of radius R_i and n is the number of nanoparticles examined in each sample.

$$R_w = \frac{\sum_{i=1}^n N_i R_i^2}{\sum_{i=1}^n N_i R_i} \quad (1), \quad R_n = \frac{\sum_{i=1}^n N_i R_i}{\sum_{i=1}^n N_i} \quad (2), \quad PDI = \frac{R_w}{R_n} \quad (3)$$

2.4.3.8. Thermal studies by Differential Scanning Calorimetry: Thermal studies of polymer samples were performed on Perkin Elmer Differential Scanning Calorimeter DSC 8000 model and the samples were heated from -80 to 150 °C at a heating rate of 10 °C. Thermal studies of the dried polymer films were analyzed for the glass transition temperature (T_g) that corresponds to the chain mobility of the polymer. Dried polymer film which was drop casted on a glass substrate was crosslinked by exposure to UV_B irradiation at ($\lambda_{\max} = 320$ nm, 2 x 8 Watt UV_B lamp) for 15h (84 J cm⁻²). Further, the crosslinked sample was exposed to UV_C irradiation ($\lambda_{\max} = 254$ nm, 2 x 8 Watt UV_C lamp) for 5 h (15 J cm⁻²) and decrosslinked.

2.4.3.9. Self-healing studies: Polymer solution (20 mg/mL) was drop-casted on a glass substrate and dried overnight. The cut was made at a micron level with a surgical knife and investigated for self-healing with the aid of a bright field microscope. Further, the polymer films were exposed to UV_B irradiation and crosslinked which showed delayed and incomplete healing of the scratches. Interestingly, UV_C irradiation upon the crosslinked polymer film photo-trigger the switch on the self-healing behavior of the scratches mediated by [2+2] decycloaddition of the coumarin moieties. The damage recovery was estimated from the % healing efficiency, a ratio of change in the cut width and initial cut width. The average width of the scratches was determined using image-J software with taking 10 random cut width from different areas of the cut. The average width (W_n), percentage

healing efficiency (% H) was calculated using eqn. 4-5, where N_i is the number of width, W_i width at position n .

$$W_n = \frac{\sum_{i=1}^n (N_i W_i)}{\sum_{i=1}^n N_i} \quad (4)$$

$$\% H = \frac{W_{\text{initial}} - W_{\text{healed}}}{W_{\text{initial}}} \quad (5)$$

2.5. References

- 1 M. Diba, S. Spaans, K. Ning, B. D. Ippel, F. Yang, B. Loomans, P. Y. W. Dankers and S. C. G. Leeuwenburgh, *Adv. Mat. Inter.*, 2018, **5**, 1–21.
- 2 A. B. W. Brochu, S. L. Craig and W. M. Reichert, *J. Biomed. Mat. Res. Part A*, 2011, **96 A**, 492–506.
- 3 F. Vermolen, M. W. G. van Rossum, E. J. Perez and J. Adam, in *Self Healing Materials An Alternative Approach to 20 Centuries of Materials Science*, ed. S. van der Zwaag, 2007, vol. 100, pp. 337–363.
- 4 J. P. Joseph, A. Singh and A. Pal, in *Smart Polymer Nanocomposites Energy Harvesting, Self-Healing and Shape Memory Applications*, ed. M. A. A. Ponnamma, D., Sadasivuni, K.K., Cabibihan, J.-J., Al-Maadeed, Springer, 2017, pp. 181–218.
- 5 S. Roy, A. Baral and A. Banerjee, *Chem. Eur. J.*, 2013, **19**, 14950–14957.
- 6 V. K. Thakur and M. R. Kessler, *Polymer*, 2015, **69**, 369–383.
- 7 K. S. Toohey, N. R. Sottos, J. A. Lewis, J. S. Moore and S. R. White, *Nat. Mater.*, 2007, **6**, 581–585.
- 8 S. R. White, N. R. Sottos, P. H. Geubelle, J. S. Moore, M. R. Kessler, S. R. Sriram, E. N. Brown and S. Viswanathan, *Nature*, 2001, **409**, 794–797.
- 9 S. Banerjee, R. Tripathy, D. Cozzens, T. Nagy, S. Keki, M. Zsuga and R. Faust, *ACS Appl. Mater. Interfaces*, 2015, **7**, 2064–2072.
- 10 A. Lorenz, A. Senne, J. Rohde, S. Kroh, M. Wittenberg, K. Krüger, F. Clement and D. Biro, *Energy Procedia*, 2015, **67**, 126–137.
- 11 B. K. Ahn, D. W. Lee, J. N. Israelachvili and J. H. Waite, *Nat. Mater.*, 2014, **13**, 867–872.
- 12 C. Wang, H. Wu, Z. Chen, M. T. Mcdowell, Y. Cui and Z. Bao, *Nat. Chem.*, 2013, **5**, 1042–1048.
- 13 A. Faghihnejad, K. E. Feldman, J. Yu, M. V. Tirrell, J. N. Israelachvili, C. J. Hawker, E. J. Kramer and H. Zeng, *Adv. Funct. Mater.*, 2014, **24**, 2322–2333.
- 14 A. Vidyasagar, K. Handore and K. M. Sureshan, *Angew. Chem. Int. Ed.*, 2011, **50**, 8021–8024.
- 15 T. W. Chuo, T. C. Wei and Y. L. Liu, *J. Pol. Sci., Part A: Pol. Chem.*, 2013, **51**, 3395–3403.
- 16 M. Nakahata, Y. Takashima, H. Yamaguchi and A. Harada, *Nat. Commun.*, 2011, **2**, 511–516.
- 17 X. Yang, H. Yu, L. Wang, R. Tong, M. Akram, Y. Chen and X. Zhai, *Soft Matter*,

- 2015, **11**, 1242–1252.
- 18 B. Sharma, A. Singh, T. K. Sarma, N. Sardana and A. Pal, *New J. Chem.*, 2018, **42**, 6427–6432.
- 19 S. Hou and P. X. Ma, *Chem. mater.*, 2015, **27**, 7627–7635.
- 20 S. Bode, L. Zedler, F. H. Schacher, B. Dietzek, M. Schmitt, J. Popp, M. D. Hager and U. S. Schubert, *Adv. Funct. Mater.*, 2013, **25**, 1634–1638.
- 21 Q. Wang, J. L. Mynar, M. Yoshida, E. Lee, M. Lee, K. Okuro, K. Kinbara and T. Aida, *Nature*, 2010, **463**, 339–343.
- 22 H. Gong, Y. Gao, S. Jiang and F. Sun, *ACS Appl. Mater. Interfaces*, 2018, **10**, 26694–26704.
- 23 S. Burattini, H. M. Colquhoun, B. W. Greenland and W. Hayes, *Faraday Discuss.*, 2009, **143**, 251–264.
- 24 M. R. Hansen, R. Graf, S. Sekharan and D. Sebastiani, *J. Am. Chem. Soc.*, 2009, **131**, 5251–5256.
- 25 T. Maeda, H. Otsuka and A. Takahara, *Prog. Polym. Sci.*, 2009, **34**, 581–604.
- 26 N. Roy, E. Buhler and J. M. Lehn, *Poly. Int.*, 2014, **63**, 1400–1405.
- 27 H. P. Wang, Y. C. Yuan, M. Z. Rong and M. Q. Zhang, *Macromolecules*, 2010, **43**, 595–598.
- 28 Y. Chen, A. M. Kushner, G. A. Williams and Z. Guan, *Nat. Chem.*, 2012, **4**, 467–472.
- 29 H. Kautz, D. J. M. Van Beek, R. P. Sijbesma and E. W. Meijer, *Macromolecules*, 2006, **39**, 4265–4267.
- 30 N. B. Pramanik, G. B. Nando and N. K. Singha, *Polymer*, 2015, **69**, 349–356.
- 31 J. Kötteritzsch, M. D. Hager and U. S. Schubert, *Polymer*, 2015, **69**, 321–329.
- 32 O. Altintas, J. Willenbacher, K. N. R. Wuest, K. K. Oehlenschlaeger, P. Krolla-Sidenstein, H. Gliemann and C. Barner-Kowollik, *Macromolecules*, 2013, **46**, 8092–8101.
- 33 S. R. Trenor, A. R. Shultz, B. J. Love and T. E. Long, *Chem. Rev.*, 2004, **104**, 3059–3077.
- 34 G. Kaur, P. Johnston and K. Saito, *Polym. Chem.*, 2014, **5**, 2171–2186.
- 35 J. P. Joseph, A. Singh, D. Gupta, C. Miglani and A. Pal, *ACS Appl. Mater. Interfaces*, 2019, **11**, 28213–28220.
- 36 Y. Inaki and H. Hiratsuka, *J. Photopolym. Sci. Technol.*, 2000, **13**, 739–744.
- 37 J. A. Kaitz, C. M. Possanza, Y. Song, C. E. Diesendruck, A. J. H. Spiering, E. W. Meijer and J. S. Moore, *Polym. Chem.*, 2014, **5**, 3788–3794.
- 38 S. Mavila, O. Eivgi, I. Berkovich and N. G. Lemcoff, *Chem. Rev.*, 2016, **116**, 878–961.
- 39 T. Mes, R. van der Weegen, A. R. A. Palmans and E. W. Meijer, *Angew. Chem. Int. Ed.*, 2011, **123**, 5191–5195.
- 40 M. A. J. Gillissen, T. Terashima, E. W. Meijer, A. R. A. Palmans and I. K. Voets, *Macromolecules*, 2013, **46**, 4120–4125.
- 41 E. A. Appel, J. Dyson, J. del Barrio, Z. Walsh and O. A. Scherman, *Angew. Chem. Int. Ed.*, 2012, **124**, 4261–4265.
- 42 E. Harth, B. Van Horn, V. Y. Lee, D. S. Germack, C. P. Gonzales, R. D. Miller and C. J. Hawker, *J. Am. Chem. Soc.*, 2002, **124**, 8653–8660.
- 43 N. Wedler-Jasinski, T. Lueckerath, H. Mutlu, A. S. Goldmann, A. Walther, M. H.

- Stenzel and C. Barner-Kowollik, *Chem. Comm.*, 2017, **53**, 157–160.
- 44 N. Hosono, A. M. Kushner, J. Chung, A. R. A. Palmans, Z. Guan and E. W. Meijer, *J. Am. Chem. Soc.*, 2015, **137**, 6880–6888.
- 45 K. Matyjaszewski, *Macromol. Symp.*, 1996, **111**, 47–61.
- 46 A. Mühlebach, S. G. Gaynor and K. Matyjaszewski, *Macromolecules*, 1998, **31**, 6046–6052.
- 47 J. A. Pomposo, J. Rubio-Cervilla, A. J. Moreno, F. Lo Verso, P. Bacova, A. Arbe and J. Colmenero, *Macromolecules*, 2017, **50**, 1732–1739.
- 48 J. A. Pomposo, I. Perez-Baena, F. Lo Verso, A. J. Moreno, A. Arbe and J. Colmenero, *ACS Macro Lett.*, 2014, **3**, 767–772.
- 49 C.M. Hansen, in *Paint Testing Manual*, ed. J. V. Koleske, 1995, pp. 383–404.
- 50 C. M. Hansen and K. Skaarup, *J. Paint Tech.*, 1967, **39**, 511–514.
- 51 Y. Yang, P. Chen, Y. Cao, Z. Huang, G. Zhu, Z. Xu, X. Dai, S. Chen, B. Miao and L. T. Yan, *Langmuir*, 2018, **34**, 9477–9488.
- 52 Z. Huang, C. Lu, B. Dong, G. Xu, C. Ji, K. Zhao and L. T. Yan, *Nanoscale*, 2016, **8**, 1024–1032.
- 53 N. Barooah, B. C. Pemberton, A. C. Johnson and J. Sivaguru, *Photochemi. and Photobiol. Sci.*, 2008, **7**, 1473–1479.
- 54 G. S. Hammond, C. A. Stout and A. A. Lamola, *J. Am. Chem. Soc.*, 1964, **86**, 3103–3106.
- 55 E. E. Gürel, N. Kayaman, B. M. Baysal and F. E. Karasz, *J. Polym. Sci., Polym. Phys.*, 1999, **37**, 2253–2260.
- 56 S. Piçarra, J. Duhamel, A. Fedorov and J. M. G. Martinho, *J. Phys. Chem. B*, 2004, **108**, 12009–12015.
- 57 E. B. Berda, E. J. Foster and E. W. Meijer, *Macromolecules*, 2010, **43**, 1430–1437.
- 58 D. Hu, J. Yu, K. Wong, B. Bagchl, P. J. Rossky and P. F. Barbara, *Nature*, 2000, **405**, 1030–1033.
- 59 A. Y. Grosberg and D. V. Kuznetsov, *Macromolecules*, 1992, **25**, 1970–1979.
60. W. L. F. Armarego, D. D. Perrin, Purification of laboratory chemicals (4th edition), Butterworth - Hienemann educational and professional publishing ltd, 1996, pp. 15-16.
61. J. Moore, S. Stupp, *Macromolecules* 1990, **23**, 65–70.
62. H. Gao, Y. Tang, Z. Hu, Q. Guan, X. Shi, F. Zhu, Q. Wu, *Polym. Chem.*, 2013, **4**, 1107-1114.
63. R. H. Huyck , S. R. Trenor , B. J. Love, T. E. Long, *J. Macromol. Sci., Part A: Pure and Applied Chem*, 2008, **40**, 9-15.
64. N. Hosono, A. M. Kushner, J. Chung, A. R. Palmans, Z. Guan, E. W. Meijer, *J. Am. Chem. Soc.* 2015, **137**, 6880-6888.

Chapter 3

Delineating Synchronized Control of Dynamic Covalent and Non-Covalent Interactions for Polymer Chain Collapse towards Cargo Localization and Delivery

*In this chapter, water-soluble and thermo-responsive polyacrylamide polymers **CPI-2** with photodimerizable coumarin moieties grafted in the backbone are employed to design single chain polymers. The chain collapse to polymeric nanoparticles can be efficiently controlled using dual response strategies involving photodimerization under UV_B light ($\lambda_{max} = 320$ nm) as well as host-guest interaction by addition of **bis- β -CD** host. The aggregation of the nanoparticles is controlled by the interplay of lower critical solution temperatures (LCST) that can be tuned as a result of photodimerization and host-guest interaction. Further, sequential folding of the polymers is demonstrated by the addition of the host molecule followed by exposure to UV_B irradiation. Such multi-stimuli-responsive compaction of size with synergistic control of non-covalent and dynamic covalent interaction and tuning of LCST render the system suitable for compartmental loading and sustainable/burst release of hydrophilic and hydrophobic cargos e.g. rhodamine B dye and ibuprofen drug under homeostasis control.*

3.1. Introduction

Functional polymer nanoparticles have fascinated scientists owing to their immense applications in nanomedicine especially in drug delivery, sensing, and imaging.¹⁻³ However, contemporary polymeric micellar drug or cargo delivery systems suffer from several drawbacks such as uncontrolled loading, lack of suitable stimuli-switch to control release to attain a stasis control.⁴⁻⁶ Lack of such attributes in the drug delivery system leads to the supply of inefficient cargo at target sites leading to possible burst release toxicity or restricted efficiency of the approach. In addition, preparing well-distinct polymeric nanoparticles with sizes under 20 nm has remained quite challenging to date. In recent years, single chain nanoparticles (NPs) have found growing interest due to their small and controllable size (2–20 nm) leading to unique applications in drug delivery especially, with regard to crossing blood-brain-barriers and responsive nano-compartmental system.⁷⁻¹⁰ Such systems are designed by compacting polymer chain into a nanoparticle *via* unimolecular coil-to-particle transition through intrachain crosslinking employing dynamic covalent and non-covalent associations *e.g.* hydrogen bonding,^{11,12} Diels–Alder reaction,^{13,14} metal complexation,^{15,16} “click” chemistry¹⁷, and host-guest interactions.^{18,19} Noticeably, the size of NPs can be efficiently tuned by the choice of chain length, functionality loading of the polymers by means of controlled radical polymerization *e.g.* ATRP, RAFT, *etc.*²⁰⁻²²

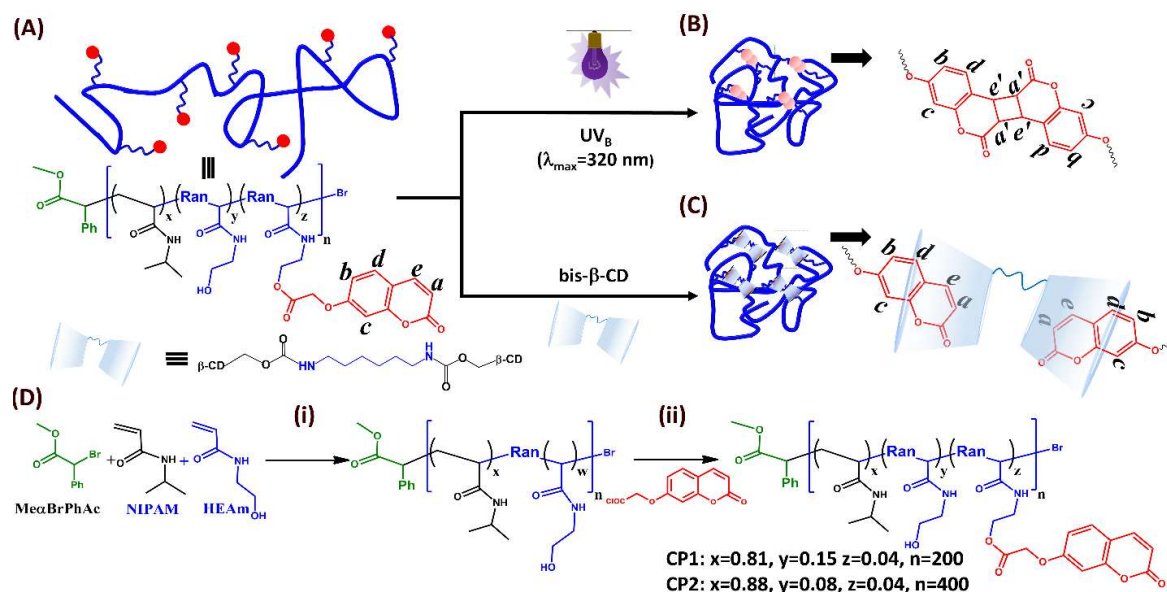
Additionally, the introduction of stimuli-responsiveness in the functional polymers *via* light, chemical environment, temperature, *etc.* exhibit further control over size and shape *via* well-ordered chain collapse.^{23,24} Among the external stimuli, light has emerged as an excellent tool for *in situ* chemical manipulation due to its efficient local application in confined space and high spatiotemporal resolution aided by the regulation of wavelength and intensity.^{25,26} Moreover, the intricacy of the photo-trigger can be improved by using a chromophore moiety that is susceptible to multiple interactions thereby, leading to a synergistic effect over the stimuli responses. Therefore, combining dynamic covalent chemistry *e.g.* reversible photodimerization in tandem with non-covalent interactions like host-guest interaction can be an interesting strategy for exploring synergistic interaction.^{27,28} In that regard, coumarin moiety is an excellent candidate that forms [2+2] cycloadducts by

reversible photodimerization and undergoes host-guest complexation with β -cyclodextrin moieties.²⁹⁻³¹ However, reports of such synergistic multiple control leading to controllable chain collapse and consequent nanostructures are rather scarce in the literature. Recently, we have reported a coumarin tethered peptide amphiphile that self-assembles to form 1D fibers that transformed into 2D nanosheet mediated by host-guest inclusion complex.³² Such photo-responsive chain collapse of coumarin functionalized polymer to form flexo-rigid polymer network was also exploited to modulate the self-healing behavior.²¹

Polymeric nanoparticles formed by stimuli-responsive chain collapse may offer a better cargo delivery vehicle with well constricted hydrophobic pockets sandwiched by hydrophilic sidechain regulating hydrodynamic size, affinity, stability and capability for self-assembly in its aqueous environment to form hierarchical structures.³³⁻³⁵ However, low efficiency in loading and lack of stimuli-responsiveness in drug release have hitherto limited the efficiency of NPs to deliver cargos and accomplish control over release under ambient conditions.³⁶⁻³⁸ Additionally, thermo-responsive polymers such as PNIPAM (poly-N-Isopropyl acrylamide), polyethylene glycol *etc.* exhibit abrupt changes in properties upon a modest change in temperature owing to the temperature induced hydrophilic to hydrophobic transition of the polymer backbone.³⁹⁻⁴³ Such property exploited for designing smart drug delivery systems enables the nanoparticles to be an efficient stimuli-responsive sustained release cargo vehicle to accomplish a therapeutic effect.¹⁸ Recently, Cheng *et. al.* demonstrated temperature and pH induced release of 5-Fluorouracil (5-FU) drug from SCPN system containing hydrogen bonding interaction.⁴⁴

Herein, we postulate a unique design of coumarin functionalized water-soluble polymer system that is suitable for multiple covalent and non-covalent interactions and render synergistic control over the tuning size of resultant NPs. Thus, random copolymers of thermo-responsive NIPAM and water-soluble HEAm (hydroxy ethyl acrylamide) with pendant coumarin moieties in the side chain are envisaged for dual control over chain collapse *via* light irradiation and host molecule addition (Scheme 3.1A). The intra-chain collapse of the polymers mediated by the homomolecular photodimerization of coumarin and host-guest complexations with **bis- β -CD** renders nanoparticles (Scheme 3.1B-C). Such multi-stimuli control over the size of the nanoparticle was utilized to demonstrate sequential

folding and defolding resulting in multiple swellable states of the nanoparticles. The thermo-responsive NIPAM copolymer imparts temperature-induced hydrophilic to hydrophobic transition above LCST to result in aggregation. Further, the system was utilized for localization and delivery of hydrophilic rhodamine B dye and hydrophobic ibuprofen drug that show differential release profiles based on the extent of compartmentalization due to chain collapse. As far as our knowledge, this is the first report of multi-stimuli control in polymer chain collapse to NPs and their utilization for cargo delivery.



Scheme 3.1. Multiple strategies to result in chain collapse of coumarin appended polymer systems. (A) Cartoon representation of single chain polymers with detailed chemical structures. Homomolecular chain collapse resulting in single chain polymeric nanoparticle (NPs) mediated by (B) UV_B irradiation ($\lambda_{\text{max}} = 320 \text{ nm}$) and (C) host-guest complexation with bis- β -CD. (D) Scheme for the synthesis of coumarin functionalized polymers CP1-2: (i) CuCl/Me₆TREN, EtOH: water (1:1), RT, 24 h, N₂. (ii) Et₃N, THF, 25 °C, 48 h, N₂.

3.2. Result and Discussion

3.2.1 Design and Characterization of Random Co-polymers.: The functional random copolymers were synthesized by controlled living atom transfer radical polymerization (ATRP) followed by tethering the coumarin units (Scheme 3.1D). Different random copolymers **P1-2** having NIPAM along with HEAm were synthesized by varying the initiator to monomer ratio followed by functionalization with coumarin moiety to result in

CP1-2 polymers. The formation of the coumarin tethered polymers was confirmed by the characteristic ^1H NMR peaks of the coumarin groups at δ 7.95, 7.59, 6.89, 6.29 ppm that indicated the incorporation of the functional moieties into the polymer side chains (see *Exp. sec.* 3.4.2.3). Size exclusion chromatographic (SEC) analyses indicated the control over the molecular weight of the polymers with reasonably good polydispersity indices (PDI). Table 3.1 summarizes the characteristic details of the native polymers including the percentage grafting as obtained from ^1H -NMR, molecular weight (M_w , M_n), *PDI*, hydrodynamic radii (R_{Ho}^{DLS}) and radii of gyration (R_{go}^{SANS}) as obtained from DLS and SANS studies respectively. DLS data showed that the native **CP1** polymer showed lower hydrodynamic radii of 13 nm than **CP2** (~35 nm). This showed a direct correlation between molecular weight and hydrodynamic radii for the polymers with comparable functionality (4%). Moreover, the R_g , as well as scaling exponent value (ν), also showed clear increased values in the case of **CP2** when compared with **CP1** in corroboration with DLS and GPC data. The scaling exponent value in the range 0.51-0.59 indicated the extended coil state of the polymer in the aqueous environment.

Table 3.1. Characterization details of native functional polymers **CP1-2**

Polymer	% coumarin ^a	M_n^b (Da)	M_w^b (Da)	<i>PDI</i> ^b	R_{Ho}^{DLS} ^c (nm)	R_{go}^{SANS} ^d (nm)	ν ^e
CP-1	4%	28357	37183	1.31	13 ± 1	17 ± 3	0.53
CP-2	4%	45197	53897	1.19	35 ± 2	27 ± 2	0.59

[a] Determined by ^1H NMR. [b] Absolute number average molecular weight (M_n) and Absolute weight average molecular weight (M_w) determined by SEC-RALS analysis in DMF with 0.05 M LiBr additive using triple detection method using PMMA 60K as narrow standard and PMMA 95 k as broad standard. [c] Hydrodynamic radii of the polymer solution as obtained from DLS. [d] Radii of gyration as determined by SANS. [e] Scaling exponent derived from the SANS analysis using generalized Gaussian coil model.

3.2.2. Photodimerization mediated Chain Collapse: Aqueous solution of polymers **CP1-2** exhibited characteristic UV absorption bands of the coumarin groups in the wavelength range of 280-350 nm in water (Figure 3.1A-B). The absorption demonstrated a gradual hypochromic shift as a consequence of photodimerization of the coumarin moieties upon

increased exposure of UV_B irradiation ($\lambda_{\text{max}} = 320 \text{ nm}$) to result in photo-dimerized **di-CP1-2** polymers. Further, the irradiated **di-CP1-2** polymer solution exhibited reversal of the absorbance upon irradiation with UV_C light ($\lambda_{\text{max}} = 254 \text{ nm}$) within 30 min indicating the dynamic nature of the process. The temporal change of the photodimerization degree (%PD) of coumarin with irradiation time was studied by UV-vis absorption spectra and calculated according to the equation $\%PD = (A_o - A_t)/(A_o) \times 100$, with A_o and A_t being the initial absorbance and the absorbance after irradiation time, t at 320 nm, respectively. The photodimerization in the case of **CP1** polymer occurred within the first 60 min of UV irradiation before attaining a saturation plateau of 70% (Figure.3.1C). **CP2** polymer showed rather delayed photodimerization as compared to **CP1** and renders only 48% PD over the same time period. Thus, the accessibility of the coumarin functionality for photodimerization depends on the polymer chain reptation time (τ) in a direct correlation with the molecular weight of the polymer ($\tau \propto M^3$).^{21,45}

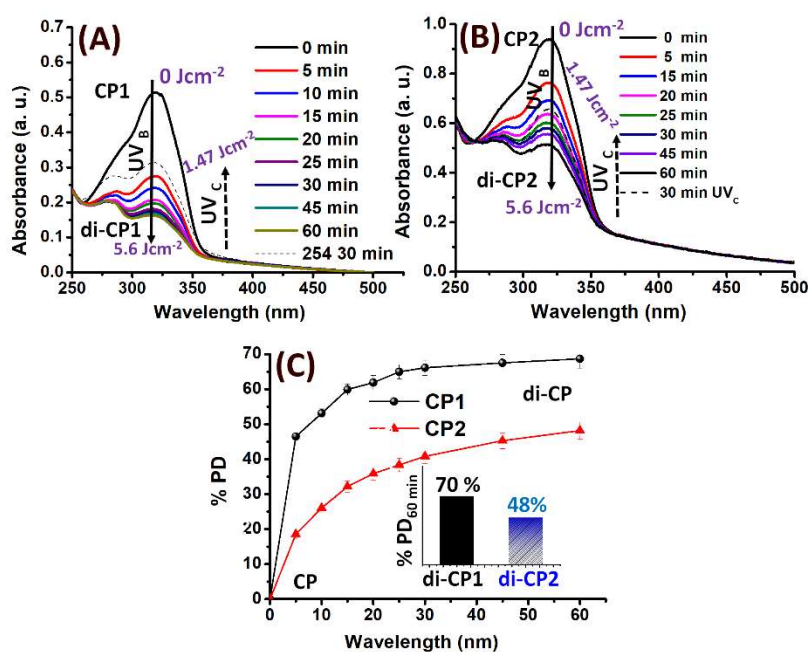


Figure 3.1. UV-vis spectra showing a decrease in absorbance on irradiation of native (A) **CP1** and (B) **CP2** polymer (0.01 mM) solution to form **di-CP1-2**. (Dotted lines shows retrieval of absorbance upon irradiation with UV_C light) (C) Increase in %PD with the time of UV_B irradiation for **CP1-2** polymer solution. (Inset shows % PD at 60 min)

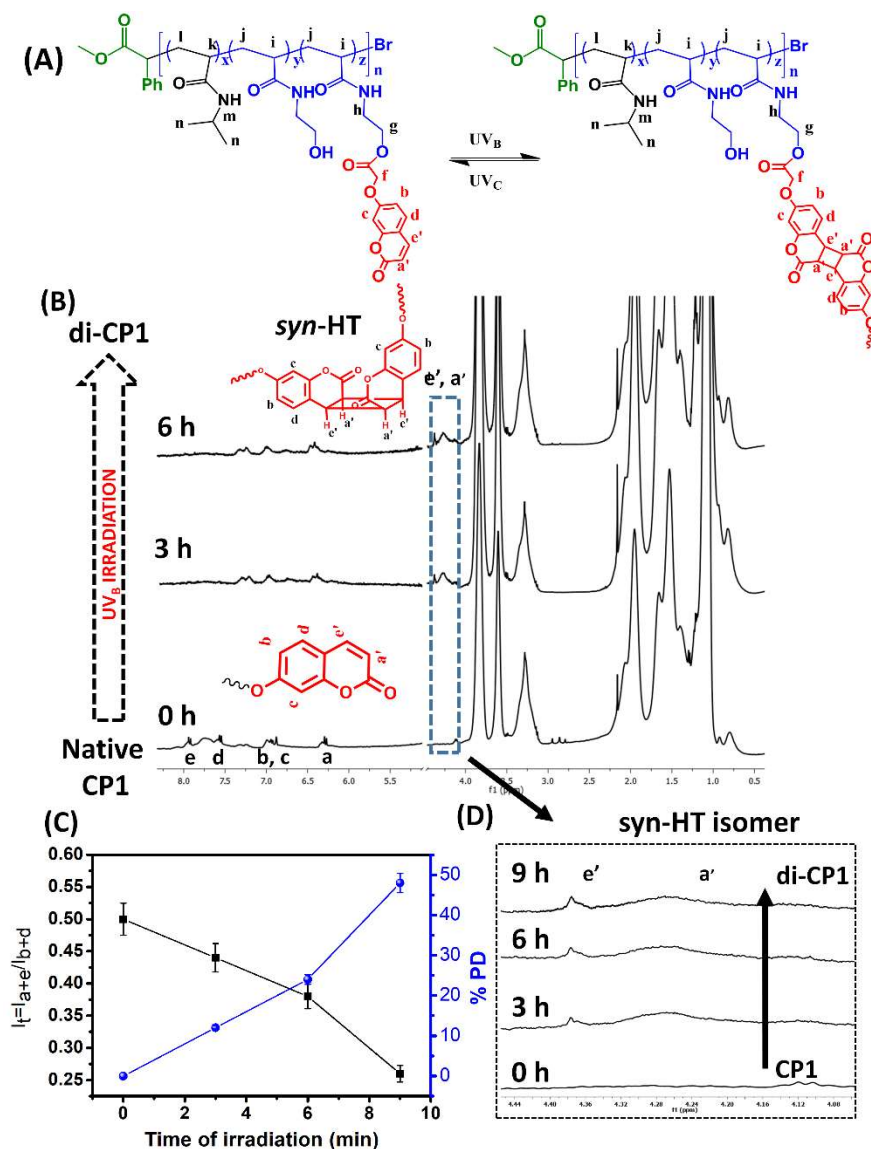


Figure 3.2. Monitoring photodimerization by ¹H-NMR. (A) Structural changes as a result of $[2\pi + 2\pi]$ photodimerization of coumarin moiety in **CP1** polymer to form cyclobutane adduct. (B) Partial ¹H NMR spectra depicting the changes in peak intensity ascribed for coumarin along with the appearance of a new peak at δ (ppm) 4.2-4.4 which denotes the presence of *syn-HT* cyclodimer as the major photodimerization product. (C) Change in integral ratio $I_f = I_{(a+e)} / I_{(b+d)}$ and %PD during photodimerization of **CP1** polymer solution (1 mM) in D₂O with UV_B Light. (D) Zoomed area of ¹H-NMR spectra showing the appearance of new peaks at δ (ppm) 4.2-4.4 that denotes the presence of *syn-HT* cyclodimer as the major photodimerization product.

The extent of photodimerization was also monitored by ¹H-NMR of the **CP1** polymer solution at a relatively higher concentration (Figure 3.2). The integral ratio of aromatic protons *a*, *e* at the photodimerization site to *b*, *c*, and *d* protons of the coumarin moieties

gradually diminished with an increase in time of UV_B irradiation owing to the formation of $[2\pi+2\pi]$ cycloadduct. The gradual appearance of characteristic cyclobutyl proton peaks at δ (ppm) 4.2-4.4 for **di-CP1** polymer indicated *syn-HT* cyclo-adduct as the major photodimerization product among all possible conformations.^{46,47} Further, DLS experiments for aqueous **di-CP1-2** polymer solutions depicted a clear trend for size reduction upon light-mediated chain collapse (Figure 3.3A-C). The hydrodynamic radii of native **CP1** polymer (13 nm) reduced to around 3.5 for NPs within 60 min of UV_B irradiation that clearly suggested 70% photodimerization to account for around 68% compaction in size. Comparatively, rather lower chain compaction in **CP2** (42%) corroborates a lower extent of photodimerization degree owing to high polymer reptation time.

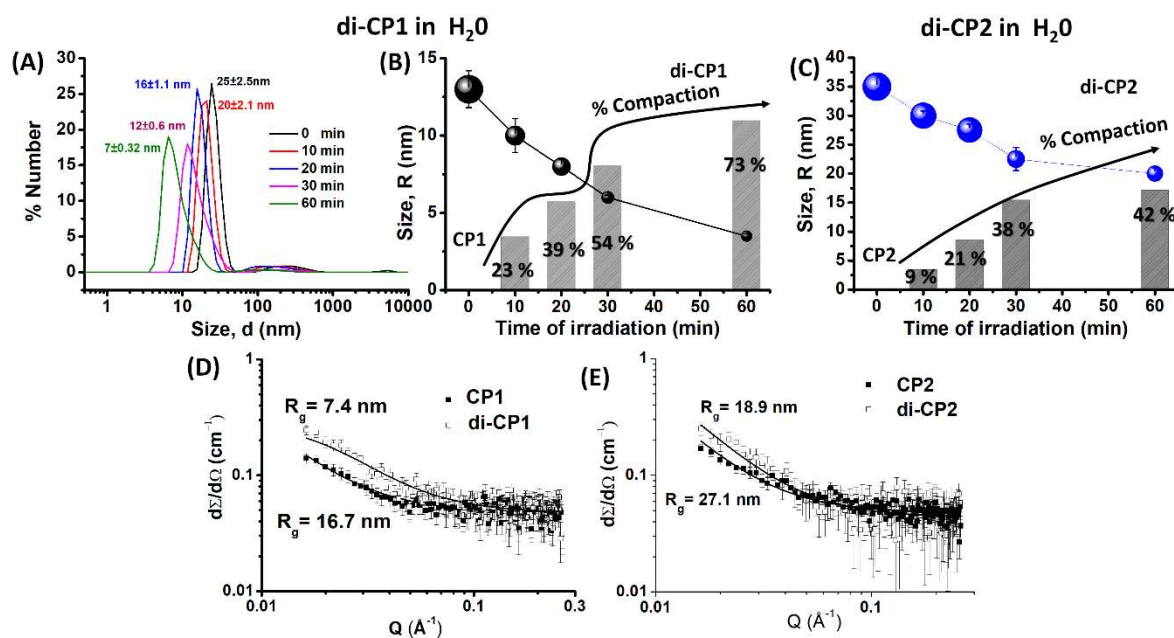


Figure 3.3. (A) DLS data showing the decrease in size of **CP1** polymer (0.01 mM) as a result of the chain compaction to form **di-CP1-2**. Change in hydrodynamic radii along with percentage compaction for (B) **CP1** and (C) **CP2**. SANS data show macromolecular form factors for polymer (D) **CP1** and (E) **CP2** and the nanoparticles (**di-CP1-2**) after UV_B irradiation for 3 h (1 mg/mL in D₂O). Lines are fitted to generalized Gaussian form factors. UV_B light (2*8 W, λ_{\max} = 320 nm) and UV_C light (1*8 W, λ_{\max} = 254 nm).

Small-Angle Neutron scattering (SANS) experiments give a better insight into the structural characteristics of the polymer chains and the extent of chain collapse mediated by the intra-chain cross-linking. The SANS data acquired before and after UV irradiation for

the sample **CP1** and **di-CP1**, respectively (Figure 3.3 D-E) showed that the scattering measured for the native polymer **CP1** solution tends to fall off at lower Q-values than that attained for the irradiated polymer **di-CP1** solution. This indicates that the extended coil state of the native polymer **CP1** solution undergoes intra-chain collapse to form **di-CP1** on irradiation.⁴⁸⁻⁵⁰ The SANS experimental data fitted to generalized Gaussian coil function allowed a precise determination of the radius of gyration (R_g) value. Thus, the native polymers **CP1-2** exhibited R_g (~ 17 nm & 27 nm) that were reduced to 7.4 and 18.9 nm respectively on chain collapse and fit within spherical dimension for **di-CP1-2**. Moreover the decrease in scaling exponent, ν of **CP1-2** (~ 0.51-0.59) to 0.31-0.34 indicated compaction of the expanded coil to globular morphology. The photodimerization degree and the resulting compaction in size for **di-CP1-2** as observed from DLS and SANS suggests intrachain collapse *via* UV_B irradiation resulting in the formation of NPs

3.2.3. Host-Guest Complexation mediated Chain Collapse: Next, we explored host-guest complexation between coumarin and β -cyclodextrin resulting in the inclusion complex that is a non-covalent approach to render the polymer chain collapse. Therefore, we designed a **bis- β -CD** crosslinker molecule with two β -cyclodextrin units bridged by a hexamethylene spacer (Scheme 3.1). The polymer tethered with coumarin moiety depicts host-guest complexation upon addition of **bis- β -CD** host as observed by an increase in absorbance in the wavelength range of 300-350 nm with a slight bathochromic shift (Figure 3.4 A-B). This indicated strong interaction of the coumarin guest with a hydrophobic compartment inside cyclodextrin resulting in the formation of **CP1 \subset bis- β -CD** inclusion complex. The binding constant (K_d) for the **CP1 \subset bis- β -CD** complex was calculated to be $3 \times 10^4 \text{ M}^{-1}$ and Job's plot analysis of change in absorbance (ΔA) along with mole fraction of **CP1** indicated 1:1 complexation stoichiometry for **CP1 \subset bis- β -CD** inclusion complex (Figure 3.4C). Moreover, ¹H NMR studies showed upfield shifts of *e*, *c*, *b*, and *d* proton of the coumarin moiety upon addition of **bis- β -CD** owing to the interaction with the hydrophobic cavity inside cyclodextrin (Figure 3.4D).

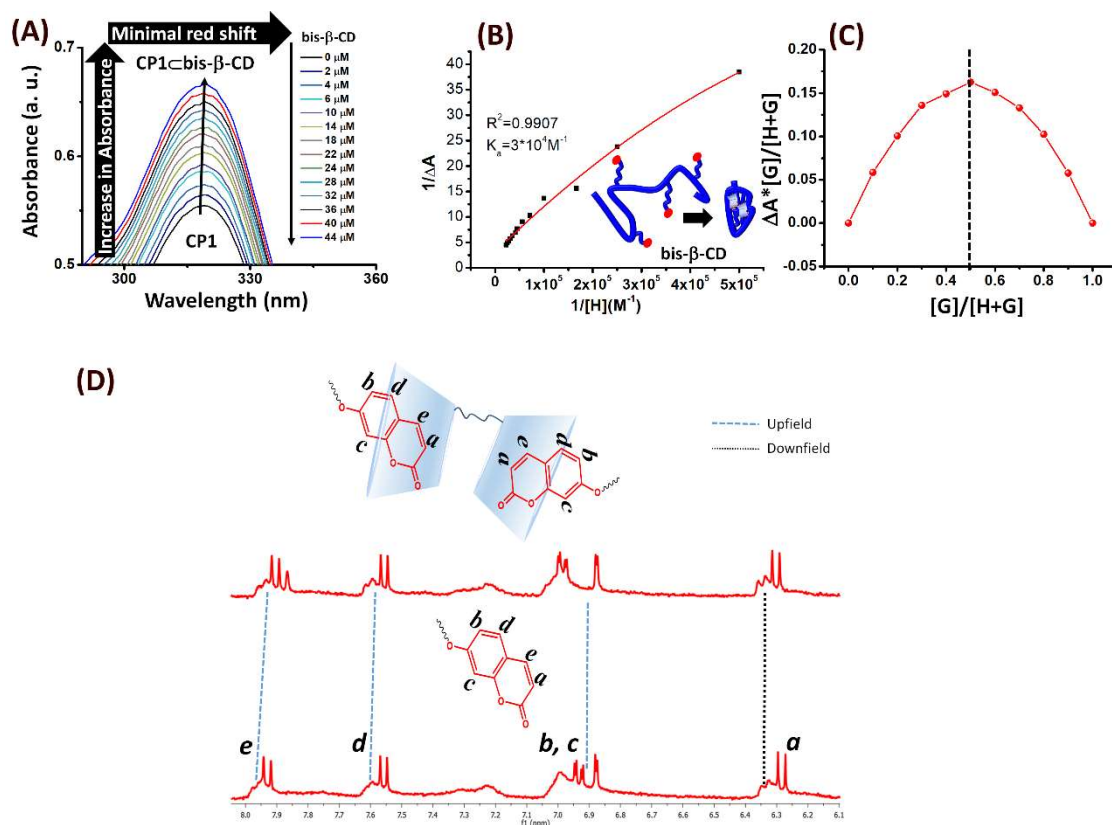


Figure 3.4. Host-guest complexation of the aqueous CP1 polymer solution with increasing concentration of host bis- β -CD as monitored by UV and ITC titrations. (A) UV studies showing an increase in absorbance on titration of CP1 (0.01 mM) with bis- β -CD and (B) binding constant calculation by non-linear fitting (C) Job's plot from UV spectra showing 1:1 complexation stoichiometry, (D) ^1H NMR spectra showing an upfield shift of proton signals of coumarin moiety in CP1 polymer, e, c, b and d on the addition of 4 equivalent of bis- β -CD due to the shielding effects on coumarin inside cyclodextrin cavity environment.

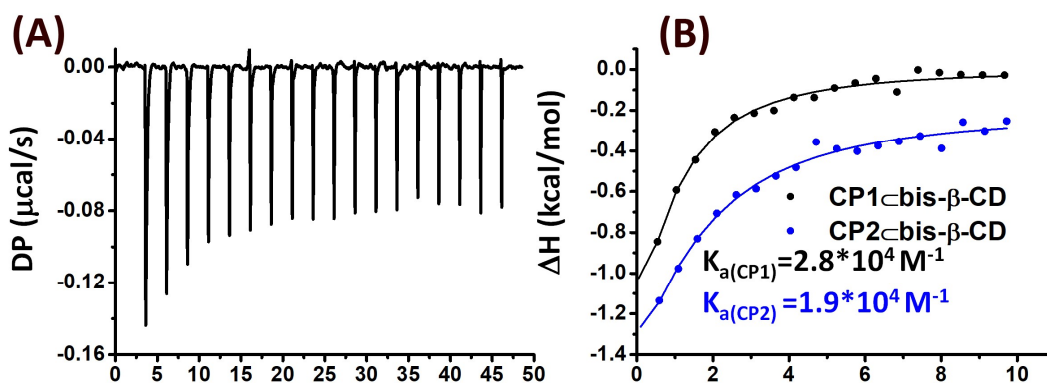


Figure 3.5. (A) ITC titration for injection of bis- β -CD solution (1 mM) in CP1 solution (0.02 mM) at 25 °C. (B) ITC binding isotherms for CP1-2bis- β -CD representing integrated heat of interaction

Table 3.2: Binding constant and other thermodynamic parameters for different polymer samples on host-guest interactions (ITC titration for 1 mM **bis- β -CD** solution in 0.02 mM **CP1**, **di-CP1**, **CP2** solution at 298 K.

	$K_a(\text{M}^{-1})$	$\Delta H(\text{KJ/mol})$	$\Delta G(\text{KJ/mol})$	$-T\Delta S (\text{KJ/mol})$
CP1 \subset bis-β-CD	2.8×10^4	-21.38	-25.43	-4.05
di-CP1 \subset bis-β-CD	3.1×10^4	-18.48	--26	-7.32
CP2 \subset bis-β-CD	1.9×10^4	-17	-24	-7.48

Further, isothermal titration calorimetry (ITC) was utilized to monitor the binding interaction between the **CP1-2** polymers and **bis- β -CD** host by determining the thermodynamic parameters and heat changes associated with the formation of the inclusion complexes. The binding isotherms fitted with one-site binding model depicted heat change (ΔH) with inflection point near to 1 indicating a 1:1 stoichiometry of functional moieties involved in **CP1-2** \subset **bis- β -CD** complex (Figure 3.5 & Table 3.2) in corroboration with the Job's plot analysis by UV titration. The negative and favorable binding enthalpy ($\Delta H = -21.38$ and $-17 \text{ kJ}\cdot\text{mol}^{-1}$) and entropy factor ($-T\Delta S = -4.05$ and $-7.48 \text{ kJ}\cdot\text{mol}^{-1}$) revealed that the binding of **CP1-2** guests with **bis- β -CD** host molecule comprised of hydrogen bonding and hydrophobic interactions. Further, the binding constant value of $K_a = 2.8 \times 10^4 \text{ M}^{-1}$ (**CP1**) and $1.9 \times 10^4 \text{ M}^{-1}$ (**CP2**) obtained from ITC titration was in corroboration with UV titration studies. Notably, the binding constants are much higher as compared that of small molecular analogues of coumarin ($100\text{-}700 \text{ M}^{-1}$) engaging in host-guest complexation with β -CD as reported by Takadate *et al.* and Cano *et al.*^{51,52} This clearly indicated the multiple units of coumarin moieties tethered on polymer chains render multivalent binding with **bis- β -CD** host molecules. Additionally, the high degree of freedom of hydrophobic coumarin moieties favored by the water-soluble polymer backbone in an aqueous environment render high binding affinity with the hydrophobic internal cavity of cyclodextrin thereby, forming a strong complex. Further, such interaction led to crosslinker mediated chain collapse resulting in NPs. DLS studies demonstrated the compaction of extended polymer chain of **CP1** ($R_H = 13 \text{ nm}$) to around 8 nm upon addition of host molecule (Figure 3.6A) providing **CP1** \subset **bis- β -CD** NPs. The SANS data showed an increased scattering intensity with a delay in fall in intensity for **CP1** \subset **bis- β -CD** NPs than that for the native **CP1** polymer solution (Figure 3.6B)

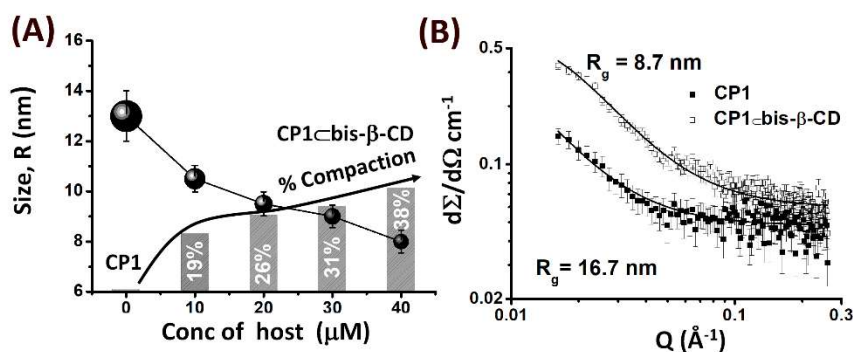


Figure 3.6. (A) DLS data showing the extent of compaction of the polymeric nanoparticle and the variation of hydrodynamic radii for **CP1-bis-β-CD** (B) Macromolecular form factors obtained by SANS study for linear precursor chains of **CP1** and the corresponding SCNPs (**CP1-bis-β-CD**) upon addition of 4 equivalents of **bis-β-CD**). Lines are fits to generalized Gaussian form factors.

This indicated chain collapse from native extended chain to globule transformation by host-guest interaction with a compaction corresponding to reduction in R_g from 17 to 8.7 nm as well as scaling exponent from 0.51 to 0.37. Table 3.3 summarizes apparent molecular weight (M_w^{app}), hydrodynamic radii (R_H^{DLS}), %compaction, radii of gyration obtained from SANS experiment (R_g^{SANS}).

Table 3.3. Detailed Characterization of the NPs designed by different chain collapse strategies

Polymer	M_w^{app} (Da) ^a	R_H^{DLS} ^b (nm)	% Compaction _{DLS}	R_g^{SANS} ^c (nm)	R_{TEM} ^d (R_{TEM} , nm)	R_{AFM} ^e (R_{AFM} , nm)	$R_{spherical}$ ^f (R_s , nm)	ν^g
di-CP-1	36067	3.5 ± 0.2	73	7.4 ± 0.6	8 ± 0.5	11 ± 1	6 ± 0.3	0.31
di-CP-2	52280	20 ± 1	42	18.9 ± 0.5	50 ± 5	38 ± 4	17 ± 2	0.37
CP- 1-bis-β- CD	36852	8 ± 0.3	38	8.7 ± 0.7	18 ± 2.8	19 ± 2.5	9 ± 0.8	0.34

^[a] Apparent molecular weight (M_w^{app}) determined by SEC-RALS analysis in DMF with 0.05 M LiBr additive using triple detection method using PMMA 60K as narrow standard and PMMA 95 k as broad standard. ^[b] Hydrodynamic radii as determined by DLS studies, ^[c] Radii of gyration as determined by SANS ^[d] Radii from analysis of TEM images ^[e] Radii from analyses of AFM images, ^[f] Spherical radii as determined from the ellipsoid particle adsorbed with height in AFM images. (di-CP1-2 are formed by UV_B irradiation (2x8W, λ_{max} = 320 nm) of 0.01 mM CP1-2 in H₂O for 1 h, CP-1-bis-β-CD formed by addition of bis-β-CD host molecule to 0.01 mM CP2 in H₂O). ^[g] Scaling exponent derived from the SANS analysis using generalized Gaussian coil model.

3.2.4. Microscopic Investigation of Nanoparticles: Microscopic analysis of **CP1-2** polymers before and after chain collapse showed a clear distinction in morphology and dimensions. AFM and TEM analyses revealed that native polymers appeared as non-specific structures (Figure 3.7), while the polymer samples upon chain collapse showed hemi ellipsoidal nanoparticles at dilute concentration. Histogram analyses of TEM and AFM images depicted that the **di-CP1-2** NPs formed *via* photodimerization of polymer samples exhibited size range of around 8-11 nm, 35-50 nm respectively whereas the **CP1-bis-β-CD** NPs formed *via* the addition of host **bis-β-CD** revealed size range of around 18-19 nm (Figure 3.8). This confirmed the morphological transformation of the extended chain of native polymer to globular nanoparticles *via* chain collapse of the polymer as shown in DLS and SANS studies. Moreover, the size compaction of native polymer to spherical nanoparticles showed a clear trend that was observed in scattering studies. Additionally, the **di-CP1-2** and **CP1-bis-β-CD** NPs exhibited good polydispersity index (PDI)

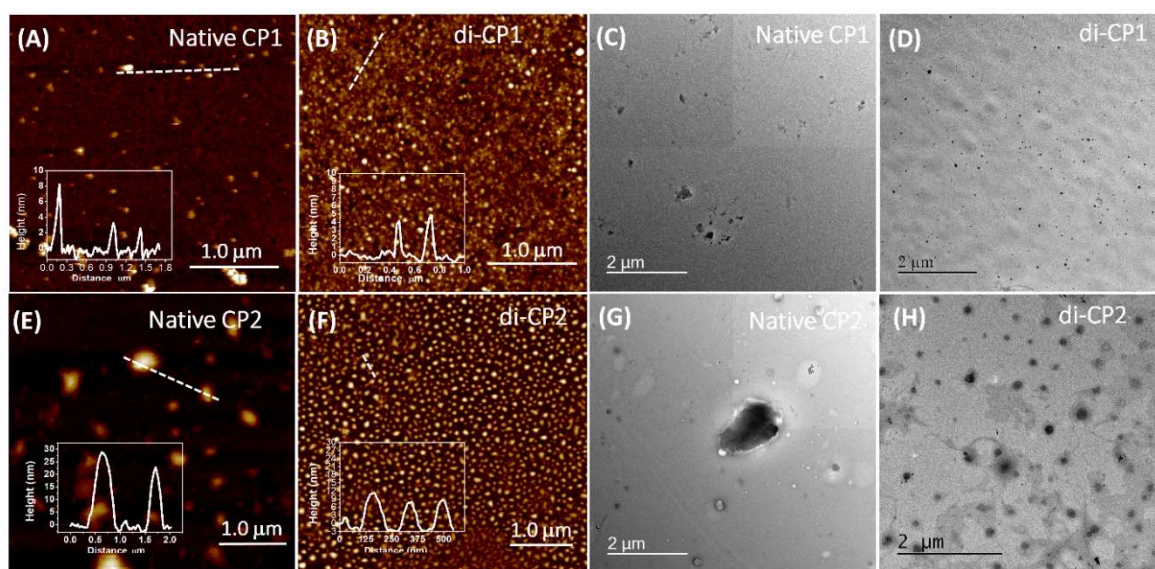


Figure 3.7. Morphological transformation polymers **CP1-2** to nanoparticles as a result of chain collapse *via* photodimerization. AFM and TEM images for native polymers showing nonspecific uncontrolled nanostructures in case of (A,C) **CP1**, (E,G) **CP2** that transform into discrete uniform nanoparticles in (B, D) **di-CP1**, (F, H) **di-CP2** (Inset showing corresponding AFM height profiles)

for the size of the nanoparticles indicating excellent control over the size compaction *via* chain collapse that depends on the chain length, %functionality of the polymer, and the strategy employed for chain collapse. Noticeably, the drop-casting of the **di-CP1-2** and **CP1- β -CD** NPs solution onto silicon surface renders adsorption mediated flattening of the soft nanoparticle to a hemi ellipsoidal structure. Therefore, the size of the spherical nanoparticles was calculated by equating hemi ellipsoid and sphere volume and listed in Table 3.3.⁵³ The spherical diameter obtained was corroborated with the values obtained in DLS experiments for **di-CP1-2** and **CP1- β -CD** NPs, thereby affirming the size compaction by chain collapse of **CP1-2** polymers *via* photodimerization and host-guest interaction.

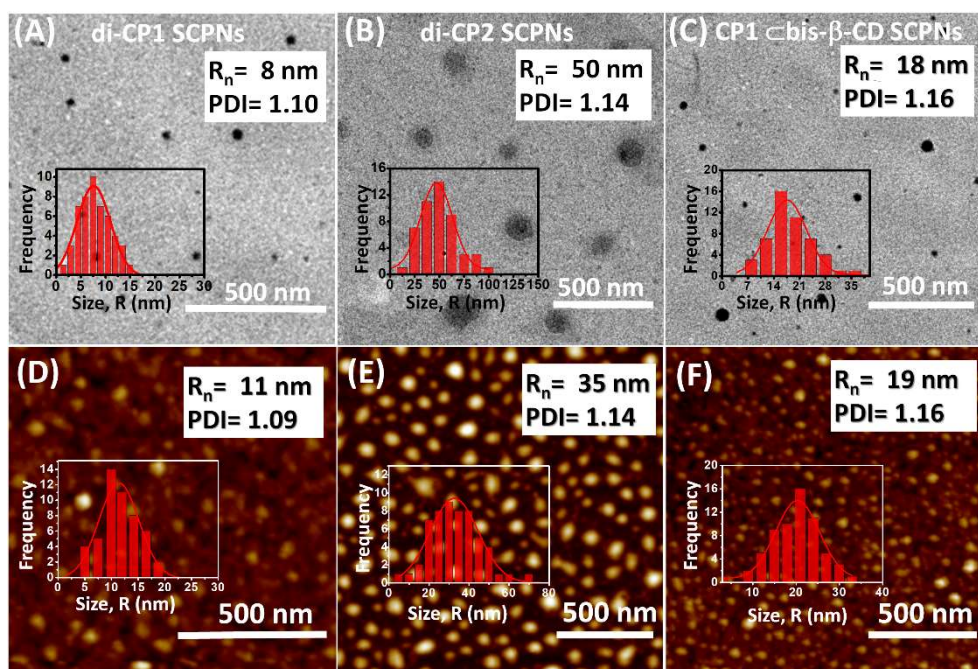


Figure 3.8. TEM and AFM images with the histograms of (A, D) **di-CP1** (B, E) **di-CP2** NPs formed as a result of chain collapse by UV_B irradiation for 1 h ($\lambda_{\text{max}} = 320$ nm, UV_B Light) in aqueous solution (0.01 mM), (C, F) **CP1- β -CD** NPs formed *via* host-guest interaction upon addition of **β-CD**

3.2.5. Modulation of Thermo-responsive Behavior: Further, the polymers possessing NIPAM comonomer as backbone was used to explore the thermoresponsive property and its

role in structural transformation. Generally, NIPAM based polymers exhibit an abrupt decrease in solubility upon the increasing temperature in water signifying hydrophilic to hydrophobic phase transition, and the critical cloud point temperature (T_{cp}) is known as LCST. This was evident from the UV-vis transmittance studies for native **CP1** polymer that rendered a rapid decrease in %Transmittance upon temperature ramp-up from 20 to 70 °C (Figure. 3.9A) with $T_{cp} \sim 38$ °C. Further, the reversible phase transition exhibited a narrow hysteresis upon cooling the hot polymer solution back to 20 °C. Native **CP1** polymer in its aqueous solution remains as hydrated coils at ambient temperature owing to the predominant hydrogen bonding interaction among the amide and hydroxy groups of the side chains with the water molecules. However, above LCST the increase in kinetic energies of the molecules results in the promotion of hydrophobic interactions between the polymer backbone and isopropyl side chains of NIPAM copolymers.⁵⁴ Thermo-responsive behavior of the **CP1** native polymer was further investigated by SANS studies at three different temperatures. The scattering intensity of **CP1** upsurges at the low-Q region with the increasing temperature that indicated the formation of mass fractal aggregates (Figure 3.9E). This led to the alteration of extended coil conformation of flexible linear chain to the structural aggregate of collapsed polymer coils owing to intra or intermolecular accumulation of hydrophobic moieties in the polymer.⁵⁵⁻⁵⁷ Further, the temperature ramp-up experiment for the photodimerized **di-CP1** nanoparticles exhibited a clear trend of increased T_{cp} from 38 to 65 °C with the photodimerization degree (Figure 3.9B). This indicated the role of photodimerized intra-chain crosslinks that is analogous to cyclic loops in the folded polymer which gives rise to a repulsive force to chain aggregation and dehydration upon temperature rise. This detainment in chain aggregation led to an increase in LCST to a higher value for **di-CP1** nanoparticles than its linear counter parts.⁵⁸⁻⁶² Moreover, the non-covalent crosslinking involving **CP1**-**bis-β-CD** host-guest complex formation also exhibited an upward shift in the LCST relative to the native **CP1**, *albeit* with rather smaller shift of T_{cp} from 38 to 50 °C (Figure 3.9C). Thus, the nature of crosslinking dictates the modulation of thermo-responsive behavior with covalent interactions like coumarin photodimerization

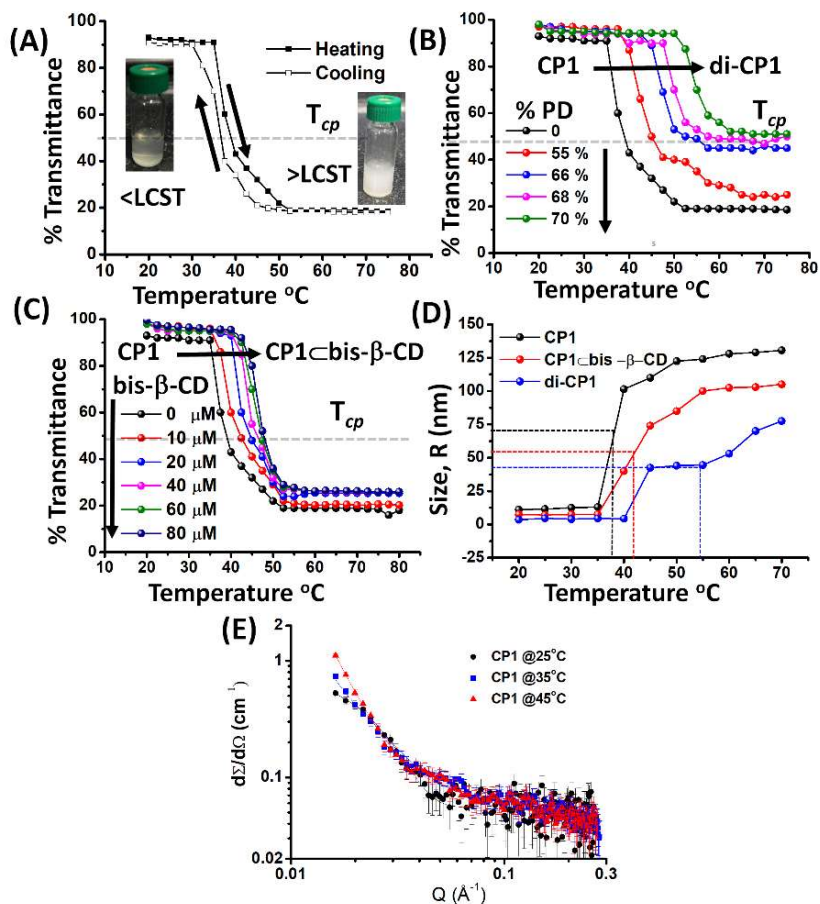


Figure 3.9. Temperature responsive LCST behavior with photodimerization and host-guest complexation of the aqueous polymer solution. (A) Determination of cloud point temperature (T_{cp}) by the change in %Transmittance at 563 nm for heating and cooling cycle for CP1, (B) Effect of photodimerization on T_{cp} of CP1 resulting in formation di-CP1 NPs (di-CP1 formation with UV_B irradiation (UV_B light, 2x8W) for 1.5 h), (C) Effect of bis- β -CD host addition on T_{cp} of CP1 solution resulting in the formation of CP1-bis- β -CD NPs. (D) DLS data showing temperature-induced aggregation on heating above T_{cp} for CP1, di-CP1, CP1-bis- β -CD ($c = 0.02$ mM for all the cases). (E) Monitoring thermoresponsiveness via SANS Macromolecular form factors obtained by SANS for CP1 polymer solution (5 mg/mL) at 25 °C, 35 °C, and 45 °C. Lines are fitted to generalized Gaussian form factors

being more effective than the non-covalent interactions *e.g.* host-guest interaction. Hence, the cross-linked polymer chains with increased rigidity rather weaken the interchain interactions that are necessary to form the nanoparticle clusters upon temperature ramp-up and exhibit higher LCST values (Figure 3.10).

Furthermore, DLS studies were performed to probe the aggregation temperature by monitoring the sudden increase in hydrodynamic radii of the nanostructures upon increase in temperature (Figure 3.9D). The temperature-induced aggregation of the nanostructures for native **CP1** was found to be ~ 38 °C that showed an upward shift for **CP1- β -CD** (~ 43 °C) and **di-CP1** (~ 50 °C) in close corroboration with %Transmittance data. Noticeably,

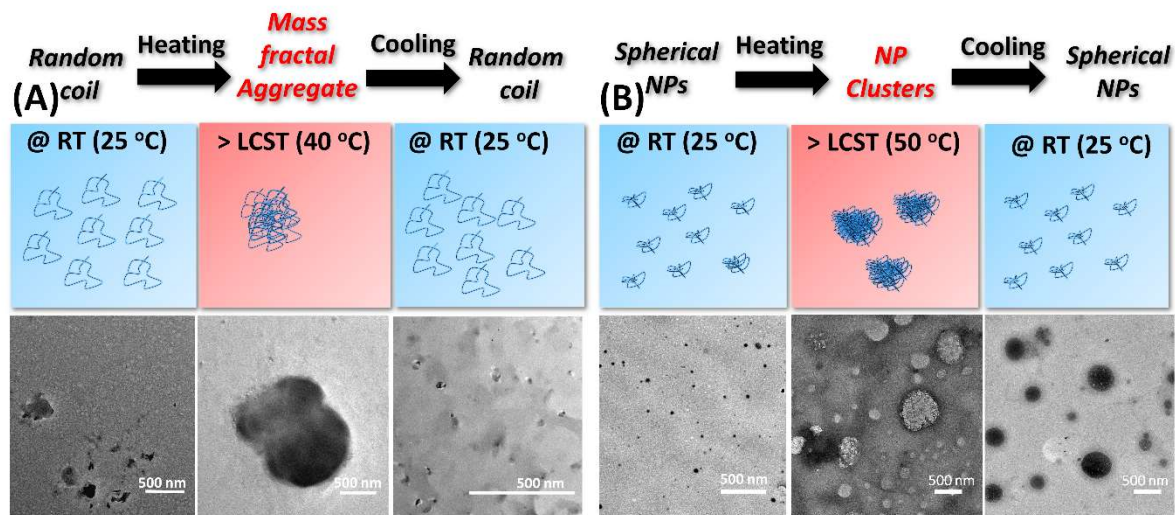


Figure 3.10. Microscopical investigation of the thermoresponsive character of **CP1** solution (0.02 mM). (A) Extended random coils and micellar aggregate of **CP1** as observed in TEM upon heating and cooling temperature beyond LCST temperature. (B) Discrete nanoparticles and nanoparticle clusters of **di-CP1** as observed in AFM and TEM images upon heating and cooling temperature beyond LCST temperature.

a smaller change in hydrodynamic radii for both **di-CP1** and **CP1- β -CD** as compared to native polymer suggests lower thermo-responsiveness owing to the increased rigidity in the flexo-rigid copolymer system. Moreover, the early aggregation and clustering of **CP1- β -CD** NPs in comparison to **di-CP1** NPs confirmed the predominant effect on intrachain collapse *via* photodimerization than by host-guest interaction on tuning thermo-responsive behavior of the polymer.

3.2.6. Synergistic and Sequential Chain Collapse: Although the role of photodimerization and host-guest interaction as two independent approaches for the intra-chain collapse of **CP1** polymer resulting in nanoparticle compartments of controlled size and thermo-responsiveness was established, the synergistic role of the interactions leading to controlled

compaction were intriguing in the context of pathway complexity of polymer self-assembly. Such multiple interactions applied in a partial stepwise manner may aid one over the other resulting in chain collapse *via* intrachain cooperativity accessing a number of swelling-deswelling stages of the resulting nanoparticles. Thus, we envisaged developing a dual response over chain collapse of the **CP1** polymer *via* the stepwise implementation of non-covalent and dynamic covalent interactions (Figure 3.11A). **CP1** polymer (**1**) was mixed with a limited amount of **bis-β-CD** host molecule (1 eqv) to form a partial **CP1**⊂**bis-β-CD** inclusion complex (**2**). This was followed by UV_B mediated photodimerization for 30 min to form dimerized complex **di-CP1**⊂**bis-β-CD** (**3**). Then UV_C irradiation for 15 min rendered decycloaddition to form decrosslinked complex (**4**). Finally, heating above the LCST resulted in nanoparticle cluster, (**5**). Hyperchromic shift of **CP1** in the range of 300-350 nm on UV titration with **bis-β-CD** clearly indicated the formation of inclusion complex (**2**) owing to the hydrophobic interaction of coumarin moieties with the cyclodextrin host (Figure 3.11B). Further, upon irradiation of **2** with UV_B rendered the hypochromic shift owing to the formation of dimerized complex **di-CP1**⊂**bis-β-CD**, (**3**) with %PD~70% (Figure 3.11B). Interestingly, the kinetics of photodimerization of **CP-1** was observed to be faster in the presence of **bis-β-CD** host and achieved 70% photodimerization degree in much less time (30 min) as compared to only CP-1. Thus, host-guest complexation provides a confined environment for coumarin moieties to come together in close proximity for cooperative photodimerization. Such cooperativity has also been reported in adamantane-β-CD and coumarin-CB[8] complexes.^{63,64} The *syn*-HT isomers of the coumarin cyclo-adduct with β-CD show quite strong host-guest interactions being retained inside the β-CD cavity and does not show any instance of guest moving apart from the host site was noticed throughout finite temperature 200 ns long trajectory of the simulation. Such strong interaction in corroboration with ITC data stems from synergic hydrogen-bonding between the coumarin cyclo-adduct and edged o-atoms of β-CD and hydrophobic interactions owing to the cyclobutane and aromatic region of coumarin. (Figure 3.11C, 3.4 & Table 3.2. However, upon irradiating (**3**) with UV_C light retrieval of absorbance was observed that indicated decycloaddition to form decrosslinked (**4**). Such dual interplay of dynamic covalent chemistry and host-guest interaction led to controlled and tunable chain collapse of

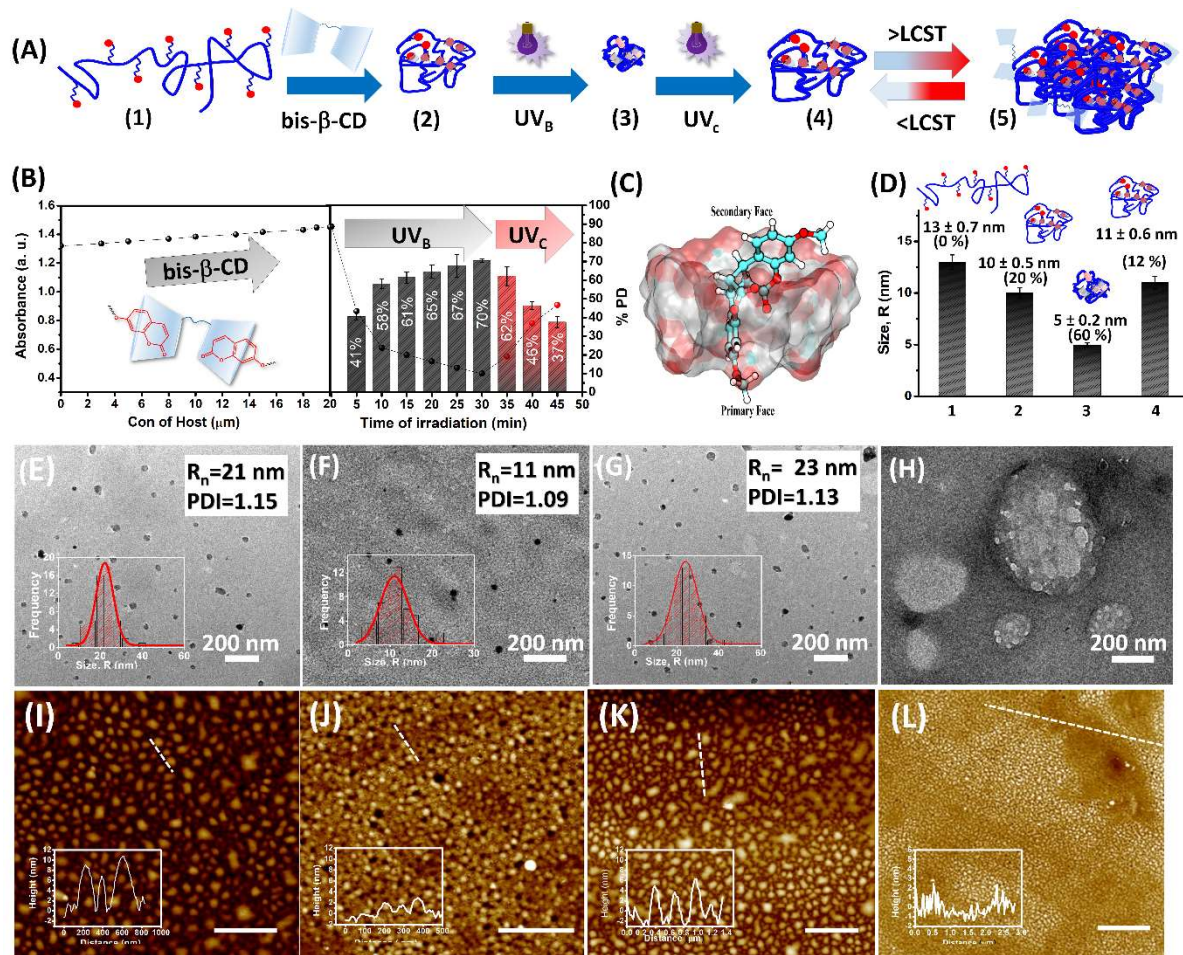
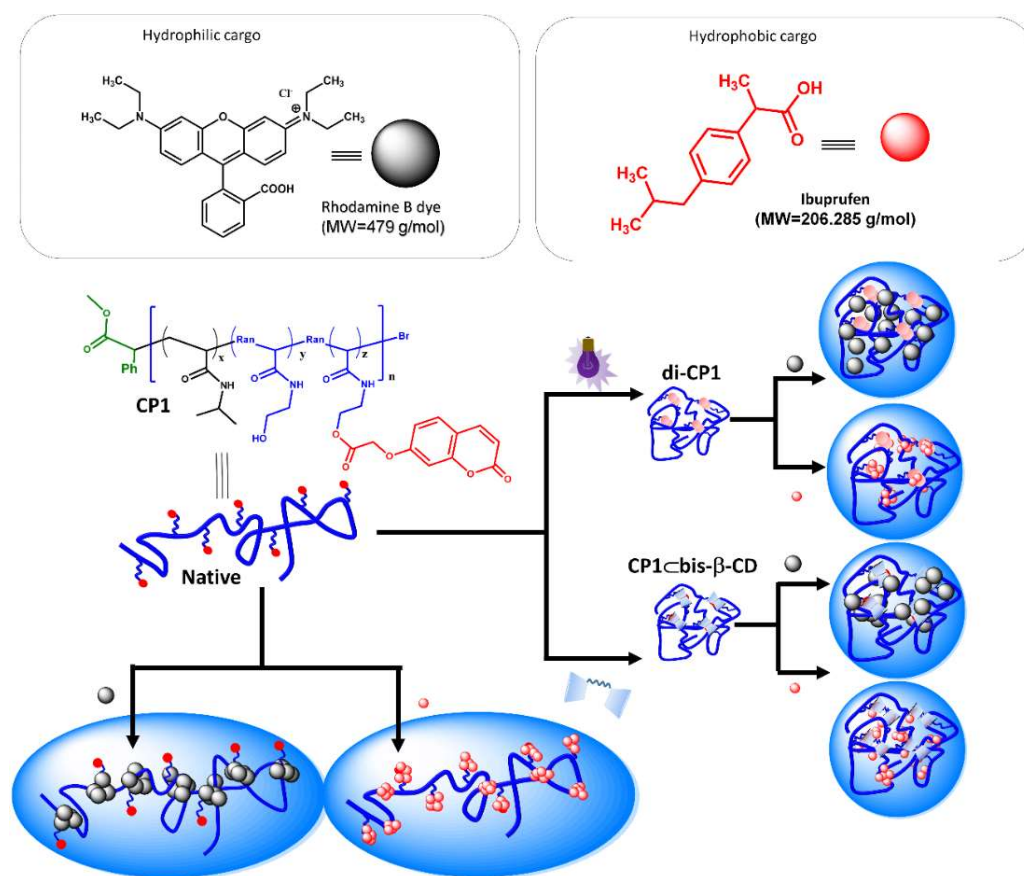


Figure 3.11. Sequential folding and defolding studies showing the tandem effect of host-guest complexation and photodimerization on chain collapse of CP1 polymer. (A) Scheme showing stepwise folding of native CP1 polymer (1) (0.02 mM) upon addition of 20 μ M bis- β -CD (1 eqv) to form CP1-bis- β -CD (2) that was further compacted on UV_B mediated photodimerization for 30 min to form di-CP1-bis- β -CD (3) and swelled by UV_C mediated defolding for 15 min to form CP1-bis- β -CD (4). Finally, the solution (4) was heated above LCST to form (5) clusters of CP1-bis- β -CD nanoparticles. (B) The hyperchromic shift upon addition of bis- β -CD to form CP1-bis- β -CD inclusion complex (2) with a subsequent decrease in absorbance upon UV_B mediated photodimerization (3). Further, UV_C irradiation rendered decrosslinked complex (4). (C) *Syn*-HT isomers of coumarin cyclo-adduct get inserted in β -CD due to a unique pattern of hydrophilic and hydrophobic interactions in outer and inner surface respectively as obtained in the MD simulation. (D) DLS studies showing bar graphs depicting hydrodynamic radii at various stages of stepwise folding and defolding (1-4) with percentage compaction at 25 °C. TEM and AFM images depicting the change in size upon different stages of stepwise folding and defolding with corresponding histograms for (E&I) CP1-bis- β -CD (2), (F&J) di-CP1-bis- β -CD (3), (G&K) decrosslinked di-CP1-bis- β -CD and (H&L) zoomed area of nanoparticle clusters.

the polymer system eventually rendering systematic folded and defolded states of the nanoparticles as studied by DLS (Figure. 3.11D, S14). Thus, native **CP1** polymer ($R_H = 13$ nm) demonstrated 20% compaction in nanoparticles size to 10 nm due to the formation of inclusion complex **(2)**, which exhibited further compaction ($\sim 60\%$) to ~ 5 nm on photodimerization resulting in the complex **(3)**. However, UVc irradiation of the dimerized complex **(3)** resulted in swelling of nanoparticle size (~ 11 nm) to form a decrosslinked complex **(4)**. Finally, the decrosslinked **(4)** nanoparticle system exhibited an increased in size due to aggregation at ~ 43 °C to form a nanoparticle cluster **(5)**. Microscopic analysis showed the transformation of extended coil state of native **CP1** polymer to partially compacted globular nanoparticles ($R_n = 21$ nm, $PDI = 1.10$) *via* formation of inclusion complex **(2)** upon addition of **bis- β -CD** host molecule (Figure 3.11E&I). The photodimerized complex **(3)** showed much compacted nanoparticles (~ 11 nm) with improved PDI and a decrease in height profile (Figure 3.11F&J, 3.12). Upon decrosslinking, the complex **(4)** exhibited swelling of size (~ 23 nm) with an increase in PDI and height (Figure 3.11G&K). Finally, the heated solution of nanoparticles from 4 above LCST rendered nanoparticle clusters 5 (size ~ 200 -400 nm) (Figure 3.11H&L). The AFM height analysis over neighboring nanoparticles cluster **(5)** area showed a large population of height distribution in two different areas bridged by a flat surface indicating segregated clustering of nanoparticles from decrosslinked complex **(4)** upon temperature ramp-up above LCST. Thus, the multi-modal chain collapse *via* a sequential approach of host-guest interaction and photodimerization works in conjunction providing an interesting strategy to control the folding of polymer chains.

3.2.7. Dye and Drug loading and release: Such approach towards designing nanocompartment with size tunability and fidelity renders polymeric nanoparticle drug delivery system with differential cargo localization and release profiles ranging from burst to sustained release patterns. Thus, we had utilized the thermo-responsive **CP1** polymeric system in native and folded SCPN state to explore the incorporation of a model hydrophilic dye e.g. rhodamine B (RhB), and model hydrophobic drug e.g. ibuprofen (Ibu) as in Scheme 3.2. The loading of RhB into native **CP1**, **di-CP1**, and **CP1- β -CD** polymers were monitored through its characteristic visible absorbance in the wavelength of 500-600 nm

(Figure 3.12A). While the incorporation of RhB in native CP-1 exhibited absorbance similar to bare dye in solution, that in **di-CP1** and **CP1 \subset bis- β -CD** NPs exhibited a hypsochromic shift. Moreover, the RhB loading content was as high as 40% in the case of CP1 polymer whereas it decreased to 20% and 14% in the case of **CP1 \subset bis- β -CD** and **di-CP1** nanoparticle (Figure 3.12C, Table 3.4) respectively. This indicates compaction of an extended coil of **CP1** polymer chains to result in limited loading of hydrophilic RhB dye. The incorporation of hydrophobic Ibu into the hydrophobic interior of the polymeric system depicted a hyperchromic shift



Scheme 3.2. Molecular structures of hydrophilic Rhodamine B, hydrophobic ibuprofen drug. Scheme of RhB and Ibu loading into **CP1**, **di-CP1**, **CP1 \subset bis- β -CD** polymers.

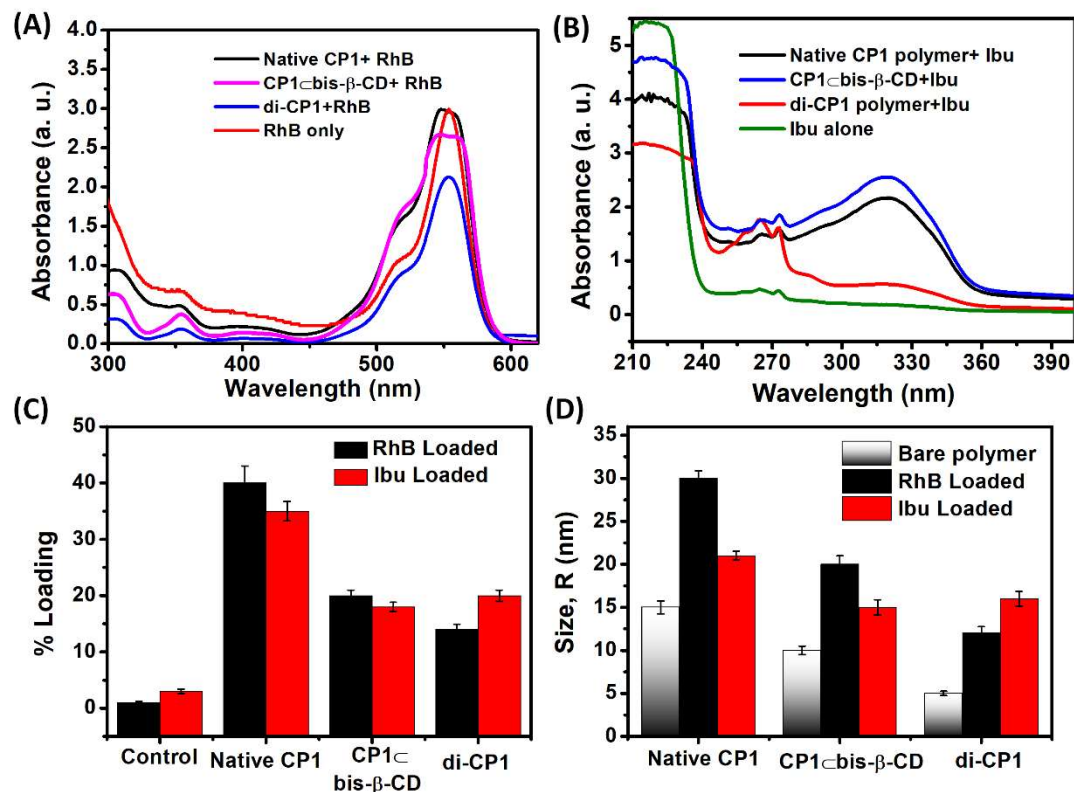


Figure 3.12: Cargo incorporation and loading studies. UV spectra showing the interaction of (A) RhB (0.2 mM) and (B) Ibu (2.6 mM) loaded in CP1, di-CP1, CP1 \subset bis- β -CD polymers (0.04 mM) by monitoring absorbance at 549 nm, 272 nm respectively. Localization and delivery of hydrophilic rhodamine B and hydrophobic ibuprofen drug from the polymers. (C) Bar diagram showing localization percentage of RhB or Ibu incorporated into CP1 polymer, di-CP1, CP1 \subset bis- β -CD nanoparticles (0.02 mM). (D) Change in size of the polymeric nanoparticles upon the cargo loading.

in the wavelength regime of 270-290 nm compared to a bare drug in solution (Figure 3.12B). The Ibu loading contents for native CP1, di-CP1, and CP1 \subset bis- β -CD polymers were found to be 35%, 20%, and 18% that is in corroboration with the extent of compaction and size of the polymeric nanoparticles (Figure 3.12C, Table 3.4). Upon loading the cargos the size of all the polymeric nanoparticles increased. However, RhB increased the size of all the polymers by 2 fold by interacting with the hydrophilic copolymers at the exterior, while hydrophobic Ibu drug influence the photodimerized polymers the most by penetrating the of the nanoparticles (Figure 3.12D). The interaction between RhB and the hydrophilic functionalities as well as Ibuprofen and hydrophobic side chains of the polymer *via* physical dispersion as well as adsorption resulting in entrapment of the cargo molecules into the

native polymer vehicle. The decrease in the adsorptive surface due to chain collapse in folded nanoparticle favour entrance of RhB as well as Ibu into interaction with its supramolecular network pocket resulting in encapsulation of the cargo within the vehicle. The native, as well as the folded polymeric system, has an optimal amount of hydrophobic NIPAM as well as hydrophilic hydroxy ethyl acrylamide side chain that gives comparative entrapment of hydrophilic RhB and hydrophobic Ibuprofen into the polymeric vehicle (Scheme 3.2)

Table 3.4: Table showing percentage loading of RhB or Ibu incorporated in native and folded polymers.

Loaded Cargo	Polymeric system	W_{cargo} (mg) ^a	W_{total} (mg) ^b	% Loading ^c	Average Cargo molecule per chain ^d
RhB	Nil	0.06	2.9	2	
RhB	Native CP1	3.6	8.9	40	34
RhB	di-CP1	1.2	8.4	14	9
RhB	CP1 \subset bis- β -CD	1.6	8.1	20	12
Ibu	Nil	0.11	2.7	4	
Ibu	Native CP1	3.1	8.7	35	66
Ibu	di CP1	1.82	9.1	20	32
Ibu	CP1 \subset bis- β -CD	1.48	8.2	18	26

^[a] Amount of loaded drug in polymeric solution determined by UV spectra by monitoring the absorbance at 272 nm (Ibu) or 459 nm (RhB) ^[b] Weight determined by lyophilisation of the RhB or Ibu loaded polymer solution after dialysis with the release of free drug and lyophilisation ^[c] % loading of the drug was determined by equation (9) in Section 3.4.2.12.) ^[d] Determined from the amount of cargo in mmol in one molecule of polymer and multiplying with the Avogadro number ($N_A=6.022*10^{23}$)

Next, the *in vitro* release patterns of different cargos were investigated by UV-vis spectra for different polymers in PBS. The cargo release profiles exhibited a cumulative release (75%) of the hydrophilic dye from RhB-loaded CP1 polymer within 10 h indicating a burst release, that gradually increased to 80% after 24 h (Figure. 3.13A). However, the release was suppressed to around 20% and 7% for RhB loaded compacted CP1 \subset bis- β -CD and di-CP1 nanoparticles owing to firm internalization of dye in the compact hydrophilic side

chains. However, with increasing temperature of the medium to 50 °C, the cumulative dye release significantly increased from CP1 β -bis- β -CD and di-CP1 systems to around 42% (2 fold) and 35% (5 fold) respectively within 8 h. Such a burst release of dye is a result of

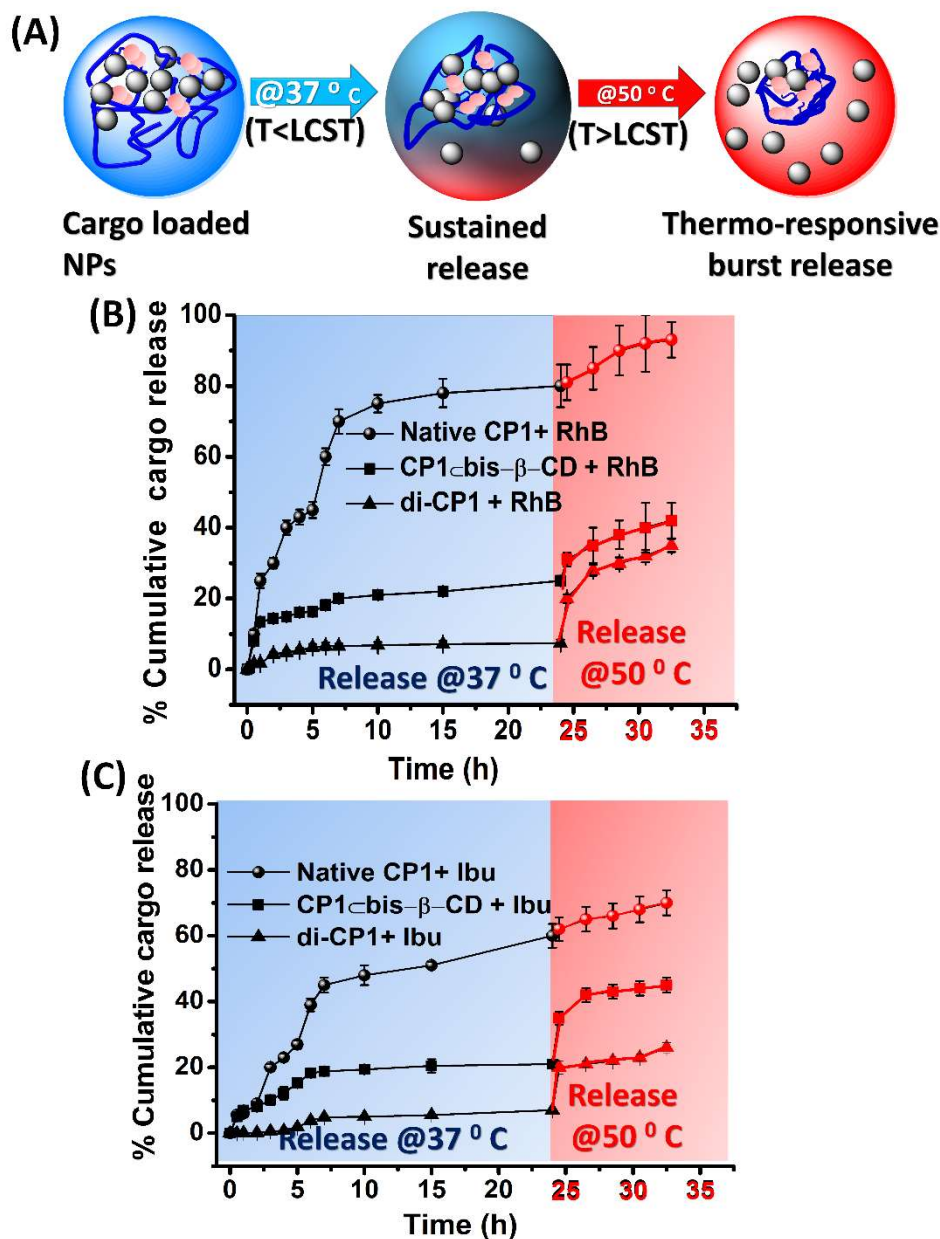


Figure 3.13. (A) Scheme showing RhB loaded polymeric nanoparticle which triggers sustained release at ambient temperature and eventually triggers release on temperature ramp up above LCST. The cumulative drug release pattern of (B) hydrophilic RhB dye and (C) hydrophobic Ibu drug from CP1 polymer, di-CP1, CP1 β -bis- β -CD nanoparticles into PBS buffer 10 mM (pH 7) at 37 °C for 24 h and thereafter release on increase in temperature to 50 °C up to 8h.

increased interaction between the polymeric sidechains thereby releasing the adhered hydrophilic cargo. The hydrophobic drug exhibited a sustained drug release pattern (Figure. 3.13B) from Ibu-loaded **CP1** polymer at 37 °C which was 45% in 10 h and 60% in 24 h. However, Ibu loaded **CP1-bis-β-CD** and **di-CP1** chain compacted nanoparticles exhibited sustained release profiles (21% and 7% respectively after 24 h). Upon increasing temperature to 50 °C, the cumulative drug release from Ibu loaded **CP1-bis-β-CD** and **di-CP1** nanoparticles increased to 45% (2.14 fold) and 26% (3.7 fold) within 8 h for respectively. Higher Ibu release in **CP1-bis-β-CD** NPs at T > LCST was due to the dissociation of the inclusion complex, while LCST induced drug release from **di-CP1** NPs was conspicuously lower in extent owing to the presence of retained hydrophobic cyclobutane loops in its chain collapsed sites. Thus, the polymeric systems displayed a collection of polymeric nanocompartments that aided distinctive localization and release of versatile cargos. Moreover, an increase in temperature above LCST instigated an augmented cargo release demonstrating an interesting design strategy of a heat-responsive antipyretic drug delivery system to maintain human body temperature by regulated homeostasis control.

3.3. Conclusion

Thus, in summary, multi-stimuli-responsive design of random copolymers **CP1-2** tethered with coumarin moieties were elegantly exploited towards controlled chain collapse to render polymeric nanoparticles (NPs). Both photoresponsive reversible dynamic covalent chemistry and non-covalent host-guest interaction demonstrated controlled chain collapse to render **di-CP1-2** and **CP1-2-bis-β-CD** nanoparticles. The extent of compaction was more efficient for the covalent approach owing to robust cyclobutane adduct as compared to the non-covalent inclusion complex. Moreover, an optimum amount of chain length and functionality was found to be significant for attaining maximum compaction. Further, the polymers exhibited excellent thermo-responsive behavior owing to an LCST induced hydrophilic to hydrophobic phase transition. The chain collapse strategies seem to have a direct implication over the LCST modulation owing to the introduction of crosslinking in

the extended coil of native polymers. Moreover, a synchronous host-guest interaction and photodimerization were elegantly exploited to result in sequential folding and defolding to tune the size of nanoparticles. We demonstrated control over the temperature-induced phase transition to render localized aggregation of the polymeric nanoparticles into clusters. Lastly, the polymers in native and folded states are employed to encapsulate versatile cargos of hydrophilic RhB dye or hydrophobic Ibu drug with excellent control. Additionally, variable release patterns ranging from sustained to on-demand burst release from different polymeric states were observed suggesting stimuli-responsive control over the release that may be utilized in the human body for antipyretic drug therapy to attain homeostasis control. Thus, the elegant design of polymeric versatile zero dimensional material formed by single chain technology and chain collapse presents versatile nano compartments for achieving a plethora of drug release platforms.

3.4. Experimental Section

3.4.1. Materials:

Solvents used in the syntheses were reagent grade. Ethanol, DCM, DMF, THF, N, N-dimethylacetamide were dried as per literature protocol.⁶⁵ The reagents triethyl amine, thionyl chloride was purchased from Alfa-aeser and used without further purification. The chemicals 7-hydroxy coumarin, β -cyclodextrin, hexamethyl diisocyanate (HDI), Cu(I)Cl were purchased from Sigma. The reagents methyl α -bromo phenyl acetate (MeBrPhAc), tris[2-(dimethylamino)ethyl]amine (Me₆TREN) were purchased from TCI and were used without further purification. The monomers, 2-hydroxy ethyl acrylamide (HEAm) was purchased from TCI and were passed through basic alumina and N-isopropylacrylamide (NIPAM) was recrystallized from n-hexane to remove inhibitor MEHQ before using them for ATRP. A regenerated seamless cellulose dialysis tubing wherein the membrane is partially permeable, having a molecular weight cut off between 12,000 to 14,000 Da was purchased from Himedia and used after activation.⁶⁶

3.4.2. Instrumentations:

NMR spectra were acquired on a 400 MHz Bruker machine. The chemical shifts were reported in ppm with downfield of tetramethylsilane using the resonance of the deuterated solvent as an internal standard. Splitting patterns were designated as singlet (s), doublet (d), triplet (t), and multiplet (m). %Functionality was calculated using the formula, %Functionality = $\{(I_x)/(I_x+I_f)\} \times 100$ where I_x is integral per proton of corresponding functional group, I_f is the integral proton of end group (*e.g.* isopropyl methyl group of NIPAM chain).

Mass was determined using AB Sciex 5800 MALDITOF system in DHB matrix. Size exclusion chromatography (SEC) was performed on a Malvern Viscotek instrument having RI, right angle light scattering (RALS) detectors using D₄₀₀₀ column with DMF with 0.05 M LiBr as eluent at 25 °C with a flow rate of 0.7 mL/min. The results were analyzed by using Omniseq software. The sample peaks were analyzed for Absolute M_n , M_w , PDI by PMMA triple detector calibration using PMMA-60k narrow standard and verified by PMMA-95 k broad standard.

Dynamic light scattering measurements were done on Malvern Zetasizer Nano ZS ZEN3600 equipped with a Helium–Neon laser (wavelength, $\lambda = 633$ nm with backscattering angle of 173°).

ITC Samples were prepared by filtering solutions through a 0.2 μm PTFE-filter in a glass cuvette. Isothermal titration calorimetric measurements were performed on a Malvern MicroCal PEAQ-ITC, which is composed of a reference cell and a sample cell of 300 μL . Degassing of the sample solutions was done prior to titration and kept constant temperature. In a typical run, a 40 μL syringe was full of the host (1.00 mM) and the cell was loaded with guest **CP1-2** polymer (0.02 mM, 300 μL). The titration of the host with the guest was carried out at 25 °C, with a constant rate of 750 rpm, 19 injections of 2 μL , a time interval of 150 s. The enthalpy change per mole of each added host **bis- β -CD** in the sample cell was recorded continuously. The control titrations of **bis- β -CD** into the water were also completed under similar conditions. The enthalpy changes of the titrations of the blank test were deducted from the sample titration data.

UV crosslinking was performed using a UV chamber equipped with 2* 8W UV_B lamp ($\lambda_{\max} = 320$ nm, Intensity at 15 cm = 790 $\mu\text{W}/\text{cm}^2$) and 1*8W UV_C lamp ($\lambda_{\max} = 254$ nm, Intensity at 15 cm = 820 $\mu\text{W}/\text{cm}^2$) and the aqueous samples were kept at a distance of 15 cm for irradiation. The luminous intensity of irradiation at time t was determined in J/cm^2 by the formula $[(\mu\text{W}/\text{cm}^2)/10^6]*t$ (s). UV spectra including absorbance and transmittance studies was recorded using Shimadzu UV-6000 UV-vis spectrophotometer in a wavelength range of 800 to 200 nm.

The samples were drop-casted on a silicon wafer and AFM height images were recorded using tapping mode on a Bruker multimode 8 scanning probe microscope with silicon cantilever.

Samples were drop cast on a carbon coated Cu grid and TEM images were recorded using JEOL JEM 2100 with a Tungsten filament at an accelerating voltage of 120 kV.

3.4.3. Methods:

3.4.3.1. Synthesis and characterization of the polymers:

A. Random copolymerization of Hydroxy ethyl acrylamide (HEAm) with *N*-Isopropyl acrylamide (NIPAM) by ATRP method followed by grafting with coumarin moieties.

ATRP polymerization was performed with NIPAM and HEAm as co-monomers (Scheme 1). Coumarin carboxylic acid chloride was then tethered to the resulting copolymers using esterification. The detailed synthetic procedures of **CP1-3** are described as follows.

i. Random copolymerization by ATRP:

NIPAM, HEAm, Cu(I)Cl, Me₆TREN, and ethanol: water (1:1) were added in a schlenk tube under N₂ environment, capped with a rubber septum followed by degassing using N₂ bubbling for 15 minutes. Initiator (MeBrPhAc) was then added to the mixture and was degassed again for 15 minutes. The reaction mixture was stirred at room temperature for 24 hours followed by dilution with water. The solution was dialyzed against water for 3 days to remove the copper catalyst as well as unreacted monomers. NMR and GPC analysis confirmed the polymer with the percentage of comonomers and M_w , M_n , PDI .

P-1. Precursor Random copolymer of HEAm with NIPAM (DP = 200): NIPAM (16 mmol), HEAm (4 mmol), Cu(I)Cl (0.1 mmol), Me₆TREN (0.2 mmol), and ethanol: water

(1:1) were added in a schlenk tube under N₂ environment, capped with a rubber septum followed by degassing using N₂ bubbling for 15 minutes. Initiator (MeBrPhAc, 0.1 mmol) was then added to the mixture and was degassed again for 15 minutes. The polymerization was carried out by stirring at room temperature for 24 hours. Then the reaction mixture was diluted with water and was dialyzed against water for 3 days to remove the copper catalyst as well as unreacted monomers. ¹H NMR (400 MHz, D₂O): δ (ppm) 3.89– 3.71 (m, 17H, **CH**-(CH₃)₂), 3.64-3.57 (m, 9H, **CH**₂CH₂OH), 3.36–3.11 (m, 9H, CH₂**CH**₂OH), 2.12-1.8 (m, 22H, **CH**₂), 1.72-1.25 (m, 41H, **CH**₂), 1.10-0.9 (m, 103H, CH-(**CH**₃)₂) %HEAm = 19%. SEC analysis (DMF, PMMA standard): *M_n* = 26605 g/mol; *M_w* = 32078 g/mol; *M_w*/*M_n* = 1.20.

P-2. Precursor Random copolymer of HEAm with NIPAM (DP = 400): NIPAM (32 mmol), HEAm (8 mmol), Cu(I)Cl (0.1 mmol), Me₆TREN (0.2 mmol), and ethanol: water (1:1) were added in a schlenk tube under N₂ environment, capped with a rubber septum followed by degassing using N₂ bubbling for 15 minutes. Initiator (MeBrPhAc, 0.1 mmol) was then added to the mixture and was degassed again for 15 minutes. The polymerization was carried out by stirring at room temperature for 24 hours. Then the reaction mixture was diluted with water and was dialyzed against water for 3 days to remove the copper catalyst as well as unreacted monomers. ¹H NMR (400 MHz, D₂O): δ (ppm) 3.89–3.71 (m, 24H, **CH**-(CH₃)₂), 3.64-3.57 (m, 8H, **CH**₂CH₂OH), 3.36–3.11 (m, 8H, CH₂**CH**₂OH), 2.12-1.8 (m, 25H, **CH**₂), 1.72-1.25 (m, 42H, **CH**₂), 1.10-0.9 (m, 170H, CH-(**CH**₃)₂) %HEAm = 12 %. SEC analysis (DMF, PMMA standard): *M_n* = 41693 g/mol; *M_w* = 48393 g/mol; *M_w*/*M_n* = 1.16.

ii. Grafting of coumarin moieties on the polymers:

The synthesis of coumarin carboxylic acid chloride was performed according to the literature procedure. The coumarin carboxylic acid chloride solution in THF was added to a stirred solution of precursor polymer **P1-2** with Et₃N in THF under an N₂ environment. The solution was stirred under an N₂ environment at 50 °C for 5 hours. Then cooled back to 25 °C under N₂ environment for 48h. The solution was dialyzed against water for 3 days to remove the Et₃N as well as unreacted functionalities.

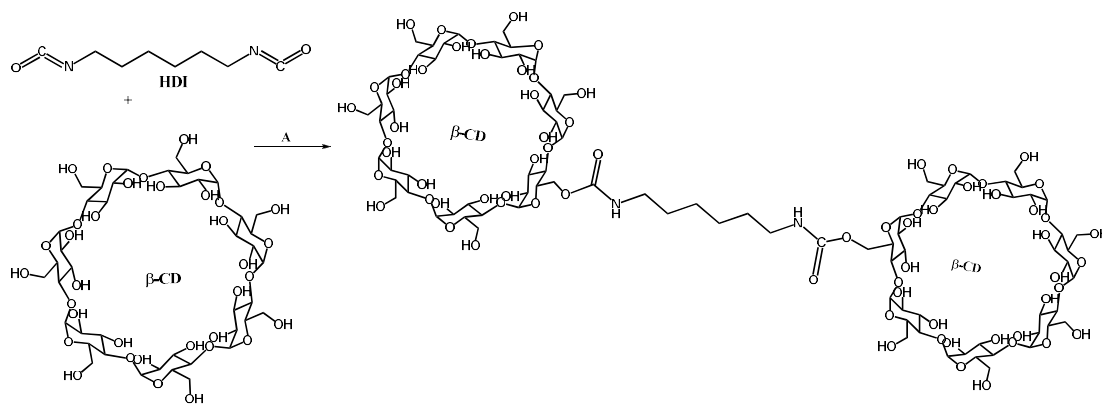
Polymer CP1: The solution of coumarin carboxylic acid chloride (1.01 mmol) in 20 mL THF was added to a stirred solution of polymer **P1** (0.02 mmol) with Et₃N (1.62 mmol) in 10 mL THF under N₂ environment. The solution was stirred under N₂ environment at 50 °C for 5 hours. Then cooled back to 25 °C under N₂ environment for 48 hours. The solution was dialyzed against water for 3 days to remove the Et₃N as well as unreacted functionalities. ¹H NMR (400 MHz, D₂O): δ (ppm) 7.95-7.90 (m, 1H, >C=**CH**-), 7.59-7.52 (m, 1H, >C=**CH**-), 6.96-6.84 (m, 2H, =CH-**CH**=C-**CH**=), 6.24-6.23 (m, 1H, =**CH**-CO-O-), 3.89– 3.71 (m, 22H, **CH**-(CH₃)₂), 3.64-3.57 (m, 11H, **CH**₂CH₂OH), 3.36–3.11 (m, 10H, CH₂**CH**₂OH), 2.12-1.8 (m, 27H, **CH**₂), 1.72-1.25 (m, 57H, **CH**₂), 1.10-0.9 (m, 146H, CH-(**CH**₃)₂). %Coumarin = 4%. SEC analysis (DMF, PMMA standard): $M_n = 27357$ g/mol; $M_w = 37183$ g/mol; $M_w/M_n = 1.31$.

Polymer CP2: The solution of coumarin carboxylic acid chloride (1.3 mmol) in 20 mL THF was added to a stirred solution of polymer **P2** (0.01 mmol) with Et₃N (2.02 mmol) in 10 mL THF under N₂ environment. The solution was stirred under N₂ environment at 50 °C for 5 hours. Then cooled back to 25 °C under N₂ environment for 48 hours. The solution was dialyzed against water for 3 days to remove the ET₃N as well as unreacted functionalities. ¹H NMR (400 MHz, D₂O): δ (ppm) 7.95-7.90 (m, 1.3H, >C=**CH**-), 7.59-7.52 (m, 1H, >C=**CH**-), 6.96-6.84 (m, 2H, =CH-**CH**=C-**CH**=), 6.24-6.23 (m, 1H, =**CH**-CO-O-), 3.89– 3.71 (m, 23H, **CH**-(CH₃)₂), 3.64-3.57 (m, 6H, **CH**₂CH₂OH), 3.36–3.11 (m, 6H, CH₂**CH**₂OH), 2.12-1.8 (m, 25H, **CH**₂), 1.72-1.25 (m, 43H, **CH**₂), 1.10-0.9 (m, 168H, CH-(**CH**₃)₂). % Coumarin = 4%. SEC analysis (DMF, PMMA standard): $M_n = 45197$ g/mol; $M_w = 53897$ g/mol; $M_w/M_n = 1.19$.

B. Synthesis of bis-β-CD crosslinker:

β-CD (2 g, 2.6 mmol) was dissolved in 30 mL of dried *N,N*-dimethylacetamide. After adding hexadimethyl isocyanate (0.16 g, 1 mmol), the solution was reacted at 70 °C for 3 hours. The solution was then cooled to room temperature and then precipitated from methanol/water 9:1 mixture. The precipitate was collected after centrifugation at 1000 rpm

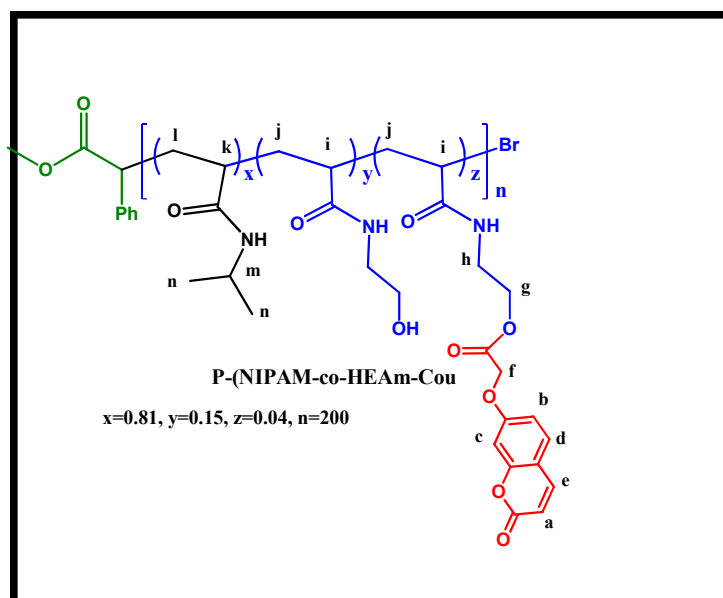
for 10 min and dried under vacuum with P_2O_5 at room temperature. The product (**bis- β -CD**) was obtained with a yield of 70%. 1H NMR (400 MHz, D_2O): δ (ppm) 4.99-5.02 (s, 7H, -O-**CH**-O-), 3.93-3.83 (m, 10 H, -O-**CH**- CH_2 -, -**CH**- CH_2 -O-CO-NH-), 3.85-3.75 (m, 21, -**CH**-**CH**-**CH**-, -O-**CH**- CH_2 -), 3.62-3.56 (m, 7H, O-**CH**- CH_2 -), 3.56-3.48 (m, 7H, O-**CH**-**CH**-), 3.17-3.02 (m, 2H, -NH- CH_2 - CH_2 -), 1.56-1.32 (m, 4H, -NH- CH_2 -**CH** $_2$ - **CH** $_2$ -) MALDI-TOF, $C_{92}H_{15}N_2O_{72}$ Calculated 2436.8 g/mol found $m/z = 2459.9$ g/mol [$M+Na^+$].



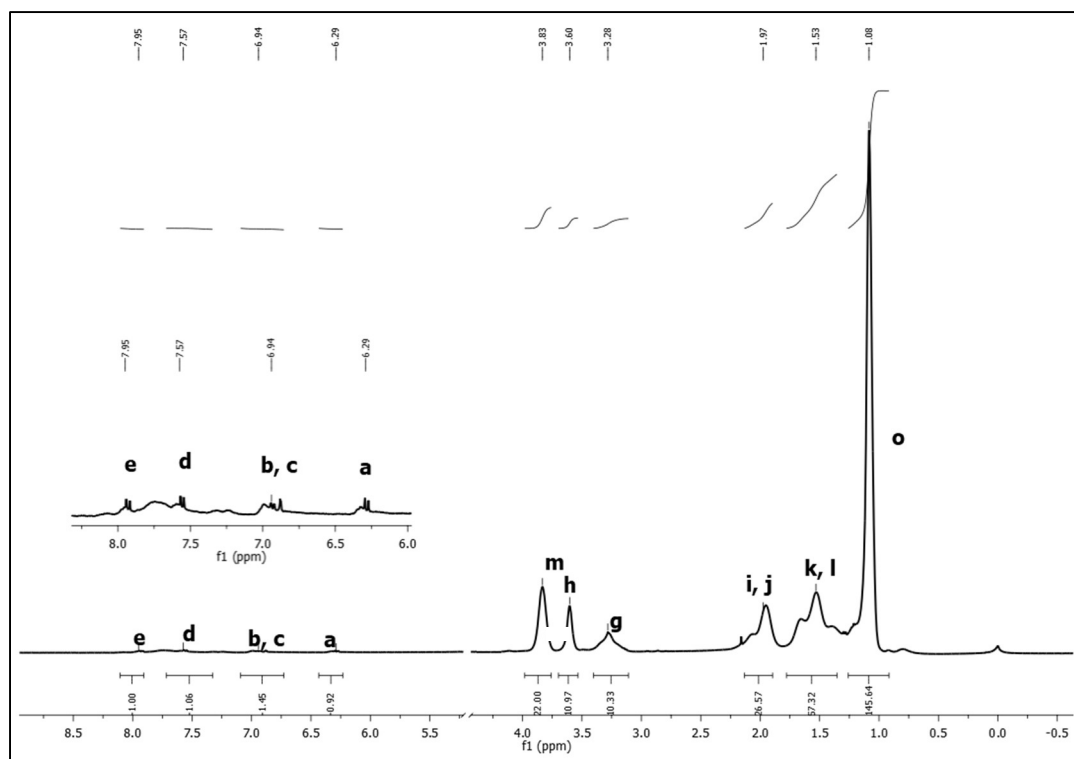
Scheme 3.3. Scheme for the synthesis of coumarin functionalized polymers: (A) DMAc, 70 °C, 3 h, 7

3.4.3.2. 1H NMR characterization of polymers (D_2O , 400MHz)

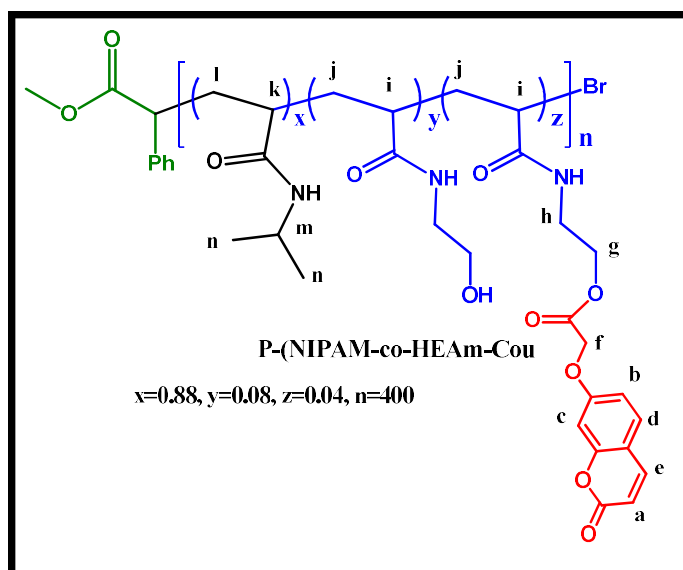
i. Polymer CP1 (DP-200)



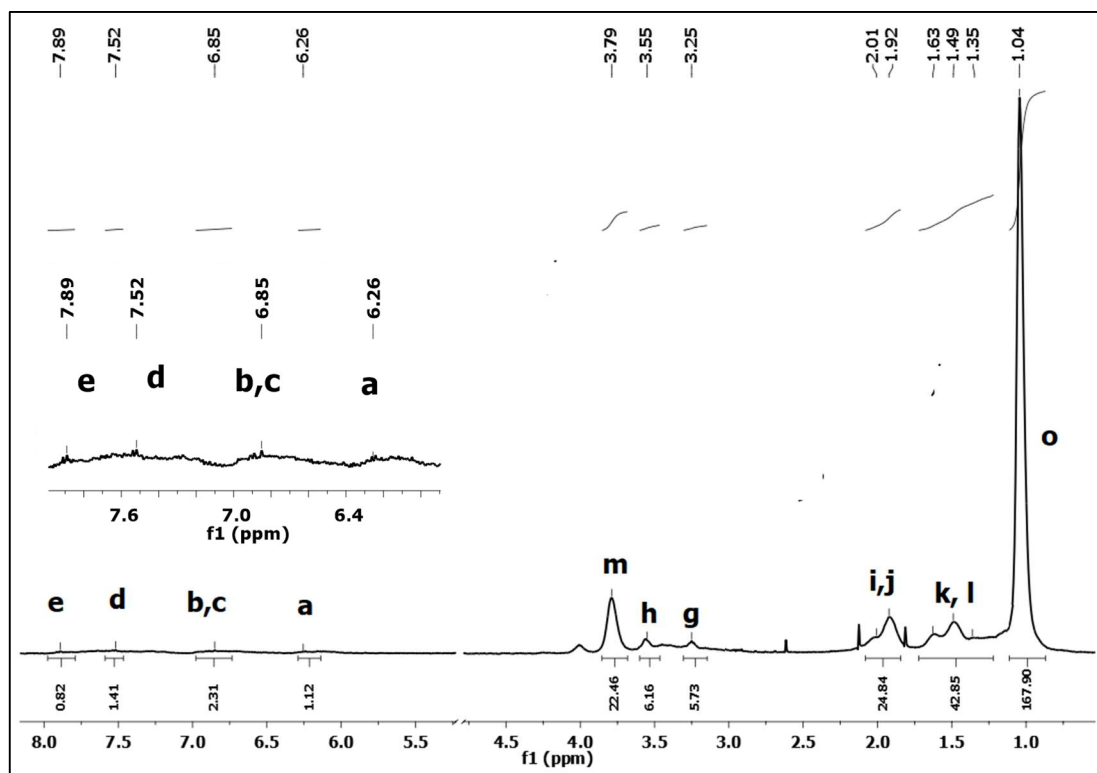
$$\% \text{ Cou} = \frac{x \frac{5}{12}}{\frac{x}{5} + \frac{144}{6}} * 100 = \frac{4.4/5}{4.4/5 + 144/6} * 100 = 4 \% \quad (x=a+b+c+d+e)$$



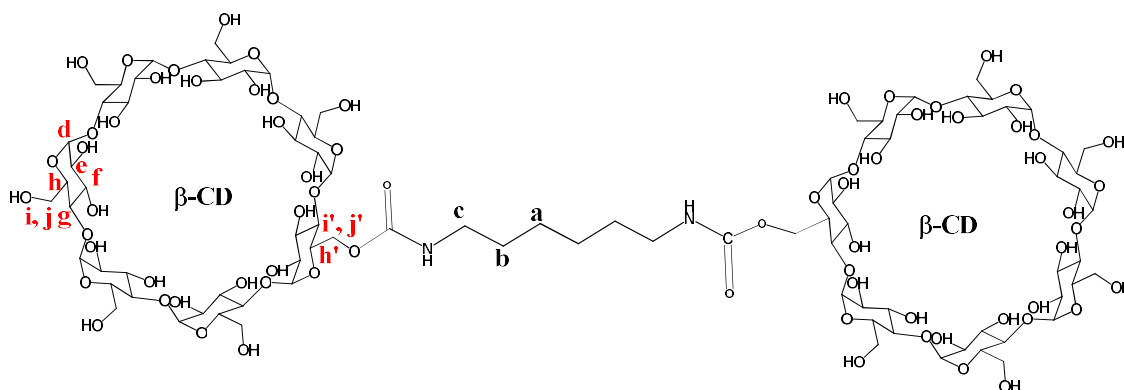
ii. Polymer CP2 (DP-400)

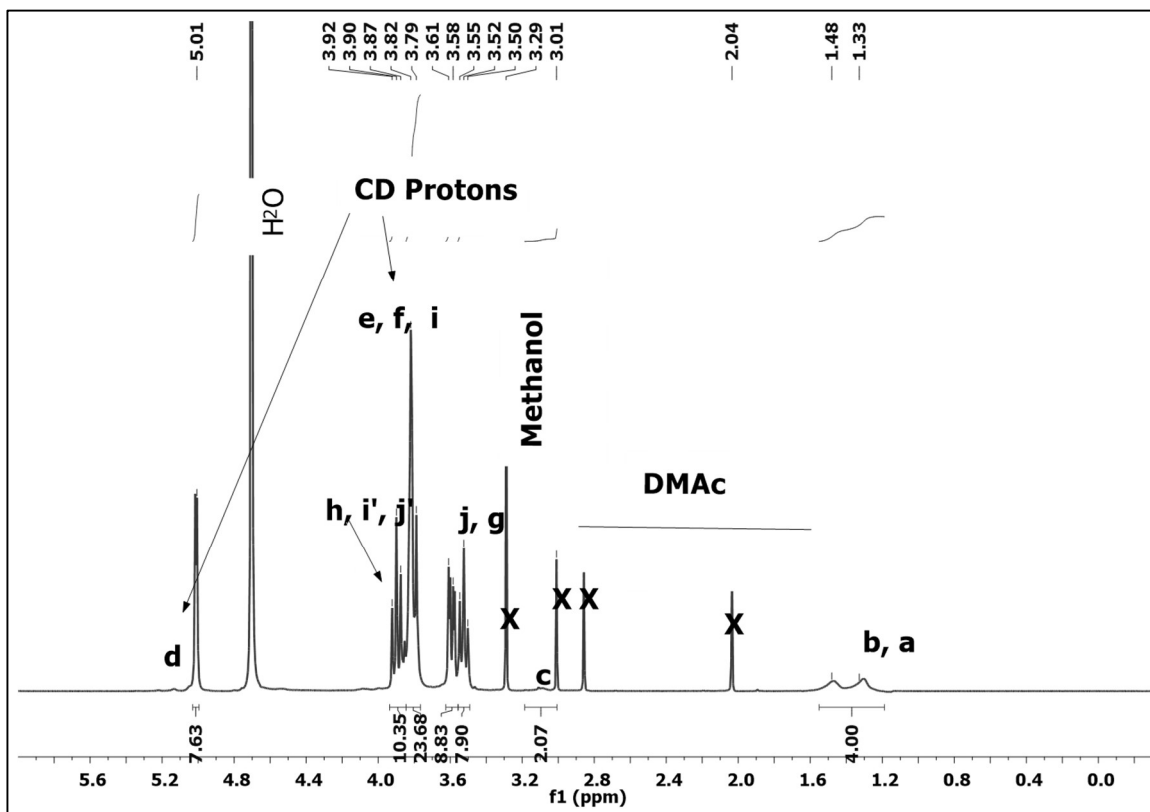


$$\% Cou = \frac{\frac{x}{5}}{\frac{x}{5} + \frac{n}{6}} * 100 = \frac{5.4/5}{5.4/5 + 168/6} * 100 = 4 \%$$

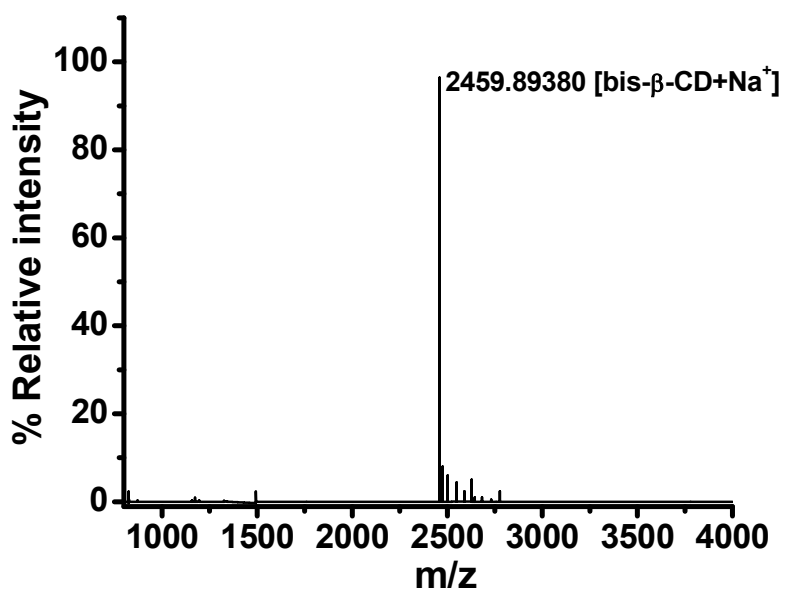


iii. bis-β-CD Crosslinker





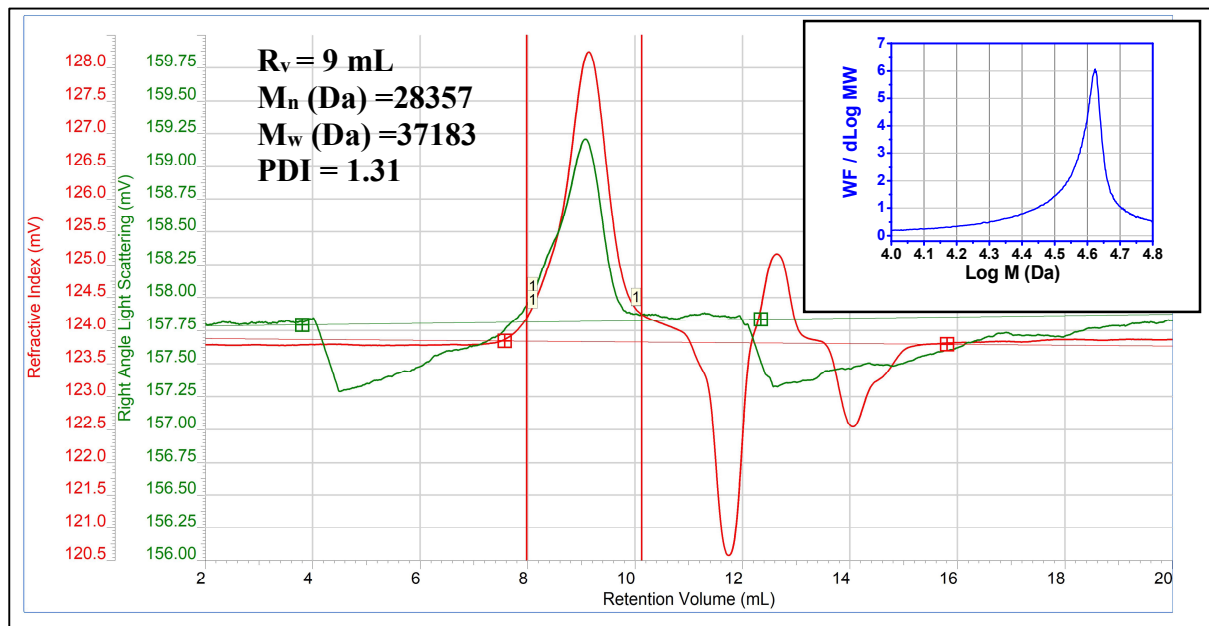
3.4.3.3. Mass spectrometry data



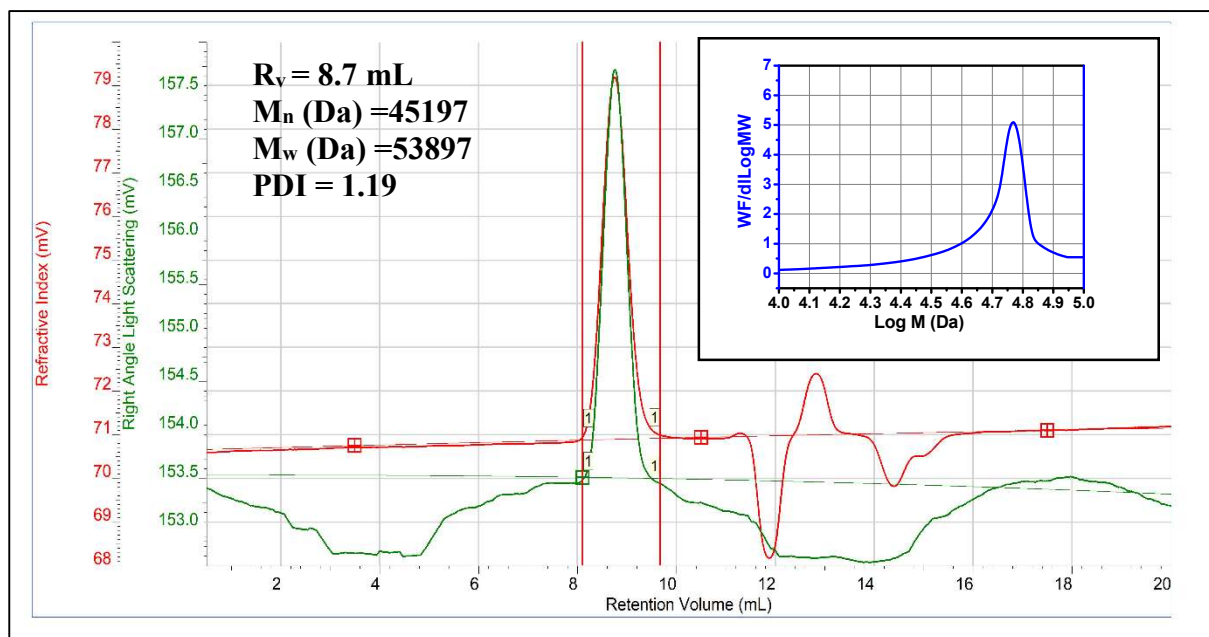
MALDI-TOF Spectra of bis- β -CD (DHB matrix)

3.4.3.4. Characterization of polymers by Size Exclusion Chromatography

i. Polymer CP1 (DP-200)



ii. Polymer CP2 (DP-400)



3.4.3.5. Monitoring photodimerization by UV and ¹H-NMR: The polymers were dissolved in Milli-Q water at a concentration of 0.01 mM. The solution was irradiated with UV_B light (2x8W) with different times of exposure and monitored for a decrease in absorbance at 300 to 350 nm. Photodimerization Degree was calculated with $PD = (A_0 - A_t)/A_0$, $\%PD = [(A_0 - A_t)/A_0] * 100$, where A_t is the absorbance at time t and A_0 is initial absorbance.

1 mM solution of the **CP1** polymer was prepared in D₂O and exposed to UV irradiation in NMR tube. ¹H NMR spectra were recorded at different time intervals (0, 3, 6, 9 h). %Photodimerization degree ($\%PD$) was calculated according to the formula $\%PD = [(I_o - I_t)/I_o] * 100$, $I_t = I_{(a+e)}/I_{(b+d)}$, where I_{a+e} and I_{b+d} are the integral areas of a, e, b, d protons, I_t is the ratio of the integral area of a+e with b+d protons at a specific time of irradiation (t). I_o is the ratio of the integral area of a+e with b+d protons for the native polymer.

3.4.3.6. Monitoring host-guest interaction by UV and ITC:

A. UV titration: The polymer **CP1** (0.01 mM) and **bis-β-CD** (1 mM) were taken in milli-Q water. Binding constant was determined to monitor the increase in absorbance at 300 to 350 nm on titration with the gradual addition of 2 mM **bis-β-CD** at 10mL per injection. The reciprocal plot of change in absorbance (ΔA) of **CP1** against the concentration of **bis-β-CD** was fitted by a non-linear least square equation to obtain binding constant value.

$$\Delta A = \frac{1}{2} \left\{ \epsilon([H]_0 + [G]_0 + \frac{1}{K_a}) \pm \sqrt{\epsilon^2([H]_0 + [G]_0 + \frac{1}{K_a})^2 - 4\epsilon^2[H]_0[G]_0} \right\} \dots \dots \dots (1)$$

Where ΔA is the absorption change of **CP1** upon addition of **bis-β-CD** as $\Delta A = A_{(\text{with bis-}\beta\text{-CD})} - A_{(\text{without bis-}\beta\text{-CD})}$, ϵ is the sensitivity factor, and $[H]_0$ and $[G]_0$ are the initial concentrations of **bis-β-CD** and **CP1**, respectively.

Job's plot was obtained by varying the molar ratio **CP1** to **bis-β-CD** at a ratio from 0 to 1 keeping the total concentration constant at 0.01 mM.

B. ITC titration: ITC isotherm for injection of 1 mM **bis-β-CD** solution in 0.02 mM **CP1** solution at 298 K, Data points were plotted as integrated heat of interactions as a function of molar ratio and fitted with one set of binding site model.

3.4.3.7. Monitoring Size compaction by DLS measurements: Samples were prepared by dissolving polymer **CP1-2** in milli-Q water at a concentration of 0.01 mM and filtered through a 0.2 μm Nylon filter prior to analysis. The samples were monitored for a change in size upon chain collapse *via* irradiation with UV_B light (2x8W) to form **di-CP1-2** NPs and addition of gradient concentration of **bis- β -CD** host to form **CP1 \subset bis- β -CD** NPs at 25 °C

3.4.3.8. Small angle Neutron scattering (SANS) studies: Neutron scattering experiments were performed by dissolving polymer solution in a deuterated solvent in order to acquire an enhanced scattering contrast. Samples were prepared by dissolving polymer **CP1-2** in D₂O (c = 1 mg/mL) and filtered through a 0.2 μm Nylon filter prior to analysis. The scattering data were acquired in quartz cuvette before and after chain collapse *via* photo irradiation and addition of **bis- β -CD** host. The experiments were performed at the SANS diffractometer at Guide Tube Laboratory, Dhruva Reactor, Bhabha Atomic Research Centre, Mumbai, India.⁶⁷ The instrument covers a Q-range of 0.017– 0.3 \AA^{-1} ($Q=4\pi \sin\theta/\lambda$, where 2θ is the scattering angle and λ is the incident neutron wavelength). The mean wavelength of the monochromatized beam from the neutron velocity selector is 5.2 \AA with a spread of $\Delta\lambda/\lambda \sim 15\%$. The angular distribution of neutrons scattered by the sample (in quartz cuvette) is recorded using a 1 m long one-dimensional He³ position-sensitive detector. Measured SANS data were corrected for background, empty-cuvette contribution, and sample transmission, and normalized to absolute cross-section units. Further, the data were fitted with SASfit software using generalized Gaussian coil model to calculate the integral structural parameters e.g. radii of gyration (**R_g**) and scaling exponent (ν). The differential scattering cross-section per unit volume ($d\Sigma/d\Omega$) as measured for a system of monodisperse particles in a medium can be expressed as⁶⁸

$$\frac{\delta\Sigma}{\delta\Omega}(\Theta) = nV^2(\rho_p - \rho_s)^2P(Q)S(Q) + B \text{ -----(2)}$$

where n denotes the number density of particles, ρ_p and ρ_s are, respectively, the scattering length densities of particle and solvent and V is the volume of the particle. P(Q) is the intra-particle structure factor and S(Q) is the inter-particle structure factor. B is a constant term representing the incoherent background, which is mainly due to

the hydrogen present in the sample. Intra-particle structure factor $P(Q)$ is decided by the shape and size of the particle and is the square of single-particle form factor $F(Q)$ as determined by

$$P(Q) = \langle |F(Q)|^2 \rangle \text{-----(3)}$$

For a spherical particle of radius R , $F(Q)$ is given by

$$F(Q) = 3 \left[\frac{\sin(QR) - QR \cos(QR)}{(QR)^3} \right] \text{-----(4)}$$

The polymer chains are modeled using the form factor of Gaussian chains. The form factor of Gaussian chain coils with the radius of gyration R_g is given by

$$P(Q) = 2 \frac{\exp(-Q^2 R_g^2) + Q^2 R_g^2 - 1}{(Q^2 R_g^2)^2} \text{-----(5)}$$

The excluded volume parameter from the Flory mean field theory (scaling exponent, ν) is an important parameter to measure the macromolecular conformation in solution. The scaling exponent can be derived from the double logarithmic SANS scattering curve as follows

$$\nu = \frac{-1}{\text{Slope}_{\text{scattering curve}}} \text{-----(6)}$$

The polydispersity in the size distribution of particle is incorporated using the following integration⁶⁹

$$\frac{\delta \Sigma}{\delta \Omega}(\Theta) = \int \frac{\delta \Sigma}{\delta \Omega}(\Theta, P) \phi(P) \delta P + B \text{-----(7)}$$

where $f(R)$ is the particle size distribution and usually accounted for by a log-normal distribution as given by

$$f(R) = \frac{1}{\sqrt{2\pi} R \sigma} \exp\left[-\frac{1}{2\sigma^2} \left(\ln \frac{R}{R_{med}}\right)^2\right] \text{-----(8)}$$

where R_{med} is the median value and σ is the standard deviation (polydispersity) of the distribution. The mean radius (R_m) is given by $R_m = R_{med} \exp(\sigma^2/2)$. The data have been analyzed by comparing the scattering from different models to the experimental data. Throughout the data analysis, corrections were made for instrumental smearing, where the calculated scattering profiles were smeared by the appropriate resolution function to compare with the measured data.⁷⁰ The fitted parameters in the analysis

were optimized using the nonlinear leastsquare fitting program to the model scattering.⁷¹

3.4.3.9. Microscopic analysis: 10 μ L of the samples (aqueous solutions of native **CP1-2** polymer, **di-CP1-2** NPs, **CP1 \subset bis- β -CD** NPs at a concentration of 0.01 mM) were drop-casted on a silicon wafer for AFM and Cu grid for TEM followed by washing with water to remove excess polymer. The samples were dried overnight. AFM height images were recorded by tapping mode on a Bruker Multimode 8 scanning probe microscope with silicon cantilever (Bruker) and analyzed using the software NanoScope Analysis 1.5. TEM images were recorded using JEOL JEM 2100 with a Tungsten filament at an accelerating voltage of 120 kV. The size distributions of the nanoparticles were analyzed using image-J software, from U.S. National Institutes of Health.

3.4.3.10. Monitoring LCST by UV-vis transmittance, DLS and SANS studies: The aqueous polymer **CP1** solution ($c = 0.02$ mM) was monitored for a decrease in %Transmittance at 563 nm upon photoirradiation or addition of host **bis- β -CD** in temperature ramp-up experiment from 20 to 70 $^{\circ}$ C at a rate of 2.5 $^{\circ}$ C/min. Size increase due to aggregation on heating above LCST for **CP1** native polymer, **di-CP1**, **CP1 \subset bis- β -CD** NPs was monitored by temperature trend analysis in DLS. samples from 20-70 $^{\circ}$ C at a rate of 5 $^{\circ}$ C/min. The polymer sample dissolved in D₂O ($c = 5$ mg/mL) and filtered through a 0.2 μ m Nylon filter prior to SANS temperature analysis.

3.4.3.11. Sequential folding study: The polymer **CP1** and **bis- β -CD** was dissolved in water to form a stock solution ($c = 0.04$ mM each). The host and guest solutions were mixed in a 1:1 ratio to form **CP1 \subset bis- β -CD** solution with 0.02 mM **CP1** and **bis- β -CD** in the solution. The resulting solution was irradiated with UV_B light for 30 min to form **di-CP1 \subset bis- β -CD** NPs. Further, the solution was irradiated with UV_C light for 15 min to form decrosslinked **di-CP1 \subset bis- β -CD**. Finally, the solution was heated above LCST to observe hydrophilic to hydrophobic transition and aggregation to form nanoclusters.

3.4.3.12. Molecular Dynamics Simulations: To obtain the atomistic details of the interactions between di-Coumarin and β -CD, we performed classical MD simulations. AMBER18 (GLYCAM06) force field was used for the parametrization of the β -CD molecule.⁷² However, the parameters for *syn*-di-HT was optimized with the general amber force field (GAFF).⁷³ TIP3P model potential was used for the water solvent for simulation.⁷⁴ A cubic simulations cell containing *syn*-di-HT isomer of coumarin dimer, β -CD, and solvent molecules with a total of 11808 atoms were chosen. The MD simulations were performed utilizing the NAMD simulation package.⁷⁵ Over 200 ns long NVT simulation trajectories were obtained to analyze the statistic using VMD visualization and analysis tools.⁷⁶

3.4.3.13. Determination of percentage loading of the cargo: RhB dye or Ibu drug was added to the polymeric system (Native CP1, di-CP1 or CP1 \subset bis- β -CD, c = 1 mg/mL) to result in a polymeric drug delivery system with 50%w/w cargo at 10 °C and kept for release in PBS buffer (10 mM, pH 7, 200 mL) at 4 °C for 24 h to release free drug *via* cellulose dialysis membrane (3-5 KDa). The cargo loaded was determined by monitoring UV absorbance at 272 nm (Ibu) or 549 nm (RhB). The samples were then lyophilized to determine the total weight of cargo loaded polymer solution.

$$\% \text{ Cargo loading} = \frac{W_{\text{Cargo}}}{W_{\text{Total}}} * 100 \text{-----} \quad (9)$$

W_{cargo} is the weight of drug loaded (mg) and W_{total} is the total weight of cargo loaded polymer solution (mg) determined after lyophilization.

3.4.3.14. *In vitro* cargo release studies: The cargo loaded polymeric drug delivery system (1 mg/mL) was kept for release studies in PBS buffer (10 mM, pH7, 200 mL) at 37 °C for 24 h to release drug *via* cellulose dialysis membrane (3-5 kDa). The release pattern was monitored through UV for 24 h, after which the temperature was increased to 50 °C to further monitor for 8h. The cargo release was determined by UV absorbance at 272 nm (Ibu) or 549 nm (RhB)

$$\% \text{ Cargo release} = \frac{W_{\text{cumulative}}}{W_{\text{cargo}}} * 100 \text{-----} \quad (10)$$

Where $W_{cumulative}$ is cumulative cargo weight released in the buffer, W_{cargo} is the amount of loaded cargo in mg.

3.5. References

- 1 M. Nahar, T. Dutta, S. Murugesan, A. Asthana, D. Mishra, V. Rajkumar, M. Tare, S. Saraf and N. K. Jain, *Crit. Rev. Ther. Drug Carrier Syst.*, 2006, **23**, 259–318.
- 2 L. E. Van Vlerken and M. M. Amiji, *Expert Opin. Drug Deliv.*, 2006, **3**, 205–216.
- 3 M. Shokeen, E. D. Pressly, A. Hagooly, A. Zheleznyak, N. Ramos, A. L. Fiamengo, M. J. Welch, C. J. Hawker and C. J. Anderson, *ACS Nano*, 2011, **5**, 738–747.
- 4 M. Sui, W. Liu and Y. Shen, *J. Cont. Release*, 2011, **155**, 227–236.
- 5 C. Yang, A. B. Ebrahim Attia, J. P. K. Tan, X. Ke, S. Gao, J. L. Hedrick and Y. Y. Yang, *Biomaterials*, 2012, **33**, 2971–2979.
- 6 A. N. Wilson and A. Guiseppi-Elie, *Inter. J. Pharm.*, 2014, **461**, 214–222.
- 7 C. K. Lyon, A. Prasher, A. M. Hanlon, B. T. Tuten, C. A. Tooley, P. G. Frank and E. B. Berda, *Polym. Chem.*, 2015, **6**, 181–197.
- 8 O. Altintas and C. Barner-Kowollik, *Macromol. Rapid Commun.*, 2012, **33**, 958–971.
- 9 M. K. Aiertza, I. Odriozola, G. Cabañero, H. J. Grande and I. Loinaz, *Cell. Mol. Life Sci.*, 2012, **69**, 337–346.
- 10 M. Ouchi, N. Badi, J. F. Lutz and M. Sawamoto, *Nat. Chem.*, 2011, **3**, 917–924.
- 11 J. Romulus and M. Weck, *Macromol. Rapid Commun.*, 2013, **34**, 1518–1523.
- 12 L. Liu and S. H. Gellman, *Macromolecules*, 2020, **53**, 8141–8143.
- 13 O. Altintas, J. Willenbacher, K. N. R. Wuest, K. K. Oehlenschlaeger, P. Krolla-Sidenstein, H. Gliemann and C. Barner-Kowollik, *Macromolecules*, 2013, **46**, 8092–8101.
- 14 Y. Zhou, Y. Qu, Q. Yu, H. Chen, Z. Zhang and X. Zhu, *Polym. Chem.*, 2018, **9**, 3238–3247.
- 15 Y. Liu, S. Pujals, P. J. M. Stals, T. Paulöhr, S. I. Presolski, E. W. Meijer, L. Albertazzi and A. R. A. Palmans, *J. Am. Chem. Soc.*, 2018, **140**, 3423–3433.
- 16 L. N. Neumann, D. A. Urban, P. Lemal, S. Ramani, A. Petri-Fink, S. Balog, C. Weder and S. Schrettl, *Polym. Chem.*, 2020, **11**, 586–592.
- 17 A. Sanchez-Sanchez, I. Pérez-Baena and J. A. Pomposo, *Molecules*, 2013, **18**, 3339–3355.
- 18 E. A. Appel, J. Dyson, J. del Barrio, Z. Walsh and O. A. Scherman, *Angew. Chem. Int. Ed.*, 2012, **124**, 4261–4265.
- 19 F. Wang, H. Pu and X. Che, *Chem. Comm.*, 2016, **52**, 3516–3519.
- 20 E. J. Foster, E. B. Berda and E. W. Meijer, *J. Pol. Sci, Part A: Pol. Chem.*, 2011, **49**, 118–126.
- 21 J. P. Joseph, C. Miglani, A. Singh, D. Gupta and A. Pal, *Soft Matter*, 2020, **16**, 2506–2515.
- 22 J. A. Pomposo, J. Rubio-Cervilla, A. J. Moreno, F. Lo Verso, P. Bacova, A. Arbe and J. Colmenero, *Macromolecules*, 2017, **50**, 1732–1739.

- 23 J. Zhuang, M. R. Gordon, J. Ventura, L. Li and S. Thayumanavan, *Chem. Rev.*, 2013, **42**, 7421–7435.
- 24 S. Guragain, B. P. Bastakoti, V. Malgras, K. Nakashima and Y. Yamauchi, *Chem. Eur. J.*, 2015, **21**, 13164–13174.
- 25 J. Zhang, Q. Zou and H. Tian, *Adv. Mater.*, 2013, **25**, 378–399.
- 26 H. Tian and S. Yang, *Chem. Soc. Rev.*, 2004, **33**, 85–97.
- 27 F. Biedermann, I. Ross and O. A. Scherman, *Polym. Chem.*, 2014, **5**, 5375–5382.
- 28 D. H. Qu, Q. C. Wang, Q. W. Zhang, X. Ma and H. Tian, *Chem. Rev.*, 2015, **115**, 7543–7588.
- 29 C. M. Chung, Y. S. Roh, S. Y. Cho and J. G. Kim, *Chem. Mater.*, 2004, **16**, 3982–3984.
- 30 A. Chatterjee, B. Maity and D. Seth, *J. Phys. Chem. B*, 2014, **118**, 9768–9781.
- 31 G. Kaur, P. Johnston and K. Saito, *Polym. Chem.*, 2014, **5**, 2171–2186.
- 32 J. P. Joseph, A. Singh, D. Gupta, C. Miglani and A. Pal, *ACS Appl. Mater. Interfaces*, 2019, **11**, 28213–28220.
- 33 S. Mavila, O. Eivgi, I. Berkovich and N. G. Lemcoff, *Chem. Rev.*, 2016, **116**, 878–961.
- 34 M. Gonzalez-Burgos, A. Latorre-Sanchez and J. A. Pomposo, *Chem. Soc. Rev.*, 2015, **44**, 6122–6142.
- 35 M. González-Burgos, E. González and J. A. Pomposo, *Macromol. Rapid Commun.*, 2018, **39**, 1–5.
- 36 A. Sanchez-Sanchez, S. Akbari, A. Etxeberria, A. Arbe, U. Gasser, A. J. Moreno, J. Colmenero and J. A. Pomposo, *ACS Macro Lett.*, 2013, **2**, 491–495.
- 37 A. Sanchez-Sanchez, S. Akbari, A. J. Moreno, F. Lo Verso, A. Arbe, J. Colmenero and J. A. Pomposo, *Macromol. Rapid Commun.*, 2013, **34**, 1681–1686.
- 38 R. Gracia, M. Marradi, G. Salerno, R. Pérez-Nicado, A. Pérez-San Vicente, D. Dupin, J. Rodriguez, I. Loinaz, F. Chiodo and C. Nativi, *ACS Macro Lett.*, 2018, **7**, 196–200.
- 39 Y. J. Kim and Y. T. Matsunaga, *J. Mater. Chem. B*, 2017, **5**, 4307–4321.
- 40 P. Sánchez-Moreno, J. de Vicente, S. Nardecchia, J. A. Marchal and H. Boulaiz, *Nanomaterials*, 2018, **8**, 1–32.
- 41 I. A. van Hees, A. H. Hofman, M. Dompé, J. van der Gucht and M. Kamperman, *Eur. Polym. J.*, 2020, **141**, 110034.
- 42 C. Hu, W. Xu, C. M. Conrads, J. Wu and A. Pich, *Journal of Colloid and Interface Science*, 2021, **582**, 1075–1084.
- 43 M. A. Ward and T. K. Georgiou, *Polymers*, 2011, **3**, 1215–1242.
- 44 C. C. Cheng, D. J. Lee, Z. S. Liao and J. J. Huang, *Polym. Chem.*, 2016, **7**, 6164–6169.
- 45 Y. Yang, P. Chen, Y. Cao, Z. Huang, G. Zhu, Z. Xu, X. Dai, S. Chen, B. Miao and L. T. Yan, *Langmuir*, 2018, **34**, 9477–9488.
- 46 G. S. Hammond, C. A. Stout and A. A. Lamola, *J. Am. Chem. Soc.*, 1964, **86**, 3103–3106.
- 47 N. Barooah, B. C. Pemberton, A. C. Johnson and J. Sivaguru, *Photochem. Photobio. Sci.*, 2008, **7**, 1473–1479.
- 48 M. González-Burgos, A. Arbe, A. J. Moreno, J. A. Pomposo, A. Radulescu and J. Colmenero, *Macromolecules*, 2018, **51**, 1573–1585.

- 49 R. Upadhyaya, N. S. Murthy, C. L. Hoop, S. Kosuri, V. Nanda, J. Kohn, J. Baum and
A. J. Gormley, *Macromolecules*, 2019, **52**, 8295–8304.
- 50 A. Pal, S. Datta, V. K. Aswal and S. Bhattacharya, *J. Phys. Chem. B*, 2012, **116**,
13239–13247.
- 51 A. Takadate, H. Fujino and S. Goya, *Yakugaku Zasshi-J. Pharm. Soc. Jap.*, 1983, **103**,
193–197.
- 52 C. Folch-Cano, C. Olea-Azar, E. Sobarzo-Sánchez, C. Alvarez-Lorenzo, A.
Concheiro, F. Otero and C. Jullian, *J. Sol. Chem.*, 2011, **40**, 1835–1846.
- 53 E. B. Berda, E. J. Foster and E. W. Meijer, *Macromolecules*, 2010, **43**, 1430–1437.
- 54 C. Wu and S. Zhou, *Macromolecules*, 1995, **28**, 8381–8387.
- 55 X. Li, H. Shamsijazeyi, S. L. Pesek, A. Agrawal, B. Hammouda and R. Verduzco,
Soft Matter, 2014, **10**, 2008–2015.
- 56 J. Clara-Rahola, A. Fernandez-Nieves, B. Sierra-Martin, A. B. South, L. A. Lyon, J.
Kohlbrecher and A. Fernandez Barbero, *J. Chem. Phys.*, , DOI:10.1063/1.4723686.
- 57 A. M. Al-Baradi, S. Rimmer, S. R. Carter, J. P. De Silva, S. M. King, M. Maccarini,
B. Farago, L. Noirez and M. Geoghegan, *Soft Matter*, 2018, **14**, 1482–1491.
- 58 X. P. Qiu, F. Tanaka and F. M. Winnik, *Macromolecules*, 2007, **40**, 7069–7071.
- 59 S. Honda, T. Yamamoto and Y. Tezuka, *J. Am. Chem. Soc.*, 2010, **132**, 10251–10253.
- 60 J. Roovers and P. M. Toporowski, *Macromolecules*, 1983, **16**, 843–849.
- 61 Y. Zhao, L. Tremblay and Y. Zhao, *Macromolecules*, 2011, **44**, 4007–4011.
- 62 F. Tanaka, *J. Chem. Phys.*, 1987, **87**, 4201–4206.
- 63 W. S. Chung, N. J. Turro, J. Silver and W. J. le Noble, *J. Am. Chem. Soc.*, 1990, **112**,
1202–1205.
- 64 B. C. Pemberton, N. Barooah, D. K. Srivatsava and J. Sivaguru, *Chem. Comm.*, 2010,
46, 225–227.
- 65 W. L. F. Armarego, *Purification of laboratory chemicals*, 2017.
- 66 I. M. Rosenberg, *Protein Analysis and Purification Benchtop Techniques*, Springer
Science & Business Media, 2013.
- 67 P. S. G. V. K. Aswal, *Curr. Sci.*, 2000, **79**, 947.
- 68 E. W. Kaler, *J. Appl. Cryst.*, 1988, **21**, 729–736.
- 69 J. S. Pedersen, *Adv Coll. Inter Sci.*, 1997, **70**, 171–210.
- 70 J. S. Pedersen and C. Riekkel, *J Appl. Cryst.*, 1991, **24**, 893–909.
- 71 P. R. Bevington, *Data Reduction and Error Analysis for the Physical Sciences*,
McGraw-Hill, New York, 1969.
- 72 D. A. Case, T. E. Cheatham, T. Darden, H. Gohlke, R. Luo, K. M. Merz, A. Onufriev,
C. Simmerling, B. Wang and R. J. Woods, *J. Comp. Chem.*, 2005, **26**, 1668–1688.
- 73 J. Wang, R. M. Wolf, J. W. Caldwell, P. A. Kollman and D. A. Case, *J. Comput.*
Chem., 2004, **56531**, 1157–1174.
- 74 W. L. Jorgensen, J. Chandrasekhar, J. D. Madura, R. W. Impey and M. L. Klein, *J.*
Chem. Phys., 1983, **79**, 926–935.
- 75 J. C. Phillips, R. Braun, W. Wang, J. Gumbart, E. Tajkhorshid, E. Villa, C. Chipot,
R. D. Skeel, L. Kalé and K. Schulten, *J. Comput Chem.*, 2005, **26**, 1781–1802.
- 76 W. Humphrey, A. Dalke and K. Schulten, *J. Mol. Graph.*, 1996, **14**, 33–38.

Chapter 4

Tandem Interplay of Host-guest Interaction and Photo-responsive Supramolecular Polymerization to 1D and 2D Functional Peptide Materials

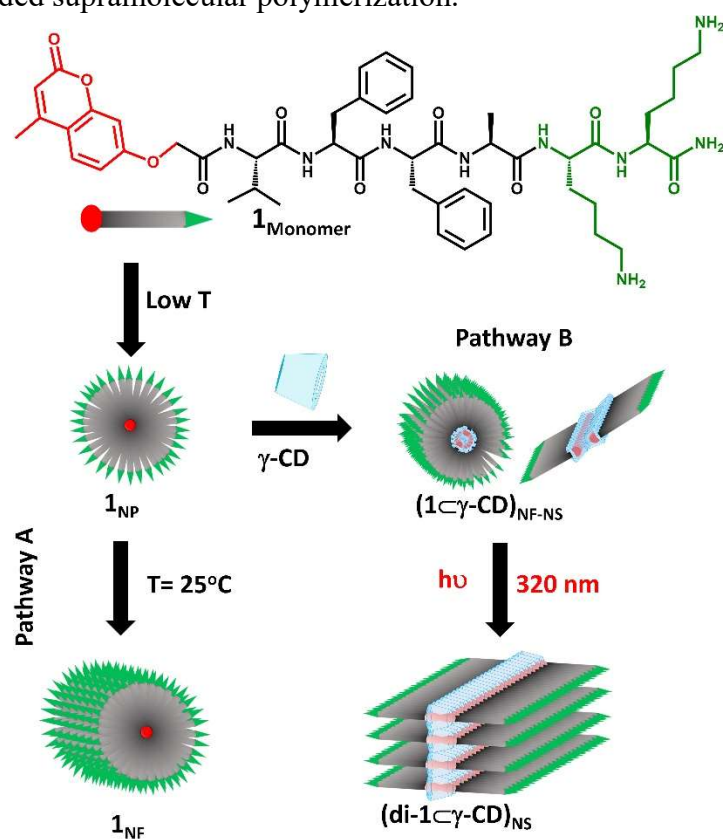
In this chapter, Peptide 1 with an A β 42 amyloid nucleating core and photodimerizable 4-methylcoumarin moiety at its N terminus demonstrates step-wise self-assembly in water to form nanoparticles, with eventual transformation into 1D nanofibers. Addition of γ -cyclodextrin (γ -CD) to 1 with subsequent irradiation with UV light at 320 nm resulted in morphological conversion to free standing 2D nanosheets mediated by the host-guest interaction. Mechanical agitation of the 1D and 2D nanostructures led to seeds with narrow polydispersity indices, which by mediation of seeded supramolecular polymerization found seamless control over the dimensions of the nanostructures. Such structural and temporal control to differentiate the pathway was exploited to tune the mechanical strength of hierarchical hydrogel materials. Finally, the peptide fibers and sheets were envisaged as excellent exfoliating agents for inorganic hybrid materials e.g. MoS₂.

4.1. Introduction

Over the recent decade, there has been a remarkable upsurge in designing complex functional supramolecular system in a bid to mimic natural biomolecular system.¹⁻³ However, predominantly thermodynamically controlled artificial supramolecular systems have always lagged behind the natural systems with temporal and adaptive structural control owing to the pathway dictated out-of-equilibrium self-assembly. Bottom-up self-assembly to one dimensional (1D) anisotropic materials *e.g.* nanofibers, nanorods and nanotubes have been of particular interest for their immense applications in nanomedicine, catalysis *etc.*⁴ Of late, two dimensional (2D) nanomaterials engineered with well-defined thickness and dimension has emerged with paramount importance, due to high order, flexibility and the augmented anisotropy of the materials owing to their molecular thickness and infinite planar dimensions.⁵ However, a precise control over the shape and size of the nanomaterials derived from the complex supramolecular systems remained elusive to chemists until a recent times when the concept of pathway complexity, with the coexistence of multiple competitive pathways in a self-assembly process, provided a new paradigm and tool to control the fate of supramolecular systems under a variety of conditions.⁶⁻¹⁰ Arresting the metastable state allows access to kinetically trapped species,¹¹⁻¹⁴ which can be employed in seeded supramolecular polymerization mediated by nucleation-elongation process, similar to the living polymerization in covalent polymers.¹⁵ The model of pathway complexity in functionalized porphyrin, perylene bisimide, naphthalene diimide and corannulene molecules to form kinetically or thermodynamically controlled aggregates by tweaking the conditions, *e.g.* temperature and solvents, was successfully demonstrated by the groups of Sugiyasu, Takeuchi, Wurthner, Ghosh and Aida.¹⁶⁻²⁰ In another interesting strategy, interplay of dynamic covalent chemistry and self-replication was exploited by Otto *et al.* to grow kinetically controlled peptide fibers from metastable macrocycles.²¹ However, such control over dimension was limited only in 1D materials until recently, when Sugiyasu *et al.* reported J- and H-type aggregation in porphyrin derivatives to promote supramolecular 1D nanofibers and 2D nanosheets.²² Recently, our group also demonstrated pathway driven self-assembly of peptide amphiphile based on A β 42 amyloid nucleating core *i.e.* ¹⁸VFFA²¹ to control the length dimension of the fibers that dictated the mechanical properties of the

resulting fibrous hydrogel.²³ Now, we intend to explore the possibility of designing new 2D peptide material by tethering a functional moiety with orthogonal interaction to the same peptide sequence, ^NVFFA^C, that may alter the pathway.

Herein, we postulate stepwise self-assembly of short peptide amphiphile, **1** mediated by β -sheet interaction to grow 1D nanofiber (**1**_{NF}) in water through formation of metastable nanoparticles, **1**_{NP} (Scheme 4.1). Also, the addition of equimolar γ -CD and subsequent UV irradiation ($\lambda = 320$ nm) converts the **1**_{NP} to 2D nanosheet (**di-1** $\subset\gamma$ -CD)_{NS} via host-guest interaction and photodimerization of pendant 4-methylcoumarin moiety. For the first time, we report design and precise control of the template-less free standing peptide nanosheet mediated by seeded supramolecular polymerization.



Scheme 4.1. Molecular structure of peptide **1** and its cartoon representation. **1**_{monomer} in HFIP to form metastable nanoparticle, **1**_{NP} at low temperature with eventual formation of nanofiber, **1**_{NF} on increasing temperature (Pathway A). Addition of γ -CD to the metastable nanoparticles followed by UV irradiation ($\lambda = 320$ nm) leads to formation of 2D nanosheet (**di-1** $\subset\gamma$ -CD)_{NS} (Pathway B).

The dimensional variations of the supramolecular polymer are successfully exploited in generating hydrogels with tunable mechanical properties. Towards the end, we successfully demonstrate very efficient, environmentally benign method of MoS₂ exfoliation using the advantages of surface functionality and dimensions of the peptide materials.

4.2. Results and discussion

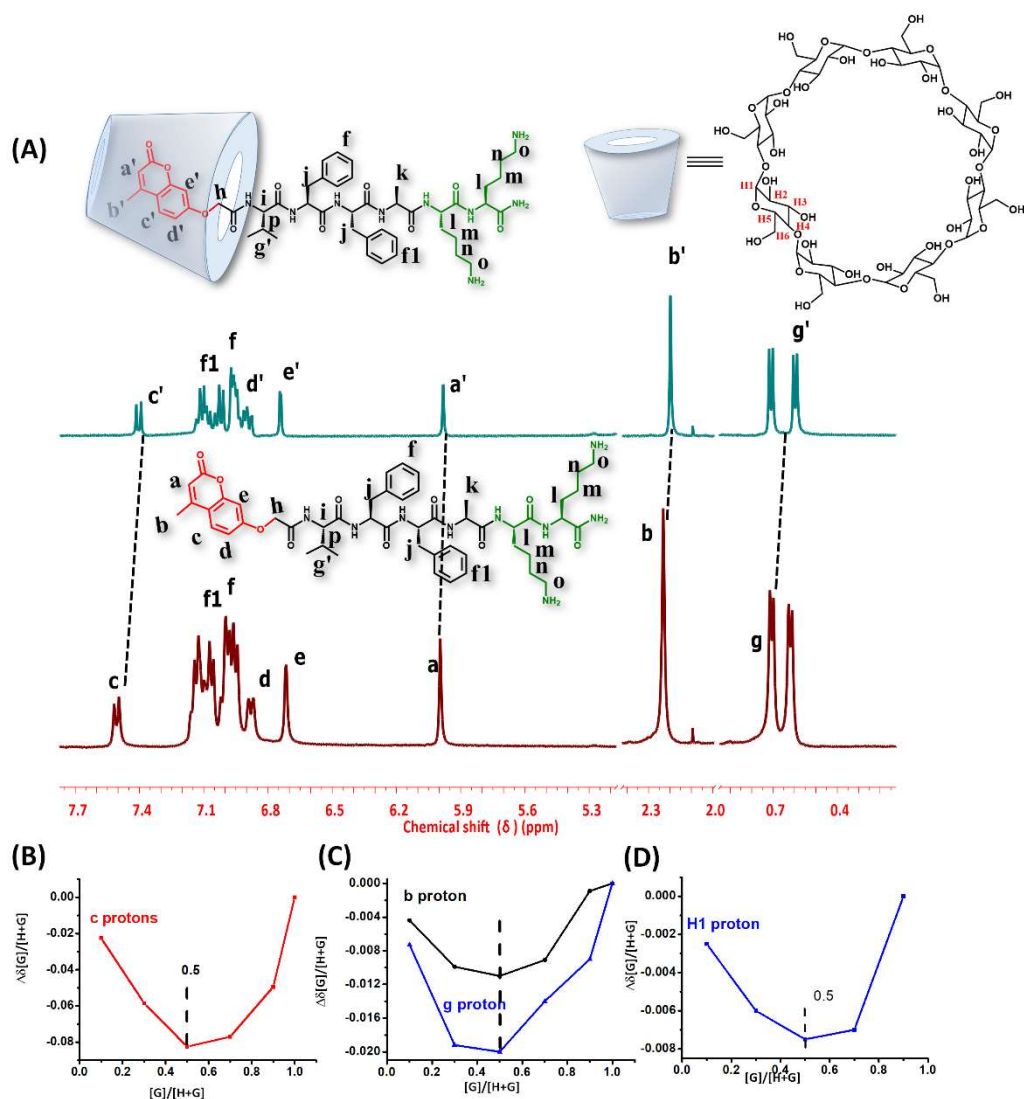


Figure 4.1. (A) Comparative ¹H NMR spectra of the free peptide **1** (6 mM) and host-guest complex of peptide **1** with equimolar γ -CD in D₂O showing upfield shift of *a*, *b*, *c* protons of the 4-methylcoumarin moiety Job's plot obtained by titrating **1** (G) with γ -CD (H) at different ratio in D₂O at 25 °C. The changes of chemical shifts of (B) H_c protons (C) H_b & H_g protons of 4-methylcoumarin moiety & valine methyl respectively and (D) H₁ ring protons of γ -CD are plotted with the mole fraction of **1** and γ -CD

4.2.1. Stepwise self-assembly of peptide: The peptide, **1** was designed by tethering a hydrophobic 4-methylcoumarin group at the *N*-terminal and two hydrophilic lysine units at the *C*-terminal of a amyloid A β 42 inspired peptide sequence, N VFFA C to maintain the hydrophobic–hydrophilic balance to make **1** self-assemble in water (pH = 6.5). The attractive hydrogen bonding interaction among the amide functionalities and π - π stacking interactions among the aromatic moieties promote parallel stacking amphiphiles to form secondary structures. The 4-methylcoumarin group is also capable of forming host-guest complex with γ -CD.¹¹ Complexation behavior of **1** with γ -CD was investigated by ¹H NMR spectroscopy. The protons marked as *a*, *b*, *c* of the 4-methylcoumarin moiety exhibited remarkable upfield shifts upon addition of equimolar γ -CD (Figure 4.1A-B), that could be attributed to the shielding effects of γ -CD cavity. Job’s plot analysis by plotting the change of chemical shift of the coumarin protons vs. the mole fraction of **1**, indicated 1:1 complexation stoichiometry (Figure 4.1 B- D). UV spectra showed gradual disappearance of 4-methylcoumarin absorption at 320 nm with irradiation of **1**- γ -CD complex and free **1** to render PD values of 66% and 74% respectively (Figure 4.2). Such a correlation of PD values in presence or absence of γ -CD suggests a photodimerization process occurring exterior to the γ -CD cavity with subsequent penetration of the resulting dimers in the cavity to result pseudo-[2]-rotaxane like **di-1** \subset γ -CD.^{24–26}

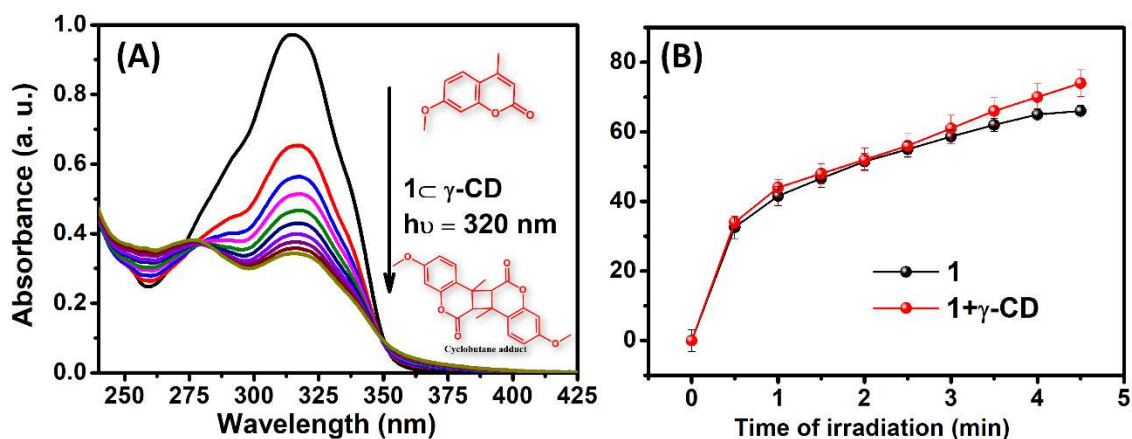


Figure 4.2. (A) UV spectra depicting photodimerization of 4-methylcoumarin moiety for equimolar mixture of **1** and γ -CD (0.125 mM) in water, (B) Increase in percentage photodimerization degree (% PD) with time of UV irradiation for **1** and **1**+ γ -CD.

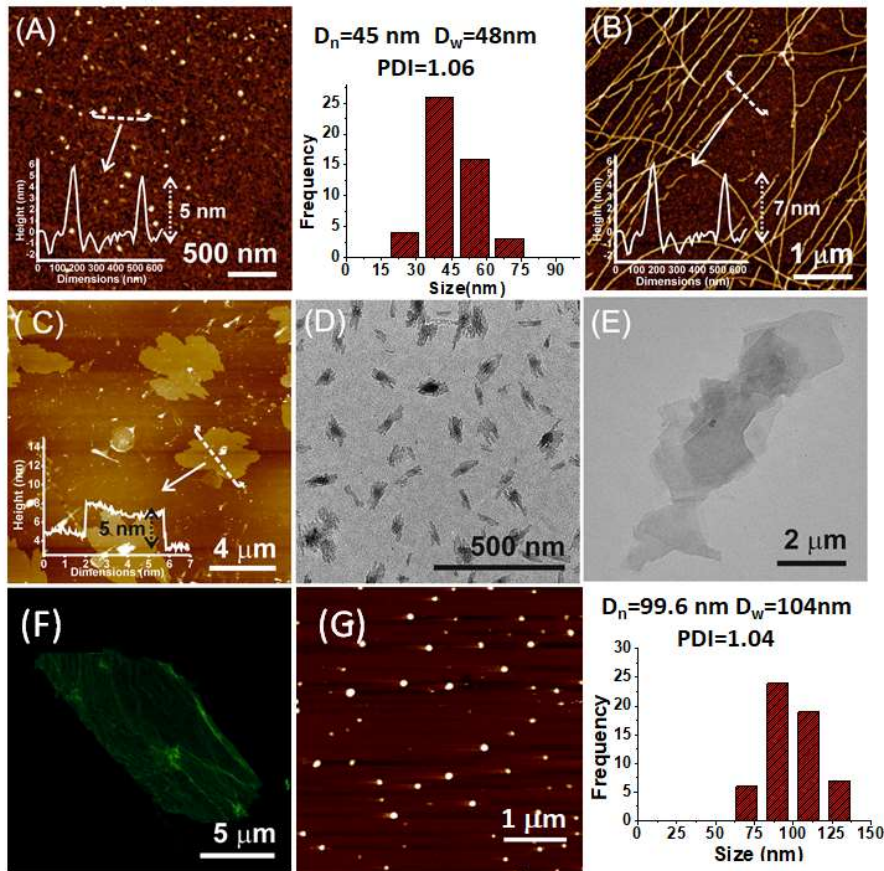


Figure 4.3. Microscopic images showing nanostructures of 1_{NP} , 1_{NF} , $(di-1C\gamma-CD)_{NS}$. AFM height images for (A) 1_{NP} (0.25 mM) at 10 °C with its histogram (B) 1_{NF} after incubating 1_{NP} at 25 °C for 1 day, (C) $(di-1C\gamma-CD)_{NS}$ after irradiating equimolar mixture of $\gamma-CD$ with 1_{NP} at 25 °C for 4 h. TEM images for $(di-1C\gamma-CD)_{NS}$ after mixing equimolar ratio of $\gamma-CD$ with 1_{NP} followed by UV irradiation ($\lambda = 320$ nm) for (D) 2 h & (E) for 8 h. (F) Confocal fluorescence images for $(di-1C\gamma-CD)_{NS}$ upon binding with thioflavin-T ($\lambda_{ex} = 488$ nm). (G) UV irradiation of $(di-1C\gamma-CD)_{NS}$ solution furnished nanoparticles (height 15-25 nm) ($\lambda = 254$ nm, 8 h, 2* 8W UV_C lamp) with its corresponding histogram

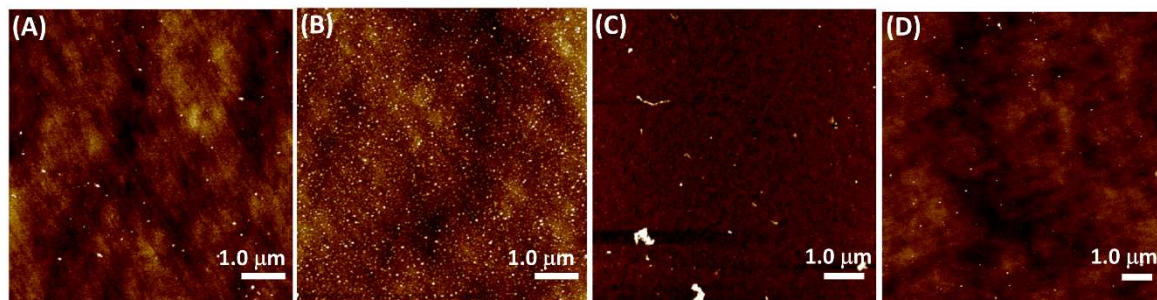


Figure 4.4. AFM height images of peptide **1** (0.125 mM) in a mixture of HFIP-Water (A) 1:3 (B) 1:1 at 10 °C after an incubation period of 2 h and (C) 1:3 (D) 1:1 at 25 °C after a incubation period of 5 h.

Peptide **1** was molecularly dissolved in hexafluoroisopropanol (HFIP) to erase any pre-assembly history. An aliquot from the HFIP stock solution of **1** was then injected in water at 10 °C (final HFIP content ~ 5 v/v%). Tapping mode AFM shows the presence of uniform sized nanoparticle (Figure 4.3A), (diameter 45 nm, height ~4-6 nm) at 10 °C, which persisted in that shape for 20 min at 10 °C before rapidly converting into nanofibers. Solvent mixtures with higher v/v% of HFIP in water seemed to stabilize the nanoparticles for longer time (~ 5 h) even at 25 °C (Figure 4.4). The metastable **1**_{NP} eventually transformed into nanofibers (diameter ~7-8 nm, height ~ 6-7 nm) with the kinetics depending on temperature and solvent composition (Figure 4.3B). Interestingly, upon UV irradiation ($\lambda = 320$ nm) for 2 h, (**1**- γ -CD)_{NS-NF} resulted immediate formation of 2D nanosheet, (**di-1**- γ -CD)_{NS} exclusively (height ~ 4-6 nm) with the area of the nanosheet increasing with the duration of irradiation (Figure 4.3C-E). Confocal fluorescence images shows green fluorescence of thioflavin-T bound to (**di-1**- γ -CD)_{NS} (Figure 4.3F). Remarkably, the nanosheet could reversibly be transformed to nanoparticle (Figure 4.3G) upon UV irradiation ($\lambda = 254$ nm) for 8 h.

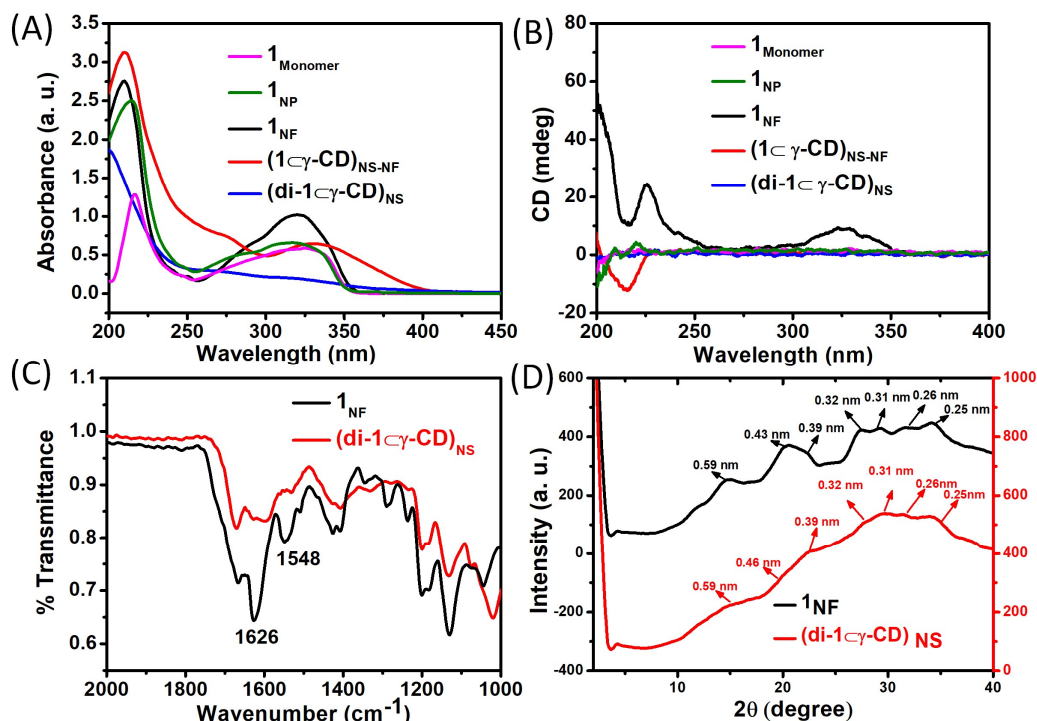


Figure 4.5. (A) Absorption and (B) circular dichroism (CD) spectra of **1**_{monomer}, **1**_{NP}, **1**_{NF}, (**1**- γ -CD)_{NS-NF} and (**di-1**- γ -CD)_{NS}. (concentration = 0.1 mM). (C) Magnified FTIR spectra of freeze-dried sample of **1**_{NF} and (**di-1**- γ -CD)_{NS} at 25 °C (concentration = 10 mM). (D) XRD spectrum showing characteristic peaks of both peptide **1**_{NF} and (**di-1**- γ -CD)_{NS} solutions (10 mM).

The self-assembly was monitored with UV and CD spectra. In comparison to the nanofiber $\mathbf{1}_{\text{NF}}$, $(\mathbf{1}\subset\gamma\text{-CD})_{\text{NS-NF}}$ showed a clearly distinct absorption spectrum with red-shifted band, that eventually diminished in $(\text{di-}\mathbf{1}\subset\gamma\text{-CD})_{\text{NS}}$ as a consequence of UV irradiation (Figure 4.5A). CD spectra of $\mathbf{1}_{\text{NF}}$ exhibited a CD band at 220 nm characteristic of β -sheet structure, along with an induced CD band at 320 nm due to the π - π^* transition of 4-methylcoumarin moiety (Figure 4.5B). However, host-guest complexation and irradiation as in $(\mathbf{1}\subset\gamma\text{-CD})_{\text{NS-NF}}$ and $(\text{di-}\mathbf{1}\subset\gamma\text{-CD})_{\text{NS}}$ diminished the ICD band of the 4-methylcoumarin, *albeit* retaining the β -sheet structure. FT-IR peaks at 1626 cm^{-1} (amide I) and 1548 cm^{-1} (amide II) suggest parallel β -sheet structures for 1D nanofibers and 2D nanosheets (Figure 4.5C).²⁷ X-ray diffraction peak of $\mathbf{1}_{\text{NF}}$ at $d = 0.43\text{ nm}$ and 0.32 nm suggest β -sheet distances between the amides and π - π distances between the aromatic amino acids, that shows minor increase in the β -sheet distances ($d = 0.46\text{ nm}$) after incorporation of the γ -CD moieties (Figure 4.5D).²⁸

4.2.2. Seeded supramolecular polymerization in 1D and 2D pathways: The fibers and sheets as observed from AFM are quite polydisperse in terms of length (PDI = 1.76) and area (PDI= 3.09) (Figure 4.6A). The kinetic evolution of the nanostructures encouraged us to perform seeded supramolecular polymerization to circumvent the barrier/lag time for the nucleation-elongation to respective nanostructures. Shear-mediated breakage of long $\mathbf{1}_{\text{NF}}$ or $(\text{di-}\mathbf{1}\subset\gamma\text{-CD})_{\text{NS}}$ produced short seeds with the reactive ends on either sides or peripheries, that promotes the growth of the nanostructures upon adding a solution of metastable species (*e.g.* $\mathbf{1}_{\text{NP}}$). $\mathbf{1}_{\text{NF}}$ and $(\text{di-}\mathbf{1}\subset\gamma\text{-CD})_{\text{NS}}$ were either probe-sonicated for 10 min or stirred at $\sim 600\text{ rpm}$ for 6 h respectively to obtain short seeds with narrow PDI (1.05-1.16) keeping the original shapes retained (Figure 4.6B). Different ratios of $\mathbf{1}_{\text{NF}}$ seeds and metastable nanoparticles, $\mathbf{1}_{\text{NP}}$ were incubated to grow un-agitated at $15\text{ }^\circ\text{C}$. The fiber seeds directed the metastable nanoparticles towards fiber growth resulting in a linear relation between seed-nanoparticle ratio and average length of the nanofibers with narrow PDI (Figure 4.7A-C). Incubation of different ratios of $(\text{di-}\mathbf{1}\subset\gamma\text{-CD})_{\text{NS}}$ seeds and a mixture of $\mathbf{1}_{\text{NP}}$ and γ -CD for 1 day showed increase in area for the seeded nanosheet, even without UV irradiation (Figure 4.7 D-F). However, unlike the linear growth of the length of $\mathbf{1}_{\text{NF}}$ with the amount of $\mathbf{1}_{\text{NP}}$, the increase in area rather showed a non-linear relation to the amount of $\mathbf{1}_{\text{NP}}$,

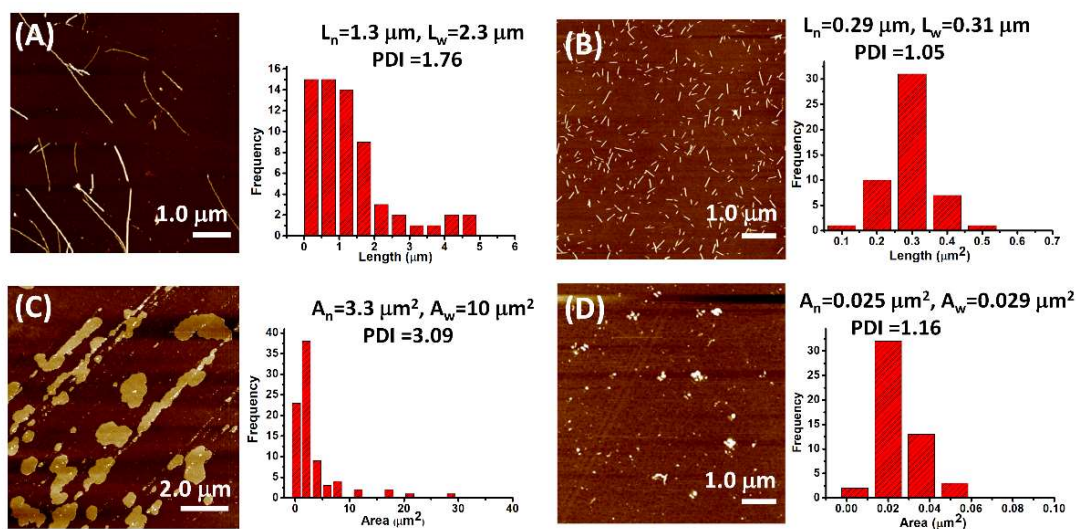


Figure 4.6. AFM images and corresponding histogram analysis showing generation of short seeds of 1_{NF} and $(di-1C\gamma-CD)_{NS}$. (A) Polydisperse 1_{NF} (0.2 mM) ($L_n=1285$ nm, PDI = 1.76), (B) Generation of short fiber seeds by probe sonication to result seeds with $L_n = 294$ nm, PDI = 1.05 (C) Nanosheets of $(di-1C\gamma-CD)_{NS}$ irradiated at 320 nm for 8 h (8 Watts* 2 UV_B lamp) ($A_n=3.3$ μm^2 , PDI=3.09) (D) Generation of short seeds with small area and narrow PDI ($A_n = 0.025$ μm^2 , PDI = 1.16) by mechanical stirring at 1000 rpm for 1 day.

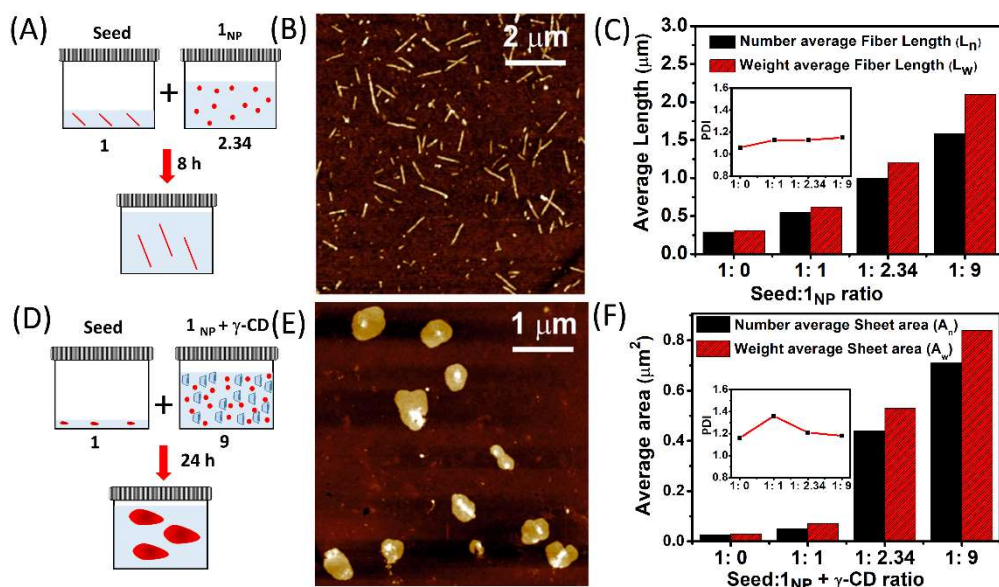


Figure 4.7. Seeded supramolecular polymerization to control the dimension of the fibers and sheets. (A) Cartoon representation showing nucleation mediated growth with 1_{NF} seeds to 1_{NP} of 1 : 2.34 ratio (top) and (D) $(di-1C\gamma-CD)_{NS}$ to $1_{NP} + \gamma-CD$ (bottom) in a 1 : 9 ratio and corresponding AFM height images of (B) Seeded nanofibers and (E) seeded sheet. Histogram analyses of the (C) Seeded nanofibers and (F) Seeded sheets after incubating the solution un-agitated for 8 h and 1 day respectively

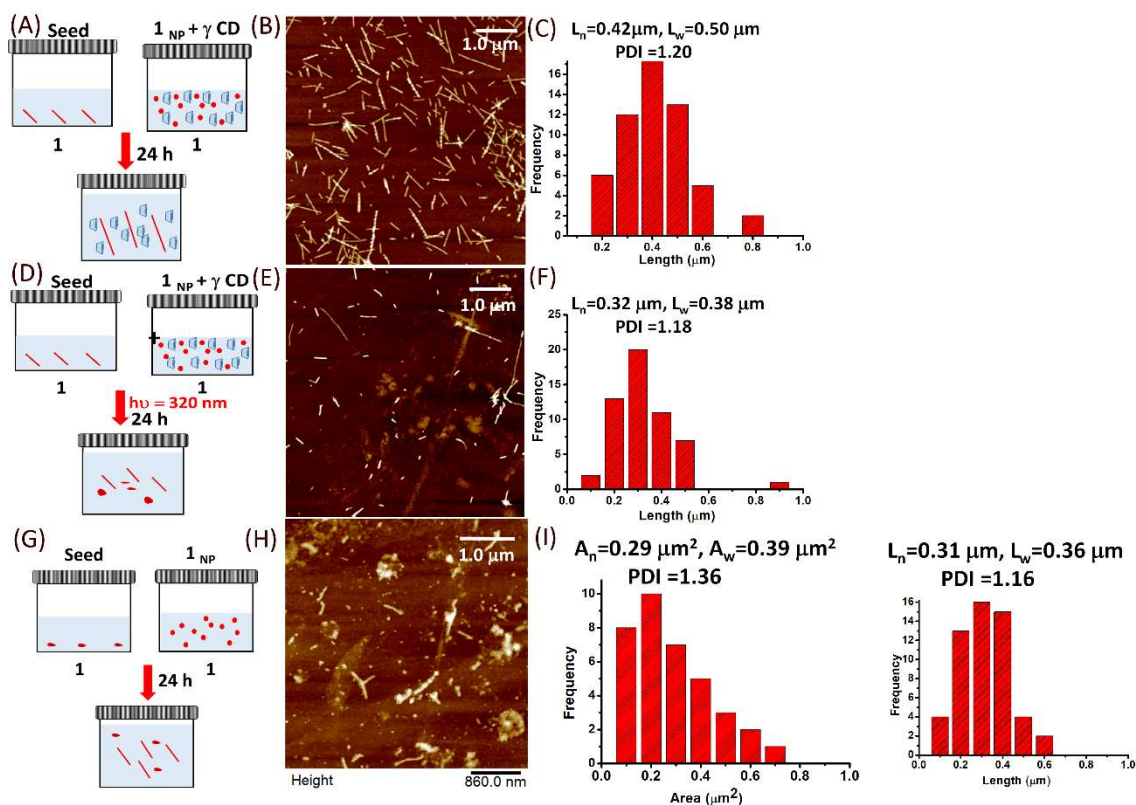


Figure 4.8. Cross-seeding experiment incubating 1_{NF} seed with monomer $1_{NP} + \gamma\text{-CD}$ in 1:1 ratio at 15°C (A-C), with UV irradiation (D-F) and $(\text{di-}1\subset\gamma\text{-CD})_{NS}$ seed with 1_{NP} for one day (G-I). The AFM images and histogram analysis suggest 1_{NF} seed mediated growth of the fibers.

and $\gamma\text{-CD}$ added to $(\text{di-}1\subset\gamma\text{-CD})_{NS}$ seeds. Interestingly, when we performed the cross-seeding experiments incubating 1_{NF} seeds with a mixture of 1_{NP} and $\gamma\text{-CD}$ in dark, the seeds promoted fiber growth and resulted moderate length control (Figure 4.8A-C). However, UV irradiation during the course of seeded supramolecular polymerization, altered the pathway towards formation of $(\text{di-}1\subset\gamma\text{-CD})_{NS}$ in an uncontrolled manner while the dimension of the 1_{NF} seeds remained unchanged (Figure 4.8A-C). This suggests competition of the hydrogen bonding interaction among the peptide units and host-guest interaction between 1_{NP} and $\gamma\text{-CD}$, *albeit* hydrogen bonding interaction dominating over host-guest interaction. However, UV irradiation and subsequent formation of strong pseudorotaxane complex *e.g.* $(\text{di-}1\subset\gamma\text{-CD})_{NS}$ enhanced the stability of host-guest interaction and resulted in mixed population (Figure 4.8D-F) of 1_{NF} fiber seed and polydisperse nanosheets $(\text{di-}1\subset\gamma\text{-CD})_{NS}$.

Similarly, incubation of $(\text{di-1}\zeta\text{-CD})_{\text{NS}}$ seeds with $\mathbf{1}_{\text{NF}}$ in absence of $\gamma\text{-CD}$ led to mixed population of sheet seeds and nanofibers arising out of uncontrolled growth (Figure 4.8 G-I). This clearly indicates the choice of suitable seeds and monomer is crucial to reign control over the size and shape of the resulting nanostructures.

4.2.3. Pathway dictated hydrogel formation:

Next, the functional aspects of such dimensionally different nanostructures were investigated. The surface of the peptide nanofibers and 2D nanosheets are positively charged at physiological pH owing to the protonation of lysine side chains. Addition of negatively charged counter anions as in sodium phosphate buffer (10 mM, pH = 7) promotes entanglement through physical cross-linking.^{23,29} While interfiber ion-bridging furnished hydrogel from $\mathbf{1}_{\text{NF}}$, $(\text{di-1}\zeta\text{-CD})_{\text{NS}}$ rather resulted in a viscous solution. It may be presumably due to effective entanglement of the $\mathbf{1}_{\text{NF}}$ nanofibers as compared to minimal physical crosslinking of the nanosheets to form 3D hierarchical structures. The hydrogel from $\mathbf{1}_{\text{NF}}$ depicted frequency independent behavior in oscillatory rheological study with G' value 4 order of magnitude higher than that of the viscous solution of $(\text{di-1}\zeta\text{-CD})_{\text{NS}}$ and showed efficient thixotropic shear recovery character for both moduli G', G'' (Figure 4.9).

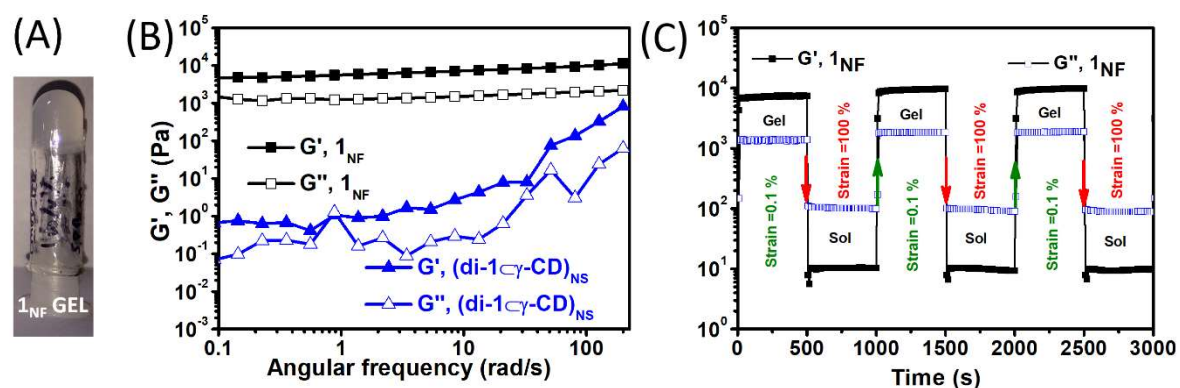


Figure 4.9. (A) Representative image of an inverted vial containing hydrogel of $\mathbf{1}_{\text{NF}}$ in sodium phosphate buffer. (B) Frequency sweep oscillatory rheology for the hydrogels obtained by crosslinking of the $\mathbf{1}_{\text{NF}}$ and $(\text{di-1}\zeta\text{-CD})_{\text{NS}}$ in sodium phosphate buffer (10 mM, pH 7.0). (C) Thixotropic studies for the hydrogel of $\mathbf{1}_{\text{NF}}$ (8.46 mM) in SPB buffer (pH 7.0). Black and red color indicate storage modulus (G' , Pa) and is loss modulus (G'' , Pa).

4.2.4. Environment friendly exfoliation of MoS₂:

Further, we envisaged the cationic surfaces of the peptide materials for efficient exfoliation of inorganic chalcogenides *e.g.* MoS₂. The layer-dependence of the MoS₂ sheet renders profound alteration of its optoelectronic, magnetic and semiconducting properties with interesting

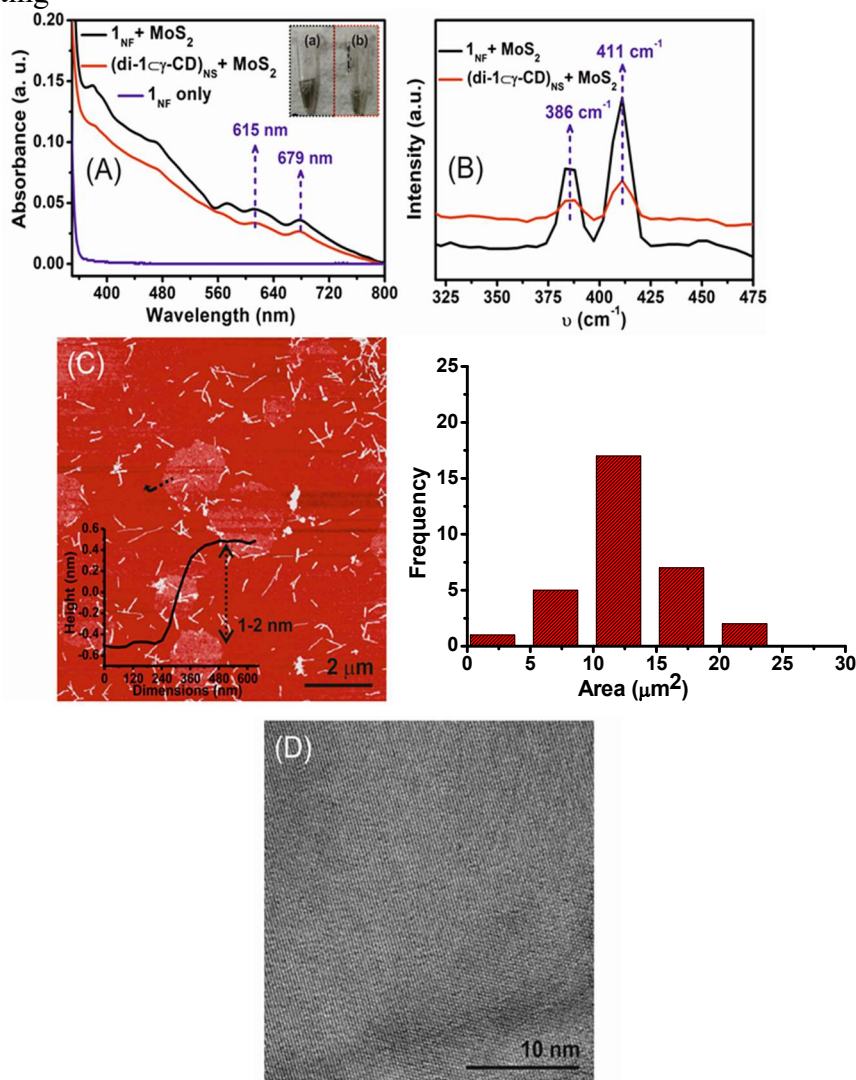


Figure 4.10. (A) UV-vis spectra of the exfoliated MoS₂ in presence of 1_{NF} and (di-1C_γ-CD)_{NS} (0.1 mM). Inset depicts the stable greenish black dispersion of MoS₂ in 1_{NF} (left) and (di-1C_γ-CD)_{NS} (right) after 7 days. (B) Raman spectra showing Raman active vibrational modes of the exfoliated MoS₂. (C) AFM height image shows the exfoliated MoS₂ sheet with its corresponding histogram (inset depicting the height of 1-2 nm) (D) Phase contrast HRTEM images of exfoliated MoS₂ in 1_{NF}.

application in energy storage, photovoltaics and thermoelectric materials^{30,31} and justifies its exfoliation in single or few layers. Eventhough mechanical exfoliation in presence of suitable ligands renders pristine, high quality structures of two-dimensional MoS₂ sheet, it is limited by colloidal stability, use of toxic reagents, harsh exfoliation conditions *etc.*^{32,33} The environmentally benign supramolecular peptide fibers, **1_{NF}** and nanosheets, (**di-1Cγ-CD**)_{NS} were mechanically stirred with 0.16 mg of MoS₂ for 12 h to result greenish black dispersions with characteristic absorption peaks of exfoliated MoS₂ at 615 nm and 679 nm (Figure 4.10A). Raman active vibrational modes E¹_{2g} and A_{1g} at 386 cm⁻¹ and 411 cm⁻¹ respectively confirms the presence of exfoliated MoS₂ for both **1_{NF}** and (**di-1Cγ-CD**)_{NS} solution (Figure 4.10B). AFM height image and HRTEM confirms the presence of fibers with layers of MoS₂ in an undistorted lattice with hexagonal symmetry (height 1-2 nm), corresponding to mono- and bilayer of the chalcogenides and an average exfoliated chalcogenides area of 13 μm² (Figure 2.10C-D). Notably, the dispersions of MoS₂ in **1_{NF}** is quite stable for *ca.* 1 month, while the composites from (**di-1Cγ-CD**)_{NS} precipitate after a week. This corroborates with increased exposure of cationic lysine units on the **1_{NF}** relative to (**di-1Cγ-CD**)_{NS} resisting the aggregation of dispersions of MoS₂ and results a higher degree of colloidal stability.

4.3. Conclusion

In summary, we demonstrated an elegant pathway dependent self-assembly of peptide amphiphile to differentiate in 1D and 2D supramolecular polymers mediated by hydrogen bonding, host-guest interaction and photodimerization. Selection of the right kind of seeds promotes the unprecedented growth of nanofibers or nanosheets *via* seeded supramolecular polymerization with excellent control over the shape and dimension. Such structural history and adaptive control over the peptide materials could further be utilized for modulating the mechanical stiffness of the crosslinked hierarchical three-dimensional hydrogel network. The dimensional flexibility and surface charges were judiciously exploited for efficient exfoliation of MoS₂ in single or bilayer of thickness and increased surface area. This work establishes a new strategy interplayed by multiple orthogonal interactions to dictate the fate

of assembly in multiple pathways with unprecedented topological control over dimensions. It opens a new paradigm to relate the design and functional properties of nanocomposites for application in adaptive materials and devices.

4.4. Experimental Section

4.4.1. Materials:

All Fmoc protected amino acids, activator (diisopropyl carbodiimide), piperazine, triisopropylsilane, anisole, 1,2-ethanedithiol, thioflavin-T (ThT) and MoS₂ were purchased from Sigma Aldrich. 4-methylcoumarin carboxylic acid was synthesized according to previous literature method.³⁴ Oxyma, Fmoc-Rink amide MBHA resin, HPLC grade acetonitrile, water, ethanol, and DMF were obtained from Merck. Trifluoroacetic acid (TFA) and Hexafluoroisopropanol (HFIP) was purchased from SRL and TCI chemicals respectively.

4.4.2. Instrumentation:

Solid Phase Peptide Synthesis was performed in Liberty Blue CEM, Matthews, NC, USA and the synthesized peptide was characterized using reverse phase C18 column Waters HPLC coupled with Q-TOF MS detector. UV spectra were recorded using Shimadzu UV 6000 UV-vis spectrophotometer in a wavelength range of 800 to 200. NMR spectra were acquired on a 400 MHz Bruker (400 MHz for ¹H-NMR). The chemical shifts were reported in ppm downfield of tetramethylsilane using the resonance of the deuterated solvent as internal standard. CD spectra were recorded using JASCO J-1500 Circular Dichroism Spectrometer, Easton, MD, USA. The wavelength range was selected from 195 nm to 400 nm with a scan speed of 100 nm min⁻¹ using 2 mm path length CD quartz cuvette. FTIR spectra were recorded in CaF₂ cell using a Cary 600 series spectrometer from Agilent technologies. The samples were drop casted on silicon wafer and AFM height images were recorded using tapping mode on a Bruker Multimode 8 scanning probe microscope with silicon cantilever. For obtaining the fluorescence images of the Thioflavin-T (ThT) stained nanostructures the confocal laser scanning microscope LSM 880 (Carl Zeiss) equipped with

a confocal detector was used. An objective lens with a 100x magnification and the fixed laser line 488 nm was used for excitation. Fluorescence emission spectra were recorded using FS5 spectrofluorometer from Edinburgh instruments. TEM images were recorded using JEOL JEM 2100 TEM with a Tungsten filament at an accelerating voltage of 120 kV. XRD spectra were recorded using Bruker D8 advance Powder X-ray Diffractometer operated at 20 mA current and 40 KV using Cu K α source with wavelength of 1.54 Å. The linear viscoelastic region, storage modulus, loss modulus and thixotropic studies were calculated using Anton Paar MCR 302 advanced Rheometer device equipped with Rheoplus 302 software using cone plate (CP25-2) geometry at measuring distance of 0.2 mm at 25°C. Raman spectra were collected in WITEC Focus Innovations Alpha 300 Raman confocal microscope with an excitation laser wavelength of 532 nm.

4.4.3. Methods:

4.4.3.1. Synthesis of peptide 1:

Microwave Automated Solid Phase Peptide Synthesizer (Liberty Blue CEM, Matthews, NC, USA) was used to synthesize peptide **1**. Fmoc-Rink Amide MBHA Resin was first swelled in dimethylformamide (DMF) for 30 minutes. All Fmoc protected amino acids were weighed as per the desired scale of the reaction followed by dissolving in required DMF solution. Deprotection of Fmoc group from the amino acid was achieved by using 20% piperazine in DMF containing 10% ethanol in the microwave reactor. Required mass of piperazine was vortexed in 10% of ethanol followed by addition of the remaining 90% of DMF for completely solubilization. Diisopropylcarbodiimide (DIC, activator) and oxyma (activator base) in DMF, were used as activators for the coupling reaction between acid and amine to form the peptide bond. A cycle of coupling, deprotection steps was repeated to synthesize the required peptide anchored to the resin. The peptide was then cleaved from the resin upon shaking with a cocktail solution, a mixture of trifluoroacetic acid (TFA)/triisopropylsilane (TIPS)/water/1, 2-ethanedithiol (EDT) (95: 2: 2: 1, v/v/v/v) for 3 h at room temperature. The resin was then filtered and the filtrate containing desired peptide and excess TFA was evaporated. The peptide **1** was then precipitated from cold diethyl ether and dried to obtain white powder. The peptide was purified by RP-HPLC using a Waters Semi-Preparative

binary HPLC system using a C18-reverse phase column with an acetonitrile-water mobile phase containing 0.1% TFA. It was dissolved in minimum amount of HFIP and dried once again. This erased any assembly history of the peptides during lyophilisation/freeze drying process. The purified peptide was confirmed by ESI-MS recorded with Waters HPLC Q-TOF mass instrument. LCMS (ESI) m/z: C₅₀H₆₇N₉O₁₀ Calculated 954.12 g/mol; found 954.78 g/mol

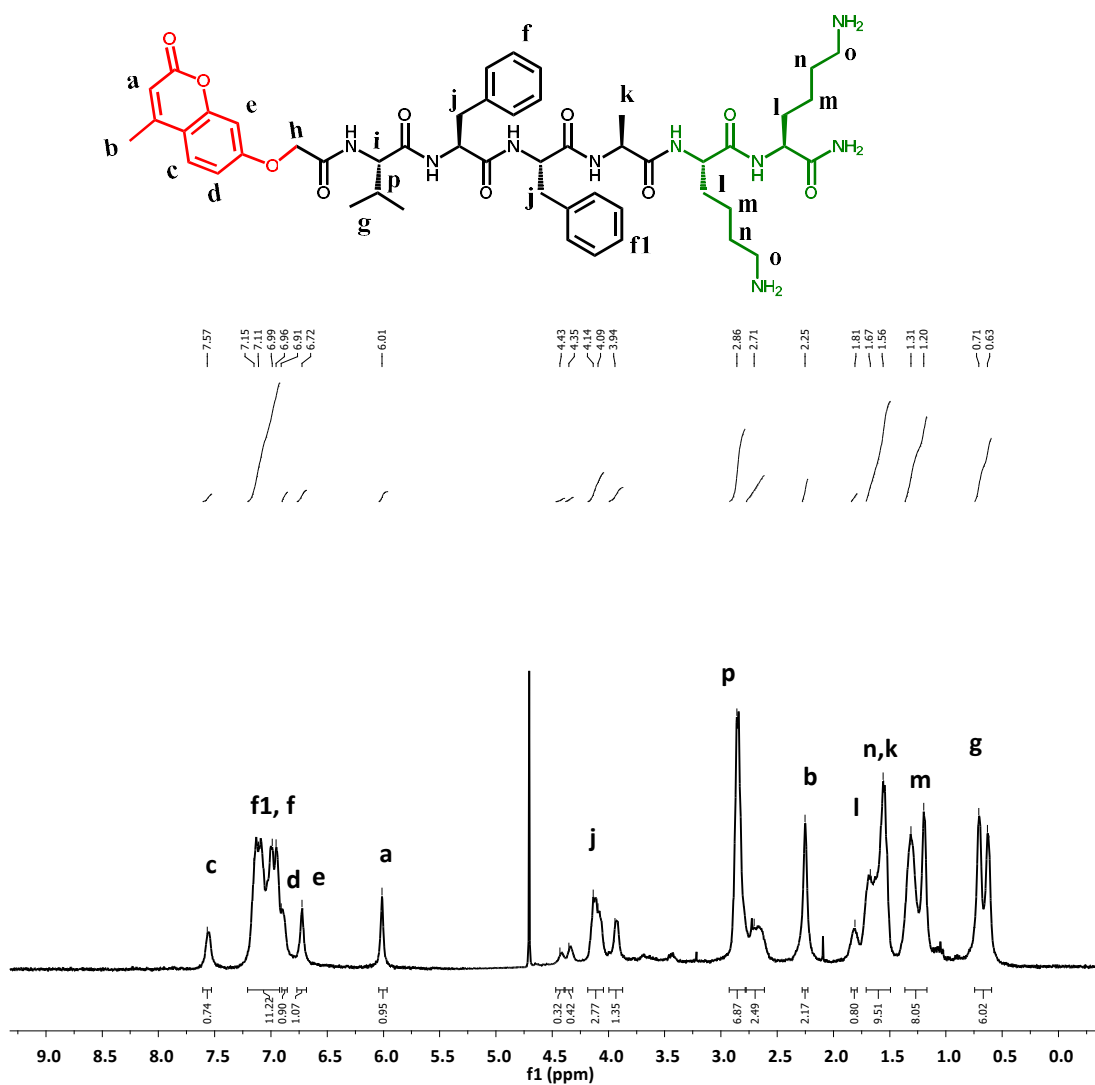


Figure 4.11: ¹H NMR of peptide 1 (10 mM) (400 MHz, D₂O, 298 K)

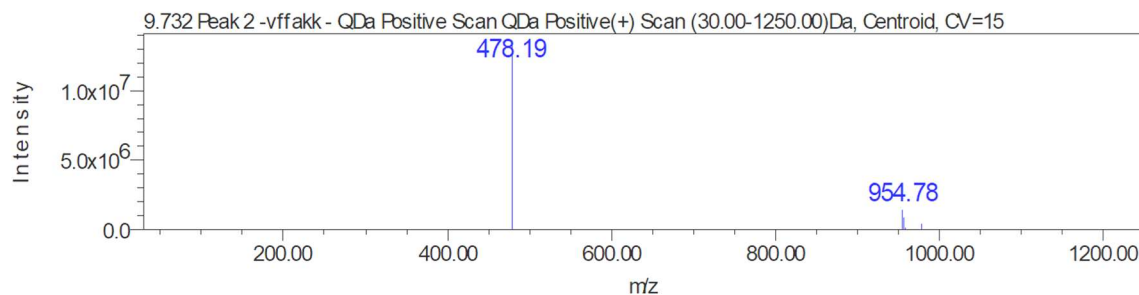


Figure 4.12. Mass spectrometry data of **1**

4.4.3.2. Preparation of Nanoparticles and Nanofibers: Peptide, **1** was dissolved in HFIP to form stock solution of 6.25 mM at 10 °C. 10 µL of the stock solution was added to 0.5 ml of water and mixture of HFIP-water in the ratio 1:3, 1:1 at 10 °C to a final concentration of 0.125 mM. At this temperature in all the cases, formation of the metastable nanoparticles were observed. The temperature was raised in a controlled manner using stuart waterbath (SWB15D) to 25 °C to observe transformation into nanofibers.

4.4.3.3. Preparation of Nanosheets: 16 µL of the stock solution of **1** (6.25 mM) in HFIP was added to equimolar γ -CD (0.5 ml) at 10 °C to a final concentration of 0.2 mM. The corresponding solution was kept for UV irradiation ($\lambda = 320$ nm, 8 Watts x 2 lamp) for 8 h. Further microscopic analysis was performed to observe formation of 2D nanosheets.

4.4.3.4. Atomic Force Microscopy (AFM): 15 µL of the sample solution (0.2 mM) was drop-casted on Silicon wafer, placed on an ice-waterbath maintained at 10 °C. After 5 minutes, the silicon wafer was washed with 500 µL water to remove excess peptide and it was then left to be air-dried in a desiccator. AFM height images were recorded by tapping mode on a Bruker Multimode 8 scanning probe microscope with silicon cantilever (Bruker) and analysed using the software NanoScope Analysis 1.5.

4.4.3.5. Transmission Electron Microscopy (TEM): 6 µL of sample solution was drop-casted on a 300 mesh carbon-coated copper grid. After ~ 5 min, excess solution was blotted

using Whatmann filter paper. Extra solution was wicked off by Whatmann filter paper from all edges of the grid carefully. Grids having samples were then dried in the desiccator under vacuum for 1 day. TEM images were recorded using JEOL JEM 2100 with a Tungsten filament at an accelerating voltage of 120 kV.

4.4.3.6. Thioflavin-T binding and Confocal microscopy images: ThT undergoes excitation at 440 nm and gives rise to emission band at 480-500 nm only when it is bound to an ordered secondary structures of protein, peptides. 2 μL of ThT solution (2 mM DMF stock) was added to 400 μL of sample solution in eppendorf tube. After 2 minutes of vortexing and incubation for 5 min, fluorescence emission spectra were recorded. One dimensional ordered supramolecular nanofibers, 2D nanosheet showed much higher emission intensity as compared to ThT in water. For obtaining the confocal fluorescence images of the Thioflavin-T (ThT) stained nanostructures, the confocal laser scanning microscope LSM 880 (Carl Zeiss) equipped with a confocal detector was used. The solution (0.2 mM, 30 μL) was spotted on a glass slide and covered with cover slip and kept at room temperature overnight for drying. An objective lens with a 100x magnification and the fixed laser line 488 nm was used for excitation.

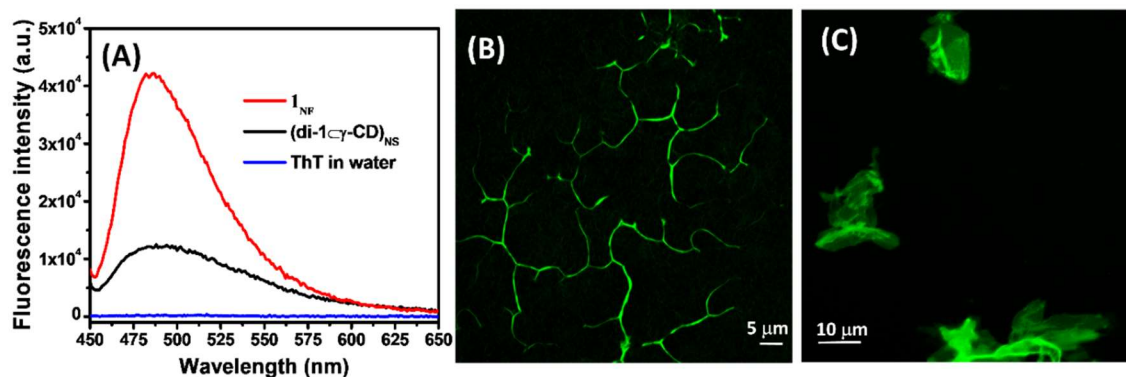


Figure 4.13. (A) Fluorescence emission spectra as a consequence of ThT binding to the 1D nanofiber 1_{NF} from aqueous solution of peptide **1** (0.5 mM) and 2D nanosheet $(\text{di-1-}\gamma\text{-CD})_{\text{NS}}$ from equimolar solution of **1** with $\gamma\text{-CD}$ (0.5 mM). Control experiment was performed by adding ThT in water. ThT stained confocal microscopy images of (B) nanofibers from **1** and (C) nanosheets from equimolar mixture of **1** and $\gamma\text{-CD}$ (0.2 mM) after 8 h of irradiation with UV light at 320 nm (2* 8W UV_B lamp).

4.4.3.7. FT-IR studies: The peaks at 1626 cm^{-1} (amide I) and 1548 cm^{-1} (amide II) indicate the existence of parallel β -sheet. The strong absorbance at 3274 cm^{-1} , 3060 cm^{-1} and 2935 cm^{-1} correspond to the N-H stretching, $-\text{CH}_3/-\text{CH}_2$ anti-symmetric and symmetric stretching, respectively. The peak associated with 1670 cm^{-1} is due to bound TFA counterions.

4.4.3.8. X-Ray Diffraction studies: The XRD pattern of the fibers and sheets (10 mM) were recorded on Bruker X-ray diffractometer at a range of 2° - 40° . $\mathbf{1}_{\text{NF}}$ and $(\mathbf{di-1}\text{C}\gamma\text{CD})_{\text{NS}}$ (10mM) solution was drop-casted on glass substrate separately and kept for drying overnight and analysed by XRD. Both the fibers and sheets showed peaks, *albeit* sharper for the fibers. The peaks at $2\theta = 20, 30$ corresponding to $d = 0.43$ and 0.32 nm account for the β -sheet distance between amides and π - π distance between aromatic amino acids residues for $\mathbf{1}_{\text{NF}}$. For $(\mathbf{di-1}\text{C}\gamma\text{CD})_{\text{NS}}$ there was a minor variation in the β -sheet distance $d = 0.46$ nm.

4.4.3.9. Generation of Seeds by mechanical agitation:

a) **Generation of fibre seeds by probe sonication:** 500 μL of pre-assembled $\mathbf{1}_{\text{NF}}$ solution (0.2 mM) was taken in 2 ml eppendorf which was fixed with a stand in a glass beaker having ice cold water. Then probe microtip (4417 number) was dipped into the sample and was sonicated using QSonica (model number Q700, power 700 watts and frequency 20 kHz) at an amplitude of 20% for ~ 10 minutes (5 sec on and 5 sec off to avoid heating due to the probe).

b) **Generation of sheet seeds by mechanical stirring:** 500 μL of sheet solution $(\mathbf{di-1}\text{C}\gamma\text{CD})_{\text{NS}}$ (0.2 mM) was taken in 2 ml eppendorf and was kept on stirring at 600 rpm for 6 h using IKA magnetic stirrer. The formation of the short seeds were monitored by recording the AFM of the samples.

4.4.3.10. Analysis of average length (fibers) and area (sheets) from AFM images: AFM images were recorded for the short seeds and growing fibers, sheets as obtained from different ratio of seeds and monomers. The length distributions of the fibers were analyzed using image-J software, from the U.S. National Institutes of Health. 100 random fibers and 50 sheets each were selected from different areas of the images and a histogram was

generated by choosing bin and frequency in Microsoft Excel. The average lengths, areas and PDI were estimated by calculating number average length, Area (L_n, A_n) and weight average fiber length, area (L_w, A_w) and the ratio $L_w/L_n, A_w/A_n$ using eqn. 1-3, where N_i is the number of fibers and sheets of length L_i and area A_i , respectively and n is the number of fibers and sheets examined in each sample.

$$L_w = \frac{\sum_{i=1}^n N_i L_i^2}{\sum_{i=1}^n N_i L_i}, \quad A_w = \frac{\sum_{i=1}^n N_i A_i^2}{\sum_{i=1}^n N_i A_i} \quad (1)$$

$$L_n = \frac{\sum_{i=1}^n N_i L_i}{\sum_{i=1}^n N_i}, \quad A_n = \frac{\sum_{i=1}^n N_i A_i}{\sum_{i=1}^n N_i} \quad (2)$$

$$PDI = L_w/L_n \quad PDI = A_w/A_n \quad (3)$$

4.4.3.11. Seeded Supramolecular Polymerization: Seeded supramolecular polymerization (SSP) was performed taking different ratio of the nanofiber (1_{NF}) seeds and metastable nanoparticles (1_{NP}) (Table 4.1) at 15 °C to furnish different length distribution of the fibers. In absence of the monomer (1_{NP}), the length distribution of the seeds remains unchanged even after 4 days. In a separate experiment, seeds of 2D nanosheet, ($di-1-\gamma-CD$)_{NS} were added in different ratio to equimolar mixture of monomers (1_{NP}) with $\gamma-CD$ at 15 °C in order to furnish sheets with growing area distribution.

Table 4.1. Different ratios of seed and nanoparticles of 1 taken for seeded supramolecular polymerization

S No	Fiber Seed : 1_{NP}	Volume of Fiber seed solution	Volume of monomer (1_{NP})	Total volume
1	1: 9	10 μ L	90 μ L	100 μ L
2	1: 2.34	30 μ L	70 μ L	100 μ L
3	1: 1	50 μ L	50 μ L	100 μ L
	Sheet Seed : $1_{NP}+\gamma-CD$	Volume of sheet seed solution	Volume of equimolar monomer(1_{NP}) + γCD	
1	1: 9	10 μ L	90 μ L	100 μ L
2	1: 2.34	30 μ L	70 μ L	100 μ L
3	1: 1	50 μ L	50 μ L	100 μ L

Cross-seeding experiments were performed incubating 1:1 ratio of the nanofiber ($\mathbf{1}_{\text{NF}}$) seeds and a mixture of metastable nanoparticles ($\mathbf{1}_{\text{NP}}$) and γ -CD at 15 °C for 1 day. In one case the solution were irradiated ($\lambda = 320$ nm) for 9 h during incubation period. In absence of UV irradiation, the $\mathbf{1}_{\text{NF}}$ seed promoted fiber growth with slight increase in PDI values. This suggests competition of the hydrogen bonding interaction among the peptide units and host-guest interaction between $\mathbf{1}_{\text{NP}}$ and γ -CD, *albeit* hydrogen bonding interaction dominating over host-guest interaction. However, UV irradiation and subsequent formation of strong pseudo-rotaxane complex e.g. $(\mathbf{di-1}\subset\gamma\text{-CD})_{\text{NS}}$ enhanced the stability of host-guest interaction and resulted in mixed population of $\mathbf{1}_{\text{NF}}$ fiber seed and polydisperse nanosheets $(\mathbf{di-1}\subset\gamma\text{-CD})_{\text{NS}}$. In a separate cross-seeding experiment, seeds of 2D nanosheet, $(\mathbf{di-1}\subset\gamma\text{-CD})_{\text{NS}}$ were added to monomers ($\mathbf{1}_{\text{NP}}$) in 1:1 ratio at 15 °C and were incubated for 1 day. Formation of uncontrolled $\mathbf{1}_{\text{NF}}$ fibers from $\mathbf{1}_{\text{NP}}$ was observed (PDI = 1.33) while dimension of $(\mathbf{di-1}\subset\gamma\text{-CD})_{\text{NS}}$ seeds of the nanosheets remained unchanged.

4.4.3.12. Hydrogel formation and rheological study: The $\mathbf{1}_{\text{NF}}$ and $(\mathbf{di-1}\subset\gamma\text{-CD})_{\text{NS}}$ solutions of concentration 8.46 mM (1 wt%) were prepared in sodium phosphate buffer (SPB) (10 mM at pH 7). These phosphate counter anions in the sodium phosphate buffer entangled the positively charged peptide nanofibers to form a network structure resulting in the formation of hydrogel. Similarly, the height of the 2D nanosheets, $(\mathbf{di-1}\subset\gamma\text{-CD})_{\text{NS}}$ also increased with upon interaction with the phosphate ions.

For rheological characterization of the hydrogel, Anton Paar rheometer device using a cone and plate (CP-25-2) geometry with an adjustable peltier temperature controlling system was utilized. An oscillatory stress amplitude sweep experiment was performed at a constant angular frequency of 10 rad/s for the strain range 0.01-100 at 25 °C to discern the linear viscoelastic region at measuring distance of 0.2 mm. The G' , G'' and yield stress values from the hydrogel of $\mathbf{1}_{\text{NF}}$ showed much higher values as compared to that from $(\mathbf{di-1}\subset\gamma\text{-CD})_{\text{NS}}$.

Oscillatory frequency sweep experiments were performed in the linear viscoelastic region with a constant strain of 0.1% to ensure that calculated parameters correspond to an

intact network structure. The software converted the torque measurements into either G' (the storage modulus) and G'' (the loss modulus). Thixotropic studies for the hydrogel from $\mathbf{1}_{\text{NF}}$ in 10 mM SPB was measured using parallel plate at a constant value for angular frequency (10 rad/s) and strain (0.1%) at 25 °C. Data points were plotted between storage (G'), loss (G'') moduli and time. The gel network was completely broken at 100% strain, however, it regains its gelation ability when the strain value was set back to 0.1 %. Three consecutive cycles were performed with change in strain of 0.1-100- 0.1-100-0.1% with a constant angular frequency of 10 rad/s.

4.4.3.13. MoS₂ Exfoliation study: Stock dispersions were prepared by adding bulk MoS₂ (0.16 mg) in powder form to 0.25 ml solutions of $\mathbf{1}_{\text{NF}}$ as well as ($\mathbf{di-1}\subset\gamma\text{-CD}$)_{NS} (2 mM each). Afterwards the dispersions were stirred overnight at ~250 rpm. The dispersions were characterized by UV-vis spectroscopy at 0.1 mM. It gives the characteristics peaks of exfoliated MoS₂ at 615 nm and 679 nm. A little higher absorbance values for the exfoliated MoS₂ peaks for $\mathbf{1}_{\text{NF}}$ which could be attributed to the more exposed amphiphilic character compared to the ($\mathbf{di-1}\subset\gamma\text{-CD}$)_{NS}. Also, the dispersions of MoS₂ in $\mathbf{1}_{\text{NF}}$ is quite stable for *ca.* 1 month, while the composites from ($\mathbf{di-1}\subset\gamma\text{-CD}$)_{NS} precipitate after a week. Samples for Raman spectra analysis were prepared by dropcasting 10 μL of stock solution on silicon wafer. Raman spectra provide characteristic information for the thickness of layers. Raman spectra provides strong signals for the two Raman active modes E'_{2g} and A_{1g} confirming the presence of exfoliated MoS₂ for both $\mathbf{1}_{\text{NF}}$ and ($\mathbf{di-1}\subset\gamma\text{-CD}$)_{NS} solution vibrational Raman active modes. The signal for exfoliated MoS₂ using nanofibers are sharper than that from nanosheet.

AFM samples were prepared by dropcasting 10 μL (0.1 mM) of $\mathbf{1}_{\text{NF}} + \text{MoS}_2$, ($\mathbf{di-1}\subset\gamma\text{-CD}$)_{NS} + MoS₂ on silicon wafer and dried overnight in desiccator. Height of the short nanofiber and exfoliated MoS₂ sheet is 6-7 nm and 1-2 nm (mono- and bilayer) respectively. The formation of short fibers is attributed with the breaking of long polydispersed fibers which rendered the exfoliation of bulk MoS₂ imparting green color to the solution. TEM samples were prepared by dropcasting 6 μL (0.1 mM) of $\mathbf{1}_{\text{NF}} + \text{MoS}_2$, ($\mathbf{di-1}\subset\gamma\text{-CD}$)_{NS} + MoS₂ on 300 mesh carbon coated copper grid.

4.5. References

- 1 J. -M Lehn, *Angew. Chem. Int. Ed.*, 1990, **29**, 1304–1319.
- 2 G. M. Whitesides and B. Grzybowski, *Science*, 2002, **295**, 2418–2421.
- 3 T. F. A. De Greef, M. M. J. Smulders, M. Wolffs, A. P. H. J. Schenning, R. P. Sijbesma and E. W. Meijer, *Chem. Soc. Rev.*, 2009, **46**, 5476–5490.
- 4 S. I. Stupp and L. C. Palmer, *Chem. Mater.*, 2014, **26**, 507–518.
- 5 W. Bai, Z. Jiang, A. E. Ribbe and S. Thayumanavan, *Angew. Chem. Int. Ed.*, 2016, **55**, 10707–10711.
- 6 P. A. Korevaar, C. J. Newcomb, E. W. Meijer and S. I. Stupp, *J. Am. Chem. Soc.*, 2014, **136**, 8540–8543.
- 7 P. A. Korevaar, S. J. George, A. J. Markvoort, M. M. J. Smulders, P. A. J. Hilbers, A. P. H. J. Schenning, T. F. A. De Greef and E. W. Meijer, *Nature*, 2012, **481**, 492–496.
- 8 E. Mattia and S. Otto, *Nat. Nanotechnol.*, 2015, **10**, 111–119.
- 9 A. Sorrenti, J. Leira-Iglesias, A. J. Markvoort, T. F. A. De Greef and T. M. Hermans, *Chem. Soc. Rev.*, 2017, **46**, 5476–5490.
- 10 Z. M. Hudson, C. E. Boott, M. E. Robinson, P. A. Rupar, M. A. Winnik and I. Manners, *Nat. Chem.*, 2014, **6**, 893–898.
- 11 S. Ogi, K. Sugiyasu, S. Manna, S. Samitsu and M. Takeuchi, *Nat. Chem.*, 2014, **6**, 188–195.
- 12 B. Kemper, L. Zengerling, D. Spitzer, R. Otter, T. Bauer and P. Besenius, *J. Am. Chem. Soc.*, 2018, **140**, 534–537.
- 13 A. Mishra, D. B. Korlepara, M. Kumar, A. Jain, N. Jonnalagadda, K. K. Bejagam, S. Balasubramanian and S. J. George, *Nat. Commun.*, 2018, **9**, 1295.
- 14 J. S. Valera, R. Gómez and L. Sánchez, *Small*, 2018, **14**, 1702437.
- 15 K. Matyjaszewski, *Macromolecules*, 2012, **45**, 4015–4039.
- 16 S. Ogi, V. Stepanenko, K. Sugiyasu, M. Takeuchi and F. Würthner, *J. Am. Chem. Soc.*, 2015, **137**, 3300–3307.
- 17 S. Ogi, T. Fukui, M. L. Jue, M. Takeuchi and K. Sugiyasu, *Angew. Chem. Int. Ed.*, 2014, **126**, 14591–14595.
- 18 Z. Chen, Y. Liu, W. Wagner, V. Stepanenko, X. Ren, S. Ogi and F. Würthner, *Angew. Chem. Int. Ed.*, 2017, **56**, 5729–5733.
- 19 G. Ghosh and S. Ghosh, *Chem. Comm.*, 2018, **54**, 5720–5723.
- 20 J. Kang, D. Miyajima, T. Mori, Y. Inoue, Y. Itoh and T. Aida, *Science*, 2015, **347**, 646–651.
- 21 A. Pal, M. Malakoutikhah, G. Leonetti, M. Tezcan, M. Colomb-Delsuc, V. D. Nguyen, J. van der Gucht and S. Otto, *Angew. Chem. Int. Ed.*, 2015, **127**, 7963–7967.
- 22 T. Fukui, S. Kawai, S. Fujinuma, Y. Matsushita, T. Yasuda, T. Sakurai, S. Seki, M. Takeuchi and K. Sugiyasu, *Nat. Chem.*, 2017, **9**, 493–499.
- 23 A. Singh, J. P. Joseph, D. Gupta, I. Sarkar and A. Pal, *Chem. Comm.*, 2018, **54**, 10730–10733.
- 24 Q. Zhang, D. H. Qu, X. Ma and H. Tian, *Chem. Comm.*, 2013, **49**, 9800–9802.
- 25 N. Cheng, Y. Chen, J. Yu, J. J. Li and Y. Liu, *ACS Appl. Mater. Interfaces*, 2018, **10**, 6810–6814.
- 26 N. Barooah, B. C. Pemberton, A. C. Johnson and J. Sivaguru, *Photochemi. and*

- Photobiol. Sci.*, 2008, **7**, 1473–1479.
- 27 Y. Lin, M. R. Thomas, A. Gelmi, V. Leonardo, E. T. Pashuck, S. A. Maynard, Y. Wang and M. M. Stevens, *J. Am. Chem. Soc.*, 2017, **139**, 13592–13595.
- 28 I. W. Hamley, A. Dehsorkhi and V. Castelletto, *Chem. Comm.*, 2013, **49**, 1850–1852.
- 29 V. D. Nguyen, A. Pal, F. Snijkers, M. Colomb-Delsuc, G. Leonetti, S. Otto and J. Van Der Gucht, *Soft Matter*, 2016, **12**, 432–440.
- 30 C. N. R. Rao, H. S. S. Ramakrishna Matte and U. Maitra, *Angew. Chem. Int. Ed.*, 2013, **52**, 13162–13185.
- 31 H. Li, J. Wu, Z. Yin and H. Zhang, *Acc. Chem. Res.*, 2014, **47**, 1067–1075.
- 32 S. S. Chou, M. De, J. Kim, S. Byun, C. Dykstra, J. Yu, J. Huang and V. P. Dravid, *J. Am. Chem. Soc.*, 2013, **135**, 4584–4587.
- 33 N. Kapil, A. Singh, M. Singh and D. Das, *Angew. Chem. Int. Ed.*, 2016, **128**, 7903–7907.
- 34 R. H. Huyck, S. R. Trenor, B. J. Love, T. E. Long, R. H. Huyck, S. R. Trenor, B. J. Love, T. E. Long, R. H. Huyck, S. R. Trenor, B. J. Love and T. E. Long, *J. Macrom Science w, Part A: Pure and Applied Chemistry Science*, 2008, **40**, 9–15.

Chapter 5

Dynamic Covalent Crosslinks in Peptide–polymer Conjugate towards Strain-Stiffening Behavior

*Reinforcement owing to inner stress formation is of supreme importance in life and is the basis for a lot of biomechanical pathways. For example, cells strengthen their contiguous matrix by dragging on collagen and fibrin fibers. Moreover, molecular motors promote rapid fluidization and dynamically stiffen the cytoskeleton by pulling polar actin filaments in opposite directions at the subcellular level. In this chapter, we exhibit dynamic amide crosslinking of fibers from peptide **1** having an A β 42 amyloid nucleating core and a photo-dimerizable 4-methylcoumarin moiety at its N terminus with thermoresponsive poly(*N*-isopropylacrylamide) (PNIPAM) generating inner stress by the initiation of a coil-to globule transition upon responding to the lower critical solution temperature (LCST) of PNIPAM. This results in a macroscopic stiffening response that manifests in higher order of magnitude in moduli. Furthermore, the network of covalently photo-fixated peptide fibers with the thermo-responsive crosslinker intensely stiffens in response to applied shear stress exhibiting power law elasticity with exponents that match with the actinomyosin network. Hence, the system presents a precise design of peptide–polymer conjugate network that exhibits stiffening behavior in response to temperature and external stress conditions and has morphological and mechanical features analogous to cells and tissues.*

5.1. Introduction

Filamentous biomaterials which are three dimensional networks of protein biopolymers such as the actin, myosin, microtubules, fibrin, *etc.* are the framework of cells and tissues of the human body helping to sustain its lifespan.¹⁻³ The highly dynamic architectures of the constituents and their intercrosslinks make them perform in a robust and adaptive manner.⁴⁻⁸ Simultaneously, active augmentation in the mechanical activity of the given structural architecture can be realized by minor changes in its design. Recent reports on work done in cells, tissues, and reconstituted protein networks revealed dramatic alteration in the firmness of a system to higher orders of magnitude *via* the interplay of extrinsic and intrinsic stresses and strains.^{9,10} One such interfering regulatory methodology is the application of minute and extremely localized forces on the stiffening network. Molecular motors such as microtubule-associated kinesins and dyneins, and the actin-associated myosins that initiate the movement and homogeneous fluidization of the cellular cytoskeleton convey these forces at subcellular levels to avail motility.¹¹⁻¹⁴ Contractile cells in, smooth muscle (SMCs) that are responsible for the protective pre-stress on the aortic wall and platelets that help in the breakdown and self-contraction of blood clots *etc.*¹⁵⁻¹⁷ count for the same force outside the cellular matrix. Such microscopic tweaking of mechanical response is the origin of an amount of extremely functional biomechanical behaviors and allows not only robust performance at diverse length scales but also receptiveness to a plethora of stimuli. Inspired from such biological regulatory pathways, recently Rowan and co-workers elegantly exploited thermo-responsive polymers such as PEG to enhance the mechanical activity of cellulose nanocrystal –poly-(vinyl acetate) composite material and polyisocyanopeptide hydrogels upon induction of coil to globule collapse.¹⁸⁻²⁰ Gels made from these materials exhibited reversible stiffening due to rejuvenation of a crosslinked network of fibers *via* the collapse of the thermoresponsive component above LCST point which softened on cooling *via* rehydration of collapsed globules. Later, Zeng and coworkers also reported a synthetic flexible polymeric network of polyethylene glycol and polyethylenimine *via* dynamic covalent bonding that mimick biologically active mechanical responsive systems.²¹ Additionally, Sijbesma *et al.* reported synthetic semiflexible polymeric fibrous system of bis-urea bolamphiphiles doped with azide moieties which on crosslinking with alkyne functionalized direct-arm, multi-arm and

thermo-responsive PNIPAM polymer, exhibited strain-stiffening behavior by “click” reaction and was enhanced by covalent fixation of fibers *via* polydiacetylene linkage.^{22–24}

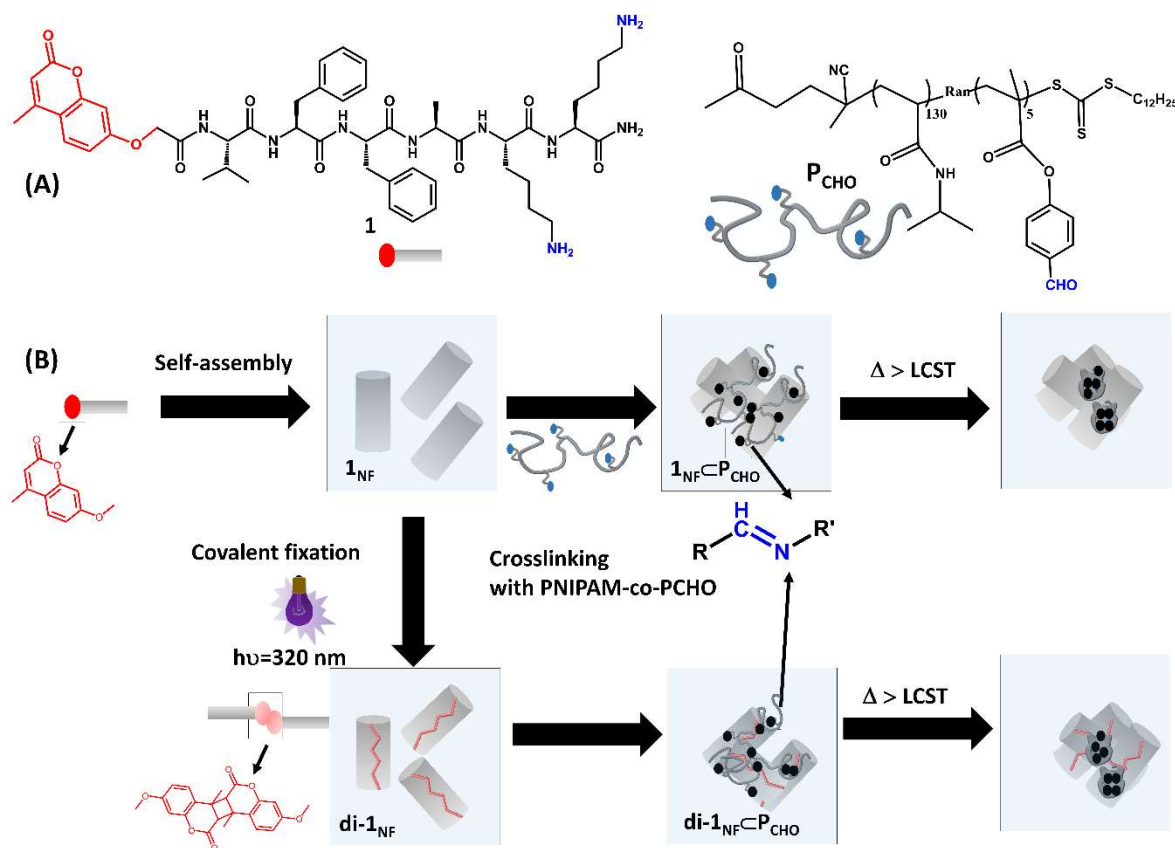
Herein, we display a precise design of self-assembling photo-responsive bio-inspired minimalistic peptide cross-linked with thermoresponsive polymer resulting in peptide-polymer conjugate network hydrogels. Coumarin tethered Peptide **1** self assembles to form **1_{NF}** nanofiber that was photofixated to form covalently fixated di-**1_{NF}** nanofiber and eventually both the fiber system were crosslinked with aldehyde functionalised polymer **P_{CHO}** to form **1_{NF}C P_{CHO}** as well as di-**1_{NF}C P_{CHO}** network induced stiffening *via* interplay of cycloaddition, Schiff-base formation and temperature. (Scheme 5.1). This resembles isotropic stiff polymer network with highly compliant cross-linker as reported theoretically by Storm *et al.*²⁵ that exhibits strain-stiffening behavior. Remarkably, the peptide-polymer conjugate network showed noticeable strain-stiffening performance beyond some critical stress value. This stiffening response can be certainly altered by changing the concentration of the fibrous network and temperature as well as by careful selection of the cross-linker with optimised chain length and functionality. This strategy is based on dynamic covalent bonds that show strain-stiffening properties anticipated for diverse application in the utilization of nanomaterials for the design and fabrication of biomimetic systems for applications like tissue engineering, drug delivery *etc.*

5.2. Results and discussion

5.2.1. Design and characterisation of the peptide-polymer conjugate

system: In chapter 4, we demonstrated the design of coumarin tethered VFFAKK peptide amphiphile **1** (Scheme 5.1) as interesting motif that undergoes stepwise self-assembly in water into one dimensional **1_{NF}** fibers from metastable nanoparticles through an interplay of intermolecular hydrogen bonds, π - π as well as hydrophobic interactions.^{26,27} The fibers can further be mechanically reinforced with covalent bonds *via* photodimerization of the **1_{NF}** fibers into di-**1_{NF}** fibers owing to the formation of a coumarin cyclobutane bridge. Microscopic analyses of TEM and AFM images (Figure 5.1 A-D) show that **1_{NF}** fibers have an average persistence length of 2.2 μm and a cross-sectional diameter of 8-10 nm. Covalent

fixation of $\mathbf{1}_{\text{NF}}$ to result in $\mathbf{di-1}_{\text{NF}}$ fibers display an increased persistence length of around 2.4 μm with a trivial change in cross-sectional diameter. Such value of persistence length is comparable to that of the actin filament (1.5 μm) and thus exhibit an increase in the bending stiffness on covalent fixation.



Scheme 5.1. Design to construct biomimetic peptide polymer conjugate. (A) Molecular structure of the self-assembling peptide ($\mathbf{1}$) and the linear, thermo-responsive poly-(NIPAM-co-formyl phenyl methacrylate) (\mathbf{P}_{CHO}) linker. (B) Hierarchical self-assembly of $\mathbf{1}$ through intermolecular H-bonding and hydrophobic interactions of peptide to result in $\mathbf{1}_{\text{NF}}$ peptide fibers followed by covalent fixation *via* photodimerization upon irradiation with UV_B light ($\lambda_{\text{max}}=320$ nm, 2*8W, 4h) to form $\mathbf{di-1}_{\text{NF}}$ dipeptide fibers. Further crosslinking of both $\mathbf{1}_{\text{NF}}$ and $\mathbf{di-1}_{\text{NF}}$ with \mathbf{P}_{CHO} *via* amide formation result in $\mathbf{1}_{\text{NF}}\subset\mathbf{P}_{\text{CHO}}$ as well as $\mathbf{di-1}_{\text{NF}}\subset\mathbf{P}_{\text{CHO}}$ networks respectively. Temperature induced coil-to-globule transition of \mathbf{P}_{CHO} linker on heating above LCST to result in pulling of $\mathbf{1}_{\text{NF}}\subset\mathbf{P}_{\text{CHO}}$ and $\mathbf{di-1}_{\text{NF}}\subset\mathbf{P}_{\text{CHO}}$ fibers.

The morphology of 1_{NF} and $di-1_{NF}$ fibers were further investigated with small-angle X-ray scattering (SAXS). The scattering profiles (Figure 5.1C) overlap over the whole q -range depicting minor structural changes upon topochemical dimerization. Furthermore, the slope is close to -1 in the low q -region and the results were consistent with the microscopy results indicating retainment of 1D morphology even after the photodimerization. Aqueous solutions of 1_{NF} and $di-1_{NF}$ fibers having lysine side chain, was ligated with aldehyde functionalized P_{CHO} with aldehyde to amine effective functionality ratio equal to 0.75 to render non fixated $1_{NF} \subset P_{CHO}$ and covalently fixated $di-1_{NF} \subset P_{CHO}$ network respectively.

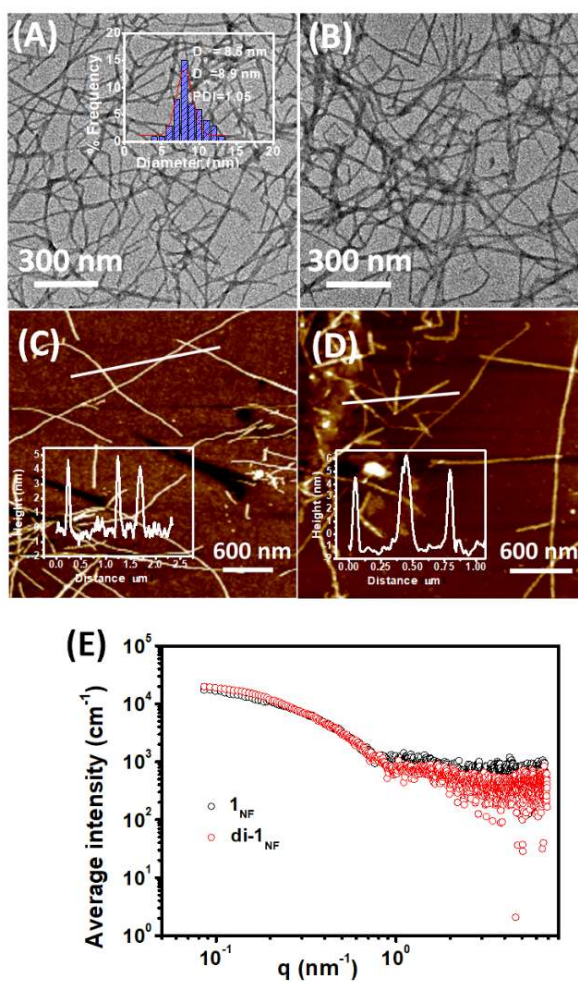


Figure 5.1. Monitoring self-assembly and covalent fixation (A) Microscopical investigation by TEM of (A) 1_{NF} (Inset showing histogram for the cross-sectional diameter of fibers), (B) $di-1_{NF}$ fibers and AFM of (C) 1_{NF} (D) $di-1_{NF}$ fibers ($c=0.125$ mM) (E) SAXS studies showing form factor for 1_{NF} and $di-1_{NF}$ peptide nanofibers. ($c = 3$ mM)

$^1\text{H-NMR}$ showed imine crosslinking mediated network formation involving 70-80% of the aldehyde group reacted with peptide to render downfield shift in coumarin (Figure 5.2A). The amide I peak and amide II peak of peptide fibers due to C=O stretching and N-H bending vibration due to self assembled fibers was present in both networks which indicated that morphology remained intact even after the network formation. Moreover, the diminishing of aldehyde C=O stretching vibration in P_{CHO} polymer at 1730 cm^{-1} as well as the appearance of a new peak at around 1640 cm^{-1} corresponding to C=N stretching that indicated imine formation as a result of dynamic covalent interactions in the peptide-polymer conjugate (Figure 5.2B).

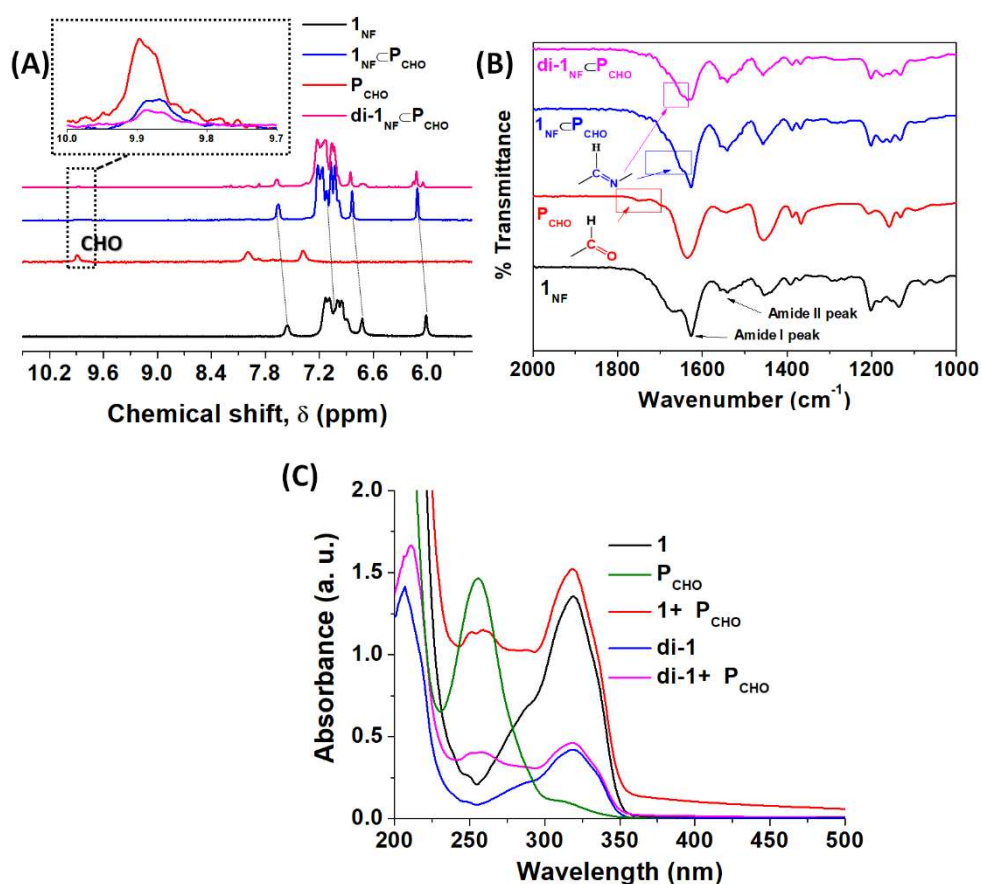


Figure 5.2. Monitoring dynamic covalent imine formation and photodimerization. (A) Partial $^1\text{H-NMR}$ spectra showing interaction of peptide fibers, 1_{NF} and $\text{di-}1_{\text{NF}}$ ($c=3\text{ mM}$) with P_{CHO} polymer chain. (B) FTIR spectra showing characteristic changes in peptide fiber due to interaction with polymer ($c = 3\text{ mM}$). (C) UV spectra showing the interactions in peptide-polymer conjugate as well as photodimerization of coumarin ($c = 0.125\text{ mM}$).

The diminishing of carbonyl UV absorbance peak in the polymer on network formation also indicated the formation of the peptide-polymer conjugate. Percentage photodimerization (% PD) in the case of covalently fixated **di-1_{NF}** fiber was determined to be 72 % (Figure 5.2C).

Moreover, aggregation of size was seen in temperature trend study in DLS both in case of **P_{CHO}** polymer solution as well as **1_{NF}-P_{CHO}** polymer-peptide network which indicated hydrophilic to hydrophobic coil to aggregated globule transition of the polymer with onset at around 20-25°C (Figure 5.3A). SAXS experiment performed both below and above the LCST of **P_{CHO}** that portrayed scattering of the chemically crosslinked network **1_{NF}-P_{CHO}** at 20 °C upon heating above LCST to 55°C which showed excess scattering intensity at low q values as well as an increase in slope from -0.74 to -1.14 on heating the solution to a higher temperature (Figure 5.3B). This indicated the generation of fibrillar bundles of the peptide network generated due to LCST induced transformation of extended coils of **P_{CHO}** to globular aggregations and concomittant pulling of the peptide fibers.^{28,29}

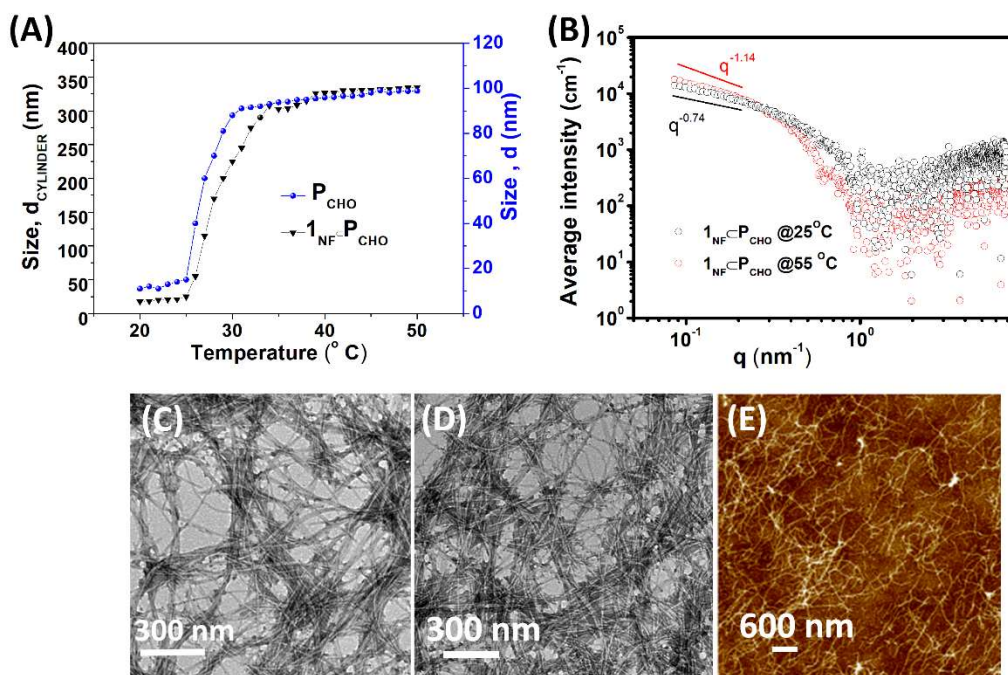


Figure 5.3. (A) DLS Temperature trend size graph showing LCST induced structural transformation of extended coils of **P_{CHO}** to globular aggregations and corresponding bundling in **1_{NF}-P_{CHO}** network (c=2.5mM) (B) SAXS studies showing form factor for **1_{NF}-P_{CHO}** peptide fiber network before and after heating above LCST. Network formation as monitored by TEM for (C) **1_{NF}-P_{CHO}**, (D) **di-1_{NF}-P_{CHO}** fibers and (E) AFM of **1_{NF}-P_{CHO}** network after heat treatment. (c=0.125 mM).

Morphological characterisation of the peptide–polymer conjugate before and after crosslinking in $\mathbf{1_{NF} \text{---} P_{CHO}}$ by TEM indicated bundling of the peptide fibers due to pulling by LCST induced coil to globule transition of the polymer chains similar to the polyisocyanopeptide (PIC) strain-stiffening hydrogels shown by Rowan’s group^{30,31}, where stiffening is supported by additional physical aggregation of individual peptide fibers resulting in network formation (Figure 5.3C-E).

5.2.2. Monitoring LCST induced heat-stiffening: The initial morphological and scattering studies indicated the LCST behavior of the thermoresponsive polymers exhibited to induce local contractile forces to the meshworks of peptide polymer network that might lead to heat stiffening property. After ligating the peptide with polymer, solutions were immediately transferred to the rheometer plate where the thermal analysis was performed by subjecting the network to a linear temperature ramp from 20 to 50 °C with recording the change in moduli in small-amplitude oscillatory strains of 1 % and angular frequency of 6.28 rad/sec. At 25 °C, increasing the overall concentrations with a fixed aldehyde to amine effective functionality ratio $\{[\mathbf{P_{CHO}}]/[\mathbf{1_{NF}}]\} = 0.75$ produced progressively stiffer materials with moduli G' ranging from 6 to 1000 Pa in the concentration range between 2.5 and 12 mM (Figure 5.4A). The nonfixated $\mathbf{1_{NF} \text{---} P_{CHO}}$ network in temperature ramp study showed an increase of G' by more than one order of magnitude with increasing temperature (Figure 5.3A). Moreover, the photo-fixated $\mathbf{di-1_{NF} \text{---} P_{CHO}}$ network showed an increase in storage moduli ranging from 8 to 3000 Pa with enhancement in the onset temperature for stiffening (Figure 5.4B). The onset temperature for stiffening ($T_{\text{stiffening}}$) goes down for both non-fixated and covalently fixated networks with increase in overall concentration. However the normalized extend of stiffening for non-fixated and fixated network showed comparable behavior across all concentration, *albeit* the covalently fixated network showed a rather increase in the stiffening at some concentrations (Figure 5.4 C). Next, the network solution of $\mathbf{1_{NF} \text{---} P_{CHO}}$ (5 mM) was crosslinked using varying concentrations of $\mathbf{P_{CHO}}$ ranging from 0.1 to 1.6 mM, resulting in aldehyde to amine ratios between 0.23 and 1.25. Crosslinking at a ratio of 0.23 produced a viscoelastic liquid like network in which G' exhibited a higher stiffening temperature of 38 °C (Figure 5.4 D). As the ratio of aldehyde to amine increased

to 0.48, the G' of the network crossed the threshold onset for stiffening. Above the critical network ratio of 0.75, the G' increases on heat ramp (ratio=1.25) exhibiting more than 3 orders of magnitude, from 9 Pa at 20 °C to 2000 Pa at 50 °C. However, when the ratio was increased to 1.25, plateau G' was lowered due to the enhanced interaction of more PNIPAM sidechains with own hydrophobic aldehyde functionality thereby decreasing the interfiber interaction. Similar trends have also been observed in studies on reconstituted biofilamentous networks where the degree of the stiffening is directly proportional to the comparative ratio of force-generating and crosslinking components in the network.^{13,23,32,33}

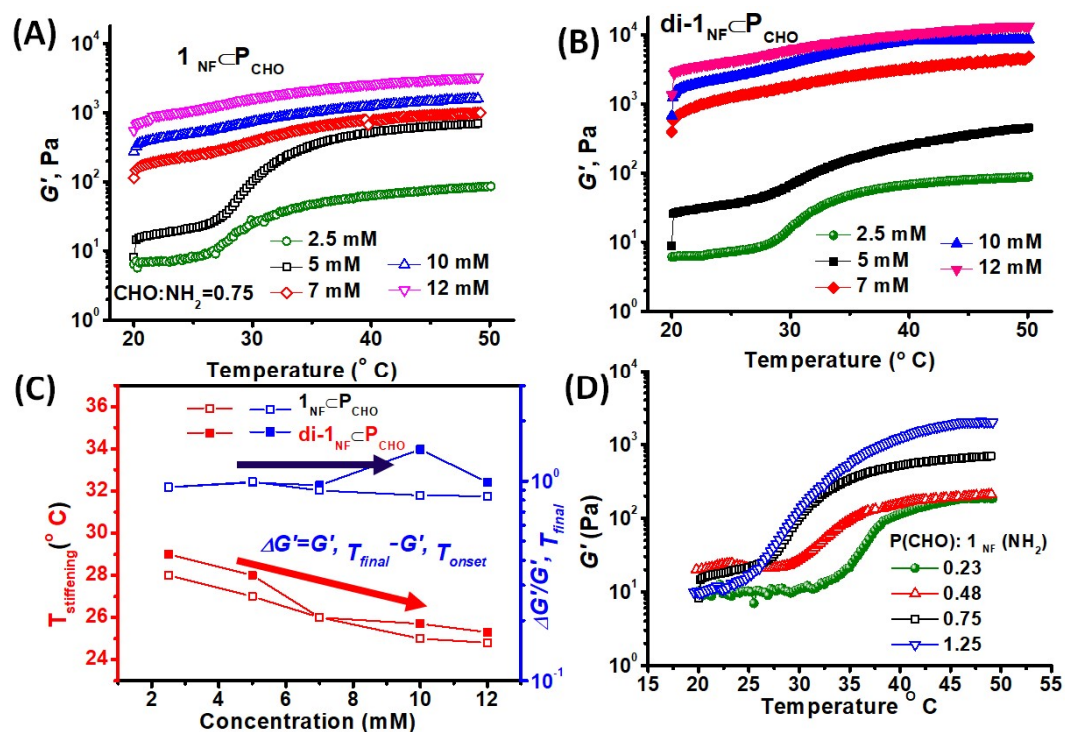


Figure 5.4. Thermal stiffening of peptide –polymer network. Linear storage modulus G' vs temperature recorded by applying % strain at 1% and the angular frequency at 6.28 rad s^{-1} at a linear heating rate of $2 \text{ }^\circ\text{C min}^{-1}$ for different concentrations of (A) $1_{NF}P_{CHO}$ and (B) $di-1_{NF}P_{CHO}$ networks crosslinked using a fixed ratio of aldehyde to amine groups = 0.75. (C) Graph showing a change in the stiffening onset temperature and extent of stiffening for $1_{NF}P_{CHO}$ (Empty symbol) and $di-1_{NF}P_{CHO}$ (Filled symbol) given by the equation $(\Delta G', T_{final} - G', T_{onset}) / G', T_{final}$, where G', T_{final} and G', T_{onset} is the storage modulus at 50 °C and at stiffening onset temperature respectively. (D) G' vs T for 5 mM $1_{NF}P_{CHO}$ network crosslinked using different $[CHO]/[NH_2]$ functional ratios.

e. g. [myosin]/[actin] in cytoskeleton systems. The remarkable increase in the G' prompted by \mathbf{P}_{CHO} coil-to-globule transition suggests the isotropic nature of induced deformation.^[15] To identify the underlying mechanism governing the stiffening of peptide-polymer conjugate, the moduli of the networks were monitored by performing heating-cooling cycle after mixing $\mathbf{1}_{\text{NF}}$ fibers with \mathbf{P}_{CHO} (with chemical crosslinking) and \mathbf{P} (PNIPAM polymer

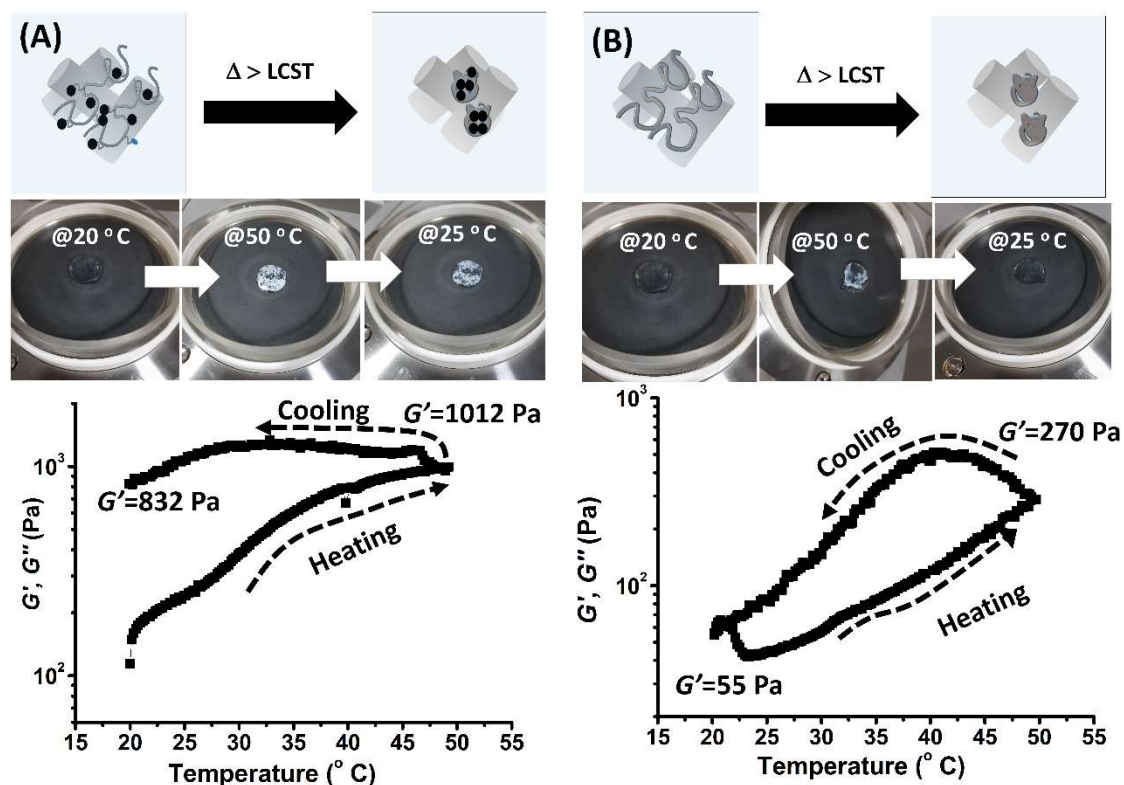


Figure 5.5: Proposed mechanism of $\mathbf{1}_{\text{NF}}\text{-P}_{\text{CHO}}$ heat stiffening transition. (A) Mechanism proposed for the stiffening transition at a constant overall volume observed in a chemically crosslinked $\mathbf{1}_{\text{NF}}\text{-P}_{\text{CHO}}$ network showing irreversible retainment of the network on cooling back to room temperature. (B) Formation of a physical network between $\mathbf{1}_{\text{NF}}$ and polymer \mathbf{P} without aldehyde functionality showing reversal of the network to a transparent solution on cooling back to room temperature. Storage (G') moduli vs temperature at % Strain = 1% and angular frequency = 6.28 rad s^{-1} at a heating/cooling rate of $2 \text{ }^\circ\text{C min}^{-1}$

without aldehyde resulting in no chemical crosslinking) (Figures 5.5). For a chemically crosslinked network, heating above the LCST of \mathbf{P}_{CHO} prompts a 100-fold increase in G' that infers strong pulling of \mathbf{P}_{CHO} on $\mathbf{1}_{\text{NF}}$ fibers as the crosslinker undergoes a coil-to-globule transition. After cooling back to 25 °C, the network remained in a stiffened state showing an

irreversible transition. Interestingly, a solution of **1_{NF}** fibers and **P** without chemical crosslinking between the two components was also found to undergo an increase in moduli at around 30 °C (Figure 5.5B). These results suggest that the collapse of the thermo-responsive linker brings **1_{NF}** fibers into contact creating a physical network even in the absence of chemical crosslinks. However upon cooling back to room temperature, the storage modulus of the physical network came back to original value. Thus at the same fiber concentration, the physical network relaxes back to loosened fibers on cooling to room temperature due to swelling of PNIPAM chains, while covalent network rather portrayed distinct irreversibility indicating inter chain-fiber loops as a result of dynamic covalent crosslinks. This indicated that although physical connections can increase the strength of elastic material, chemical crosslink is necessary to have resulted in significantly long lasting stiffening material over comparable concentration of crosslinking fibers.

5.2.3. Evaluation and quantitation of strain-stiffening *via* prestress

protocol: Biological networks are reported to show a distinct nonlinear response to deformation beyond a characteristic critical stress σ_c when imparted to the material. To carefully capture linear and nonlinear regimes of our crosslinked networks, a standard rheological pre-stress protocol³⁴ was used for the measurements, and the differential modulus K' (the elastic part of which relates the change in stress with strain $K' = \delta\sigma/\delta\gamma$) was measured by parallel superposition of an oscillatory and a steady prestress σ . Plotting K' against σ gave low-stress area where the elastic response was linear with K' equal to the plateau modulus G_0 , and a high stress area beyond the critical stress σ_c where K' becomes strongly dependent on σ and scales with stress as $K' = \sigma^m$, m being the stiffening index. The nonfixated **1_{NF}◻P_{CHO}** network were found to strain-stiffen with the modulus of the material characterized by a plateau storage modulus G_0 at low σ that increased exponentially to 2 order of magnitude beyond the critical stress σ_c (Figure 5.6 A). Upon increasing the overall concentration of **1_{NF}**, G_0 increased with critical stress σ_c ranging from 0.14-2.32 Pa similar to biological networks.¹⁰ Moreover, non-linear mechanics of covalently fixated **1_{NF}◻P_{CHO}** network showed the profound influence of fiber reinforcement *via* photodimerization

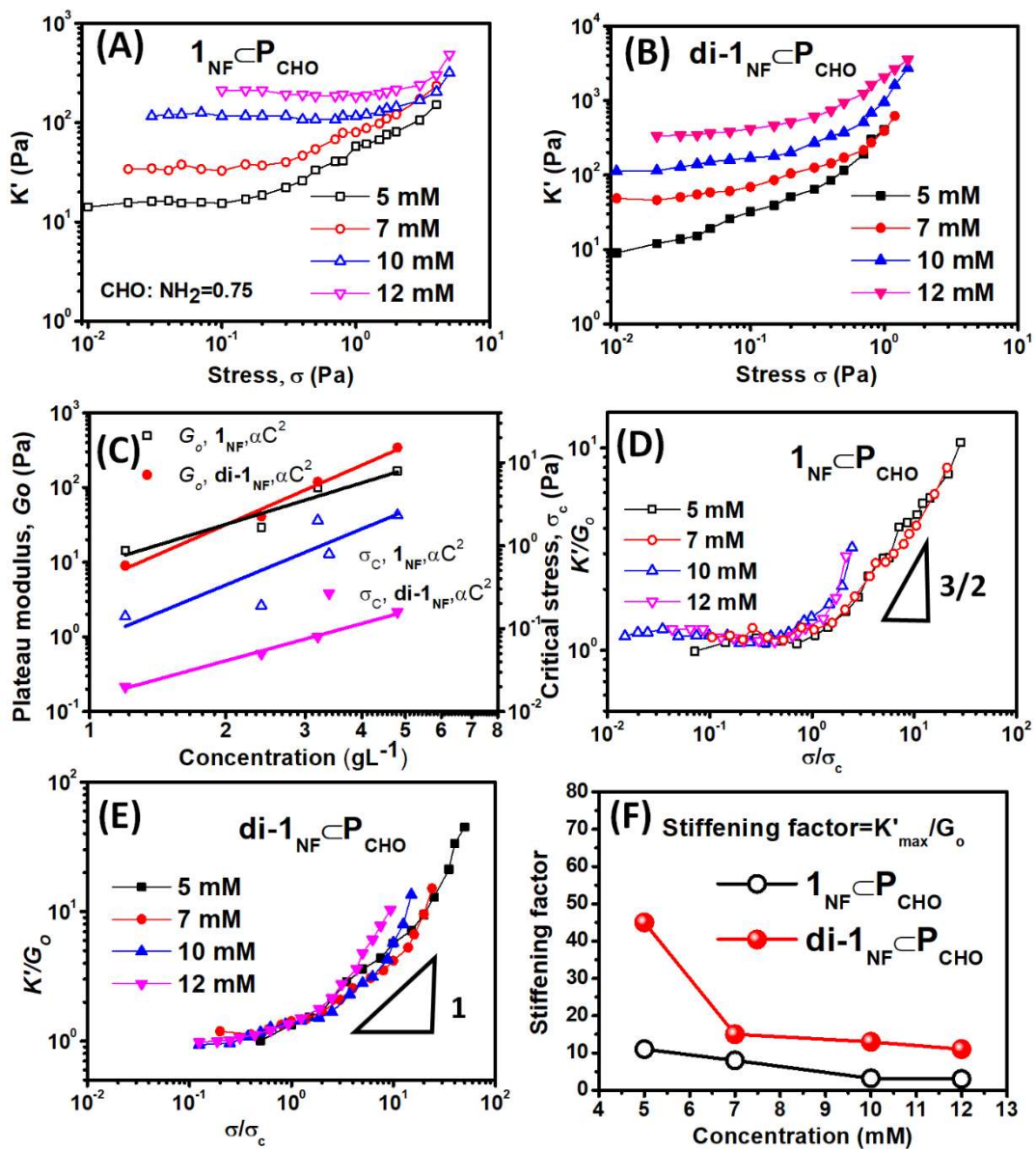


Figure 5.6. Differential moduli against stress after heating the networks to 50 °C and cooling back to 25 °C at different concentrations of (A) 1_{NF}-P_{CHO} and (B) $di-1_{NF}\text{-P}_{CHO}$ network keeping the ratio of aldehyde: amine constant at 0.75. Note that the y-axis spans 3 orders of magnitude in stiffness with a concentration range less than 1 order of magnitude. (C) Double logarithmic plot of plateau moduli G_0 and critical stress σ_c against concentration (The solid lines are linear fits and show that both scale with $c^{2.0}$ and the concentration is in g/L unit). Scaling K' with G_0 and σ with σ_c causes a collapse of the data to a single master curve for (D) 1_{NF}-P_{CHO} that shows $K' \propto \sigma^{3/2}$ and (E) $di-1_{NF}\text{-P}_{CHO}$ that shows $K' \propto \sigma^1$ only at high σ (E) Stiffening factor, K'_{max}/G_0 as a function of concentration.

resulting in enhancement of stiffening range to 3 order of magnitude with further lowering of critical stress range from 0.02-0.16 Pa (Figure 5.6B). Scaling analysis performed to quantify the dependence on the concentration (c) of both G_0 and σ_c revealed a $G_0 \propto c^2$ and $\sigma_c \propto c^2$ relationship over the whole c range studied (Figure 5.6 C). Such scaling matches with the typical square dependence reported in both theoretical and literature values.^{35,36} The curves fall to a master curve when scaled against G_0 and σ_c (Figure 5.6 D-E) and a corresponding plot of **1NF****PCHO** network suggest that stiffening index of $m=3/2$ is reached at high stresses. This was in corroboration with stiffening index, m of single component polymer system reported by Kouwer *et al.*¹⁹ which signifies enthalpic pulling of fiber network along its length. Further, the data of covalently fixated **di-1NF****PCHO** network featured a linear relationship between K' and σ ($K' \propto \sigma^1$) above σ_c which was more similar to reports of biopolymer networks from reconstituted proteins.¹³ Further the enhancement in stiffening factor *i. e.* K'_{max}/G_0 that corresponds to the stiffening range of the network increased from 11 in case of **1NF****PCHO** to 45 in case of **di-1NF****PCHO** which indicated the profound influence of covalent fixation on stiffening mechanism under external stress conditions (Figure 5.6 F). Moreover, the relation of stiffening factor K'_{max}/G_0 with σ_c and concentration underline the importance of mechanical sensitivity and stress response of the network in crowded concentration. Table 5.1 summarise the strain-stiffening features of the reported neurofilament networks matches with our **1NF**, **di-1NF** network thereby stressing the biomimetic nature of these materials.

Table 5.1. Comparison of **1NF**, **di-1NF** network with neurofilaments

Characteristic network parameter	1NF PCHO Network	di-1NF PCHO Network	Neurofilaments ^{36,37}
Persistence length, l_p [nm]	2200 ^a	2400 ^a	200
Concentration, c [mg mL ⁻¹]	1.2-4.8	1.2-4.8	
G_0 [Pa]	14-167	8-342	0.5-30
Critical stress (σ_c) [Pa]	0.14-2.32	0.02-0.16	0.1-4
High stress regime	$K' \propto \sigma^{1.5}$	$K' \propto \sigma^1$	$K' \propto \sigma^1$
Fibre diameter [nm]	8-10 nm ^b	8-10 nm ^b	10 nm

^[a] Determined from easyworm software as described in experimental sect 5.4.2.6 ^[b] Calculated from TEM graphical analysis

5.2.4. Large amplitude oscillatory strain measurements: Dynamic strain amplitude was performed to determine the mechanical performance of the network at low concentration on subjecting to large deformations. In the dynamic amplitude sweep, the oscillation is performed by keeping the angular frequency constant (1 rad/s) and the amplitude of the cycles is increased with time. Practically, multiple oscillation cycles are completed and on attaining a constant level, average of last cycles is recorded.^{38,39} Thus, rate of deformation here depends on the rheological performance of the material. We selected strain amplitude sweeps measurement to probe the effect of covalent fixation on the mechanical performance of a network sample at a low concentration regimen that is optimally soft and does not slip easily. Variation of G' and G'' with strain amplitude (γ_0) for **1NF-PCHO** and covalently fixated **di-1NF-PCHO** network display a plateau region of G' similar to plateau moduli in pre-stress measurements at small strain amplitudes, followed by a decrease at higher strain amplitude (Figure 5.7A-B). The strain at which onset of the decrease in G indicates the limit of linear response. This strain is lower for the **di-1NF-PCHO** network. Lissajous plots, showing stress and strain during one cycle of oscillation (Figure 5.7 C-D) indicate that at low strain values of 6.3%, the shape of the plots is elliptical, indicative of a linear viscoelastic response due to network viscoelasticity. With the increase in the shear strain amplitude, the Lissajous plots become non-elliptical, implying non-linear response. The upward convex trend of the Lissajous plots at strain amplitude around 25 % signifies a non-linear increase in stress with a small increase in strain within a cycle of deformation and indicates strain-stiffening mediated rigidification of the network (Figure 5.8C-D ii). This non-linear increase in stress with strain at a cycle persisted even at higher strain amplitudes upto initial areas of network dissociation upto strain amplitudes of 159-251% (Figure 5.8C-D iii-iv). Such strain-stiffening was correlated with the strain-induced increase in the number of elastically active network density in the network due to pulling by polymer chain crosslinks.^{38,51,52} Quantification of this nonlinear behavior was done by calculating the 'strain-stiffening index', S , from Lissajous plots which is defined as $S = (G'_L - G'_M) / G'_L$, where G'_M is the tangent modulus when strain (t) = 0 and G'_L is the secant modulus when strain (t) = strain (t), within a cycle

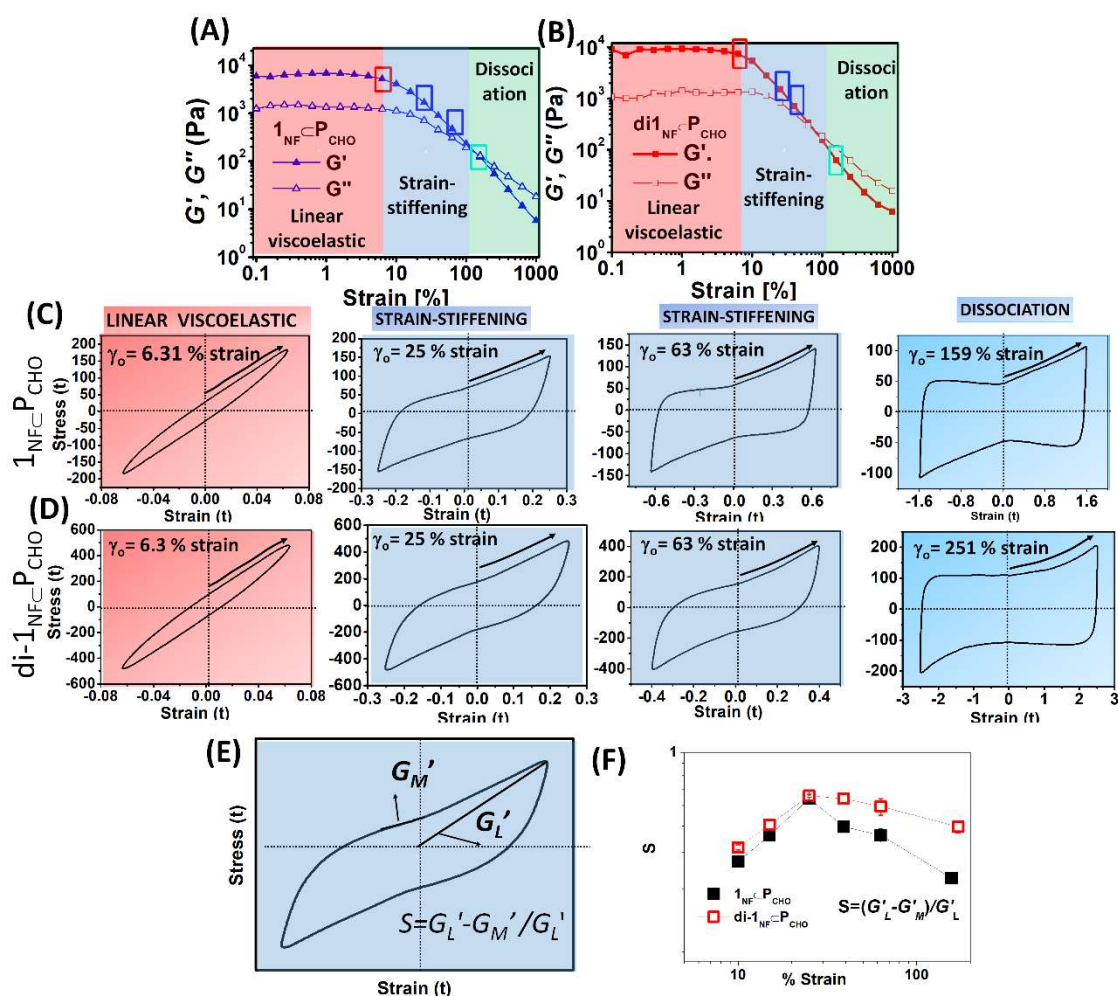


Figure 5.7: Dynamic strain amplitude sweep measurements after heating the networks to 50 °C and cooling back to 25 °C ($c=7$ mM) of (A) $1_{NF-C-P_{CHO}}$ and (B) $di-1_{NF-C-P_{CHO}}$ networks with aldehyde: amine effective functionality ratio of 0.75. (Three regions identified based on the variation in dynamic moduli with strain amplitude (% Strain) *i. e.* linear viscoelastic region, strain-stiffening region, and dissociation region). The Lissajous plots at representative strain amplitudes corresponding to each of the three regions for (C) $1_{NF-C-P_{CHO}}$ and (D) $di-1_{NF-C-P_{CHO}}$ networks (The black arrow in Lissajous plots shows the trend of the curve indicating the strain-stiffening behavior). (E) Schematic representation for the calculation of intracycle stiffening index, S from Lissajous plots, and (F) corresponding changes in S in strain-stiffening region with an increase in strain amplitudes ranges for the covalently fixated and non-fixated network.

of oscillation. At small strains, when the Lissajous plots are elliptical, G'_M and G'_L are equal, At higher strains, if $G'_L > G'_M$, then S is positive, indicating strain-stiffening, and if $G'_L < G'_M$, then S is negative, indicating dissociation. S values obtained from Lissajous plots were

plotted against representative strain amplitude. For non-fixated network ($\mathbf{1}_{NF}\text{-P}_{CHO}$) the strain-stiffening S which was 0 at 6.3% strain, showed onset of strain-stiffening with an increase in S upto 0.6 till 25% strain. Further, the system showed a decrease in strain-stiffening index to 0.25 with an increase in strain amplitude upto 159% till the onset of dissociation (Figure 5.7 F). In the case of fixated network ($\mathbf{di-1}_{NF}\text{-P}_{CHO}$), the strain-stiffening index reached a value of 0.62 at 25% strain that remained with a permanent value of 0.44 even at a higher strain amplitude of 251% at dissociation onset. This observation in corroboration with the prestress protocol indicated the increase in stiffening range of the fixated network due to augmented bending stiffness of the covalently fixated fiber bundles on crosslinking with PNIPAM polymer chains.

The dynamic strain amplitude measurements at a temperature above LCST of the polymer at 35°C showed increase in the G'' as G''/G''_{LVR} overshoot before the dissociation that corresponds to enhanced strain-stiffening due to pulling of the fibers *via* coil to globule transition of the polymer. (Figure 5.8). Covalently fixated $\mathbf{di-1}_{NF}\text{-P}_{CHO}$ peptide-polymer network showed enhanced G''/G''_{LVR} overshoot than $\mathbf{1}_{NF}\text{-P}_{CHO}$ that again underlined the significant effect of covalent fixation on the stiffening mechanism.

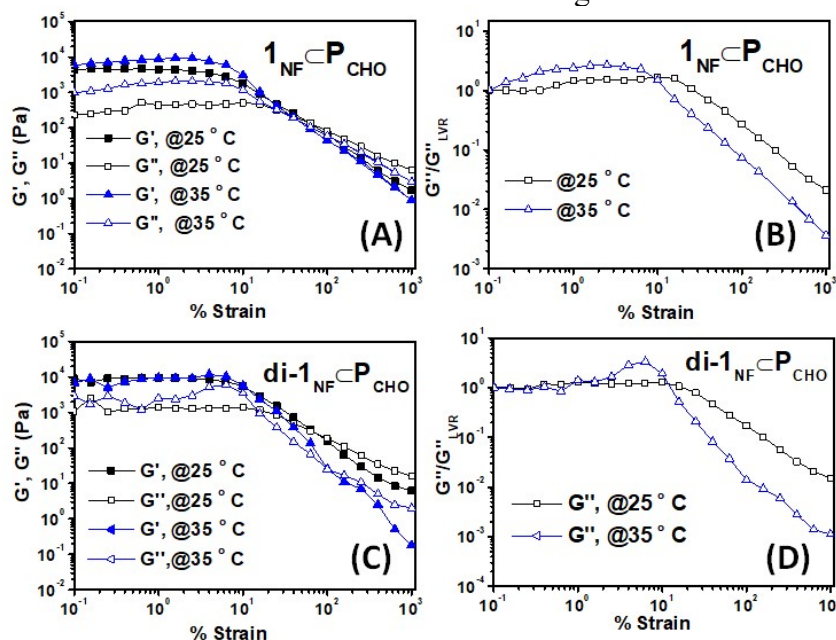


Figure 5.8: Dynamic oscillatory strain amplitude sweep measurements at 25 °C and 35 °C with aldehyde: amine ratio 0.75 and corresponding G''/G''_{LVR} . Graphs for (A&B) $\mathbf{1}_{NF}\text{-P}_{CHO}$ and (C&D) $\mathbf{di-1}_{NF}\text{-P}_{CHO}$ networks (LVR=Linear viscoelastic region, $c=7$ mM)

5.3. Conclusion

In summary, we have shown that chemical crosslinking of 1_{NF} fibers with an aldehyde functionalized polymer P_{CHO} exhibiting LCST behavior endows the resultant network with thermo and stress-responsiveness. The dual strategy of 1_{NF} fibers formed by self-assembling interactions crosslinked by dynamic covalent interactions with polymer crosslinker and reinforcement of the system *via* photo-fixation of nanofibers are introduced. The coil-to-globule transition of P_{CHO} generates internal stress within the $1_{NF} \square P_{CHO}$ matrix that led to an associated network stiffening more than 2 order of magnitude than in ambient temperature. The coil-to globule transition of the linker rigidifies 1_{NF} fibers to rapidly form elastic, strain-stiffening networks. Further, the $1_{NF} \square P_{CHO}$ and photo-fixed $di\text{-}1_{NF} \square P_{CHO}$ network showed an exponential increase in differential modulus with an increase in stress upto several order of magnitude beyond a particular critical stress point. Such critical stress regime and power law relation in mechanical study are comparable with natural biopolymers. Moreover, dynamic strain amplitude sweep measurements on the nonfixated and covalently fixated network samples showed intracycle strain-stiffening within a cycle of deformation of oscillatory strain that lasted upto onset of dissociation at high stress regime. Further, enhanced sensitivity and extensive stiffening under pre-stress conditions and amplitude oscillatory strain measurements in case covalently fixated network indicated the important effect of the increased bending stiffness of the network. Finally, we have demonstrated the control and adaptability of local contractile forces within the microenvironment of a system to improve the mechanical response in a soft material network made from synthetic building blocks to match complex biomechanical functions. This network system formed without the addition of any external cytotoxic catalyst is expected to be promising in comparison with recent reports on making use of such peptide polymer constructs as biomimetic scaffolds for supporting stem cell growth.

5.4. Experimental Section

5.4.1. Materials:

All peptide synthesis reagents and chemicals are discussed in chapter 4. 4-Formyl phenyl methacrylate monomer was synthesized according to previous literature.⁴⁰ All other monomers and reagents *e. g.* N-isopropyl acrylamide(NIPAM), 4-hydroxy benzaldehyde, methacrylic acid, 4-cyano-4-[(dodecyl-sulfanylthiocarbonyl)sulfanyl] pentanoic acid (CDP), 4-dimethyl aminopyridine (DMAP), N, N'-dicyclohexylcarbodiimide, azobisisobutyronitrile (AIBN) were purchased from Sigma and TCI.

5.4.2. Instrumentation:

Solid Phase Peptide Synthesis was performed in Liberty Blue CEM, Matthews, NC, USA, and the synthesized peptide was characterised using a reverse phase C18 column Waters HPLC coupled with Q-TOF MS detector. UV spectra was recorded using Shimadzu UV 6000 UV-vis spectrophotometer in a wavelength range of 800 to 200 nm. NMR spectra were acquired on a 500 MHz Bruker machine. The chemical shifts were reported in ppm with downfield of tetramethylsilane using the resonance of the deuterated solvent as an internal standard. Splitting patterns were designated as singlet (s), doublet (d), triplet (t), and multiplet (m). % functionality of polymer was calculated using the formula, % Functionality = $\{(I_x)/(I_x+I_f)\} \times 100$ where I_x is integral per proton of corresponding functional group, I_f is the integral proton of end group (*e. g.* Isopropyl Methyl group of NIPAM chain). Size exclusion chromatography (SEC) was performed on a Malvern Viscotek instrument having RI detector using T_{6000M}-T₃₀₀₀ column with THF as eluent at 25 °C with a flow rate of 1 mL/min. The results were analysed by using Omniseq software for M_n , M_w PDI by means of the conventional calibration method obtained using polystyrene standards (1-400KDa). Dynamic light scattering measurements were done on Malvern Zetasizer Nano ZS ZEN3600 equipped with a Helium-Neon laser (wavelength, $\lambda = 633$ nm) with backscattering angle of 173°. UV-vis transmittance study was done using Shimadzu UV 6000 UV-vis spectrophotometer in a wavelength range of 800 to 200 nm. UV crosslinking was performed using a UV chamber equipped with 2* 8W UV_B lamp ($\lambda_{max} = 320$ nm, Intensity at 15 cm =

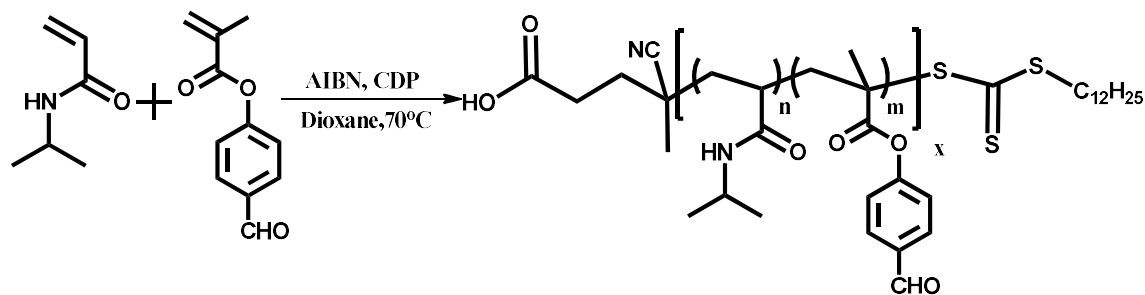
790 $\mu\text{W}/\text{cm}^2$) and the peptide sample in an aqueous solvent state was kept at a distance of 15 cm for irradiation. FTIR spectra were recorded in the range of 4000 to 400 cm^{-1} as an attenuated total reflectance (ATR) mode using Bruker Vertex 70 FTIR spectrophotometer and analysed through Opus Software. The samples were drop cast on a silicon wafer and AFM height images were recorded using tapping mode on a Bruker Multimode 8 scanning probe microscope (Bruker) of a force constant 40 N/m (Tip model RTESPA-300, Bruker) and analyzed using the software NanoScope Analysis 1.5. TEM images were recorded using JEOL JEM 2100 TEM with a Tungsten filament at an accelerating voltage of 120 kV. SAXS experiments were carried out on SAXSess mc^2 instrument (Anton-Paar) with line-collimation system using a Cu $K\alpha$ source with a wavelength of 1.54 Å. Perkin Elmer cyclone image plate recorder was used to record the data. SAXSQuant 2D software was used to reduce the two dimensional data to one dimensional, Intensity (I) vs scattering vector (q) plot. The rheological experiments were conducted using a Stress and strain controlled Anton Paar MCR302 advanced rheometer device equipped with Rheoplus 3.62 software using parallel plate (PP25-2) geometry at a measuring distance of 0.2 mm.

5.4.3. Methods:

5.4.3.1. Synthesis of peptide 1:

Microwave Automated Solid Phase Peptide Synthesizer (Liberty Blue CEM, Matthews, NC, and USA) was used to synthesize peptide 1. The detailed procedure was according to previously reported literature²⁶

5.4.3.2. Synthesis of copolymer of NIPAM and 4-Formyl phenyl metacrylate (P_{CHO})



Scheme 5.2: Synthesis scheme for P_{CHO} using RAFT polymerization

Polymer (**P_{CHO}**) was synthesized through RAFT polymerization: The monomers N-isopropyl acrylamide (NIPAM) (14.1 mmol, 0.8 g) and 4-formylphenyl methacrylate (FPMA) (0.75 mmol, 70 mg) along with initiator azobisisobutyronitrile (AIBN) (0.02 mmol, 5 mg) and CDP (0.074 mmol, 15 mg) as RAFT agent were added in 1.5 mL dioxane. The mixture was degassed by N₂ bubbling. The reaction mixture was further stirred at room temperature under N₂ environment for 24 h. After the reaction, solution was precipitated in cold dry ether followed by centrifugation to get a white precipitate that was dried in vacuum to yield **P_{CHO}** (0.375 g, 43 %)

¹H NMR (500 MHz, D₂O, 298K) δ = 10.0 (s, 1H), 7.90 (s, 2H), 7.48 (s, 2H), 6.3-6.9 (m, 14 H), 3.99 (s, 18 H), 3.21 (s, 20 H), 2.14(broad, 19 H), 1.3-1.87 (broad, 30H), 1.13 (s, 121 H), 0.88 (m, 1H)

GPC (THF, PS standards) *M_n*=15614, *M_w*=19385, *PDI*=1.23

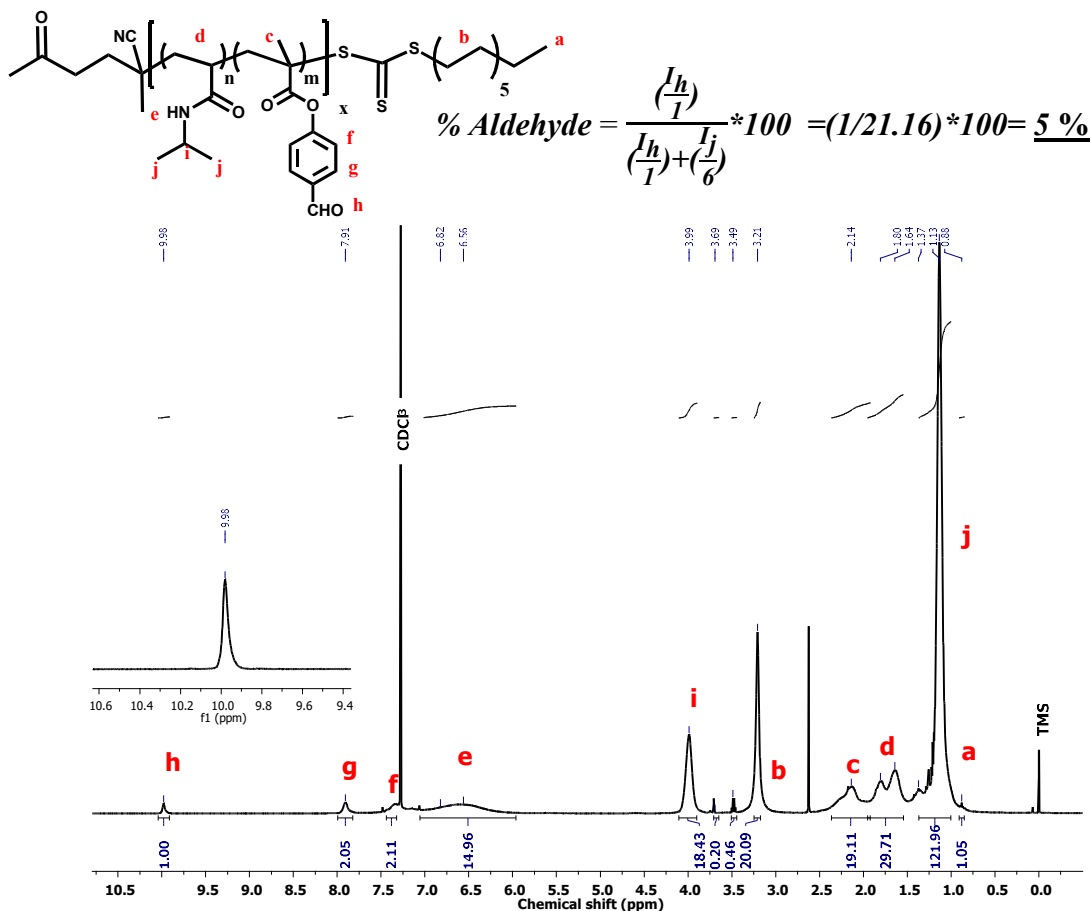


Figure 5.9: ¹H NMR spectrum of **P_{CHO}**

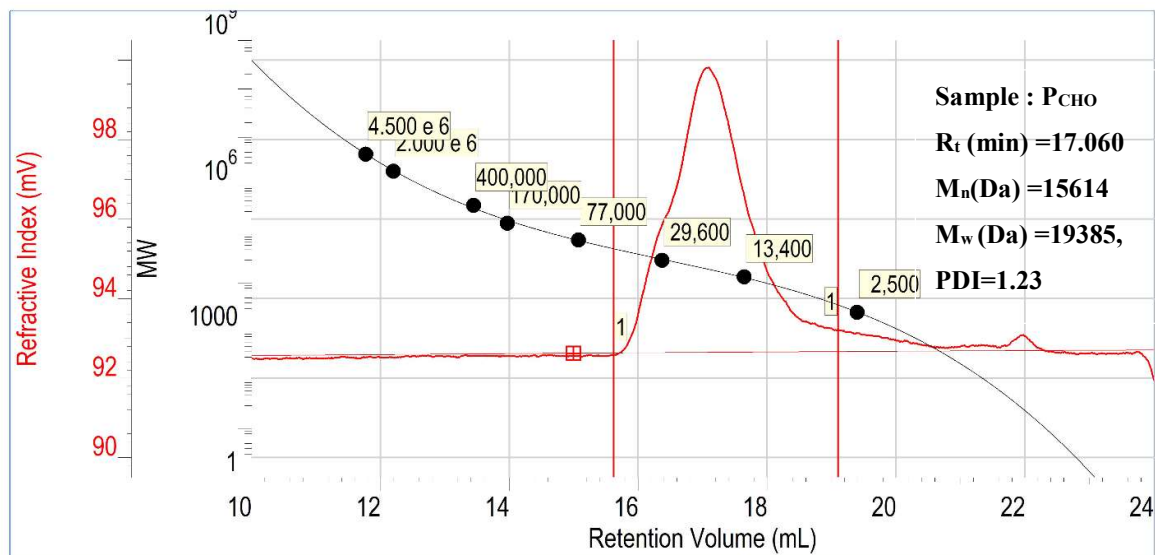


Figure 5.10: GPC trace of PCHO

5.4.3.3. Self-assembly to produce nanofibers: Peptide, **1** which was dissolved in HFIP and dried to remove self-assembly history. Then it was dissolved in water to form a solution at different concentrations at 10 °C. The temperature was raised in a controlled manner using Stuart waterbath (SWB15D) to 25 °C to observe transformation into **1_{NF}** nanofibers. The **1_{NF}** nanofibers solution was kept for UV irradiation ($\lambda = 320$ nm, 8 Watts x 2 UV_B lamp) for 4 h to form covalently fixated **di-1_{NF}** nanofibers.

5.4.3.4. Preparation of peptide-polymer conjugate: **1_{NF}** nanofiber as well as **di-1_{NF}** nanofiber solution was ligated with PCHO solution with 0.75 ratio in terms of effective functionality ratio of aldehyde to amine group at different concentration and incubated overnight to form **1_{NF}-PCHO** and **di-1_{NF}-PCHO** peptider-polymer network.

5.4.3.5. Atomic Force Microscopy (AFM): 15 μ L of 0.2 mM of the sample solution was drop-casted on a silicon wafer. After 5 minutes, the silicon wafer was washed with 500 μ L water to remove the excess sample and it was then left to be air-dried in a desiccator. AFM height images were recorded by tapping mode on a Bruker Multimode 8 scanning probe

microscope with silicon cantilever (Bruker) and analysed using the software NanoScope Analysis 1.5

5.4.3.6. Transmission Electron Microscopy (TEM): 6 μL of sample solution was drop-casted on a 300 mesh carbon-coated copper grid. After ~ 5 min, the excess solution was wicked off by Whatmann filter paper from all edges of the grid carefully. Grids having samples were then dried in the desiccator under vacuum for 1 day. TEM images were recorded using JEOL JEM 2100 with a Tungsten filament at an accelerating voltage of 120 kV.

5.4.3.7. Determination of persistence length: The persistence length of the nanofibers was calculated using the Easyworm software suite, coded in MATLAB. The contour of the nanofibers were fitted into parametric splines after uploading AFM height images. Data collected for 10 fibers was saved in one single .mat file and was uploaded in the second GUI Easyworm2 for the analysis. Easyworm2 allows the calculation of persistence length (L_p).

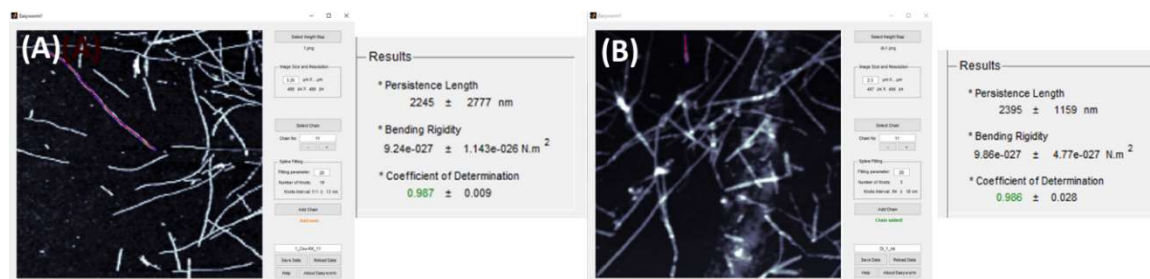


Figure 5.11: Persistence Length determination from AFM images utilizing Easyworm suite for (A) 1_{NF} fibers as well (B) photo-fixated $\text{di-}1_{\text{NF}}$ fibers.

5.4.3.8. Monitoring covalent imine bond formation and photodimerization: 3 mM of 1_{NF} , $\text{di-}1_{\text{NF}}$, $1_{\text{NF}}\text{C}\text{PCHO}$ and $\text{di-}1_{\text{NF}}\text{C}\text{PCHO}$ in D_2O were analysed by ^1H NMR at 298 K and FTIR spectroscopy by monitoring carbonyl peaks. 0.125 mM of 1_{NF} , $\text{di-}1_{\text{NF}}$, $1_{\text{NF}}\text{C}\text{PCHO}$ and $\text{di-}1_{\text{NF}}\text{C}\text{PCHO}$ in D_2O were analysed by UV spectroscopy by monitoring the UV peak at 320 nm.

5.4.3.9. Monitoring LCST by DLS: Aqueous solution of PCHO and 1NFC-PCHO were analysed temperature trend analysis in DLS by heating from 20 to 50 °C at an interval of 2.5 °C to show the aggregation on heating above LCST,

5.4.3.10. Rheological study: For rheological characterization, Anton Paar Rheometer 302 device equipped with Rheoplus ver 3.62 software and Parallel Plate (PP-25) geometry with an adjustable temperature controlling system was utilized. The measuring distance was 0.2 mm and the measuring plate area were covered with solvent trap and the geometry edges were sealed in silicon oil in order to avoid evaporation of the solvent.

Temperature ramp studies: The peptide polymer conjugate 1NFC-PCHO and di-1NFC-PCHO were taken on a measuring plate at 20 °C and the temperature ramp analysis were conducted from 20 to 50 °C at a heating rate of 2 °C/ min keeping oscillatory strain at 1 % and the angular frequency at 10 rad/sec.

Prestress protocol to generate differential modulus: The samples were subjected to a heating cooling cycle (heated of 20 to 50 °C, holding for 4 minutes, and then cooled backed to 25 °C) before the start of the measurement. Then parallel superposition of steady prestress (σ) along with 10 % of oscillatory stress at a constant angular frequency of 6.28 rad/sec gives corresponding oscillatory strain ($\Delta\gamma$). The average linear G' readings obtained from the corresponding flow curve give differential moduli, K' ($\Delta\sigma/\Delta\gamma$) which was plotted against σ values.

Large amplitude Oscillatory strain measurements: The samples were subjected to a heating cooling cycle (heated of 20 to 50 °C, holding for 4 minutes, and then cooled backed to 25 °C) before the start of the measurement. Dynamic oscillatory strain sweep measurements were carried out by varying the strain amplitude (% strain) between 0.1 and 1000% at an angular frequency of 1 rad/sec.

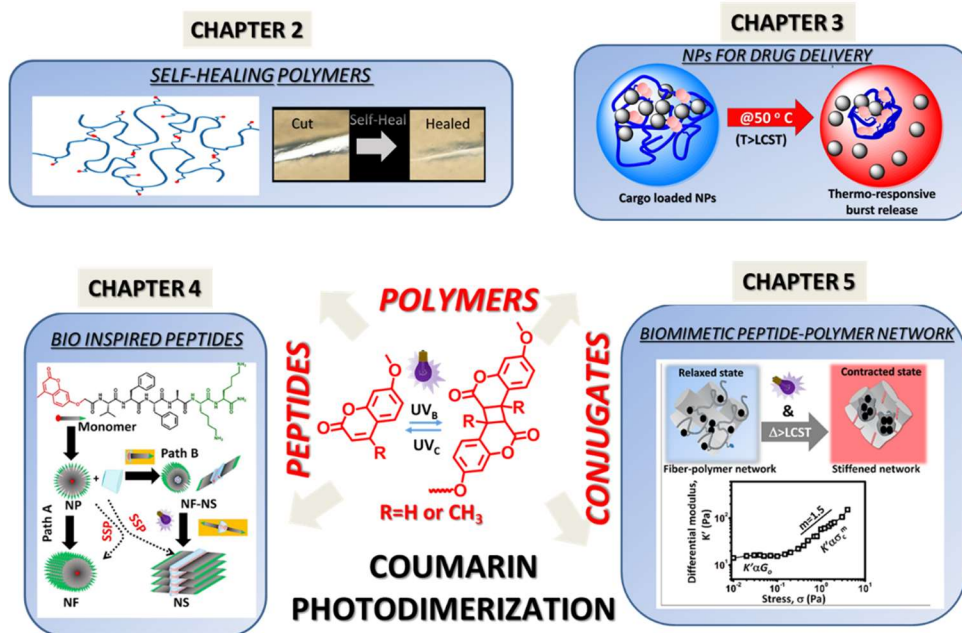
5.5. References

- 1 S. Pina, V. P. Ribeiro, C. F. Marques, F. R. Maia, T. H. Silva, R. L. Reis and J. M. Oliveira, *Materials*, 2019, **12**, 1824.
- 2 S. Bose, M. Roy and A. Bandyopadhyay, *Trends Biotechnol.*, 2012, **30**, 546-554

- 3 M. P. Nikolova and M. S. Chavali, *Bioactive Materials*, 2019, **4**, 271–292.
- 4 B. Bugyi and M. F. Carrier, *Ann. Rev. Biophys.* 2010, **39**, 449-470.
- 5 T. D. Pollard in *Cell Motility: From Molecules to Organisms* (Ed.: A. Ridley, M. Peckham, P. Clark) John Wiley & Sons, Ltd, 2004, pp 1-17.
- 6 T. D. Pollard and G. G. Borisy, *Cell*, 2003. **112**, 453-465
- 7 K. F. Swaney, C. H. Huang and P. N. Devreotes, *Ann. Rev. Bioph.*, 2010, **39**, 265–289.
- 8 M. J. Unterberger, K. M. Schmoller, C. Wurm, A. R. Bausch and G. A. Holzapfel, *Acta Biomater.*, 2013, **9**, 7343–7353.
- 9 M. L. Gardel, J. H. Shin, F. C. MacKintosh, L. Mahadevan, P. Matsudaira and D. A. Weitz, *Science*, 2004, **304**, 1301–1305.
- 10 C. Storm, J. J. Pastore, F. C. MacKintosh, T. C. Lubensky and P. A. Janmey, *Nature*, 2005, **435**, 191–194.
- 11 D. Stamenovic and N. Wang, *J. Appl. Physiol.*, 2000, **89**, 2085–90.
- 12 D. a Fletcher and R. D. Mullins, *Nature*, 2010, **463**, 485–492.
- 13 G. H. Koenderink, Z. Dogic, F. Nakamura, P. M. Bendix, F. C. MacKintosh, J. H. Hartwig, T. P. Stossel and D. A. Weitz, *PNAS*, 2009, **106**, 15192–15197.
- 14 S. V. Mikhailenko, Y. Oguchi and S. Ishiwata, *J. R. Soc. Interface*, 2010, **7**, 295–306.
- 15 S. Ghassemi, G. Meacci, S. Liu, A. A. Gondarenko, A. Mathur, P. Roca-Cusachs, M. P. Sheetz and J. Hone, *PNAS*, 2012, **109**, 5328–5333.
- 16 P. Lacolley, V. Regnault, P. Segers and S. Laurent, *Phys. Rev.*, 2017, **97**, 1555–1617.
- 17 W. A. Lam, O. Chaudhuri, A. Crow, K. D. Webster, T. Li, J. Huang and D. A. Fletcher, *Nat. Mater.*, 2011, **10**, 61–66.
- 18 E. Cudjoe, S. Khani, A. E. Way, M. J. A. Hore, J. Maia and S. J. Rowan, *ACS Cent. Sci.*, 2017, **3**, 886–894.
- 19 M. Jaspers, M. Dennison, M. F. J. Mabesoone, F. C. MacKintosh, A. E. Rowan and P. H. J. Kouwer, *Nat. Commun.*, 2014, **5**, 5808.
- 20 P. H. J. Kouwer, M. Koepf, V. A. A. Le Sage, M. Jaspers, A. M. Van Buul, Z. H. Eksteen-Akeroyd, T. Woltinge, E. Schwartz, H. J. Kitto, R. Hoogenboom, S. J. Picken, R. J. M. Nolte, E. Mendes and A. E. Rowan, *Nature*, 2013, **493**, 651–655.
- 21 B. Yan, J. Huang, L. Han, L. Gong, L. Li, J. N. Israelachvili and H. Zeng, *ACS Nano*, 2017, **11**, 11074–11081.
- 22 M. Fernandez-Castano Romera, R. P. M. Lafleur, C. Guibert, I. K. Voets, C. Storm and R. P. Sijbesma, *Angew. Chem. Int. Ed.*, 2017, **56**, 8771–8775.
- 23 M. Fernández-Castaño Romera, X. Lou, J. Schill, G. Ter Huurne, P. P. K. H. Fransen, I. K. Voets, C. Storm and R. P. Sijbesma, *J. Am. Chem. Soc.*, 2018, **140**, 17547–17555.
- 24 M. Fernández-Castano Romera, R. Göstl, H. Shaikh, G. Ter Huurne, J. Schill, I. K. Voets, C. Storm and R. P. Sijbesma, *J. Am. Chem. Soc.*, 2019, **141**, 1989–1997.
- 25 C. P. Broedersz, C. Storm and F. C. MacKintosh, *Phy. Rev. Lett.*, 2008, **101**, 1–4.

- 26 J. P. Joseph, A. Singh, D. Gupta, C. Miglani and A. Pal, *ACS Appl. Mater. Interfaces*, 2019, **11**, 28213–28220.
- 27 A. Singh, J. P. Joseph, D. Gupta, I. Sarkar and A. Pal, *Chem. Comm.*, 2018, **54**, 10730–10733.
- 28 R. Singh, S. A. Deshmukh, G. Kamath, S. K. R. S. Sankaranarayanan and G. Balasubramanian, *Comput. Mat. Sci.*, 2017, **126**, 191–203.
- 29 L. Tavagnacco, M. Zanatta, E. Buratti, B. Rosi, B. Frick, F. Natali, J. Ollivier, E. Chiessi, M. Bertoldo, E. Zaccarelli, A. Orecchini, *arXiv*, 2007, 11860.
- 30 Y. Wang, Z. Xu, M. Lovrak, V. A. A. le Sage, K. Zhang, X. Guo, R. Eelkema, E. Mendes and J. H. van Esch, *Angew. Chem. Int. Ed.*, 2020, **59**, 4830–4834.
- 31 M. Jaspers, A. C. H. Pape, I. K. Voets, A. E. Rowan, G. Portale and P. H. J. Kouwer, *Biomacromolecules*, 2016, **17**, 2642–2649.
- 32 T. B. Liverpool, M. C. Marchetti, J. F. Joanny and J. Prost, *EPL*, **85**, 18007
- 33 B. Barua, D. A. Winkelmann, H. D. White and S. E. Hitchcock-DeGregori, *PNAS*, 2012, **109**, 18425–18430.
- 34 C. P. Broedersz, K. E. Kasza, L. M. Jawerth, S. Münster, D. A. Weitz and F. C. MacKintosh, *Soft Matter*, 2010, **6**, 4120–4127.
- 35 M. L. Gardel, F. Nakamura, J. H. Hartwig, J. C. Crocker, T. P. Stossel and D. A. Weitz, *PNAS*, 2006, **103**, 1762–1767.
- 36 F. C. Mackintosh, J. Kas and P. A. Janmey, *Phys. Rev. Lett.*, 1995, **75**, 4425.
- 37 S. Rammensee, P. A. Janmey and A. R. Bausch, *Eur. Biophys. J.*, 2007, **36**, 661–668.
- 38 J. John, D. Ray, V. K. Aswal, A. P. Deshpande and S. Varughese, *Soft Matter*, 2019, **15**, 6852–6866.
- 39 K. Bertula, L. Martikainen, P. Munne, S. Hietala, J. Klefström, O. Ikkala and Nonappa, *ACS Macro Letters*, 2019, **8**, 670–675.
- 40 F. García, J. M. García, B. García-Acosta, R. Martínez-Máñez, F. Sancenón and J. Soto, *Chem. Comm.*, 2005, 2790–2792.

Conclusion, Future outlook and Perspectives



Overall, we designed photo-responsive polymeric and peptide systems based on photodimerization chemistry of coumarin moiety for nature mimicking applications. In the second chapter, we developed coumarin functionalized polymeric systems with butyl acrylate side chain and utilized them for modulation of the self-healing behavior in both autonomic and non-autonomic fashion. The third chapter delineates water-soluble NIPAM based thermo-responsive polymers tethered with coumarin groups that undergoes chain collapse *via* either photodimerization or host-guest interaction to form nano compartments. Later, these systems were used for the controlled loading and delivery of cargo molecules. The fourth chapter demonstrates amyloid inspired peptide amphiphile that *via* pathway dependant self-assembly led to the formation of 1D nanofibers and 2D nanosheets. The growth of the nanostructures was controlled by seeded supramolecular polymerization. The system also demonstrated perfect control in modulating the strength of resulting hydrogels

and exhibited excellent environment-friendly exfoliation of MoS₂. Finally, we showed a peptide-polymer system that forms conjugate network and exhibited stiffening under heat, stress conditions which are analogous to natural biopolymer network.

The coherent design of the photo-modulated polymer self-healing system discussed in chapter 1 disclosed the coexistence of autonomic and non-autonomic self-healing pathways and such photo-tunable self-healing behaviour in low viscosity processible might be substantially utilized as a smart coating of photovoltaic devices. Additionally, efforts are being driven to modify the coating with different photochemistry so that the resultant self-healing coating can be ultra-hydrophobic, water repellent and can efficiently trap the UV spectrum of sunlight so that only visible light is transmitted to the cells for energy harvesting. Next, a clever design of versatile zero-dimensional polymeric material formed by single-chain technology and chain collapse can act as nano compartments for controlled loading and result in sustained to the thermo-responsive on-demand release of versatile cargos. Further, it is predicted that the system can be translated as a smart design of remotely controlled shape-changing nanosystems for soft actuator applications in microfluidic platforms due to its effectiveness at low concentration and volume regimens. Moreover, the design of block copolymers is in progress that can chain collapse to form tadpole nanostructures which may improve the compartmental efficiency and fidelity of the system in a nanoconfined environment.

The elegant pathway-dependent self-assembly of peptide amphiphile to differentiate in 1D and 2D supramolecular polymeric nanostructures and the structural adaptive control over the resulting peptide materials could further be exploited for controlling the stiffness of the crosslinked hierarchical three-dimensional hydrogel network. The adaptive flexibility and surface charges of the material utilized for metal chalcogenides exfoliation make them suitable for organoelectronics and device fabrication application. Further efforts are underway to design peptide materials with photoresponsive materials in the NIR-vis region and thus utilize them for application as the smart synthetic matrix for tissue engineering applications. Though living supramolecular polymerization to control the dimension of supramolecular nanostructures demonstrated here are efficient, our systems are quite restricted in the choice of the monomer structures and lack any fuel-driven approach. Efforts

are underway to kinetically trap the monomer in the dormant state *via* photo controlled dormant-active seed concept, redox controlled oxidative agent fuelled supramolecular polymerisation *etc.* Further, the chiral nature of our peptide system can be efficiently mitigated to form helical nanostructures that can be utilized for the magneto-optic effect. Additionally, the control of local contractile forces like temperature and light stimuli within the microenvironment of the system to render a mechanoresponsive synthetic peptide polymer conjugate network to mimic biomechanical functions like strain-stiffening is a promising effort in this thesis work. Further investigation of various stiffening strategies such as mineralization of peptide fibers with bioglass material, tuning semi-flexible nature of the fiber through living supramolecular polymerization, enhanced flexibility of crosslinkers, increase in crosslinking sites *via* modification of peptide design *etc.* are underway in our lab for the fundamental understanding of strain-stiffening response. Also, cellular response for the nanomechanical changes in thus developed extracellular matrix mimetic materials will be examined towards the cell compatibility relative to their native components as in the bioenvironment. Thus, this thesis opens some new paradigms in the broad fields of functional materials, drug delivery, polymer and peptide self-assembly, biomimetic organoelectric and cellular matrix materials.

Publications

1. *Tandem interplay of the host-guest interaction and photo-responsive supramolecular polymerization to 1D and 2D functional peptide materials. **Joseph J. P.**; Singh, A.; Gupta, D.; Miglani, C.; Pal, A. *ACS Appl. Mater. Interfaces*, 2019, **11**, 28213–28220.
2. *Photoresponsive chain collapse in flexo-rigid functional copolymer to modulate self-healing behavior. **Joseph, J. P.**; Miglani, C.; Singh, A.; Gupta, D.; Pal, A. *Soft Matter*, 2020, **16**, 2506-2515.
3. *Delineating synchronized control of dynamic covalent and noncovalent interactions for polymer chain collapse towards cargo localization and delivery. **Joseph J. P.**; Miglani, C.; Bhatt A.; Ray D.; Singh, A.; Gupta, D.; Aswal V. K.; Pal, A. *Polym. Chem.*, 2021,**12**, 1002-1013.
4. *External cues mediated stiffening in peptide–polymer conjugate to mimick contractility in actinomyosine network. **Joseph J. P.**; Gupta, N.; Miglani, C.; Singh, A.; Gupta, D.; Pal, A. (Under review)
5. Pathway driven self-assembly and living supramolecular polymerization in amyloid-inspired peptide amphiphile. Singh, A.; **Joseph J. P.**; Gupta, D.; Sarkar, I.; Pal, A. *Chem. Comm.*, 2018, **54**, 10730-10733.
6. Supramolecular gels from sugar-linked triazole amphiphiles for drug entrapment and release for topical application. Sharma K.; **Joseph J. P.**; Sahu, A.; Yadav N.; Tyagi, M.; Singh, A.; Pal, A., Kartha K. P. R. *RSC Adv.*, 2019, **9**, 19819-19827.
7. Enzyme responsive chiral self-sorting in amyloid-inspired minimalistic peptide amphiphiles. Gupta, D.; Sasmal, R.; Singh, A.; **Joseph, J. P.**; Miglani, C.; Agasti, S. S.; Pal, A. *Nanoscale*, 2020, **12**, 18692-18700.
8. Pathway-driven peptide-bioglass nanocomposites as dynamic and self-healable matrix. Gupta, N.; Singh, A.; Dey, N.; Chattopadhyay, S.; **Joseph, J. P.**; Gupta, D.; Ganguli, M.; Pal A. *Chem. Mater.*, 2021, **33**, 2, 589–599.

9. Complexation of Azo Dye by Cyclodextrins; a Potential Strategy for Water Purification, Saifi, A.; **Joseph, J. P.**; Singh, A. P.; Pal, A.; Kumar K. *ACS Omega*, 2021, **6**, 4776–4782.
10. Photo-thermally Tuned Peptide Nanostructures towards Modulating Catalytic Hydrolase Activity. Singh, A.; **Joseph, J. P.**; Gupta, D.; Miglani, C.; Mavlanker, N.; Pal, A. 2021. (Under review)
11. Dictating fate by photochemical cues: Dormant monomers for controlled self-assembly disassembly in peptide amphiphiles. Gupta, D.; Bhatt. A.; Miglani, C.; **Joseph, J. P.**; Singh, A.; Ali, M. E.; Pal, A. Under preparation.
12. Photoresponsive thymine grafted self-healing polymers for smart coating materials. Miglani, C.; **Joseph, J. P.**; Gupta, D.; Singh, A.; Pal, A. 2021. (Under review).
13. Tunable hydrogel from dynamic interpenetrated supramolecular peptide–polysaccharide network for chondrocytes subsistence. Thomas, J.; Gupta, N.; **Joseph, J. P.**; Pal, A.; Ghosh D. Under preparation.
14. Book Chapter on “Molecular design approach to self-healing material from polymer and its composites” by Springer. **Joseph J. P.**, Singh, A., Pal, A. 2017.

(N.B. * Articles included in this thesis)

Curriculum Vitae

Jojo P. Joseph

Ph.D. Research Scholar

Institute of Nano Science and Technology (INST) &

Indian Institute of Science Education and Research (IISER) Mohali

Punjab, India



Jojo P. Joseph completed B. Pharma in 2012 from Kerala university and M. Pharma in Pharmaceutical chemistry in 2014 from Kerala university of Health sciences. He joined the third batch of PhD scholars at Institute of Nano Science and Technology (INST) and registered with Indian Institute of Science Education and Research Mohali on 28th July, 2015. His research interests include synthesis of stimuli-responsive polymers and peptides, understanding their self-assembly and utilize for biomimetic applications. He authored several research articles in reputed international journals. He has presented his research work in several national and international conferences.